

**APPLICATIONS OF MULTI-RESONANCE BROADBAND ROTATIONAL
SPECTROSCOPY TO INTERSTELLAR AND COMBUSTION
CHEMISTRY**

by

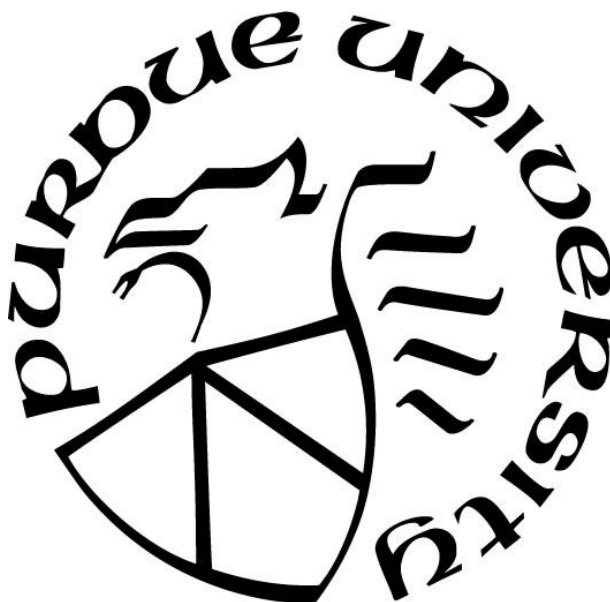
Sean M. Fritz

A Dissertation

Submitted to the Faculty of Purdue University

In Partial Fulfillment of the Requirements for the degree of

Doctor of Philosophy



Department of Chemistry

West Lafayette, Indiana

May 2020

THE PURDUE UNIVERSITY GRADUATE SCHOOL
STATEMENT OF COMMITTEE APPROVAL

Dr. Timothy Zwier, Chair

Department of Chemistry

Dr. Scott A McLuckey

Department of Chemistry

Dr. Libai Huang

Department of Chemistry

Dr. Paul Wenthold

Department of Chemistry

Approved by:

Dr. Christine Hrycyna

To My Family

ACKNOWLEDGMENTS

I would like to thank everyone who played a part in my journey from just a young buck to Dr. Fritz. First, I would like to thank Tim for accepting and mentoring me over the years. I really learned a lot from you and we both became more proficient in microwave spectroscopy together over the course of several projects. Next, my dearest regards to my microwave companions: Brian, Chamara, Alicia, Piyush, Iciar and Sven. I learned everything from the best in the business and was placed in an excellent position to succeed and secure a big bag. Big shout out to the laser lab as it was a blast to work with you guys as well. I would also like to thank all of my family and friends, especially my mom and dad, for believing in me and taking this ride with me as well. Your support never went unnoticed. Lastly, I need to thank my baby boy Clancy for being the best company a graduate student could ask for as you were always happy to see me every time I came home. Big fun and big chilling with you dude, I will never forget our time at Purdue. Love you buddy.

TABLE OF CONTENTS

TABLE OF CONTENTS.....	5
LIST OF TABLES.....	8
LIST OF FIGURES	10
ABSTRACT.....	14
CHAPTER 1. INTRODUCTION	17
1.1 Rotational Spectroscopy	17
1.2 Chirped-Pulse Fourier Transform Microwave Spectroscopy	18
1.3 Applications of Multi-Resonance CP-FTMW Spectroscopy	19
1.4 Organization of Thesis	21
1.5 References.....	21
CHAPTER 2. EXPERIMENTAL.....	23
2.1 Supersonic Expansion.....	23
2.2 Flash Pyrolysis.....	23
2.3 Multiplexed characterization of complex gas-phase mixtures combining chirped-pulse Fourier transform microwave spectroscopy and VUV photoionization time-of-flight mass spectrometry.....	26
2.3.1 Introduction.....	26
2.3.2 Apparatus	29
2.3.2.1 Pumping System.....	29
2.3.2.3 VUV photoionization Time-of-Flight Mass Spectrometer section	32
2.3.3 Characterization of Instrumental Capabilities	35
2.3.3.1 Furanic Mixture.....	35
2.3.3.2 Pyrolysis mixture.....	40
2.3.4 Conclusion	44
2.4 References.....	45
CHAPTER 3. CONFORMER-SPECIFIC MICROWAVE SPECTROSCOPY OF 3- PHENYLPROPIONITRILE BY STRONG FIELD COHERENCE BREAKING	48
3.1 Introduction.....	48
3.2 Experimental	50

3.2.1	Broadband Spectrum	50
3.2.2	Computations	50
3.2.3	Conformer-Specific Spectra	51
3.3	Results	53
3.3.1	Spectral Assignment	53
3.3.2	<i>Anti</i> -3-phenylpropionitrile	54
3.3.3	<i>Gauche</i> -3-phenylpropionitrile	56
3.4	Discussion	57
3.5	Conclusion	64
3.6	References	64
3.7	Supplementary Material	66
CHAPTER 4. STRONG FIELD COHERENCE BREAKING AS A TOOL FOR IDENTIFYING METHYL ROTOR STATES: 2-HEXANONE		70
4.1	Introduction	70
4.2	Experimental	73
4.2.1	Broadband Spectrum	73
4.2.2	Computations	74
4.2.3	Strong Field Coherence Breaking	75
4.3	Results	77
4.4	Discussion	80
4.5	Conclusions	82
4.6	References	83
4.7	Supplementary Material	85
CHAPTER 5. MEASURING COMBUSTION INTERMEDIATES VIA BROADBAND CHIRPED-PULSE MICROWAVE SPECTROSCOPY		90
5.1	Introduction	90
5.2	Experimental Procedures	92
5.3	Results and Discussion	95
5.4	Conclusion	101
5.5	References	102

CHAPTER 6. CONTINUING PROMISING EXPERIMENTS: PENTANAL, TRANS-2-PENTENAL AND <i>o</i> -, <i>m</i> -, and <i>p</i> -VINYLANISOLE.....	105
6.1 Introduction.....	105
6.2 Experimental.....	107
6.3 Results.....	110
6.3.1 Pentanal.....	110
6.3.2 <i>trans</i> -2-pentenal.....	112
6.3.3 <i>p</i> -Vinylanisole.....	115
6.3.4 <i>m</i> -Vinylansiole.....	116
6.3.5 <i>o</i> -Vinylanisole.....	118
6.4 Discussion.....	119
6.5 Conclusions.....	124
6.6 References.....	125
6.7 Supplementary Material.....	127
APPENDIX.....	143
PUBLICATIONS.....	148

LIST OF TABLES

Table 3.1 Molecular structure constants for <i>anti</i> and <i>gauche</i> conformers determined experimentally and calculated at the DFT B2PLYP-D3BJ/aug-cc-pVTZ level of theory	59
Table 3.2 Percent errors in rotational constants calculated at the B2PLYP-D3BJ/aug-cc-pVTZ, B3LYP/def-2TZVP and MP2/6-311++G (d,p) levels of theory.....	61
Table 3.3 Rotational transitions assigned in the final fit for <i>anti</i> -3-phenylpropionitrile. Frequencies reported are experimental and the error is calculated after fitting with Pickett's SPFIT program.	66
Table 3.4 Rotational transitions assigned in the final fit for <i>anti</i> -3-phenylpropionitrile. Frequencies reported are experimental and the error is calculated after fitting with Pickett's SPFIT program.	68
Table 4.1 Experimentally determined structural parameters of the three identified conformations of 2-hexanone.....	80
Table 4.2 Observed A and E species frequencies ($\nu_{\text{Obs.}}$) of 51 rotational transitions of the <i>tgt</i> conformer of 2-hexanone. $\nu_{\text{Obs.}} - \nu_{\text{Calc.}}$ values as obtained after a fit with the program XIAM.....	87
Table 4.3 Observed A and E species frequencies ($\nu_{\text{Obs.}}$) of 18 rotational transitions of the <i>tgt</i> conformer of 2-hexanone. $\nu_{\text{Obs.}} - \nu_{\text{Calc.}}$ values as obtained after a fit with the program XIAM.....	88
Table 4.4 Observed A and E species frequencies ($\nu_{\text{Obs.}}$) of 31 rotational transitions of the <i>ttt</i> conformer of 2-hexanone. $\nu_{\text{Obs.}} - \nu_{\text{Calc.}}$ values as obtained after a fit with the program XIAM.....	88
Table 5.1 Flow conditions of the jet stirred reactor. Stoichiometry, residence time (in ms), pressures (in mbar), argon dilution in %, and ozone concentration in ppm of the JSR experiments.	93
Table 6.1 Experimentally determined structural parameters of the four identified conformations of pentanal	120
Table 6.2 Experimentally determined structural parameters of the two identified conformations of <i>trans</i> -2-pentenal	123
Table 6.3 Experimentally determined structural parameters of the two identified conformations of <i>p</i> - and <i>m</i> -vinylanisole and the single conformation of <i>o</i> -vinylanisole.....	124
Table 6.4 Observed frequencies ($\nu_{\text{Obs.}}$) of 26 rotational transitions of the <i>syn trans trans</i> conformer of pentanal. $\nu_{\text{Obs.}} - \nu_{\text{Calc.}}$ values as obtained after a fit with the program SPFIT/SPCAT.....	127
Table 6.5 Observed frequencies ($\nu_{\text{Obs.}}$) of 20 rotational transitions of the <i>syn trans gauche</i> conformer of pentanal. $\nu_{\text{Obs.}} - \nu_{\text{Calc.}}$ values as obtained after a fit with the program SPFIT/SPCAT.	128

Table 6.6 Observed frequencies ($\nu_{\text{Obs.}}$) of 27 rotational transitions of the <i>syn gauche trans</i> conformer of pentanal. $\nu_{\text{Obs.}} - \nu_{\text{Calc.}}$ values as obtained after a fit with the program <i>SPFIT/SPCAT</i>	128
Table 6.7 Observed frequencies ($\nu_{\text{Obs.}}$) of 8 rotational transitions of the <i>eclipsed gauche trans</i> conformer of pentanal. $\nu_{\text{Obs.}} - \nu_{\text{Calc.}}$ values as obtained after a fit with the program <i>SPFIT/SPCAT</i>	129
Table 6.8 Observed frequencies ($\nu_{\text{Obs.}}$) of 23 rotational transitions of the <i>trans eclipsed</i> conformer of <i>trans</i> -2-pentenal. $\nu_{\text{Obs.}} - \nu_{\text{Calc.}}$ values as obtained after a fit with the program <i>SPFIT/SPCAT</i>	130
Table 6.9 Observed frequencies ($\nu_{\text{Obs.}}$) of 23 rotational transitions of the <i>trans syn</i> conformer of <i>trans</i> -2-pentenal. $\nu_{\text{Obs.}} - \nu_{\text{Calc.}}$ values as obtained after a fit with the program <i>SPFIT/SPCAT</i> . ..	131
Table 6.10 Observed frequencies ($\nu_{\text{Obs.}}$) of 71 rotational transitions of the <i>up up</i> conformer of <i>p</i> -vinylanisole. $\nu_{\text{Obs.}} - \nu_{\text{Calc.}}$ values as obtained after a fit with the program <i>SPFIT/SPCAT</i>	132
Table 6.11 Observed frequencies ($\nu_{\text{Obs.}}$) of 77 rotational transitions of the <i>up down</i> conformer of <i>p</i> -vinylanisole. $\nu_{\text{Obs.}} - \nu_{\text{Calc.}}$ values as obtained after a fit with the program <i>SPFIT/SPCAT</i>	134
Table 6.12 Observed frequencies ($\nu_{\text{Obs.}}$) of 82 rotational transitions of the <i>up up</i> conformer of <i>m</i> -vinylanisole. $\nu_{\text{Obs.}} - \nu_{\text{Calc.}}$ values as obtained after a fit with the program <i>SPFIT/SPCAT</i>	136
Table 6.13 Observed frequencies ($\nu_{\text{Obs.}}$) of 96 rotational transitions of the <i>up down</i> conformer of <i>m</i> -vinylanisole. $\nu_{\text{Obs.}} - \nu_{\text{Calc.}}$ values as obtained after a fit with the program <i>SPFIT/SPCAT</i>	138
Table 6.14 Observed frequencies ($\nu_{\text{Obs.}}$) of 72 rotational transitions of <i>o</i> -vinylanisole. $\nu_{\text{Obs.}} - \nu_{\text{Calc.}}$ values as obtained after a fit with the program <i>SPFIT/SPCAT</i>	141

LIST OF FIGURES

Figure 2.1 Flash pyrolysis micro-reactor assembly used to thermally decompose samples entrained in buffer gas.	25
Figure 2.2 (a) Assembly drawing of the combined CP-FTMW/TOFMS vacuum chamber in a 3D rendering, (b) a side-on cross-section view and enhanced view of the Wiley-McLaren region, (c) an enhanced view of the skimmer and Wiley-McLaren extraction region, and (d) a close up of the VUV cell. Components labelled: (1) pulsed valve, (2) broadcasting horn, (3) receiving horn, (4) VUV cell, (5) TOF tube, (6) skimmer, (7) repeller plate, (8) draw-out-grid.....	31
Figure 2.3 Schematic diagram of the chirped-pulse Fourier Transform microwave electronics for broadband acquisition over the 2-8 and 8-18 GHz regions. Components unique to the 2-8 GHz range are shown in blue, while those used only for generation and detection in the 8-18 GHz range are in red. All other components are common to the two frequency ranges.	34
Figure 2.4 (a) Broadband CP-FTMW spectrum of a gas-phase mixture of 2-methoxyfuran, furfuryl alcohol, and furfural, compared to the microwave transitions for the three molecules using known experimental rotational constants. ²¹⁻²³ The inset shows a close-up view of three transitions due to the three components of the mixture, demonstrating the isomer specificity afforded by the high resolution of the method. (b) Time-of-flight mass spectrum following 118 nm VUV photoionization of this same mixture.....	36
Figure 2.5 The Boltzmann plot for 2-methoxyfuran. The rotational temperature was calculated to be 1.30 (± 0.09) K	38
Figure 2.6 The Boltzmann plot for furfuryl alcohol. The rotational temperature was calculated to be 1.12 (± 0.10) K	39
Figure 2.7 The Boltzmann plot for furfural. The rotational temperature was calculated to be 0.89 (± 0.09) K.....	39
Figure 2.8 (a) 118 nm photoionization TOF mass spectrum at the indicated SiC wall temperatures for flash pyrolysis of <i>o</i> -guaiacol. (b) CP-FTMW spectrum in a small frequency window around the $3_{2,1}$ - $2_{2,0}$ transition of the <i>o</i> -hydroxyphenoxy radical. The transitions in blue are split due to coupling of the electron spin angular momentum with the molecules rotational angular momentum. (c) CP-FTMW spectra in small frequency regions around microwave transitions due to cyclopentadienone (right) and vinylacetylene (left).	43
Figure 3.1 Schematic diagram of the reaction of benzyl radical with cyanomethyl radical to form 3-phenylpropionitrile.	48
Figure 3.2 Schematic Diagram for the modified Strong Field Coherence Breaking scheme.....	52
Figure 3.3 ((a) and (b)): Broadband CP-FTMW spectra of 3-phenylpropionitrile over the 8-18 GHz region produced by sweeping in the forward direction (black) and in the reverse direction (red) while at (a) 10% TWTA and (b) 100% TWTA power (~ 200 W).....	54

Figure 3.4 ((a) and (b)): Conformer-specific spectra for (a) <i>anti</i> and (b) <i>gauche</i> conformers of 3-PPN using the modified line picking scheme. Black lines display simulated spectra. Transitions whose intensities are modulated by more than 10% are displayed in red and blue.....	55
Figure 3.5 (a) Comparison of the experimental broadband spectrum of 3-PPN under LFP conditions (black trace) with the final fit for both conformers. The red lines belong to the <i>gauche</i> conformer and the blue lines belong to the <i>anti</i> conformer. (b) Hyperfine structure present in the <i>gauche</i> conformer. (c) Demonstration of the absence of hyperfine structure in the <i>anti</i> conformer.	56
Figure 3.6 The Boltzmann plot for <i>gauche</i> -3-propionitrile. The rotational temperature was calculated to be 1.17 (± 0.24) K.....	60
Figure 3.7 The Boltzmann plot for <i>gauche</i> -3-propionitrile. The rotational temperature was calculated to be 1.48 (± 0.10) K.....	61
Figure 3.8 Difference spectra demonstrating the new line picking scheme and its advantages for modulating the intensities of more transitions when multiple single-frequency coherence-breaking pulses (SFP) are applied. The red and blue spectra show the modulated transitions due to just one SFP applied after the broadband chirp, resonant with a microwave transition of a single conformer. The black spectrum shows the transitions modulated by application of both SFPs after the chirp. Five new lines appear in this difference spectrum.....	62
Figure 4.1 Top down and side views of the four lowest energy conformers of 2-hexanone predicted at the B3LYP/Def2TZVP level of theory, including Grimme's dispersion correction.	73
Figure 4.2 Experimental 1M average broadband spectrum of 2-hexanone with the best fits of the three identified conformers present. The blue, red and green lines are assigned to the <i>tgt</i> , <i>ttt</i> and <i>ttg</i> conformers, respectively.....	75
Figure 4.3 ((a) and (b)): Conformer-specific and methyl rotor specific spectra for the 0a ₁ methyl rotor state of the (a) all <i>trans</i> and (b) <i>tgt</i> conformers of 2-hexanone using strong field coherence breaking. Black lines are simulated spectra. Transitions whose intensities were modulated by more than (a) 35% and (b) 25% are displayed in red and blue, respectively. ((c) and (d)): Conformer-specific and internal methyl rotor specific spectra for the 1e methyl rotor states of (c) <i>tgt</i> and (d) all <i>trans</i> conformers of 2-hexanone using strong field coherence breaking. Black lines are observed e-state transitions in the spectrum. Transitions whose intensities were modulated by more than (c) 50% and (d) 40% are displayed in blue and red, respectively. Asterisks denote the resonant single frequencies used in the experiment.....	77
Figure 4.4 The Boltzmann plot for the <i>ttt</i> conformer of 2-hexanone. The rotational temperature was calculated to be 0.9 (± 0.11) K	85
Figure 4.5 The Boltzmann plot for the <i>tgt</i> conformer of 2-hexanone. The rotational temperature was calculated to be 1.48 (± 0.10) K	86
Figure 4.6 The Boltzmann plot for the <i>ttg</i> conformer of 2-hexanone. The rotational temperature was calculated to be 0.87 (± 0.17) K	86
Figure 5.1 Schematic of the experimental set-up, which consists of the gas-delivery system, the jet-stirred reactor and the microwave spectrometer.....	92

Figure 5.2 Schematic representation of the strong-field coherence breaking approach to identify rotational transitions that belong to the same molecular structure. Short pulses of intense microwave radiation of specific frequencies are used to break the coherence that was generated by the initial broadband microwave sweep. Via comparison to the unperturbed FID, difference spectra are formed that reveal a set of rotational transitions due to a single species in the mixture..... 95

Figure 5.3 Broad-band rotational spectra from 8 to 18 GHz after sampling from a reacting mixture of (a) DME/O₂/Ar at 580 K, (b) DMM/O₂/Ar at 700 K, and (c) C₂H₄/O₂/O₃/Ar at 298 K. The observed differences are indicative of the different mixture compositions sampled from the reactive mixture. See text for details concerning their assignments to specific molecular structures. 96

Figure 5.4 The unique identification capabilities of broad-band microwave spectroscopy is shown by identification of (a) the 2_{1,1}-2_{1,2} transition of dimethyl ether, (b) the 2_{1,1}-2_{1,2} transition of formaldehyde, (c) the 1_{0,1}-0_{0,0} transition of methyl formate, and (d) the 2_{1,2}-1_{1,1} transition of formic acid anhydride after sampling from reactive mixtures. 98

Figure 5.5 Upper trace: Broadband microwave spectra after sampling from the DME/O₂/Ar mixture. Lower trace: Difference spectra after implementation of the SFCB method. The six transitions whose intensities were modulated by more than 20% are marked. Numbers denote the single frequency pulses used in the experiment..... 100

Figure 6.1 Structural representation of pentanal and *trans*-2-pentanal..... 106

Figure 6.2 Structural representation of *p*-, *m*- and *o*-vinylanisole 107

Figure 6.3 Side views of the four lowest energy conformers of pentanal predicted at the B3LYP/Def2TZVP level of theory, including Grimme's dispersion correction..... 109

Figure 6.4 Side views of the five identified structures of *p*-, *m*- and *o*-vinylanisole predicted at the B3LYP/Def2TZVP level of theory, including Grimme's dispersion correction..... 109

Figure 6.5 Experimental 1M average broadband spectrum of pentanal with the best fits of the four identified conformers present. The blue, red, green and purple lines are assigned to the *syn gauche trans*, *trans trans*, *trans gauche* and *eclipsed gauche trans* conformers, respectively. 111

Figure 6.6 ((a) and (b)): Conformer-specific spectra of the (a) *syn gauche trans* and (b) *syn trans trans* conformers of pentanal using strong field coherence breaking. Black lines are simulated spectra. Transitions whose intensities were modulated by more than (a) 30% and (b) 40% are displayed in blue and red, respectively. 112

Figure 6.7 Side views of the four lowest energy conformers of pentanal predicted at the B3LYP/Def2TZVP level of theory, including Grimme's dispersion correction..... 113

Figure 6.8 Experimental 1M average broadband spectrum of *trans*-2-pentenal with the best fits of the two identified conformers present. The blue and red lines are assigned to the *trans syn* and *trans eclipsed* conformers, respectively..... 114

Figure 6.9 ((a) and (b)): Conformer-specific spectra of the (a) *trans eclipsed* and (b) *trans syn* conformers of *trans*-2-pentenal using strong field coherence breaking. Black lines are simulated spectra. Transitions whose intensities were modulated by more than (a) 50% and (b) 30% are displayed in red and blue, respectively. 115

Figure 6.10 Experimental broadband spectrum of <i>p</i> -vinylanisole with the best fits of the two identified conformers present. The blue and red lines are assigned to the <i>up down</i> and <i>up up</i> conformers, respectively.	116
Figure 6.11 Experimental broadband spectrum of <i>m</i> -vinylanisole with the best fits of the two identified conformers present. The green and purple lines are assigned to the <i>up up</i> and <i>up down</i> conformers, respectively.	117
Figure 6.12 Experimental broadband spectrum of <i>o</i> -vinylanisole with the best fit of the only structure present in orange.	119

ABSTRACT

The chemical complexity of the interstellar medium and combustion environments pose a challenge to the scientific community seeking to provide a molecular understanding of their combustion. More refined spectroscopic tools and methodologies must be developed to selectively detect and characterize the widening array of fuel and interstellar species. The direct relationship between molecular structure and rotational frequencies makes rotational spectroscopy highly structural specific; therefore, it offers a powerful means of characterizing polar molecules. However, rotational spectra usually contain transitions from multiple components with multiple conformations as well as other dynamical properties interleaved with one another, making the assignment of the spectra very challenging. This thesis describes experimental work using broadband microwave spectroscopy and vacuum ultraviolet time-of-flight mass spectrometry to address a number of challenging problems in the spectroscopy of gas complex mixtures.

In the first part of my work, we report details of the design and operation of a single apparatus that combines Chirped-Pulse Fourier Transform Microwave spectroscopy (CP-FTMW) with VUV photoionization Time-of-Flight Mass Spectrometry (VUV TOFMS). The supersonic expansion used for cooling samples is interrogated first by passing through the region between two microwave horns capable of broadband excitation and detection in the 2-18 GHz frequency region of the microwave. After passing through this region, the expansion is skimmed to form a molecular beam, before being probed with 118 nm (10.5 eV) single-photon VUV photoionization in a linear time-of-flight mass spectrometer. The two detection schemes are powerfully complementary to one another. CP-FTMW detects all components with significant permanent dipole moments. Rotational transitions provide high-resolution structural data. VUV TOFMS provides a gentle and general method for ionizing all components of a gas phase mixture with ionization thresholds below 10.5 eV, providing their molecular formulae. The advantages, complementarity, and limitations of the combined methods are illustrated through results on two gas-phase mixtures made up of (i) three furanic compounds, two of which are structural isomers of one another, and (ii) the effluent from a flash pyrolysis source with *o*-guaiacol as precursor.

The broadband spectrum of 3-phenylpropionitrile was recorded under jet-cooled conditions over the 8-18 GHz region. A novel multi-resonance technique called strong field coherence breaking (SFCB) was implemented to record conformer-specific microwave spectra.

This technique involves sweeping the broadband chirp followed by selectively choosing a set of single frequencies pulses to yield a set of rotational transitions that belong to a single entity in the gas-phase mixture, aiding assignment greatly. Transitions belonging to *anti* and *gauche* conformers were identified and assigned and accurate experimental rotational constants were determined to provide insight on the molecular structure. Experimental rotational transitions provided relative abundances in the supersonic expansion. A modified line picking scheme was developed in the process to modulate more transitions and improve the overall efficiency of the SFCB multiple selective excitation technique.

The rotational spectrum of 2-hexanone was recorded over the 8-18 GHz region using a CP-FTMW spectrometer. SFCB was utilized to selectively modulate the intensities of rotational transitions belonging to the two lowest energy conformers of 2-hexanone, aiding the assignment. In addition, the SFCB method was applied for the first time to selectively identify rotational transitions built off the two lowest energy hindered methyl rotor states of each conformer, $0a_1$ and $1e$. Since these two states have rotational energy levels with different nuclear spin symmetries, their intensities could be selectively modulated by the resonant monochromatic pulses used in the SFCB method. The difference spectra, final fit and structural parameters are discussed for the three assigned conformers of 2-hexanone.

Developing new experimental techniques that allow for species identification and quantification in the high-temperature environment of reacting flows is a continuing challenge in combustion research. Here, we combine broadband chirped-pulse microwave (rotational) spectroscopy with an atmospheric-pressure jet-stirred reactor as a novel method to identify key reactive intermediates in low-temperature and ozone-assisted oxidation processes. In these experiments, the gas sample, after being withdrawn from reactive dimethyl ether/ O_2 /Ar, dimethoxy methane/ O_2 /Ar, and ethylene/ O_2 / O_3 /Ar mixtures, expands via a supersonic expansion into the high vacuum of a microwave spectrometer, where the rotationally cold ensemble of polar molecules is excited with short MW radiation frequency ramps (chirps). The response of the molecular ensemble is detected in the time domain and after a Fourier transformation, the spectral composition of the transient emission is obtained in the frequency domain. The observed rotational frequencies are uniquely correlated to molecular structures and allow for an unambiguous identification of the sampled species. Detection and identification of intermediates such as formaldehyde, methyl formate, formic acid, formic acid anhydride, and the primary ethylene

ozonide via literature-known rotational frequencies are evidence for the superb identification capabilities of broadband chirped-pulse microwave spectroscopy. Strong-field coherence breaking is employed to identify and assign transitions due to a specific component. The observation of van der Waals complexes provides an opportunity to detect combustion intermediates and products that are impossible to detect by rotational spectroscopy as isolated molecules.

Lastly, preliminary data on important combustion precursors is studied including pentanal, *trans*-2-pentenal and *o*-, *m*- and *p*-vinylanisole. The rotational spectrum of these five molecules is recorded from the 8-18 GHz region under jet-cooled conditions. For pentanal and *trans*-2-pentenal, SFCB was utilized to dissect the broadband spectrum, identifying the four and two lowest energy structures, respectively. The structural parameters and final fits are provided.

CHAPTER 1. INTRODUCTION

1.1 Rotational Spectroscopy

Rotational spectroscopy is a powerful tool to measure the structure of polar gas phase molecules. Rotation about three inertial axes is quantized leading to observed frequencies and splitting patterns that are directly correlated to the three moments of inertia, I , as defined in Equation 1, where m is the mass and r is the distance from the atom to the rotational axis of interest.¹

$$I = \sum m_i r_i^2$$

Three mutually perpendicular rotational axes (a -, b - and c -) that intersect at the center of mass of the molecule can be defined to calculate the moment of inertia about each axis individually. The labelling scheme for the rotational axes is chosen such that $I_a < I_b < I_c$ so that $A > B > C$. The rotational constants of a molecule are defined in this frame as follows:

$$A = \frac{h}{8\pi^2 c I_a}, B = \frac{h}{8\pi^2 c I_b}, C = \frac{h}{8\pi^2 c I_c}$$

where c is the speed of light and h is Planck's constant.

Using the convention above, molecules can be classified into groups based upon their rotational constants including linear ($A > B = C = 0$), prolate symmetric top ($A > B = C$), oblate symmetric top ($A = B > C$), symmetric top ($A = B = C$) and an asymmetric top ($A \neq B \neq C$).¹

After accurate determination of the rotational constants, the majority of the rotational spectrum can be accounted for including other rotational motions including centrifugal distortion, nuclear quadrupolar coupling and methyl internal rotation, providing an even more precise structural characterization of the molecule.

1.2 Chirped-Pulse Fourier Transform Microwave Spectroscopy

Prior to the advent of chirped-pulse Fourier transform microwave (CP-FTMW) spectroscopy, typical microwave spectroscopy studies were carried out using Fabry-Pérot cavity spectrometers.^{2,3} These gas phase experiments provide unprecedented resolution and precision allowing for unambiguous identification of a chemical species as the observed frequencies are a direct measure of the structure and can be assigned based on comparison to ab initio predictions or via isotopic substitutions that give atomic positions.^{2,3} However, these strengths of microwave spectroscopy have also served as a drawback. Since the broadband spectrum contains millions of resolution elements, the spectrum must be scanned at high resolution which can be quite time consuming, with scans requiring hours and even days.⁴ Also, narrowband spectrometers provide a rotational spectrum with a frequency bandwidth of about 1 MHz per measurement region, providing the user with only a small, magnified region of the spectrum.⁴ For these reasons, microwave spectroscopy is not traditionally viewed as a survey technique for obtaining a chemist's view of a system.

Microwave spectroscopy was revolutionized with the invention of CP-FTMW spectroscopy by the Pate group at the University of Virginia.⁵ Using state of the art fast electronics and broadcasting and receiving horns, the broadband pulse is stretched in time so that it delivers sufficient power at each frequency allowing a 10 GHz bandwidth to be swept linearly in 1 μ sec.⁴ These high bandwidth frequency sweeps will interact with the sample of interest polarizing the molecules and the ensuing free induction decay (FID) can be collected before dephasing of the coherence can occur. The resulting signal, S , from chirped pulse excitation is as follows:

$$S \propto \omega \cdot \mu^2 \cdot E_{pulse} \cdot \Delta N_0 \cdot \left(\frac{\pi}{\alpha}\right)^{1/2}$$

where ω is the frequency, μ is the transition dipole moment, E_{pulse} is the electric field strength, ΔN_0 is the population difference between the rotational states being probed, and α is the linear sweep rate.⁵ CP-FTMW experiments have provided high resolution ~ 10 kHz and broad spectral coverage ~ 10 GHz, resulting in 10^6 resolution elements per shot, yielding a full picture of the chemical system and structural parameters in a matter of minutes.⁴ CP-FTMW spectroscopy allows for quick signal averaging to observe less abundant isotopes⁶ and Kraitchman equations^{7,8} can be applied to determine atomic positions and bond lengths/angles to high accuracy. Not only can the chemical species be identified, CP-FTMW spectroscopy can also be utilized to determine the rotational temperatures and fractional abundances of each species contributing to the spectrum as expressed by the following equation:

$$W = \frac{4\pi^{\frac{3}{2}}\omega_0^2 S\mu_i^2 g_l g_l \epsilon N_{tot}}{c\sqrt{\alpha}kTQ_{rot}} e^{\frac{-E_l}{kT_{rot}}}$$

where W is the integrated line intensity, E_l is the lower state energy, k is the Boltzmann constant, T_{rot} is the rotational temperature and Q_{rot} is the partition function.⁹ With these capabilities, CP-FTMW spectroscopy continues to grow in numerous facets, as a detector in kinetic studies^{10,11}, as a probe of chemical reaction dynamics¹²⁻¹⁴ as well as a probe for double resonance experiments.^{15,16}

1.3 Applications of Multi-Resonance CP-FTMW Spectroscopy

With rapid data acquisition and strong sensitivity and resolution, CP-FTMW spectroscopy has become a powerful tool in conjunction with high level predictions to unambiguously identify and structurally characterize polar chemical species in a gas mixture at faster-than-ever rates.⁴ However, one of the daunting challenges associated with broadband rotational spectroscopy lies

in the difficulty assigning complex spectra resulting from multi-component chemical systems. As the molecules present increase in size, they possess more rotational transitions at a given temperature. If the molecule has flexible degrees of freedom (e.g., torsional degrees of freedom associated with hindered rotation about C-C single bonds), they can support numerous conformational isomers, nuclear hyperfine coupling and methyl internal rotation, yielding a rotational spectrum with transitions from all components entangled with each other. Even with exceptional theoretical predictions, assignment of the broadband spectrum can be a significant challenge. One solution to this hindrance has been the employment of a newly developed multi-resonance technique called strong field coherence breaking (SFCB).¹⁵ This method combines sweeping the broadband chirp to excite the sample in the strong-field regime with a series of single frequency pulses that “break” the coherence the broadband pulse creates between pairs of states. Subtraction of a broadband spectrum taken in the absence of the coherence-breaking SFP’s recorded under the same conditions provides a set of rotational transitions belonging to a single component whose coherence was modulated by the single-frequency microwave pulses.¹⁵ This final difference spectrum (usually plotted as the magnitude of the difference) is utilized to begin the initial fitting process and repeated as necessary until all rotational transitions are accounted for.

Multi-resonance techniques can be critical to our understanding of complex chemical systems including the interstellar medium and combustion chemistry. Modelling the interstellar medium and combustion greatly benefit from experimental data on reaction pathways, kinetics and product branching ratios of the individual reactions composing the chemical network. In order to provide more accurate chemical pictures, models need to include larger molecules posing a challenge for laboratory-based experiments. With a shape sensitive and entity specific

spectroscopic tool in SFCB, laboratory studies can begin to include larger molecules providing a powerful means of characterizing reactive intermediates and conformational isomers. In this thesis, SFCB has been implemented to sort through congested spectra of several molecules of importance to combustion and the interstellar medium, including those containing multiple structural isomers, splittings due to methyl internal rotation and effluent resulting from a jet-stirred reactor. By utilizing SFCB, deconvolution of broadband spectra is possible, enabling the assignment of chemical species and extraction of rich structural information of each component. We thereby establish SFCB as an important tool for the advancement of CP-FTMW spectroscopy and our understanding of dense, complicated chemistry.

1.4 Organization of Thesis

The goal of this dissertation is to use multi-resonance techniques to study the nitriles and oxygenated biofuels that are thought to be relevant to interstellar and combustion chemistry. Chapter 2 provides the details of the experimental apparatus used to carry out the experiments. Chapter 3 provides the spectroscopic characterization of 3-phenylpropionitrile, a particularly interesting recombination product of two resonantly stabilized radicals in Titan's atmosphere. These results provide the spectroscopic signatures for their detection in space. Chapter 4 describes how SFCB can be utilized to understand not only the conformational preferences of the oxygenated biofuel 2-hexanone, but also demonstrates for the first time the use of SFCB in assigning internal rotor specific microwave spectra. Chapter 5 presents the results of using CP-FTMW spectroscopy as a tool to identify reactive intermediate resulting from a jet-stirred reactor.

1.5 References

¹I. N. Levine *Physical Chemistry*; 6th ed.; McGraw-Hill: New York (2009).

- ²T. J. Balle, E. J. Campbell, M. R. Keenan, W. H. Flygare, J. Chem. Phys. **71**, 2723 (1979).
- ³T. J. Balle, E. J. Campbell, M. R. Keenan, W. H. Flygare, J. Chem. Phys. **72**, 922 (1980).
- ⁴G. B. Park, R. W. Field, J. Chem. Phys. **144**, 200901 (2016).
- ⁵G. G. Brown, B. C. Dian, K. O. Douglass, S. M. Geyer, S. T. Shipman and B. H. Pate, Rev. Sci. Instrum. **79**, 053103 (2008).
- ⁶A. L. Steber, J. L. Neill, D. P. Zaleski, B. H. Pate, A. Lesarri, R. G. Bird, V. Vaquero-Vara and D. W. Pratt, Faraday Discuss. **150**, 227 (2011).
- ⁷J. Kraitchman, Am. J. Phys. **21**, 17 (1953).
- ⁸C. C. Costain, J. Chem. Phys. **29**, 864 (1958).
- ⁹J. M. Oldham, C. Abeysekera, B. Joalland, L. N. Zack, K. Prozument, I. R. Sims, G. B. Park, R. W. Field, A. G. Suits, J. Chem. Phys. **141**, 154202 (2014).
- ¹⁰C. Abeysekera, B. Joalland, N. Ariyasingha, L. N. Zack, I. R. Sims, R. W. Field, and A. G. Suits, J. Phys. Chem. Lett. **6**, 1599 (2015).
- ¹¹C. Abeysekera, L. N. Zack, G. B. Park, B. Joalland, J. M. Oldham, K. Prozument, N. M. Ariyasingha, I. R. Sims, R. W. Field, and A. G. Suits, J. Chem. Phys. **141**, 214203 (2014).
- ¹²K. Prozument, Y. V. Suleimanov, B. Buesser, J. M. Oldham, W. H. Green, A. G. Suits, and R. W. Field, J. Phys. Chem. Lett. **5**, 3641 (2014).
- ¹³B. C. Dian, G. G. Brown, K. O. Douglass, and B. H. Pate, Science **320**, 924 (2008).
- ¹⁴N. M. Kidwell, V. Vaquero-Vara, T. K. Ormond, G. T. Buckingham, D. Zhang, D. N. Mehta-Hurt, L. McCaslin, M. R. Nimlos, J. W. Daily, B. C. Dian, J. F. Stanton, G. B. Ellison, and T. S. Zwier, J. Phys. Chem. Lett. **5**, 2201 (2014).
- ¹⁵A. O. Hernandez-Castillo, C. Abeysekera, B. M. Hays, and T. S. Zwier, J. Chem. Phys. **145**, 114203 (2016).
- ¹⁶S. M. Fritz, A. O. Hernandez-Castillo, C. Abeysekera, B. M. Hays, and T. S. Zwier, J. Mol. Spectrosc. **349**, 10 (2018).

CHAPTER 2. EXPERIMENTAL

2.1 Supersonic Expansion

All experiments were carried out utilizing a supersonic jet expansion. This is a powerful technique for cooling gas phase molecules to low temperatures where the broadband spectra acquired are drastically simplified and sensitivity is increased. A supersonic expansion is created by pulsing a high-pressure buffer gas (typically several bar He, Ne, or Ar) through a small orifice (500-1000 μm diameter) into vacuum. During the expansion, the random, thermal motion of the atoms is turned into directed motion along the expansion axis. When a molecular sample is entrained in this buffer gas expansion, its internal energy is removed by collisions with the cold buffer gas, cooling the molecules into their zero-point vibrational levels.¹⁻³ Jet cooled molecules typically have internal temperatures of 10-20 K, 1-5 K and $< 1\text{K}$ for the vibrational, rotational and translational degrees of freedom, respectively.

The collision frequency is at its maximum nearest the exit of the nozzle², as the gas expands the collision rate drops nearly quadratically with distance from the nozzle orifice, generating a collisionless environment downstream where the molecular sample and the buffer gas atoms travel unidirectionally and with a narrow velocity spread. It is in this region that the spectroscopic interaction with the isolated molecules occurs. For the time-of-flight mass spectrometer, the free jet expansion is skimmed, forming a molecular beam of the coldest part of the expansion.

2.2 Flash Pyrolysis

Flash pyrolysis is the direct thermal decomposition of molecules or mixtures in the absence of oxygen. In contrast to an electric discharge, pyrolysis provides temperature-dependent control over

the production of transient species when they can be produced from an appropriate precursor. The microreactor is an adapted version of Peter Chen's hyperthermal nozzle⁴, which was originally designed as a source to produce radicals and other reactive intermediates⁵⁻⁷. In order to study thermal decomposition mechanisms of molecules relevant to biomass pyrolysis⁸⁻¹¹ and potential biofuels¹² the Chen nozzle was modified by the Ellison group at Boulder¹³. The microreactor offers a short residence time which diminishes bimolecular chemistry and allows the identification of unimolecular reaction schemes. The residence time is short enough that it is possible to detect radicals and other reactive intermediates. To couple the flash pyrolysis microreactor with a broadband CP-FTMW spectrometer, the design used in the Ellison's group was modified¹³. The schematics of this design are shown in Figure 2.1, taken from ref. 13. It consists of a 2 mm ID X 5 mm OD X 3.5 cm long silicon carbide (SiC) tube). The SiC tubes are prepared with a resistance of 1k Ω -5k Ω by either increasing or decreasing the resistance by conditioning with sand paper or a graphite pencil, respectively. The SiC rod is mounted inside an alumina tube to reduce radiative heat loss. The tubular reactor is inserted into a copper heatsink and held concentric with a faceplate of a pulsed valve outfitted with a 1 mm diameter nozzle orifice. Two sets of perpendicular set screws are used to hold the SiC and alumina tubes separately in place. The electrical current used to heat the SiC tube is provided through copper wires connected to molybdenum clips that hold two carbon discs, which are themselves in direct contact with the SiC tube. About two-thirds of the full length of the reactor is resistively heated, and the temperature of the outer wall is measure by a tungsten/rhenium type C thermocouple.

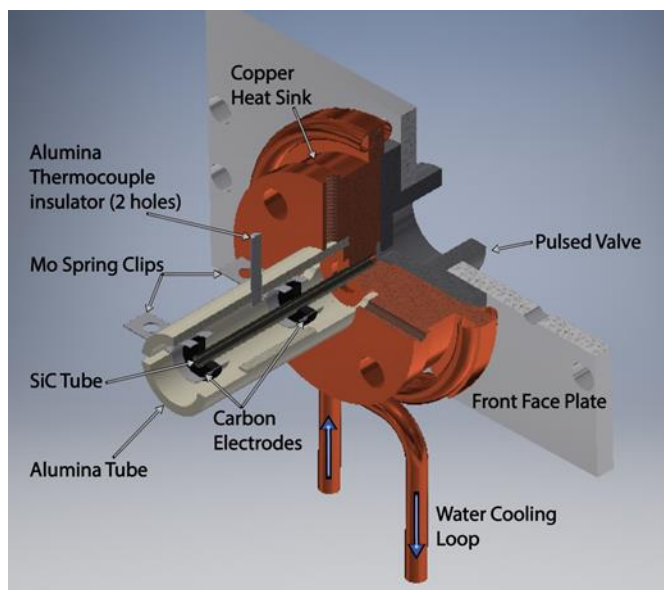


Figure 2.1 Flash pyrolysis micro-reactor assembly used to thermally decompose samples entrained in buffer gas.

A water-cooled copper heat sink is placed concentrically between the SiC tube and the valve faceplate to prevent the pulsed valve from getting heated by the micro-reactor. The maximum practical operable temperature of the micro-reactor is about 1900 K. Upon exiting the reactor, the molecules are immediately jet-cooled, quenching further reactions and cooling the internal degrees of freedom for spectroscopic interrogation. The micro-reactor is resistively heated and in order to control the current flow through the SiC tube, the tube is incorporated into a circuit consisting of a set of 6 light bulbs (250 watt) wired in parallel with one another, but in series with the SiC tube and controller. The power is provided and controlled by a 120 VAC source (typically a Variac). By adding bulbs in a parallel circuit, the net resistance of the bulbs decreases and the circuit current increases at a set source voltage, resulting in a temperature increase of the SiC tube. The Mo clip closest to the pulse valve should be connected to neutral (white cable) and the hot side (black cable) should be connected to the Mo clip farther from the valve. Once under vacuum and all connected, one bulb is placed in the circuit and the temperature is slowly increased by dialing up the power

on the variac to a setting of 40. The temperature is carefully monitored at this stage as the power is gradually increased until the resistance of the SiC rod drops and a noticeable surge in temperature is observed. At this point, the temperature can be adjusted to the desirable range by adding more bulbs to the circuit as well as slowly adjusting the variac.

Tests carried out by JAFCl identified that there is a small leakage current to the face plate of the valve. A circuit designed to control and stabilize the temperature of the SiC tube was developed by Jim Zimmerman (JAFCl), but was not fully tested and therefore has not yet been incorporated into the pyrolysis source SOP. This is an area where future time investment could be very helpful, as temperature stability is crucial to use of the SFCB methods on radicals.

2.3 Multiplexed characterization of complex gas-phase mixtures combining chirped-pulse Fourier transform microwave spectroscopy and VUV photoionization time-of-flight mass spectrometry

2.3.1 Introduction

Chirped pulse Fourier transform microwave (CP-FTMW) spectroscopy is a powerful tool for determining the structures of gas phase molecules with high precision.¹⁴ Fast electronics and strong electric fields are utilized to polarize all rotational transitions lying in a 10 GHz bandwidth within 1 μ sec, and the resulting free induction decay (FID) is collected to obtain a spectrum at faster-than-ever rates.^{14,15} The frequency patterns from the resulting spectrum can be fit to theoretical predictions and provide a direct measure of the geometry through the rotational constants and projections of the permanent dipole moments along the inertial axes.¹⁵ With rapid data acquisition, signal averaging to observe less abundant isotopes is readily achievable¹⁶ and Kraitchman equations^{17,18} can be applied to determine atomic positions and bond lengths/angles to high accuracy. CP-FTMW spectroscopy can also be utilized to determine the rotational temperatures and fractional abundances of each species contributing to the spectrum.^{19,20}

The applications of CP-FTMW spectroscopy continue to grow in ever-widening scope, as a detector in kinetic studies¹⁹⁻²¹, as a probe of chemical reaction dynamics²²⁻²⁴ and as a probe for double resonance experiments.^{25,26} However, one of the considerable challenges of using CP-FTMW spectroscopy as a stand-alone method is that, if the carriers of the microwave transitions arise from a multi-component gas-phase mixture, the microwave transitions due to each component are intermingled with one another, complicating the assignment process. When all components have known microwave spectra, the high resolution of the method allows look-up tables to play a role in semi-automated analysis. However, when the mixture contains unknown components, spectral assignment can become slow or impossible. Furthermore, while all molecules with permanent dipole moments are detectable, the CP-FTMW signal scales as the square of the dipole moment, making it difficult to detect mixture components that are non-polar or weakly polar ($\mu < 1$ D).

Time-of-flight mass spectrometry (TOFMS) is a widely used analytical technique to determine the molecular weights of the components of gas phase mixtures. When photoionization is used as the ionization mechanism (e.g., from a laser source), the components are ionized and accelerated into a field free region where the unique arrival time at the detector is dependent upon its mass-to-charge ratio. Using a soft ionization technique such as vacuum ultraviolet (VUV) radiation, fragmentation upon photoionization is typically small^{27,28}, so that the VUV TOF mass spectrum records the molecular weights and approximate relative abundances of the components of the mixture. However, as a stand-alone method, the mass spectrum itself determines only molecular formulae, and hence does not identify the presence and relative abundances of structural and/or conformational isomers. Admittedly, other methods requiring more sophisticated light sources have made headway in isomer-specific identification. For instance, with tunable VUV radiation

such as is available from a synchrotron, the unique ionization energies of isomers can be used in favorable cases to deduce isomer-specific composition.²⁹⁻³¹ In addition, previous work using a molecular beam source with non-resonant strong field ionization in a time of flight mass spectrometer has been used to quantify isomers.³² Nevertheless, a general solution to isomer-specific detection would benefit greatly from supplementing mass spectrometry with other methods better suited to the task of isomer-specific detection.

Motivated by the complementary data provided by the two methods, we have incorporated into our CP-FTMW spectrometer a TOF mass spectrometer, resulting in a powerful multiplexed approach for determining gas phase structures. With the capability to interrogate the same molecular sample with both methods under a range of conditions, the correlation between the microwave transition intensities and the mass-resolved ion intensities in the TOF mass spectrum can be used to determine the molecular formulae of the carriers of the microwave transitions. The new instrument has great potential to extend and speed gas phase analysis of complex mixtures. This advantage extends particularly to circumstances in which the components of the gas phase mixture undergo chemical reaction, whose extent can be followed simultaneously in both the microwave and TOF spectra. Furthermore, the generality of VUV single-photon photoionization also enables detection of chemical components that do not have a dipole moment, as long as the VUV photon energy is sufficient to ionize all the mixture's components.

Herein, we describe an instrument recently modified so as to incorporate capabilities to acquire simultaneous rotational and mass spectra under identical conditions. The new chamber was designed by Dr. Brian Hays with contributions from myself on assembly and characterization. We demonstrate the capability of the new instrument by studying gas mixtures of two complementary types. First, a mixture of three stable furanic compounds containing two structural isomers is

probed: furfural ($\text{C}_5\text{H}_4\text{O}_2$), furfuryl alcohol ($\text{C}_5\text{H}_6\text{O}_2$) and 2-methoxyfuran ($\text{C}_5\text{H}_6\text{O}_2$), demonstrating the complementary strengths of the methods. While only two parent masses are identified via VUV TOF mass analysis, the CP-FTMW spectrum incorporates transitions due to all three components, including the global minimum conformational isomer of furfuryl alcohol. We extract fractional abundances from the CP-FTMW spectrum and compare these to the VUV photoionization signals in the TOF mass spectrum. Second, a mixture resulting from flash pyrolysis of guaiacol is studied. In this case, the relative intensities of the signal in both microwave and mass spectra are followed with changes in the temperature of the pyrolysis source to identify and facilitate assignment of the molecular carriers in the pyrolysis source.

2.3.2 Apparatus

2.3.2.1 Pumping System

Figure 2.2 shows an assembly drawing of the chamber we have designed for simultaneous CP-FTMW and photoionization TOFMS detection. This chamber is a modified version of a CP-FTMW spectrometer described previously.³³ A new (60cm (length) x 30cm x 30cm) rectangular steel chamber was designed with two sets of flanges on each side to provide two platforms for simultaneous microwave and time-of-flight measurements. The chamber is evacuated by two 25-cm dia. diffusion pumps (Varian VHS 10) located behind the TOF section. The diffusion pumps are backed by a roots blower (BOC Edwards EH500) and a roughing pump (Alcatel 2063). The base pressure of the chamber is 1×10^{-5} torr with no gas flow and maintains an operating pressure of 1×10^{-4} torr when the pulsed valve is operating at flows of about $0.85 \text{ bar-cm}^3 \text{ sec}^{-1}$. The interior of the microwave portion of the chamber is covered with sheets of microwave absorber (Emerson and Cuming Eccosorb HR-25/ML; LS-24) to reduce reflections due to microwave radiation resonances, thus preventing damage of the electronics.

2.3.2.2 Chirped-pulse Fourier Transform Microwave section

The CP-FTMW section of the chamber has been upgraded from its original configuration³³ by incorporation of a new set of horns that extend the frequency coverage from 2-18 GHz. As a result, we provide a brief overview of the electronics used to provide this frequency coverage. A schematic diagram for the microwave electronics is shown in **Figure 2.3**. Chirped pulses in the 2-8 GHz or 8-18 GHz ranges are initiated by a 10 GS/s arbitrary waveform generator (AWG; Tektronix 7101), which is referenced by a 100 MHz quartz oscillator that is driven, in turn, by a 10 MHz Rb-disciplined crystal oscillator (Stanford Research Systems FS725). The AWG outputs broadband chirps and other waveforms at frequencies up to 5 GHz and serves as the trigger for the other electronics involved. The waveform from the AWG passes through a 5 GHz low pass filter (Lorch 10LP-5000-S) and is levelled with a pre-amplifier (Mini-Circuits ZX60-6031E-S+ 6000 MHz, +14.2 dB gain). Depending on the frequency region of interest, the waveform will be multiplied with a quadrupler (Phase One PS06-0161) to achieve an 8-18 GHz chirp or a doubler (TRW Microwave RX8008) to generate a 2-8 GHz chirp. After multiplication, the output power is set with a step attenuator (Weinschel AF117A-69-11) and is amplified with a 200 W travelling wave tube amplifier (TWTA; Amplifier Research model AT4004, 8-18 GHz) in the 8-18 GHz regime or a 13 W solid state amplifier (Mercury Systems L0208-41-T113) for the 2-8 GHz regime. The output from either amplifier is broadcast into the vacuum chamber with a 2-18 GHz broadcasting horn (Steatite; Q-par Antennas QWH-SL-2-18-S-HG-R), which thereby interacts with the molecules of interest.

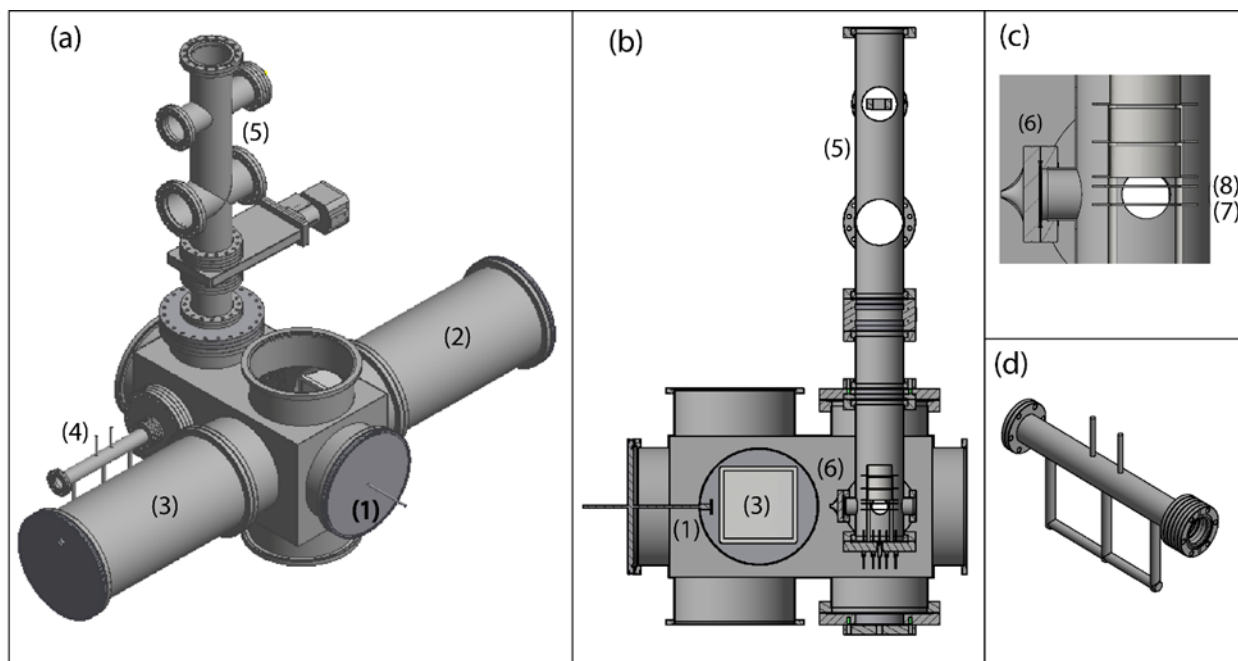


Figure 2.2 (a) Assembly drawing of the combined CP-FTMW/TOFMS vacuum chamber in a 3D rendering, (b) a side-on cross-section view and enhanced view of the Wiley-McLaren region, (c) an enhanced view of the skimmer and Wiley-McLaren extraction region, and (d) a close up of the VUV cell. Components labelled: (1) pulsed valve, (2) broadcasting horn, (3) receiving horn, (4) VUV cell, (5) TOF tube, (6) skimmer, (7) repeller plate, (8) draw-out-grid.

The sample is introduced into the chamber using a pulsed valve (General Valve, Series 9) with a 1 mm orifice operating at 10 Hz. The valve is supported by a bracket mounted on a 10 cm nipple that also enables mechanical adjustment of the pulsed valve outside the vacuum chamber. The gaseous sample undergoes a supersonic expansion, entering the region between the horns 12.5 cm from the nozzle orifice. Given the size of the horns (15 cm X 15 cm in cross section), the center of the transmitted microwaves are about 20 cm downstream from the nozzle orifice. There is a 15 cm space between the broadcasting and collection horns.

The molecular sample is polarized by the microwave pulse, and subsequently undergoes free induction decay (FID). This time-domain signal is collected with a receiving horn, before passing through a PIN diode limiter (Advanced Control Components ACLS 4619F- C36-1K) and a reflective single pole single throw switch (Advanced Technical Materials S1517D isolation 80

dB, 2-18 GHz). In the 2-8 GHz range, a +46 dB low noise amplifier (Miteq AMF-5F-02000800-15-10P) amplifies the FID, while a +45 dB low noise amplifier (Miteq AMF-6F-0600-1800-15-10P) serves the 8-18 GHz regime. In the latter range, the amplified signal is down-converted using a triple balanced mixer (Miteq TB0440LW1) with an 18.9 GHz phase locked dielectric resonator oscillator (PLDRO, Microwave Dynamics PLO-2000-18.90). The signal then passes through a DC block (MCL 15542 BLK-18) and a 12 GHz low pass filter (Lorch 7LA-12000-S) before it is phase coherently averaged by a 13 GHz, 40 GS/s real time digitizer (Guzik ADC6131). The time domain signal is filtered with a Kaiser-Bessel window and a custom MATLAB program is used to fast Fourier transform the time domain spectrum to obtain the frequency domain spectrum.

2.3.2.3 VUV photoionization Time-of-Flight Mass Spectrometer section

After measurement of the rotational spectrum, the expansion-cooled gas pulse travels further downstream. The coldest part of the expansion is sampled through a 2 mm skimmer located 35 cm from the pulsed valve where it is introduced into a 1.0 m Wiley-McLaren time-of-flight mass spectrometer. The TOF tube is evacuated by a 350 L/s turbo pump (Osaka Vacuum TG350F) backed by a roughing pump (Alcatel 2010I) to standing and operating pressures of 1×10^{-9} torr and 5×10^{-7} torr, respectively.

The cold molecules in the skimmed beam are ionized with VUV radiation (118 nm) generated by frequency tripling in a Xe/Ar mixture in a custom built VUV cell adapted from previous designs.^{34,35} Typical pulse energies of 25-40 mJ/pulse of 355 nm light from a Nd:YAG laser (Continuum YG661-20(680)) are brought into the cell through a 250 mm focal length AR coated UV fused silica lens mounted 7.5 cm before the entrance window to the cell. The VUV cell is 31 cm long and has a gas manifold attached to an inlet port to allow for the introduction of argon and xenon which serves as the tripling medium. A pressure gauge (Cecomp Electronics

DPG1000G-760TORRA-1) is fixed to a second port on the VUV cell to allow for accurate measurements of the pressures of each gas. The VUV cell was filled with 10 torr of xenon and 100 torr of argon to generate VUV radiation, a 1:10 ratio in keeping with optimal performance found in previous studies.³⁴ One of the tubes of the gas manifold can be cooled with dry ice, creating temperature differentials that facilitate better mixing of the gas by convection. A MgF₂ lens (148 mm focal length, 2.5 cm dia.) affixed to the end of the VUV tube is used to focus the VUV light and spatially separate it from the 355 nm light in the TOF source region where ionization occurs. As noted above, the AWG serves as the master clock for all other components involved in the experiment, including the digital delay generator (Burkeley Nucleonics model 577) which triggers the Nd:YAG laser. The gaseous sample is photoionized in a single-photon photoionization using the 118 nm light generated in the VUV cell. Photoionization occurs between the repeller plate and the draw-out-grid of a Wiley-McLaren³⁶ TOF source, which are separated by two cm from one another. Typical voltages of +3000 V and +2750 V are placed on repeller and draw-out-grids under Wiley-McLaren conditions that give best peak resolution. A grounding plane at the entrance to the Einzel lens serves as entrance to the field-free region.

The ion packet is subsequently focused by an Einzel lens operating at +1700 V, traverses the flight tube before passing through a grounded screen mounted just before the detector, which ends the field-free region. The ions are accelerated onto the front surface of an 18 mm dual chevron microchannel plate (MCP) (Jordan TOF Products, Inc. C0701) with a gain of 10^7 at a typical front-surface potential of -2500 V. Typical voltages of +3000 V and +2750 V are used for repeller and draw-out-grids under Wiley-McLaren conditions that give best peak resolution. The mass resolution, $m/\Delta m$, of the TOF mass spectrometer calculated from the mass 98 peak in the mixture mass spectrum, as described below, is 360.

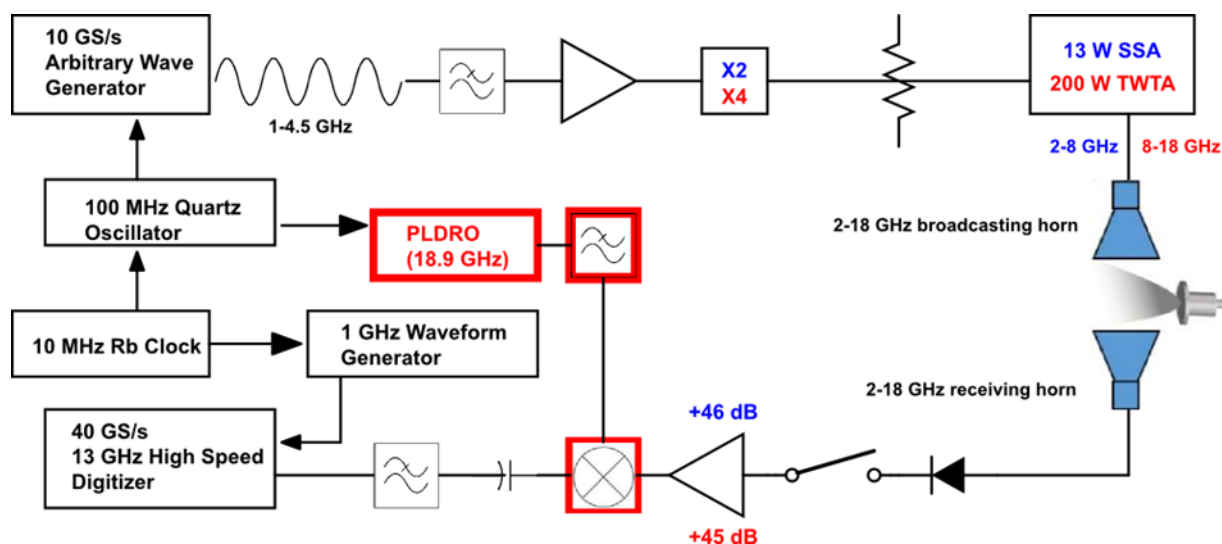


Figure 2.3 Schematic diagram of the chirped-pulse Fourier Transform microwave electronics for broadband acquisition over the 2-8 and 8-18 GHz regions. Components unique to the 2-8 GHz range are shown in blue, while those used only for generation and detection in the 8-18 GHz range are in red. All other components are common to the two frequency ranges.

The current pulses from the mass-resolved photoions are amplified a second time by 25 times in a fast amplifier (Stanford Research Systems SR445) before being displayed on a 3.5 GHz, 40 GS/s digital phosphor oscilloscope (Tektronix DPO 7354C). The oscilloscope is triggered to start recording when the Q-switch of the Nd:YAG laser fires to obtain the time-of-flight signals, from which the mass-to-charge ratios of the photoions are deduced.

Each gas pulse was 500 μsec long, and 20 molecular FIDs each 16 μs in length were collected during each gas pulse.

In studying the pyrolysis of *o*-guaiacol, a commercial sample (98%, Sigma Aldrich) without further purification was inserted in a stainless-steel sample holder and heated to 95°C. The samples were introduced into a 2 mm silicon carbide (SiC) micro-reactor. Details of the design and operation of the pyrolysis microreactor are described earlier and elsewhere.³⁷

2.3.3 Characterization of Instrumental Capabilities

2.3.3.1 Furanic Mixture

In order to test the new instrument, we selected a mixture of three liquid samples that were chemically similar, but contained two structural isomers. In so doing, we demonstrate the complementary strengths of the CP-FTMW and VUV TOFMS methods when they are combined with one another in a single instrument. In particular, a mixture of 2-methoxyfuran ($C_5H_6O_2$, 97%, Sigma-Aldrich), furfuryl alcohol ($C_5H_6O_2$, 98%, Sigma-Aldrich) and furfural ($C_5H_4O_2$, 99%, Sigma-Aldrich) was used for this test, with chemical structures shown in **Figure 2.4(b)**. Introduction of the furfural and 2-methoxyfuran vapors was accomplished by picking up the vapors by streaming helium over the liquid samples (2.4 bar backing pressure) contained in a cotton-filled stainless-steel sample holder incorporated into the gas line, located outside of the vacuum chamber.

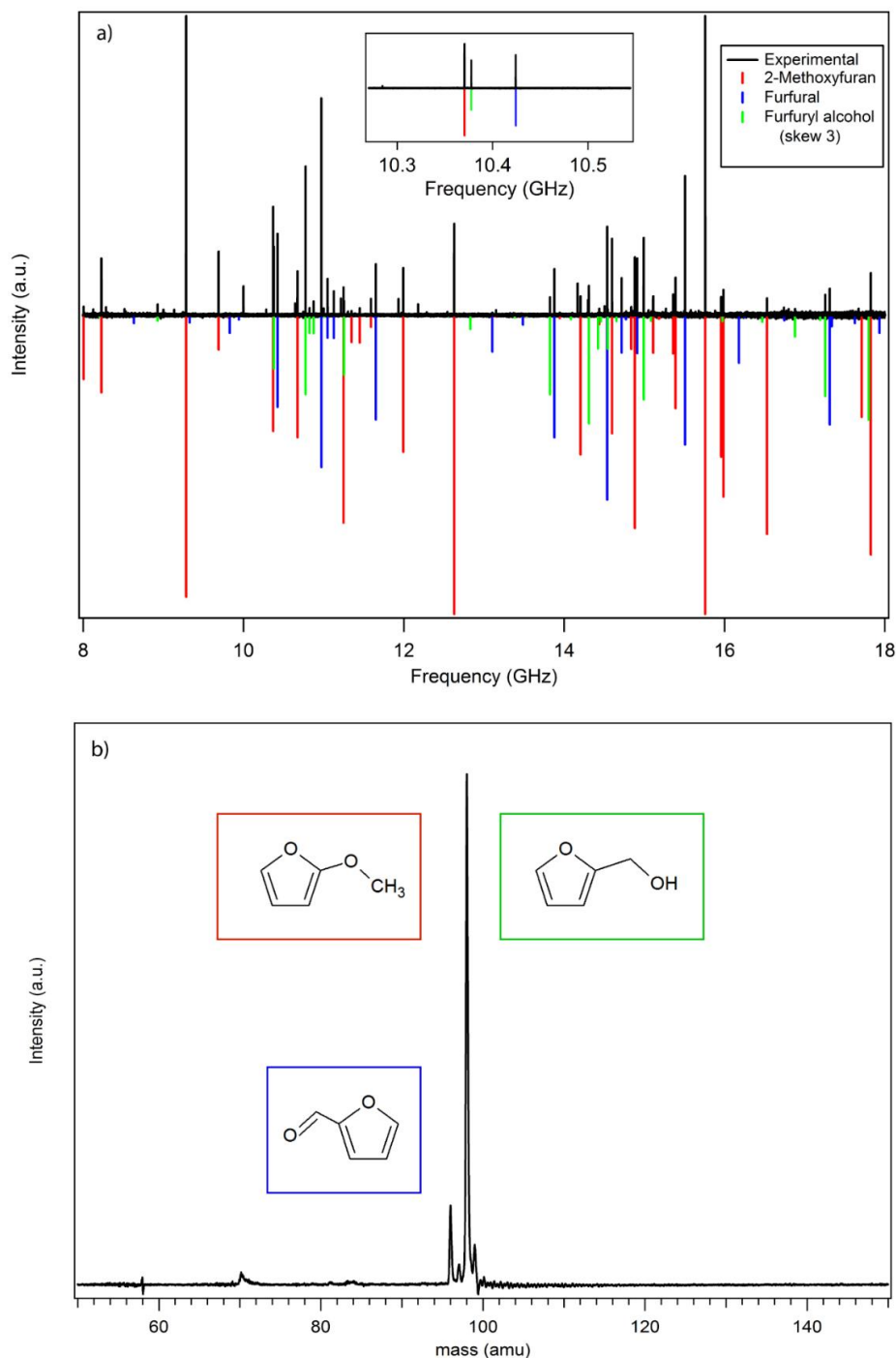


Figure 2.4 (a) Broadband CP-FTMW spectrum of a gas-phase mixture of 2-methoxyfuran, furfuryl alcohol, and furfural, compared to the microwave transitions for the three molecules using known experimental rotational constants.²¹⁻²³ The inset shows a close-up view of three transitions due to the three components of the mixture, demonstrating the isomer specificity afforded by the high resolution of the method. (b) Time-of-flight mass spectrum following 118 nm VUV photoionization of this same mixture.

Furfuryl alcohol was added to the mixture in a similar way using a second sample holder located inside the vacuum chamber, which was heated to 60 °C.

The 8-18 GHz rotational spectrum of the mixture was obtained under linear fast passage conditions³⁸ (20% TWTA power), acquiring 200,000 averages in total. The experimental spectrum (**Figure 2.4(a)**) is plotted against calculated predictions using previously reported experimental rotational constants.³⁹⁻⁴¹ Rotational transitions from furfuryl alcohol (green), furfural (blue) and 2-methoxyfuran (red) were identified based on the known rotational constants for these molecules. The mass spectrum acquired simultaneously is displayed in **Figure 2.4(b)**. VUV photoionization at 118nm (10.5 eV) was used to ionize furfuryl alcohol (IE=8.88 eV)⁴², furfural (IE=9.22 eV)⁴³ and 2-methoxyfuran (IE=7.93 eV).⁴⁴

Two peaks at m/z of 96 and 98 correspond to the molecular masses of furfural (C₅H₄O₂) and the C₅H₆O₂ structural isomers furfuryl alcohol and 2-methoxyfuran, respectively. The single C-13 peaks at mass 97 and 99 are also observable in natural abundance in the TOF mass spectrum.

The obvious deduction from **Figure 2.4(b)** is that 118 nm VUV time-of-flight mass spectrometry as a stand-alone method is not able to distinguish and identify conformational or structural isomers present in the gas mixture. Other methods requiring more sophisticated light sources can make isomer-specific identification. For instance, with tunable VUV radiation such as is available from a synchrotron, the unique ionization energies of isomers can be used in favorable cases to deduce isomer-specific composition.²⁹⁻³¹

In addition, previous work using a molecular beam source with non-resonant strong field ionization in a time of flight mass spectrometer has been used to quantify isomers.³² However, based on the 118 nm photoionization mass spectrum shown in **Figure 2.4(b)**, one might anticipate the presence of just two unique components in the gas mixture. By contrast, the rotational

transitions of the structural isomers 2-methoxyfuran and furfuryl alcohol are clearly distinguishable from one another in the CP-FTMW spectrum. The rotational transitions for any conformers present are also distinct from one another and can be probed and assigned using the recently developed technique of strong field coherence breaking.^{25,26} However, in this experiment, only the global minimum energy structures for furfuryl alcohol and 2-methoxyfuran are observed: the *skew* 3 conformer of furfuryl alcohol, (*trans*-furfural) and the *syn* conformation of 2-methoxyfuran.³⁹⁻⁴¹

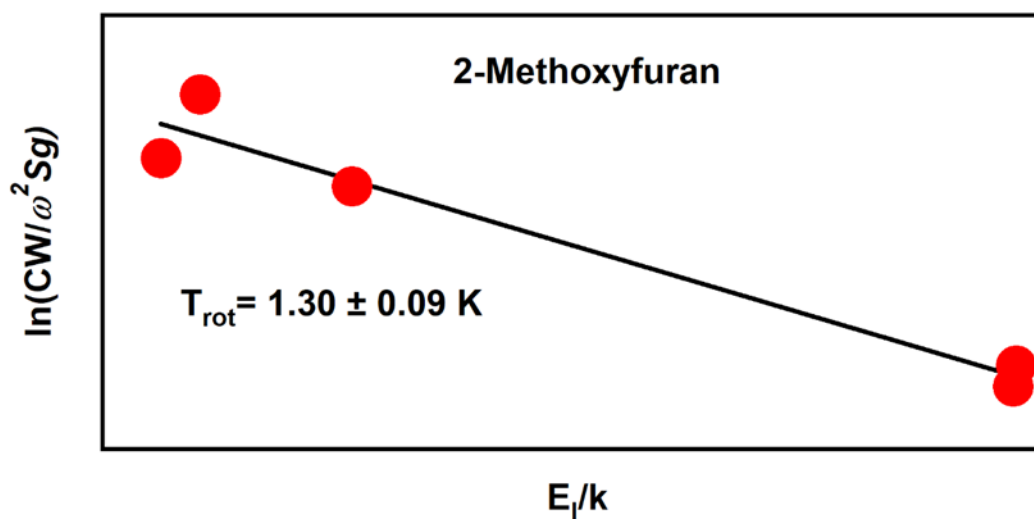


Figure 2.5 The Boltzmann plot for 2-methoxyfuran. The rotational temperature was calculated to be $1.30 (\pm 0.09) \text{ K}$

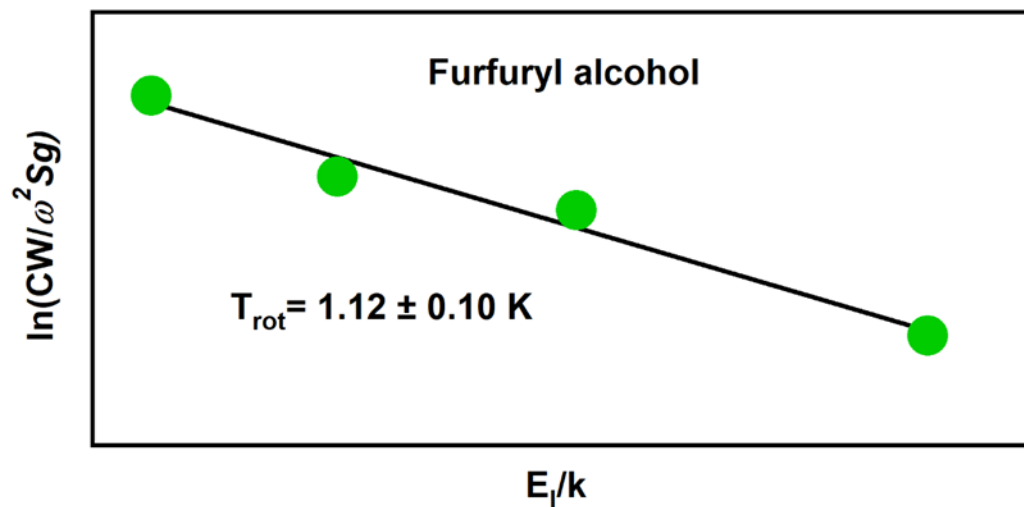


Figure 2.6 The Boltzmann plot for furfuryl alcohol. The rotational temperature was calculated to be $1.12 (\pm 0.10) \text{ K}$

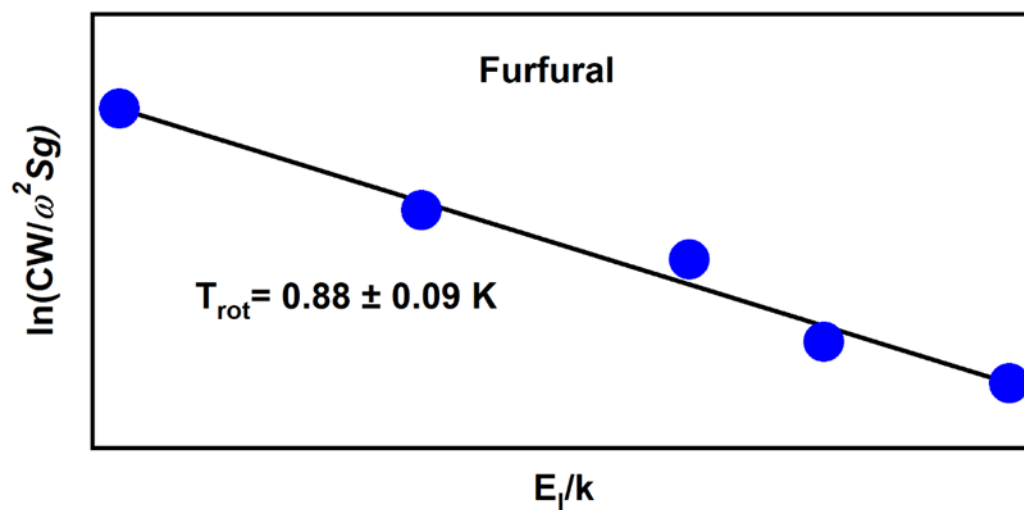


Figure 2.7 The Boltzmann plot for furfural. The rotational temperature was calculated to be $0.89 (\pm 0.09) \text{ K}$

Not only is CP-FTMW spectroscopy able to identify structural isomers, the intensities of assigned rotational transitions can be used to extract their relative abundances. The intensities of

the microwave transitions of each of the three components were fit to Boltzmann plots to derive the experimental rotational temperatures (furfural = 0.89 ± 0.09 K; 2-methoxyfuran = 1.30 ± 0.09 K; furfuryl alcohol = 1.12 ± 0.1 K, 1σ error bars) as shown in **Figures 2.5-2.7**. From the rotational temperature plots, a population analysis was carried out using the known dipole moments for the three molecules. The mixture was found to consist of 67% furfuryl alcohol, 24% 2-methoxyfuran and 9% furfural, with an average one-standard deviation error of $\pm 6\%$.

By contrast, the ion intensity for species ‘i’ in the 118 nm VUV photoionization TOF mass spectrum is proportional to the product of its fractional abundance f_i with its 118 nm photoionization cross section $\sigma_i(118 \text{ nm})$, assuming no fragmentation following photoionization:

$$I_i(m/z) \propto [f_i \cdot \sigma_i(118 \text{ nm})]$$

From the data in **Figure 2.4(b)**, the raw fractional ion intensities in the VUV TOFMS are 13% m/z 96 and 87% m/z 98, compared to percent populations of 9% m/z 96 and 91% m/z 98 based on the microwave fitting just described. These results are consistent with similar 118 nm photoionization cross sections for the three molecules, within the errors of the measurements.

2.3.3.2 Pyrolysis mixture

The combination of flash pyrolysis and CP-FTMW spectroscopy is emerging as a powerful scheme for determining the chemical structures of pyrolysis intermediates and final products at different microreactor wall temperatures.³⁷ While the temperature profile inside the SiC tube is a complicated function of conditions¹³, the outer wall temperature provides a consistent measurement of heating conditions that correlates with the temperature the gas pulse experiences inside the SiC tube, and therefore the pyrolysis conditions. Here we demonstrate how the combination of CP-FTMW and VUV TOFMS provides additional capabilities for diagnosing and spectroscopically characterizing the expansion-cooled effluent from a flash pyrolysis source^{37,44}.

In particular, we display here preliminary results on the flash pyrolysis of guaiacol, one of the principle components of lignin.⁴⁵

Figure 2.8(a) displays a series of VUV photoionization TOFMS for *o*-guaiacol (structure in bottom left) recorded as a function of the wall temperatures of the SiC tube used for flash pyrolysis, over a temperature range from 320 to 1120 K. These mass spectra are similar to those recently published by Scheer *et al.* using the same 118 nm VUV TOF techniques, although the concentrations of guaiacol in the mixture were significantly lower in that previous study in order to rigorously minimize bimolecular chemistry.¹⁰ The mass-to-charge ratios and known chemical structures of the key photoionizable components are labelled in the figure. Note that at 320 K, the *o*-guaiacol precursor experiences no fragmentation by 118 nm photoionization.

By recording a series of broadband microwave spectra under the same conditions, it is possible to detect and optimize conditions for characterizing the rotational spectra of transient species. The initial products of the thermal decomposition of *o*-guaiacol appear at m/z 109 and m/z 15 in the TOF mass spectrum, corresponding to the *o*-hydroxyphenoxy ($\text{HOC}_6\text{H}_4\text{O}$) and methyl (CH_3) radicals, respectively, that result from breaking the molecule's weakest bond. At 820 K the *o*-hydroxyphenoxy radical is present at maximum concentration, with the TOF mass spectra guiding the choice of this temperature as the best one for recording a CP-FTMW spectrum with maximum signal-to-noise ratio. An expanded view of the 12.575 to 12.600 GHz range of the microwave spectrum is shown in **Figure 2.8(b)**, highlighting the set of $3_{2,1} - 2_{2,0}$ rotational transitions of the *o*-hydroxyphenoxy radical, split by electron spin – rotation coupling. The set of transitions due to the radical in the broadband spectrum can be used to determine accurate rotational constants, centrifugal distortion constants and spin-rotation coupling constants (**Figure 2.8(b)**), locking in the structural assignment, but also providing new high resolution structural data

on this resonance-stabilized radical. The full spectroscopic characterization of this radical will be described elsewhere.⁴⁶

Decarbonylation of the *o*-hydroxyphenoxy radical generates the hydroxycyclopentadienyl radical (m/z 81), which has a total dipole moment of $\sim 1.5D$. The maximum concentration of this radical is achieved at ~ 920 K but its VUV photoionization signal is never very large. Despite a careful search, we do not see any evidence of it in the microwave spectrum at the present signal-to-noise ratio. The combination of modest dipole moment and small concentration both contribute to its signal being too small to detect. The hydroxycyclopentadienyl radical eliminates an H atom producing cyclopentadienone (m/z 80). Further heating generates vinylacetylene (m/z 52), which continues to build with pyrolysis temperature.

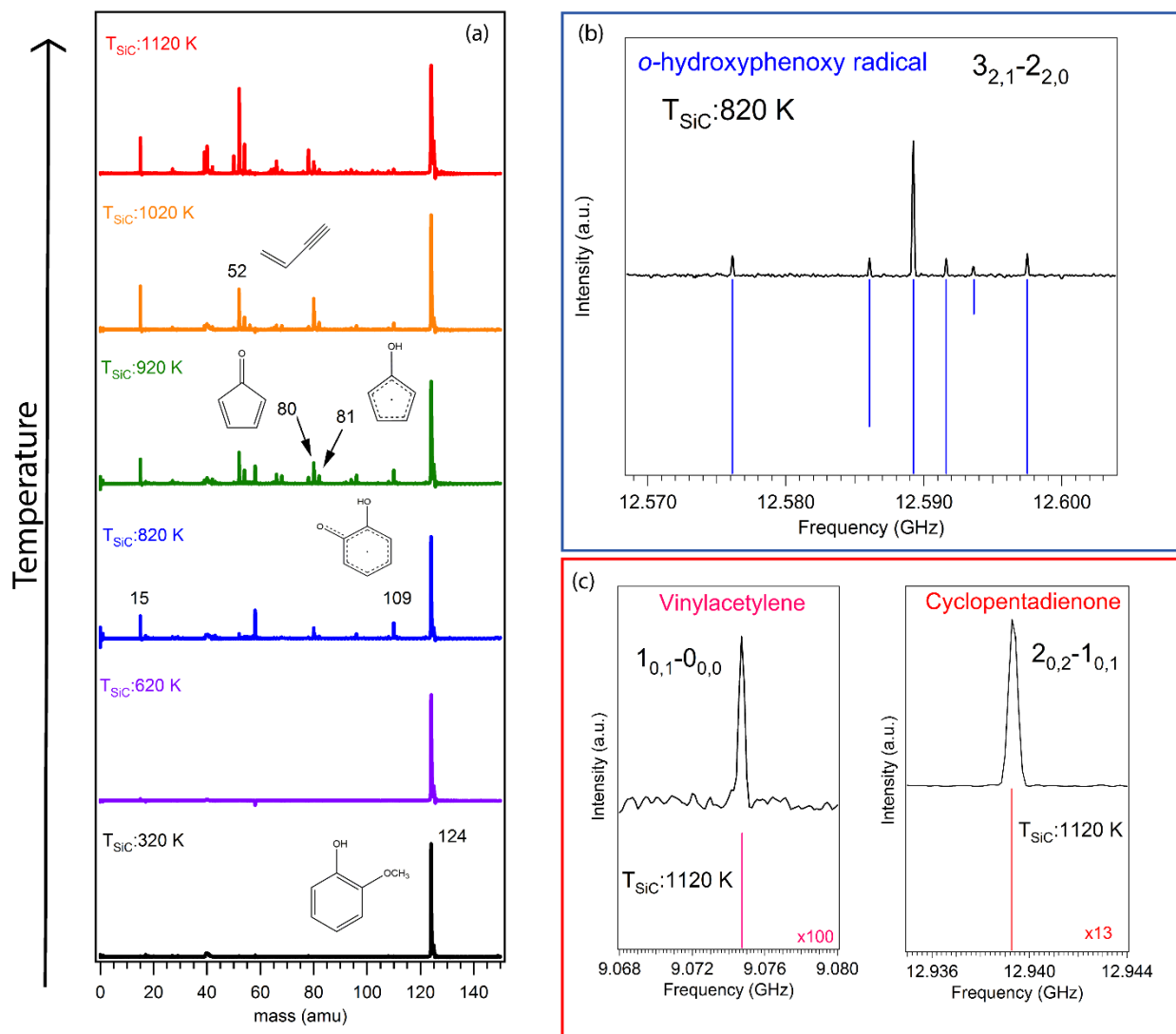


Figure 2.8 (a) 118 nm photoionization TOF mass spectrum at the indicated SiC wall temperatures for flash pyrolysis of *o*-guaiacol. **(b)** CP-FTMW spectrum in a small frequency window around the $3_{2,1}-2_{2,0}$ transition of the *o*-hydroxyphenoxy radical. The transitions in blue are split due to coupling of the electron spin angular momentum with the molecules rotational angular momentum. **(c)** CP-FTMW spectra in small frequency regions around microwave transitions due to cyclopentadienone (right) and vinylacetylene (left).

Microwave transitions due to cyclopentadienone (**Figure 2.8(c)**, right) are observed beginning at 820 K, while the vinylacetylene product only appeared in measurable concentration at 1120 K (**Figure 2.8(c)**, left). The observed decomposition pathway of *o*-guaiacol is consistent with previous literature.¹⁰

This example shows how the correlation in signals in the VUV mass spectra and microwave spectra can extend and speed the analysis of complex mixtures. VUV photoionization TOF mass spectrometry provides the molecular formulae of the mixture components, as long as they have ionization energies lower than the VUV photon energy (10.5 eV). In the case of guaiacol, this included the reactant itself, the free radicals formed in the initial pyrolysis step ($\text{CH}_3 + o$ -hydroxyphenoxy), other highly reactive intermediates (e.g., cyclopentadienone), and many of the final products. Only C_2H_2 had an ionization energy above 10.5 eV, and its presence was surmised only indirectly from the other products observed.¹⁰ On the other hand, the chemical structure of the molecular components is often not uniquely prescribed by the molecular formulae. Furthermore, free radicals and reactive intermediates often have chemical structures that have not been observed or characterized previously by high resolution methods. CP-FTMW spectroscopy is a powerful tool for this characterization, relying only on the presence of a permanent dipole moment for detection. In the pyrolysis of guaiacol, this led to the first structural characterization of the *o*-hydroxyphenoxy radical.⁴⁶ Finally, the combination of the two methods is put to particularly good use in identifying conditions under which particular pyrolysis intermediates are present with maximum intensity, improving the quality of the microwave spectra obtained.

2.3.4 Conclusion

We have described the CP-FTMW/TOF spectrometer in detail and have demonstrated its capabilities by studying two complementary gas mixtures: one consisting of three stable furanic compounds and a second resulting from flash pyrolysis. In doing so, we have shown the power of CP-FTMW spectroscopy in its ability to determine fractional abundances and detect structural isomers that would not be distinguishable in a photoionization mass spectrum at fixed photoionization energy. We have further demonstrated the value of obtaining the complementary

data from the CP-FTMW and TOFMS methods by studying the pyrolysis of *o*-guaiacol. There, the mass spectrum provides insight to the reaction pathway and enables the potential identification of intermediates that do not have a permanent dipole moment. The intensities in the mass spectrum also are useful in determining the best conditions for studying reactive intermediates and final products via CP-FTMW spectroscopy. With the data provided, we have demonstrated the promise of this instrument as a multiplexed approach to determining gas phase structures.

2.4 References

- ¹D. H. Levy, *Science* **214**, 263 (1981).
- ²D. M. Lubman, C. T. Rettner, R. N. Zare, *J. Phys. Chem.* **86**, 1129 (1982).
- ³R. E. Smalley, L. Wharton, D. H. Levy, *Accounts Chem. Res.* **10**, 139 (1977).
- ⁴P. Chen, S. D. Colson, W. A. Chupka, J. A. Berson, *J. Phys. Chem.* **90**, 2319 (1986).
- ⁵E. B. Jochnowitz, X. Zhang, M. R. Nimlos, M. E. Varner, J. F. Stanton, G. B. Ellison, *J. Phys. Chem. A* **109**, 3812 (2005).
- ⁶H. W. Rohrs, C. T. Wickham-Jones, G. B. Ellison, D. Berry, B. M. Argrow, *Rev. Sci. Instrum.* **66**, 2430 (1995).
- ⁷X. Zhang, A. V. Friderichsen, S. Nandi, G. B. Ellison, D. E. David, J. T. McKinnon, T. G. Lindeman, D. C. Dayton, M. R. Nimlos, *Rev. Sci. Instrum.* **74**, 30773086 (2003).
- ⁸M. W. Jarvis, J. W. Daily, H. -H. Carstensen, A. M. Dean, S. Sharma, D. C. Dayton, D. J. Robichaud, M. R. Nimlos, *J. Phys. Chem.* **115**, 428 (2011).
- ⁹A. M. Scheer, C. Mukarakate, D. J. Robichaud, G. B. Ellison, M. R. Nimlos, *J. Phys. Chem. A* **114**, 9043 (2010).
- ¹⁰A. M. Scheer, C. Mukarakate, D. J. Robichaud, M. R. Nimlos, G. B. Ellison, *J. Phys. Chem. A* **115**, 1381 (2011).
- ¹¹A. K. Vasiliou, J. H. Kim, T. K. Ormond, K. M. Piech, K. N. Urness, A. M. Scheer, D. J. Robichaud, C. Mukarakate, M. R. Nimlos, J. W. Daily, Q. Guan, H. H. Carstensen, G. B. Ellison, *J. Chem. Phys.* **139**, 104310 (2013).
- ¹²K. N. Urness, Q. Guan, T. P. Troy, M. Ahmed, J. W. Daily, G. B. Ellison, J. M. Simmie, *J. Phys. Chem. A* **119**, 9962 (2015).

- ¹³Q. Guan, K. N. Urness, T. K. Ormond, D. E. David, G. B. Ellison, J. W. Daily, *Int. Rev. Phys. Chem.* **33**, 447 (2014).
- ¹⁴G. G. Brown, B. C. Dian, K. O. Douglass, S. M. Geyer, S. T. Shipman and B. H. Pate, *Rev. Sci. Instrum.* **79**, 053103 (2008).
- ¹⁵G. B. Park and R. W. Field, *J. Chem. Phys.* **144**, 200901 (2016).
- ¹⁶A. L. Steber, J. L. Neill, D. P. Zaleski, B. H. Pate, A. Lesarri, R. G. Bird, V. Vaquero-Vara and D. W. Pratt, *Faraday Discuss.* **150**, 227 (2011).
- ¹⁷J. Kraitchman, *Am. J. Phys.* **21**, 17 (1953).
- ¹⁸C. C. Costain, *J. Chem. Phys.* **29**, 864 (1958).
- ¹⁹J. M. Oldham, C. Abeysekera, B. Joalland, L. N. Zack, K. Prozumet, I. R. Sims, G. B. Park, R. W. Field and A. G. Suits, *J. Chem. Phys.* **141**, 154202 (2014).
- ²⁰C. Abeysekera, B. Joalland, N. Ariyasingha, L. N. Zack, I. R. Sims, R. W. Field, and A. G. Suits, *J. Phys. Chem. Lett.* **6**, 1599 (2015).
- ²¹C. Abeysekera, L. N. Zack, G. B. Park, B. Joalland, J. M. Oldham, K. Prozument, N. M. Ariyasingha, I. R. Sims, R. W. Field, and A. G. Suits, *J. Chem. Phys.* **141**, 214203 (2014).
- ²²K. Prozument, Y. V. Suleimanov, B. Buesser, J. M. Oldham, W. H. Green, A. G. Suits, and R. W. Field, *J. Phys. Chem. Lett.* **5**, 3641 (2014).
- ²³B. C. Dian, G. G. Brown, K. O. Douglass, and B. H. Pate, *Science* **320**, 924 (2008).
- ²⁴N. M. Kidwell, V. Vaquero-Vara, T. K. Ormond, G. T. Buckingham, D. Zhang, D. N. Mehta-Hurt, L. McCaslin, M. R. Nimlos, J. W. Daily, B. C. Dian, J. F. Stanton, G. B. Ellison, and T. S. Zwier, *J. Phys. Chem. Lett.* **5**, 2201 (2014).
- ²⁵A. O. Hernandez-Castillo, C. Abeysekera, B. M. Hays, and T. S. Zwier, *J. Chem. Phys.* **145**, 114203 (2016).
- ²⁶S. M. Fritz, A. O. Hernandez-Castillo, C. Abeysekera, B. M. Hays, and T. S. Zwier, *J. Mol. Spectrosc.* **349**, 10 (2018).
- ²⁷L. Cao, F. Muhlberger, T. Adam, T. Streibel, H. Z. Wang, A. Kettrup, and R. Zimmerman, *Anal. Chem.* **75**, 5639 (2003).
- ²⁸Y. J. Shi and R. H. Lipson, *Can. J. Chem.* **83**, 1891 (2005).
- ²⁹S. R. Leone, M. Ahmed, and K. R. Wilson, *Phys. Chem. Chem Phys.* **12**, 6564 (2010).
- ³⁰F. Qi, *Proc. Combust. Inst.* **34**, 33 (2013).

- ³¹B. Yang, C. Huang, L. Wei, J. Wang, L. Sheng, Y. Zhang, F. Qi, W. Zheng, and W. K. Li, Chem. Phys. Lett. **423**, 321 (2006).
- ³²F. Cudry, J. M. Oldham, S. Lingenfelter, and A. G. Suits, J. Phys. Chem. A **119**, 460 (2015).
- ³³A. J. Shirar, D. S. Wilcox, K. M. Hotopp, G. L. Storck, I. Kleiner, and B. C. Dian, J. Phys. Chem. A **114**, 12187 (2010).
- ³⁴J. Yang, X. B. Wang, X. P. Xing, L. S. Wang, J. Chem. Phys. **128**, 201102 (2008).
- ³⁵J. M. Beames, F. Liu, M. I. Lester, and C. Murray, J. Chem. Phys. **134**, 241102 (2011).
- ³⁶W. C. Wiley and I. H. McLaren, Rev. Sci. Instrum. **26**, 1150 (1955).
- ³⁷C. Abeysekera, A. O. Hernandez-Castillo, J. F. Stanton, and T. S. Zwier, J. Phys. Chem. A **122**, 6879 (2018).
- ³⁸D. Schmitz, V. A. Shubert, T. Betz, and M. Schnell, J. Mol. Spectrosc. **280**, 77 (2012).
- ³⁹J. A. Beukes, K.-M. Marstokk, and H. Møllendal, J. Mol. Struct. **567-568**, 19 (2001).
- ⁴⁰R. A. Motiyenko, E. A. Alekseev, S. F. Dyubko, and F. J. Lovas, J. Mol. Spectrosc. **240**, 93 (2006).
- ⁴¹K.-M. Marstokk, and H. Møllendal, Acta Chem. Scand. **48**, 25 (1994).
- ⁴²A. Giuliani, I. C. Walker, J. Delwiche, S. V. Hoffman, P. Limão-Vieira, N. J. Mason, B. Heyne, M. Hoebeke, and M.-J. Hubin-Franksin, J. Chem. Phys. **114**, 14 (2003).
- ⁴³D. Klapstein, C. D. MacPherson, and R. T. O'Brien, Can. J. Chem. **68**, 747 (1990).
- ⁴⁴D. W. Kohn, H. Clauberg, and P. Chen, Rev. Sci. Instrum. **63**, 4003 (1992).
- ⁴⁵J. C. Dean, P. Navotyana, A. P. Parobek, R. M. Clayton, and T. S. Zwier, J. Chem. Phys. **139**, 144313 (2013).
- ⁴⁶A. O. Hernandez-Castillo, S. M. Fritz, J. F. Stanton, and T. S. Zwier, *manuscript in preparation*.

CHAPTER 3. CONFORMER-SPECIFIC MICROWAVE SPECTROSCOPY OF 3-PHENYLPROPIONITRILE BY STRONG FIELD COHERENCE BREAKING

3.1 Introduction

Nitriles are abundant in the atmosphere of Titan, a moon of Saturn which has an atmosphere postulated to be similar to that on prebiotic Earth.¹⁻⁵ As a result, Titan has been the subject of intense study by planetary scientists, and has benefitted from the Cassini mission and Huygens probe, which have provided unprecedented sensitivity and detail regarding the atmospheric composition as a function of altitude and latitude.^{6,7} The haze surrounding Titan is made up of large complex organics, but the detailed chemical composition and pathways by which they are made are still under active exploration.⁸ As the sophistication of photochemical models continues to increase, laboratory studies that push into larger, more complex organics are essential for constraining the models. Results from the Cassini mission have shown the presence of smaller nitriles, but the search for larger organics will require a foundation of molecular spectroscopy for their identification.⁹



Figure 3.1 Schematic diagram of the reaction of benzyl radical with cyanomethyl radical to form 3-phenylpropionitrile.

Recent models recognize the importance of both neutral and ion chemistry to the formation of complex organics.¹⁰ Solar-driven photodissociation of stable molecules produces free radicals that

subsequently react to form larger products. Among the free radicals of greatest importance are resonance-stabilized radicals, in which the unpaired electron spin density is delocalized over several resonance structures that stabilize the radical. This unusual stability causes them to react only slowly with the most stable molecules, so that their concentrations can build up relative to their non-stabilized counterparts. Since the number of possible reactions grows exponentially with size of the reactants, it is important to restrict the laboratory focus to those reactions that are most likely to play a controlling role. In this sense, radical-radical recombination reactions are important, especially when they involve two resonance-stabilized radicals (RSR), since they are present in high abundance and react via a barrierless process to form even larger hydrocarbons.¹¹ Aromatics and nitriles are both prominent in the composition of Titan. 3-phenylpropionitrile (3-PPN) is the radical-radical recombination product of two prototypical RSRs, benzyl ($\text{C}_6\text{H}_5\text{-}\dot{\text{C}}\text{H}_2$) and cyanomethyl ($\dot{\text{C}}\text{H}_2\text{-C}\equiv\text{N}$) as shown in **Figure 3.1**.

Benzyl radical is the first resonance-stabilized phenyl derivative, while cyanomethyl is the nitrile equivalent of the propargyl radical ($\dot{\text{C}}\text{H}_2\text{-C}\equiv\text{CH}$) that is a major pathway to benzene formation via self-recombination.¹²⁻¹⁴ As such, 3-PPN is postulated to be a larger phenyl derivative of some importance in Titan's atmosphere.

Resonant 2-photon ionization (R2PI) studies of 3-PPN have identified *anti* and *gauche* conformers by assigning S_0 - S_1 origin bands based on rotational band contour measurements supported by *ab initio* calculations.¹⁵ The present study complements this work by providing broadband microwave spectra of 3-PPN over the 8-18 GHz region. Transitions due to *anti* and *gauche* conformers are detected and assigned. In the process of carrying out this study, we have utilized the newly-developed method of Strong Field Coherence Breaking (SFCB) to selectively modulate the intensities of a set of transitions due to each of the conformers in a conformer-

selective fashion, aiding the assignment.¹⁶ Chirped-pulse FTMW is a powerful, widely used spectroscopic technique for determining molecular structure because the frequency patterns provide a direct measure of the geometry through the rotational constants and projections of the permanent dipole moments along the inertial axes.¹⁷ In addition, the presence of a ^{14}N nucleus with its $I=1$ nuclear spin produces nuclear hyperfine splittings that are themselves conformer-specific, providing additional evidence for the conformational assignments as well as insight to the structure. In this work, rotational constants, dipole moments, nuclear quadrupole coupling constants, centrifugal distortion constants and relative populations are determined for the two conformers of 3-phenylpropionitrile. In the process of carrying out SFCB measurements, we have refined the method from that described in the original publication¹⁶ to increase the efficiency, streamline the process, and refine the peak selection method in ways that will make it easier to implement.

3.2 Experimental

3.2.1 Broadband Spectrum

A commercial sample of 3-PPN was obtained from Sigma-Aldrich with a stated purity of 99% and used without further purification. The sample was heated to 125 °C, entrained in He buffer gas at a pressure of 2.3 bar, and expanded through the 1 mm dia. orifice of a pulsed valve (Parker General, Series 9) operating at 10 Hz. The broadband rotational spectrum of 3-phenylpropionitrile was recorded in the 8-18 GHz region using a CP-FTMW spectrometer, which has been described in detail in chapter 2 and elsewhere.¹⁸

3.2.2 Computations

Based on previous studies of 3-phenylpropionitrile¹⁵, *anti* and *gauche* conformations were anticipated and optimized in MacroModel using an Amber* force field. Density Functional Theory

(DFT) geometry optimizations based on these starting structures were carried out using the Gaussian 09 suite¹⁹ at the B3LYP/def2-TZVP, B2PLYP-D3BJ/aug-cc-pVTZ, and MP2/-6-311++G(d,p) levels of theory to obtain rotational constants, dipole moments and nuclear quadrupole coupling constants. The predictions of DFT B3LYP/def2-TZVP calculations, including Grimme's dispersion correction,²⁰ was used for the initial rigid rotor fitting because it is less expensive and was thought to provide a good preliminary estimate of the relative energies based on its use in recent studies by our group of the alkyl benzenes²¹. The barrier height due to bond rotation for both conformers was determined at the B3LYP/6-311+G (d,p) level of theory. Spectroscopic constants are reported in **Table 3.1**.

3.2.3 Conformer-Specific Spectra

Conformer-specific microwave spectra of 3-PPN were recorded using the SFCB technique introduced recently by our group¹⁶ and illustrated in **Figure 3.2**. Given the complexity of the spectrum, there was a need to modify the line picking scheme described previously to select the transitions for multiple selective excitations (MSE). The new line picking scheme involves stepwise repetition of SFCB while incorporating an additional single frequency pulse in each successive spectrum. Initially, a broadband chirp with a single frequency pulse targeting the most intense line in the linear fast passage (LFP) spectrum is probed. A difference spectrum is acquired by subtracting the broadband spectrum from the broadband spectrum with the single frequency pulse present, and plotting its magnitude, while maintaining the same collection conditions for each spectral acquisition.

During the peak selection process, threshold levels were set for peak intensity modulation by the single-frequency pulse(s) (SFP) using 70% threshold percentages with each new choice of single-frequency coherence-breaking pulse. For instance, for 3-PPN, identification of transitions

modulated by more than 70% by the first SFP rigorously insures no false positives in the difference spectrum. Successive difference spectra were plotted based on percent thresholds of 70% for second and third single frequency pulses. After enough single frequency pulses were selected to modulate the intensity of a sufficient number of lines, a final difference spectrum is obtained to produce a set of conformer-specific transitions modulated by more than 10%.

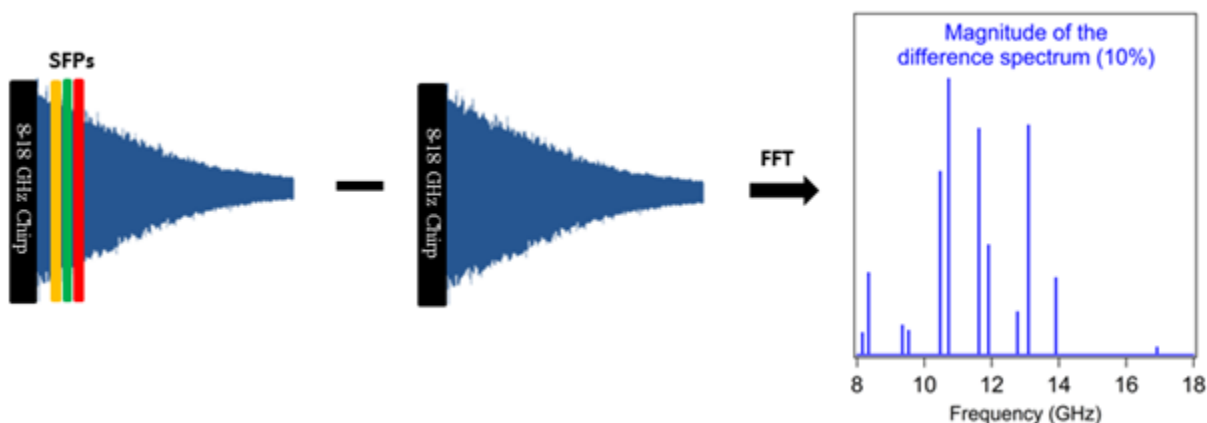


Figure 3.2 Schematic Diagram for the modified Strong Field Coherence Breaking scheme

With increased experience, the selection criteria for the resonant frequencies has also been refined, taking the following considerations into account. First, it is important to choose a resonant transition without another transition within ~ 10 MHz so that the wings on the SFP of 150 ns duration do not overlap significantly with other transitions that would reduce selectivity. This becomes increasingly challenging as the LFP spectrum becomes more dense. Second, the frequencies of the single-frequency pulses are typically chosen to avoid the edges of our frequency range, yet spread over the spectral range, so that transitions directly connected to those chosen will be in the frequency range of the broadband pulse. Third, each additional single frequency pulse is chosen to be resonant with a transition that is weak in the SFCB spectrum but is strong under LFP

conditions. Such an intensity change typically means that the transition has a big transition dipole moment and will therefore be good at modulating other lines. By not choosing the most intense transitions in the difference spectrum, transitions directly connected to the transition(s) used in preceding trials are avoided. When these criteria are used, additional transitions have their intensities modulated strongly by the new SFP that are largely complementary to those modulated by the first SFP. The same criterion is followed to accumulate more pulses in each attempt, as outlined in **Figure 3.2**.

3.3 Results

3.3.1 Spectral Assignment

A requirement for the SFCB method is the ability to operate in the rapid adiabatic passage (RAP) regime with strong coupling between the molecular dipole moment and the electric field. If the dipole moment of the molecule is large enough, adjusting the output of the electric field makes it possible to access both the strong and the weak coupling regimes.²² Forward (8 GHz \rightarrow 18 GHz) and backward (18 GHz \rightarrow 8 GHz) sweeps were recorded to demonstrate the ability of 3-PPN to enter the RAP regime with our current experimental set up. **Figure 3.3** compares the broadband spectra of 3-PPN in the 8-18 GHz frequency range sweeping in both directions at different TWTA gains. At 10% TWT amplification, the line intensities are not influenced by the sweep direction, as anticipated if the sweep conditions are in the linear fast passage (LFP) regime. In contrast, when the electric field strength is tuned to full power (TWTA: 100%), the line intensities change significantly with changing the chirp direction, demonstrating the ability to operate in the RAP regime for both conformers.

3.3.2 *Anti*-3-phenylpropionitrile

The modified line picking scheme was used to determine the single frequency pulses for the SFCB/MSE method. Under our experimental conditions, the strongest transition in the LFP spectrum was at 10.71906 GHz and the next two selected frequencies were at 13.09231 GHz and 12.76675 GHz. Following fitting, these transitions were subsequently assigned to $9_{1,8}$ - $8_{1,7}$, $11_{1,10}$ - $10_{1,9}$, and $11_{0,11}$ - $10_{0,10}$ transitions of *anti*-3-PPN, respectively. Each broadband sweep was 1 μ s in duration and each single frequency pulse lasted for 150 ns. The gap between the broadband chirp and the first single frequency pulse was 50 ns, whereas gaps between single frequency pulses were 5 ns to avoid beats.

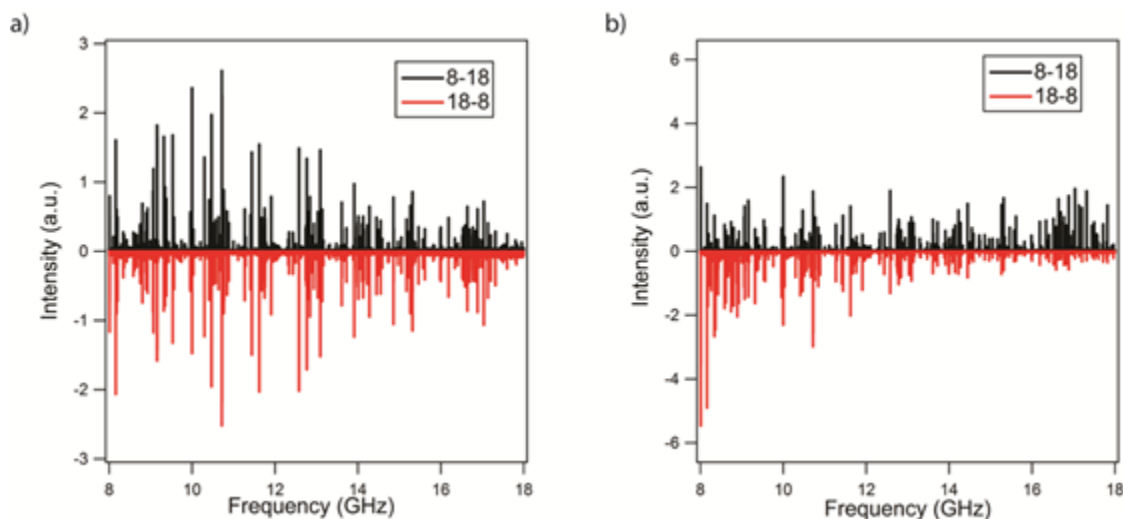


Figure 3.3 ((a) and (b)): Broadband CP-FTMW spectra of 3-phenylpropionitrile over the 8-18 GHz region produced by sweeping in the forward direction (black) and in the reverse direction (red) while at (a) 10% TWTA and (b) 100% TWTA power (~200 W).

Anti-3-PPN is a near prolate symmetric top that has the majority of its dipole along the *a*-axis ($\mu_a = -4.265$ D), a small projection along the *c*-axis ($\mu_c = -0.624$ D), and no component along the *b*-axis. **Figure 3.4(a)** presents the final difference spectrum for *anti*-3-PPN consisting of 11

conformer specific *a*-type transitions with a modulation of more than 10%. The modulated lines are plotted against B3LYP/def 2-TZVP predictions of both conformers, and by analyzing the spacing and pattern of the LFP spectrum, the modulated transitions best match *anti*-3-PPN. The conformer-specific transitions were used to obtain a preliminary fit using Pickett's SPFIT and SPCAT programs.²³ With the same set of programs, a total of 45 transitions were assigned in the final rigid rotor fit with a standard deviation in the fit of 0.054 MHz. These fit transitions are plotted in blue against the 1.5 M average LFP experimental spectrum in **Figure 3.5(a)**. The experimental rotational constants from the fit are in closest agreement with the B2PLYP-D3BJ/aug-cc-pVTZ predictions with a total error in the three rotational constants of 1.21%. The best-fit experimental parameters and the comparison with this level of theory are reported in **Table 3.1**.

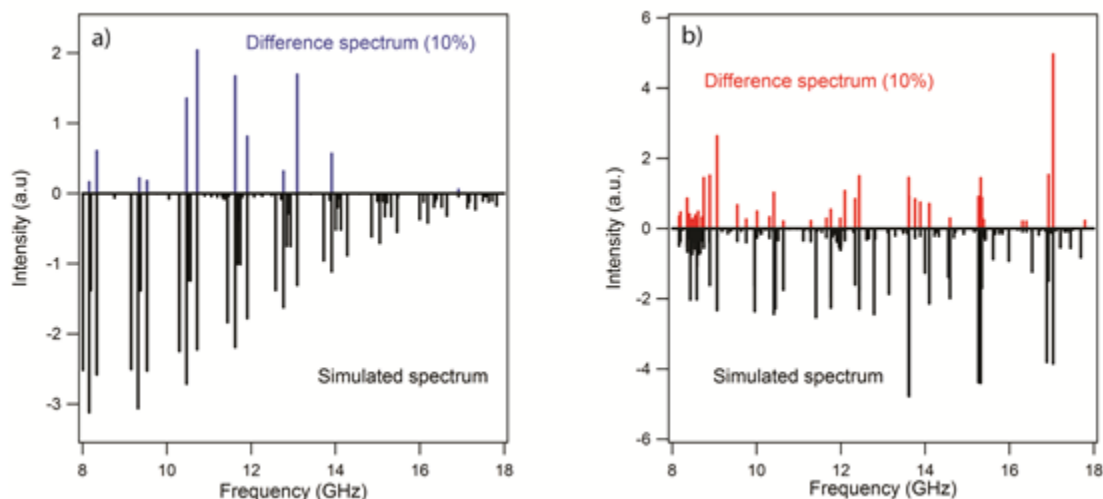


Figure 3.4 ((a) and (b)): Conformer-specific spectra for (a) *anti* and (b) *gauche* conformers of 3-PPN using the modified line picking scheme. Black lines display simulated spectra. Transitions whose intensities are modulated by more than 10% are displayed in red and blue.

Due to the nuclear spin of the nitrogen nucleus ($I(^{14}\text{N}=1)$), hyperfine splitting should be present. However, *anti*-3-PPN has most of its dipole moment along the *a*-axis where the CN functional group resides. Due to the size of the CN group and the majority of the dipole moment lying on the *a*-axis, the hyperfine structure is collapsed down to single, unresolvable transitions at our resolution, as demonstrated in **Figure 5(c)**. As a result, experimental nuclear quadrupole coupling constants could not be determined for the *anti* conformer.

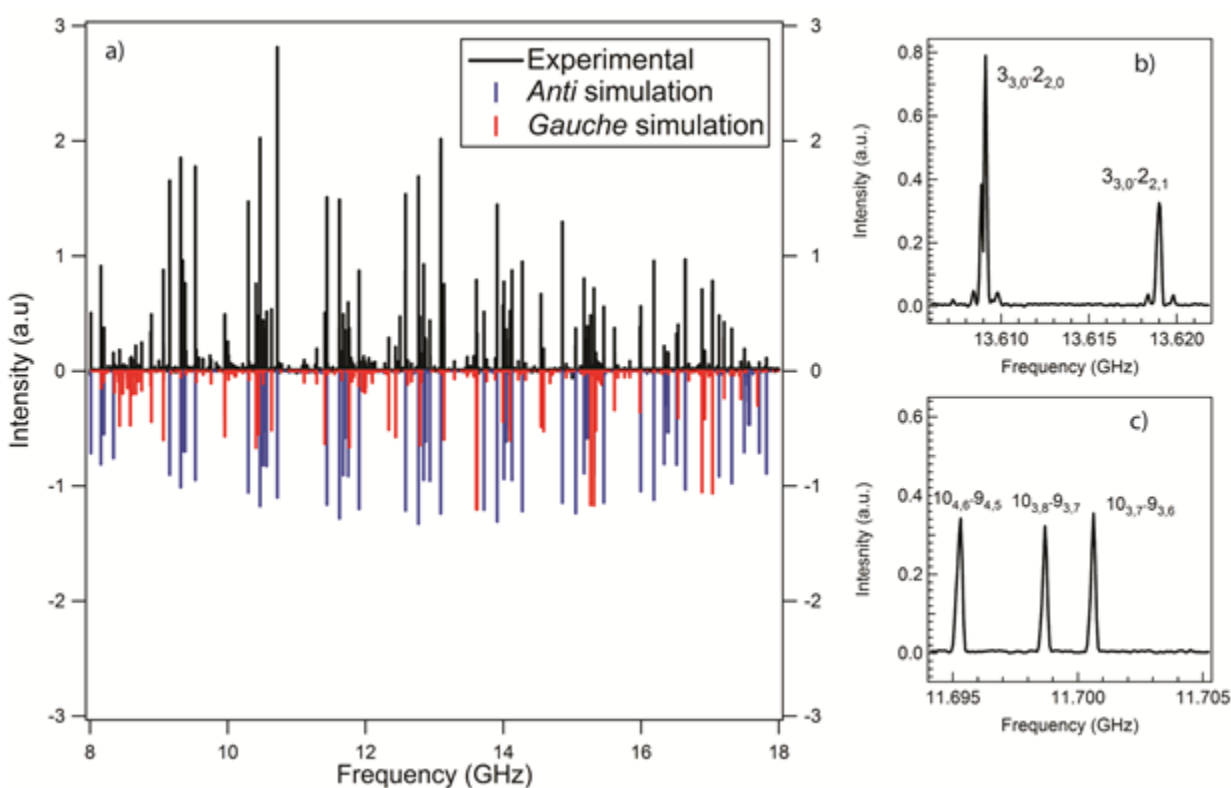


Figure 3.5 (a) Comparison of the experimental broadband spectrum of 3-PPN under LFP conditions (black trace) with the final fit for both conformers. The red lines belong to the *gauche* conformer and the blue lines belong to the *anti* conformer. (b) Hyperfine structure present in the *gauche* conformer. (c) Demonstration of the absence of hyperfine structure in the *anti* conformer.

3.3.3 *Gauche*-3-phenylpropionitrile

For *gauche*-3-PPN, the method was repeated for the remaining unassigned transitions using the same microwave settings. The strongest unassigned line in the LFP spectrum was at 9.066 GHz

and the next two selected frequencies were 16.9235 GHz and 12.09531 GHz. Following spectral fitting, these transitions are assigned as $5_{1,5}-4_{0,4}$, $6_{2,4}-5_{1,5}$, and $7_{2,5}-6_{2,4}$, respectively. *Gauche*-3-PPN is an asymmetric top with a large dipole component along the b-axis ($\mu_b = -3.507$ D), a sizable component along the a-axis ($\mu_a = -1.386$ D) and a small contribution from the c-axis ($\mu_c = +0.520$ D), yielding a significant increase in the number of conformer specific transitions. **Figure 3.3(b)** presents the magnitude of the final difference spectrum for *gauche*-3-PPN, identifying 43 conformer specific a-, b- and c-type transitions whose intensities are modulated by more than 10% with respect to the original RAP spectrum. The modulated lines are plotted against B3LYP/def 2-TZVP predictions, with the transitions best matching the *gauche* conformer.

The nuclear hyperfine structure is well-resolved in *gauche*-3-PPN, as demonstrated in **Figure 3.5(b)**, and 32 transitions due to the hyperfine structure were assigned, resulting in a total of 67 lines accounted for in the final fit with a standard deviation of 0.0258 MHz (**Figure 3.5(a)**). Experimental nuclear quadrupole coupling constants, χ_{aa} and χ_{bb-cc} , centrifugal distortion constants and experimental rotational constants were determined and are reported in **Table 3.1**. The experimental rotational constants for this conformer also best agree with the predictions from the B2PLYP-D3BJ/aug-cc-pVTZ level of theory with an error accounting for all rotational constants of 0.99%.

3.4 Discussion

We measured and assigned the rotational spectrum of *anti* and *gauche* conformers of 3-PPN in a supersonic expansion using the SFCB technique with a modified line picking scheme. The best fits from **Table 3.1** include fitting intensities to rotational temperatures via a Boltzmann plot and the line lists for both *anti* and *gauche* conformers are included in **Table 3.3** and **Table 3.4**, respectively. As expected, the two conformers had best-fit rotational temperatures that were

approximately the same, with $T_{\text{rot}}(\textit{gauche}) = 1.17 \pm 0.24$ K and $T_{\text{rot}}(\textit{anti}) = 1.48 \pm 0.10$ K, provided in **Figures 3.6** and **3.7**, respectively. Based on the experimental intensities, fractional abundances were extracted, which showed them to be nearly equal ($49 \pm 6\%$ *anti* : $51 \pm 6\%$ *gauche*). Given that the zero-point corrected relative energies of the two conformers are very close ($\Delta E(\textit{gauche-anti}) = 0.21$ kJ/mol = 17.5 cm⁻¹), and even exchange their energy ordering at some levels of theory, it is not particularly surprising that the two conformers have nearly equal population. However, the *gauche* conformer has twice the degeneracy of the *anti* conformer, due to the presence of *g*₊ and *g*₋ minima on the potential energy surface, so that a population ratio of 33% *anti*; 67% *gauche* is anticipated on that basis. A relatively low interconversion barrier would allow some conformational relaxation towards the global minimum conformer, which, if *anti*, would shift population consistent with this difference in expansion conditions. Calculations at the B3LYP/6-311+G (d,p) level were carried out to determine the interconversion barrier height by rotating the dihedral angle in ten degree steps. An isomerization barrier of 13.5 kJ/mol (1130 cm⁻¹) of energy is deduced. The relatively high energy barrier is consistent with significant population residing in both conformers, especially given the small energy difference between them, allowing only modest shifts in population with expansion conditions.

A set of molecular parameters (e.g., rotational constants, distortion constants, etc.) were fit from the experimental data and were compared with those obtained by quantum calculations. As mentioned in the experimental section, full geometry optimization was first carried out at the B3LYP/def2-TZVP level of theory. However, after the rotational spectrum was assigned, we noticed that at this level of theory, the calculated rotational constants differ up to 1.25% and 2.6% from the *anti* and *gauche* experimental rotational constants, respectively. In order to find a calculated structure that better matches the experimental observations, we explored other levels of

theory, as shown in **Table 3.2**. From this exploration, it was clear that the rotational constants calculated at B2PLYP-D3BJ/aug-cc-pVTZ level of theory were closest to experiment, predicting rotational constants with errors of 1.20% and 0.99% for *anti* and *gauche* conformers, respectively. The rotational constants predicted at the MP2/aug-cc-pVTZ level of theory are in poorest agreement with experiment, particularly for the *gauche* conformer. As other recent studies have noted,²⁴⁻²⁶ MP2 calculations are subject to large intramolecular basis set superposition errors that are greatest when remote parts of the molecule are in dispersive contact with one another, as they are in the *gauche* conformer of 3-PPN. We have noticed this type of behavior before in the conformational study of methyl butyrate²⁶ where the addition of diffuse functions increases the error with respect to the experiment, therefore, the basis-set superposition error present in MP2 calculations may be the cause for the lack of accuracy in the predictions.

Table 3.1 Molecular structure constants for *anti* and *gauche* conformers determined experimentally and calculated at the DFT B2PLYP-D3BJ/aug-cc-pVTZ level of theory

	<i>anti</i> -PPN		<i>gauche</i> -PPN	
	Experimental	Calculated	Experimental	Calculated
A (MHz)	4432.82(79)	4458.9166	2555.0155(44)	2568.8630
B (MHz)	607.9271(13)	609.5252	911.9367(11)	914.6686
C (MHz)	561.0895(14)	563.0799	763.9775(13)	765.1122
μ_a (D)	...	-4.219467	...	-1.2955
μ_b (D)	...	-0.000091	...	-3.5074
μ_c (D)	...	-0.616711	...	0.5432
χ_{aa}	1.64(10)	1.7313
χ_{bb-cc}	-5.792(12)	-6.059
d_K (MHz)	-0.00174(32)	...
D_J (MHz)	-0.0003021(81)	...
D_K (MHz)	-0.00339(34)	...
D_{JK} (MHz)	-0.00044(18)	...	0.000441(85)	...
E_{rel} (kJ/mol)		0		0.21
T (K)	1.48(0.10)		1.17(0.24)	
Population	48.9%		51.1%	
N	45	...	67	...
σ (MHz)	0.054	...	0.0258	...

The technique of SFCB is valuable in identifying transitions belonging to one component in a mixture, allowing the user to extract rotational constants and other structural information for each conformer. The original scheme for SFCB¹⁵ consisted of using single-frequency pulses (in the absence of the broadband chirp) to directly modulate a set of transitions; however, in 3-PPN, this scheme failed to modulate enough transitions to make a confident conformational assignment. Several adjustments were made to establish a new line picking scheme to speed up the line selection process and increase the number of modulated lines.

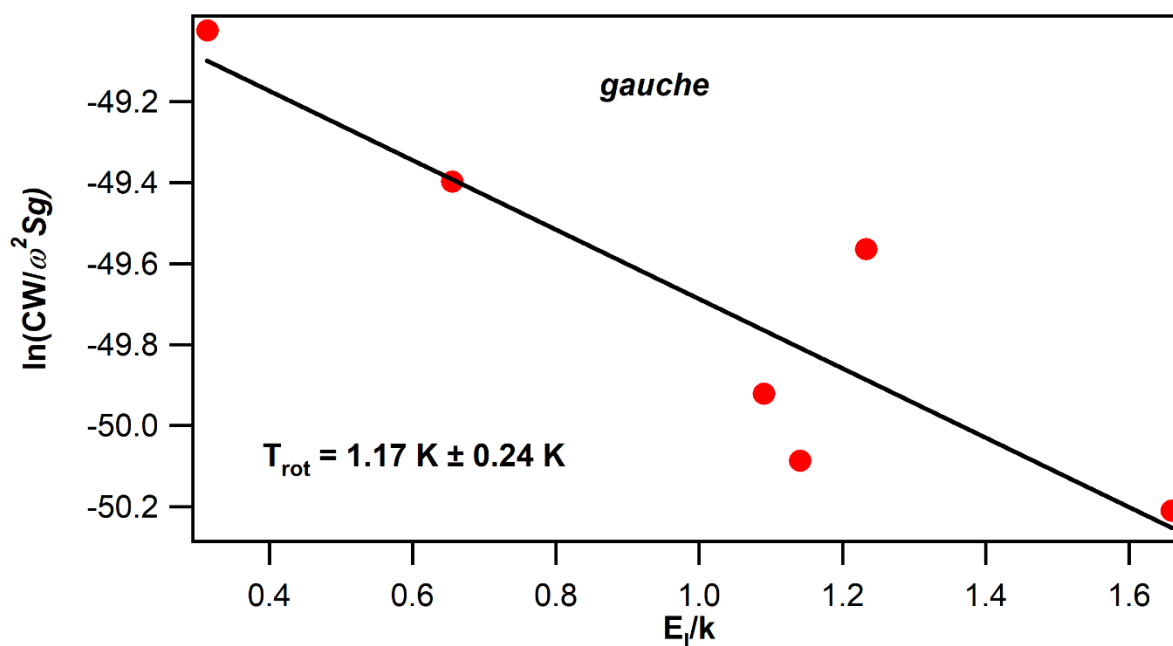


Figure 3.6 The Boltzmann plot for *gauche*-3-propionitrile. The rotational temperature was calculated to be 1.17 (± 0.24) K

The first major modification involves using the broadband chirp in conjunction with the trial single-frequency pulses. In doing so, a coherence between resonant rotational transitions is established in each attempt and subsequently broken by the single frequency pulses, thereby modulating the intensities of more transitions in the difference spectrum.

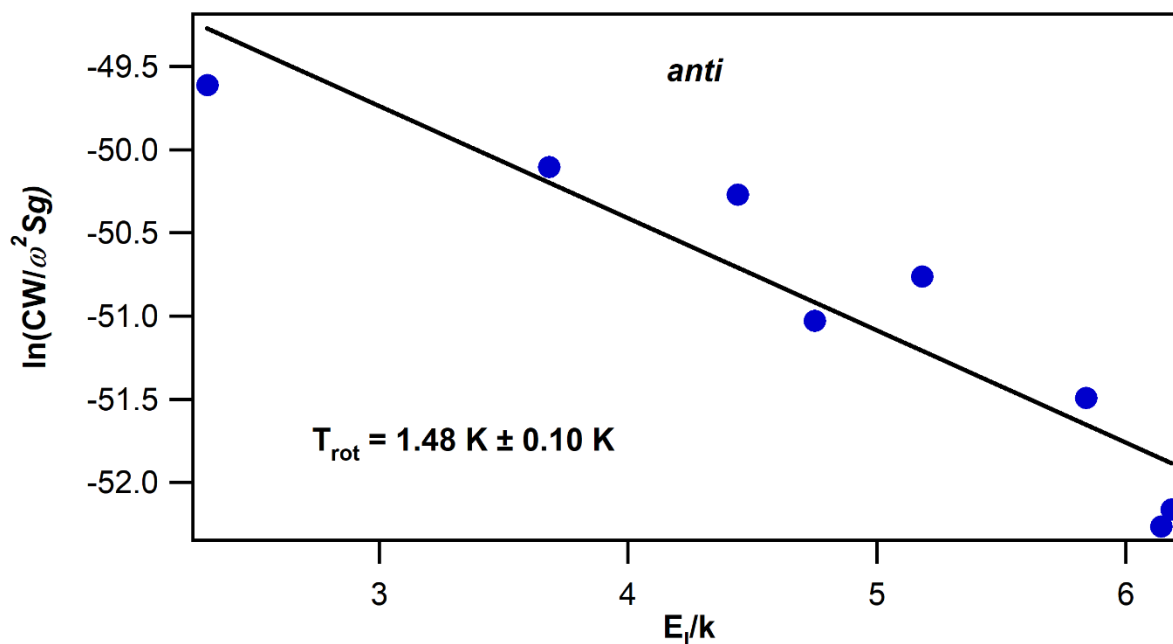


Figure 3.7 The Boltzmann plot for *gauche*-3-propionitrile. The rotational temperature was calculated to be 1.48 (± 0.10) K

Table 3.2 Percent errors in rotational constants calculated at the B2PLYP-D3BJ/aug-cc-pVTZ, B3LYP/def-2TZVP and MP2/6-311++G (d,p) levels of theory.

	<i>anti</i> -PPN			<i>gauche</i> -PPN		
	% Error (A)	% Error (B)	% Error (C)	% Error (A)	% Error (B)	% Error (C)
B2PLYP-D3BJ/aug-cc-pVTZ	0.59	0.26	0.35	0.54	0.30	0.15
B3LYP/def-2TZVP	0.81	0.17	0.27	1.43	0.47	0.68
MP2/6-311++G (d,p)	1.75	0.17	0.25	4.25	3.88	4.43

The second modification to the technique involves the sequential addition of each selected single frequency pulse after the broadband chirp to increase the number of modulated lines. The traces in **Figure 3.8** display the transitions whose intensities are modulated by more than 55% by the indicated single-frequency pulses. The top spectrum (red) shows just two transitions when the broadband chirp is followed by a SFP at 9.066 GHz ($5_{1,5}-4_{0,4}$), which is the strongest transition in the LFP spectrum for the *gauche* conformer. Since only one additional transition at 16.923 GHz was modulated by more than 55%, this frequency was then chosen as the frequency of the second

SFP. The spectrum in blue shows the lines that were modulated when one SFP was set at 16.923 GHz ($6_{2,4}-5_{1,5}$). In this case, seven new transitions appear in the difference spectrum, with nine in total. The spectrum shown in black was recorded using the improved line picking scheme by probing the broadband chirp followed by two SFPs at 9.066 GHz and 16.923 GHz. Compared to the two spectra above it recorded with only one SFP, adding the second SFP sequentially after the first, five additional transitions appear in the difference spectrum. This demonstrates that the refined method provides an increase in the number of lines modulated and therefore produced more transitions to choose from when selecting the SFPs.

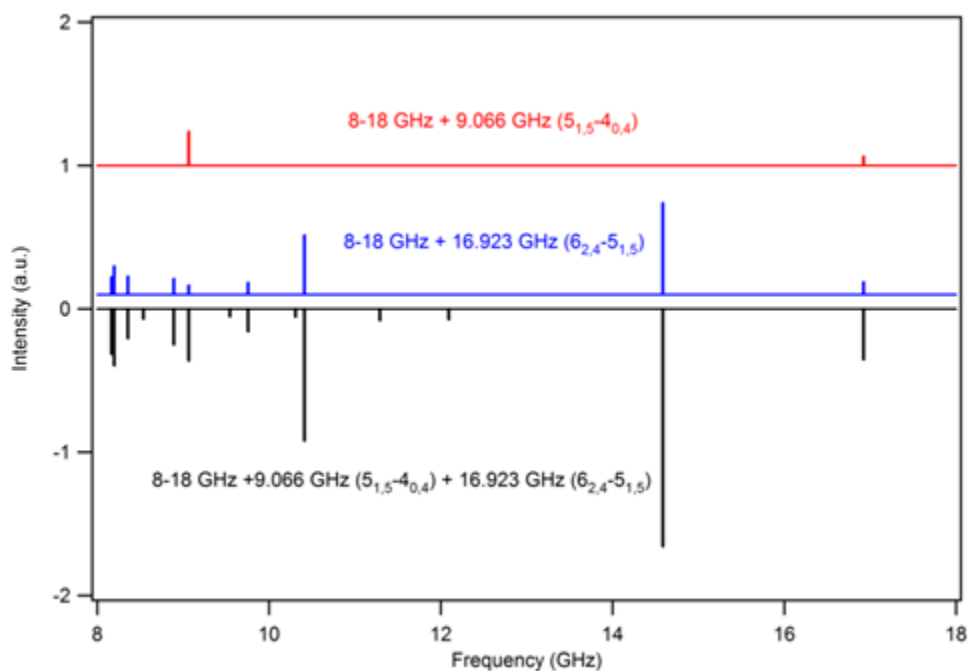


Figure 3.8 Difference spectra demonstrating the new line picking scheme and its advantages for modulating the intensities of more transitions when multiple single-frequency coherence-breaking pulses (SFP) are applied. The red and blue spectra show the modulated transitions due to just one SFP applied after the broadband chirp, resonant with a microwave transition of a single conformer. The black spectrum shows the transitions modulated by application of both SFPs after the chirp. Five new lines appear in this difference spectrum.

Lastly, we set a modulation threshold that is higher during the line-picking process (50-70%), so as to ensure fidelity in picking transitions only due to the conformer of interest. However, having done so, the final difference spectrum uses a lower modulation threshold (10%) for recording the final spectrum once three frequencies have been chosen. This increases the number of transitions in the difference spectrum still further. By restricting our choice of transitions to those whose intensities are modulated significantly, we increase the probability of transferring population to a larger number of transitions, and thus detecting more conformer-specific lines. Overall, these adjustments to the line picking scheme allowed for a set of MSE pulses that provided a confident assignment of both conformers.

The pathways to formation of large, complex organics in Titan's atmosphere is still an area of intense investigation. Among them, we propose 3-PPN as a potential candidate due to its position as the product of a radical recombination of two resonance-stabilized radicals likely to be of importance in Titan's hydrocarbon and nitrile rich environment.

The largest molecule detected in the interstellar medium is benzonitrile in which 9 *a*-type rotational transitions were identified utilizing information from databases and laboratory data in the 7-29 GHz region.²⁶ As the size of the molecules detected in Titan's atmosphere or in the interstellar medium continues to increase, laboratory studies are needed to guide astronomical searches for their presence. A challenge of studying these larger molecules is spectral congestion, as multiple conformers may contribute to the spectrum. By providing a reliable set of rotational constants from measurements in the 8-18 GHz region, the strongest rotational transitions at 70 K, the temperature of Titan's atmosphere,²⁸ can be sought out for identification. At this temperature, the Boltzmann peaks for the *gauche* and *anti* conformers are at J=26, with transition frequencies near 40 GHz and 30 GHz, respectively. In the interstellar medium, where the temperatures in cold

molecular clouds such as TMC-1 are 5-10 K, the Boltzmann peaks for *anti* and *gauche* conformers are at J levels of 18 and 16 with frequencies near 21 GHz and 26 GHz, respectively. It is hoped that the present data can provide a set of unique transitions that can be used to identify 3-PPN in extraterrestrial environments.

3.5 Conclusion

Here, we demonstrate the application of strong field coherence breaking to determine the molecular structure of a molecule with potential astrochemical significance. In carrying out this study, a modified line picking scheme was developed in order to enhance and streamline the technique. Conformer-specific spectra were obtained, yielding 43 lines that belonged to the *gauche* conformer and 11 lines that belonged to the *anti* conformer. The conformer specific transitions aid in fitting the congested broadband spectrum, which provides all of the rich information about the molecular structure including rotational constants, nuclear quadrupole coupling constants and distortion constants. A population analysis was carried out with a 1:1 *anti* to *gauche* population ratio determined. It is hoped that the future searches for more complex organics will locate microwave transitions due to 3-PPN, guided by the data provided here.

3.6 References

- ¹A. Coustenis, *Astron. Geophys.* **48**, 14 (2007).
- ²N. A. Teanby, P.G.J. Irwin, R. de Kok, C.A. Nixon, A. Coustenis, B. Bezard, S.B. Calcutt, N.E. Bowles, F.M. Flasar, L. Fletcher, C. Howett, F.W. Taylor, *Icarus* **181**, 243 (2006).
- ³N. A. Teanby, P.G.J. Irwin, R. de Kok, S. Vinatier, B. Bezard, C.A. Nixon, F.M. Flasar, S.B. Calcutt, N.E. Bowles, L. Fletcher, C. Howett, F.W. Taylor, *Icarus* **186**, 364 (2007).
- ⁴D. W. Clarke, J. P. Ferris, *Orig. Life Evol. Biol.* **27**, 225 (1997).
- ⁵M. G. Trainer, A.A. Pavlov, H.L. DeWitt, J.L. Jimenez, C.P. McKay, O.B. Toon, M.A. Tolbert, *P. Natl. Acad. Sci. USA* **103**, 18035 (2006).

- ⁶A. Coustenis, R.K. Achterberg, B.J. Conrath, D.E. Jennings, A. Marten, D. Gautier, C.A. Nixon, F.M. Flasar, N.A. Teanby, B. Bezard, R.E. Samuelson, R.C. Carlson, E. Lellouch, G.L. Bjoraker, P.N. Romani, F.W. Taylor, P.G.J. Irwin, T. Fouchet, A. Hubert, G.S. Orton, V.G. Kunde, S. Vinatier, J. Mondellini, M.M. Abbas, R. Courtin, *Icarus* **189**, 35 (2007).
- ⁷J. Cui, R.V. Yelle, V. Vuitton, J.H. Waite, W.T. Kasprzak, D.A. Gell, H.B. Niemann, I.C.F. Muller-Wodarg, N. Borggren, G.G. Fletcher, E.L. Patrick, E. Raaen, B.A. Magee, *Icarus* **200**, 581 (2008).
- ⁸E. H. Wilson, S. K. Atreya, *Planet. Space Sci.* **51**, 1017 (2003).
- ⁹G. Israël, C. Szopa, F. Raulin, M. Cabane, H. B. Niemann, S. K. Atreya, S. J. Bauer, J.-F. Brun, E. Chassefière, P. Coll, E. Condé, D. Coscia, A. Hauchecorne, P. Millian, M.-J. Nguyen, T. Owen, W. Riedler, R. E. Samuelson, J.-M. Siguier, M. Steller, R. Sternberg, C. Vidal-Madjar, *Nature* **438**, 796 (2005).
- ¹⁰V.A. Krasnopolsky, *Icarus* **201**, 226 (2009).
- ¹¹D. S. N. Parker, F. Zhang, Y. S. Kim, R. I. Kaiser, A. M. Mebel, *J. Phys. Chem. A.* **115**, 593 (2011).
- ¹²H. Richter, J. B. Howard, *Phys. Chem. Chem. Phys.* **4**, 2038 (2002).
- ¹³J. A. Miller and C. F. Melius, *Combust. Flame* **91**, 21 (1992).
- ¹⁴C. Huang, F. Zhang, R. I. Kaiser, V. V. Kislov, A. M. Mebel, R. Silva, W. K. Gichuhi, A. G. Suits, *J. Astrophys.* **714**, 1249 (2010).
- ¹⁵D. E. Marten, E. G. Robertson, R. J. S. Morrison, *Chem. Phys. Lett.* **425**, 210 (2006).
- ¹⁶A. O. Hernandez-Castillo, C. Abeysekera, B. M. Hays, T. S. Zwier, *J. Chem. Phys.* **145**, 114203 (2016).
- ¹⁷G. B. Park, R. W. Field, *J. Chem. Phys.* **144**, 200901 (2016).
- ¹⁸S. M. Fritz, B. M. Hays, A. O. Hernandez-Castillo, C. Abeysekera, and T. S. Zwier, *Rev. Sci. Instrum.* **89**, 093101 (2018).
- ¹⁹D. J. Frisch, M. J.; Trucks, G. W.; Schlegel, H. B.; Scuseria, G. E.; Robb, M. A.; Cheeseman, J. R.; Scalmani, G.; Barone, V.; Mennucci, B.; Petersson, G. A.; Nakatsuji, H.; Caricato, M.; Li, X.; Hratchian, H. P.; Izmaylov, A. F.; Bloino, J.; Zheng, G.; Sonnenb, Gaussian 09, Revis. E.01, Gaussian, Inc., Wallingford CT. (2009).
- ²⁰S. Grimme, *J. Chem. Phys.* **124**, 034108 (2006).
- ²¹D. P. Tabor, D. M. Hewett, S. Bocklitz, J. A. Korn, A. J. Tomaine, A. K. Ghosh, T. S. Zwier, E. L. Sibert, *J. Chem. Phys.* **144**, 224310 (2016).
- ²²D. Schmitz, V. A. Shubert, T. Betz, M. Schnell, *J. Mol. Spectrosc.* **280**, 77 (2012).

- ²³H. M. Pickett, J. Mol. Spectrosc. **377**, 371 (1991).
- ²⁴R. M. Balabin, Mol. Phys. **109**, 943 (2011).
- ²⁵L. F. Holroyd, T. van Mourik, Chem. Phys. Lett. **442**, 42 (2007).
- ²⁶A. O. Hernandez-Castillo, C. Abeysekera, B. M. Hays, I. Kleiner, H. V. L. Nguyen, T. S. Zwier, J. Mol. Spectrosc. **337**, 51 (2017).
- ²⁷B. A. McGuire, A. M. Burkhardt, S. Kalenskii, C. N. Shingledecker, A. J. Remijan, E. Herbst, M. C. McCarthy, Science **359**, 202 (2018).
- ²⁸T. M. Selby, T. S. Zwier, J. Phys. Chem. A. **109**, 8487 (2005).

3.7 Supplementary Material

Table 3.3 Rotational transitions assigned in the final fit for *anti*-3-phenylpropionitrile. Frequencies reported are experimental and the error is calculated after fitting with Pickett’s SPFIT program.

<i>J</i>	<i>K_a</i>	<i>K_c</i>	<i>J</i>	<i>K_a</i>	<i>K_c</i>	<i>v</i> _{Obs.}	<i>v</i> _{Obs.} − <i>v</i> _{Calc.}
upper level			lower level			MHz	<i>SPFIT</i> MHz
7	1	7	6	1	6	8013.7500	0.0203
7	0	7	6	0	6	8159.3750	0.0144
8	1	8	7	1	7	9156.5620	0.0231
8	0	8	7	0	7	9316.5620	0.0167
8	2	7	7	2	6	9346.8808	0.0134
7	2	6	6	2	5	8179.8120	0.0116
7	2	5	6	2	4	8203.6250	0.0121
7	1	6	6	1	5	8341.3120	0.0190
8	2	6	7	2	5	9382.5620	0.0148
8	1	7	7	1	6	9530.6870	0.0216
9	1	9	8	1	8	10298.6200	0.0259
9	0	9	8	0	8	10470.5600	0.0195
9	2	8	8	2	7	10513.4400	0.0153
9	2	7	8	2	6	10564.1200	0.0182
9	1	8	8	1	7	10719.0600	0.0241
10	1	10	9	1	9	11439.8150	0.0288
10	0	10	9	0	9	11621.0600	0.0232
10	2	9	9	2	8	11679.3700	0.0173
10	2	8	9	2	7	11748.5000	0.0222
10	1	9	9	1	8	11906.3100	0.0266

Table 3.3 cont.

11	1	11	10	1	10	12580.1900	0.0317
11	0	11	10	0	10	12767.8100	0.0278
11	2	10	10	2	9	12844.5000	0.0194
11	2	9	10	2	8	12935.8700	0.0270
11	1	10	10	1	9	13092.3100	0.0292
12	0	12	11	0	11	13910.7500	0.0333
12	2	11	11	2	10	14008.8100	0.0216
12	2	10	11	2	9	14126.2500	0.0323
13	1	13	12	1	12	14858.0000	0.0376
12	1	11	11	1	10	14276.8125	0.0319
10	3	8	9	3	7	11698.8321	0.0417
10	3	7	9	3	6	11700.7568	0.0412
13	0	13	12	0	12	15049.8125	0.0397
8	3	6	7	3	5	9356.8750	0.0337
8	3	5	7	3	4	9357.5000	0.0345
9	3	7	8	3	6	10527.6250	0.0377
9	3	6	8	3	5	10528.7500	0.0374
12	1	12	11	1	11	13719.6250	0.0346
13	2	11	12	2	10	15319.7500	0.0382
13	1	12	12	1	11	15459.6875	0.0347
14	1	14	13	1	13	15995.5000	0.0406
14	2	12	13	2	11	16515.9375	0.0441
14	1	13	13	1	12	16640.6875	0.0379
15	2	13	14	2	12	17714.6250	0.0499
15	1	14	14	1	13	17819.6875	0.0416

Table 3.4 Rotational transitions assigned in the final fit for *anti*-3-phenylpropionitrile. Frequencies reported are experimental and the error is calculated after fitting with Pickett's SPFIT program.

<i>J</i>	<i>K_a</i>	<i>K_c</i>	<i>F</i>	<i>J</i>	<i>K_a</i>	<i>K_c</i>	<i>F</i>	<i>v</i> Obs.	<i>v</i> Obs. – <i>v</i> Calc.
upper level				lower level				MHz	SPFIT MHz
3	3	1	4	2	2	0	3	13609.1250	0.0368
3	3	0	4	2	2	1	3	13619.0625	0.0367
4	3	2	5	3	2	1	4	15265.1250	0.0323
4	3	2	4	3	2	1	3	15264.7500	0.0375
6	0	6	7	5	1	5	6	8891.0625	0.0289
6	0	6	6	5	1	5	5	8891.5000	0.0303
7	3	5	8	7	2	6	8	8882.3750	0.0404
5	3	3	6	5	2	4	6	8666.5000	0.0321
4	3	2	5	4	2	3	5	8616.3750	0.0396
4	3	2	4	4	2	3	4	8616.0625	0.0581
5	1	4	4	4	1	3	3	8703.3750	0.0223
6	3	4	7	6	2	5	7	8751.6250	0.0312
5	1	5	6	4	0	4	5	9066.0000	0.0251
5	1	5	5	4	0	4	4	9065.2500	0.0309
5	1	5	4	4	0	4	3	9066.1875	0.0273
8	3	6	9	8	2	7	9	9068.8125	0.0574
8	3	6	8	8	2	7	8	9069.0000	0.0597
3	2	2	4	2	1	1	3	9957.1875	0.0284
3	2	2	3	2	1	1	2	9956.0000	0.0469
3	2	2	2	2	1	1	1	9957.8125	0.0462
3	2	1	4	2	1	2	3	10448.0625	0.0282
3	2	1	2	2	1	2	1	10447.6250	0.0480
3	2	1	3	2	1	2	2	10448.9375	0.0551
6	1	6	7	5	0	5	6	10411.7500	0.0259
6	1	6	6	5	0	5	5	10411.0625	0.0298
4	2	3	5	3	1	2	4	11409.8750	0.0263
4	2	3	4	3	1	2	3	11408.7500	0.0395
4	2	3	3	3	1	2	2	11410.3125	0.0361
7	1	7	8	6	0	6	7	11764.1875	0.0251
7	1	7	7	6	0	6	6	11763.7500	0.0275
5	2	4	6	4	1	3	5	12788.9375	0.0269
5	2	4	4	4	1	3	3	12789.2500	0.0328
5	2	4	5	4	1	3	4	12787.8125	0.0360
8	0	8	9	7	0	7	8	12810.5625	0.0197

Table 3.4 cont.

8	1	8	9	7	0	7	8	13139.9375	0.0252
8	1	8	8	7	0	7	7	13139.5625	0.0263
6	0	6	7	5	0	5	6	9757.6250	0.0206
6	0	6	6	5	0	5	5	9757.4375	0.0211
7	0	7	7	6	1	6	6	10637.6250	0.0269
7	0	7	8	6	1	6	7	10637.3750	0.0261
7	1	7	8	6	1	6	7	11110.1250	0.0197
7	0	7	8	6	0	6	7	11291.4375	0.0189
7	0	7	7	6	0	6	6	11291.2500	0.0193
6	1	6	7	5	1	5	6	9545.1250	0.0219
4	3	1	5	3	2	2	4	15315.1875	0.0316
6	0	6	7	5	0	5	6	9757.6250	0.0206
6	0	6	6	5	0	5	5	9757.4375	0.0211
7	2	5	8	6	2	4	7	12095.3125	0.0270
7	2	5	7	6	2	4	6	12095.5000	0.0276
7	1	6	8	6	1	5	7	12098.8750	0.0259
9	0	9	10	8	1	8	9	13994.2500	0.0324
8	1	7	9	7	1	6	8	13759.4375	0.0356
8	2	6	9	7	2	5	8	13883.6875	0.0309
5	2	3	6	4	1	4	5	14585.6250	0.0333
5	2	3	4	4	1	4	3	14585.3125	0.0398
5	2	3	5	4	1	4	4	14587.0625	0.0586
10	0	10	11	9	1	9	10	15613.8125	0.0487
9	1	9	10	8	0	8	9	14546.3750	0.0314
9	1	9	9	8	0	8	8	14546.0625	0.0317
10	1	10	11	9	0	9	10	15983.5000	0.0471
10	1	10	10	9	0	9	9	15983.3125	0.0470
8	2	7	9	7	1	6	8	16536.5625	0.0672
8	2	7	8	7	1	6	7	16535.5625	0.0676
5	3	3	6	4	2	2	5	16884.2500	0.0329
5	3	3	5	4	2	2	4	16883.7500	0.0365
6	2	4	7	5	1	5	6	16923.5625	0.0463
6	2	4	5	5	1	5	4	16923.2500	0.0499

CHAPTER 4. STRONG FIELD COHERENCE BREAKING AS A TOOL FOR IDENTIFYING METHYL ROTOR STATES: 2-HEXANONE

4.1 Introduction

Methyl rotors are pervasively present in organic molecules, with the CH_3 group undergoing hindered rotation about the single bond to the rest of the organic framework. Since the primary motion involves the three H-atoms of the methyl group, tunneling can occur between the equivalent minima on the potential energy surface, leading to tunneling splittings, energy levels and wave functions that reflect the shape and height of the barrier to methyl rotation. This potential for hindered internal rotation is highly sensitive to the local electronic structural environment of the methyl group, depending on a subtle combination of dispersive, exchange, electrostatic, and steric effects between the methyl group and the rest of the molecular frame.¹

In many circumstances, methyl internal rotation can be treated as motion on a one-dimensional potential energy curve involving the dihedral angle associated with the C-X bond joining methyl group to the molecular frame. The form of these potential energy curves are predominantly 3-fold if the frame against which the methyl rotor rotates has a distinct left-right asymmetry to it, as is often the case. Tunneling through barriers leads to splittings and energy level structure that depend sensitively on the magnitude and shape of the barriers separating minima. If tunneling were not occurring, the 3-fold potential would support a triply degenerate methyl torsion at its zero-point level; however, in the presence of tunneling, the three levels split into a nondegenerate (a_1) and a two-fold degenerate (e) sublevel in the G_6 molecular symmetry group.² When the internal rotor angular momentum quantum number ($|m|=0, 1, 2, \dots$) is included in the labeling scheme, these levels are designated as $0a_1$ and $1e$.³

Spectroscopic methods involving electronic⁴, infrared⁵, Raman^{6,7} and far-IR⁸ have been used to study the barriers to internal rotation. In the gas phase, dispersed emission spectra from single torsional levels in the excited electronic state can be used to determine the form of the hindering rotor potential and its barrier height.^{4,9} Based on the splittings and over-all rotation/internal rotation couplings, similar data on the excited state barriers can be extracted from the rotational structure of a vibronic transition. In favorable cases, infrared and Raman spectra can be used to determine the unusual frequency patterns of the methyl torsional levels; however, these torsional vibrations are usually only weakly allowed in both infrared and Raman measurements, and lie in the very far infrared region so that their detection and assignment can be difficult.¹⁰

One powerful method for studying methyl internal rotation is microwave spectroscopy¹⁰⁻¹⁸. These gas phase measurements typically occur under expansion-cooled conditions where population is removed from higher internal rotor levels. However, due to differing nuclear spin symmetries of the 0a₁ and 1e torsional levels, collisional cooling between these lowest two methyl rotor levels does not occur on the timescale of the cooling process. Microwave spectra of expansion-cooled molecules therefore exhibit rotational transitions built off both 0a₁ and 1e methyl rotor levels, with resolved methyl rotor splittings for methyl rotor barriers up to ~1000 cm⁻¹.¹² As a result, the presence of these splitting is pervasive in microwave spectra, and has been the subject of much previous work.¹⁰⁻¹⁸ Fitting these spectra can be a challenge, as rotational transitions due to 0a₁, 1e levels are intermingled with one another, and barriers to internal rotation often depend on molecular conformation^{19,20} and complex formation.¹⁴ Due to the fact that there is no interconversion between 0a₁, 1e on the timescale of the experiment, ‘a’ and ‘e’ methyl rotor levels support separate rotational manifolds, much as if they were two conformational isomers.

Recently, we have developed the method of strong-field coherence breaking (SFCB) that enables identification of sets of rotational transitions due to a single entity in a mixture, whether separate molecular components or conformational isomers.²¹ The SFCB method involves application of a set of resonant microwave frequencies at high power to interrogate the mixture following broadband chirped-pulse excitation, thereby modulating the intensities of a set of transitions sufficient in number that they can be used as the basis for a preliminary fit of that component of the mixture. This speeds analysis and assignment of the microwave spectrum, sometimes by large factors. While SFCB has been applied previously to detect and assign conformational isomers²¹⁻²³ and free radicals in a pyrolysis mixture²⁴, it has not been used yet to selectively identify microwave transitions due to methyl rotor sub-levels. With this study of 2-hexanone, we present its use for this purpose for the first time.

2-hexanone is an interesting candidate to demonstrate the power of SFCB, as it has a long alkyl chain supporting several conformational isomers as well as a methyl rotor. From a combustion standpoint, ketones play an interesting role as they are important constituents in biomass-derived liquids, and small methyl ketones have high octane numbers and show low emission of soot.²⁵⁻²⁸ Yet, the combustion chemistry of ketones such as 2-hexanone is still in its early stages of exploration. The energy level structure and conformational preferences of 2-hexanone are relevant to the initiation events in pyrolysis and combustion. Herein, we use SFCB to selectively modulate rotational transitions built off the $0a_1$ and $1e$ torsional states of each of the conformers present in an expansion-cooled sample of 2-hexanone, thereby aiding in the assignment of its methyl rotor transitions.

4.2 Experimental

4.2.1 Broadband Spectrum

The broadband rotational spectrum of 2-hexanone was recorded over the 8-18 GHz frequency regime using a chirped pulse Fourier transform microwave (CP-FTMW) spectrometer that has been described in Chapter 2 and elsewhere.²⁹ 2-hexanone (98%, Aldrich) was introduced to the gas phase by heating a stainless-steel sample holder to 60 °C. The sample was entrained in 3.1 bars of He before expanding into vacuum through the 1 mm dia. orifice of a solenoid driven pulsed valve (Parker General Series 9) operating at 10 Hz. The ensuing supersonic expansion is interrogated by the broadband microwave sweeps and the free induction decay (FID) is collected and digitized for 16 μ s using a 13 GHz, 40 GS/s real time digitizer (Guzik ADC6131). The experimental timing allowed for the collection of 20 FIDs per gas pulse separated from one another by 20 μ s. The time domain signal is filtered with a Kaiser-Bessel window and is fast Fourier transformed to obtain the final frequency domain spectrum using a custom MATLAB routine. The experimental resolution for a 16 μ s collection period is 60 kHz.

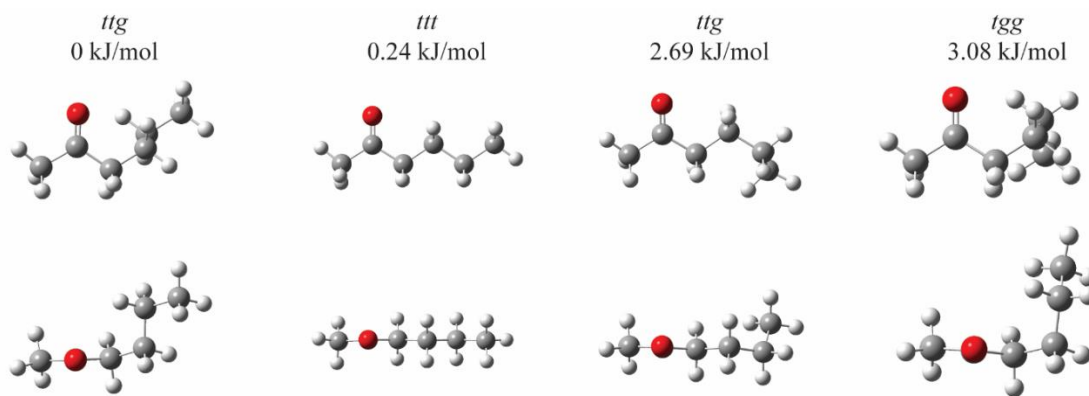


Figure 4.1 Top down and side views of the four lowest energy conformers of 2-hexanone predicted at the B3LYP/Def2TZVP level of theory, including Grimme's dispersion correction.

4.2.2 Computations

A conformational search of 2-hexanone was carried out using MacroModel with Merck molecular force field static (MMFFs).³⁰ Geometry optimizations of the possible conformations of 2-hexanone were performed using the Gaussian09 program suite³¹ at the DFT B3LYP/Def2TZVP level of theory including Grimme's dispersion (D3BJ).³² Based on the calculations, we anticipated potentially observing the four lowest energy conformers, shown in **Figure 4.1**, as these structures all fall into an energy window within ~3 kJ/mol of the global minimum.

The nomenclature to describe the conformations of 2-hexanone starts with the CH₃ next to the carbonyl group, and applying the terms *gauche* ($\pm 60^\circ$) and *trans* (180°) to describe the three backbone dihedral angles involved. Relaxed potential energy curves for methyl internal rotation of both terminal CH₃ groups were calculated for the low-energy conformers at the same level of theory used in the optimization. This was accomplished by scanning the dihedrals involving the two terminal CH₃ groups in 10° steps while optimizing the geometry along all other coordinates. The barriers heights for internal rotation of the CH₃ at the end of the alkyl chain were close to or in excess of 1000 cm^{-1} ; however, barriers heights for the methyl group next to the carbonyl moiety were less than 200 cm^{-1} for all four lowest energy conformers. Given the low barrier height, splittings due to methyl internal rotation from the methyl group next to the carbonyl were anticipated, while the methyl group at the end of the alkyl chain had a barrier too high to produce measurable splittings in our apparatus.

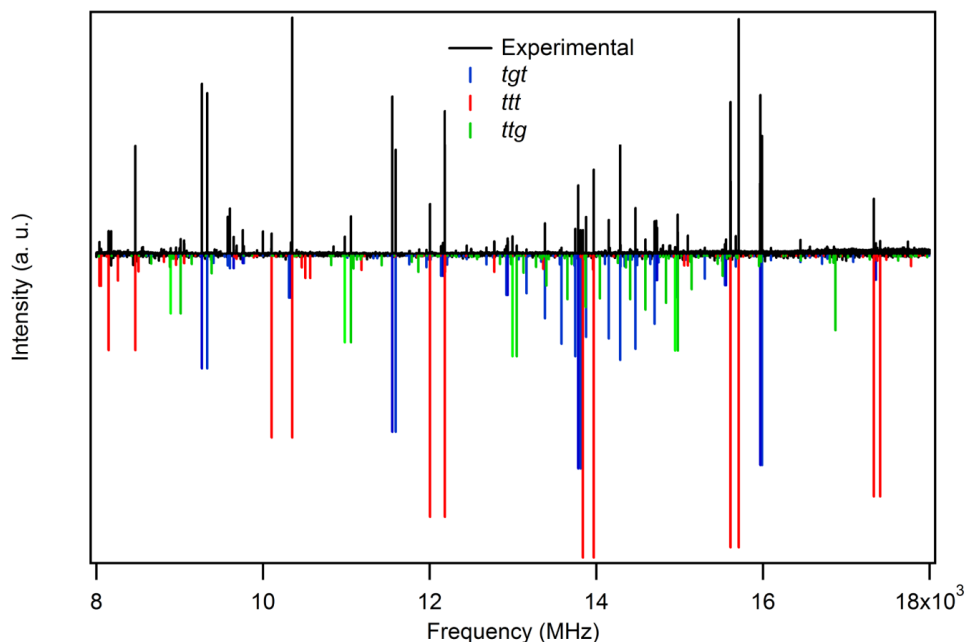


Figure 4.2 Experimental 1M average broadband spectrum of 2-hexanone with the best fits of the three identified conformers present. The blue, red and green lines are assigned to the *tgt*, *ttt* and *ttg* conformers, respectively.

4.2.3 Strong Field Coherence Breaking

With multiple conformers and methyl internal rotation contributing to the broadband spectrum shown in **Figure 4.2**, SFCB was used to provide sets of rotational transitions belonging to single components of the mixture. SFCB has been described in full detail previously.²¹ We used the modified algorithm described in Fritz et al.²³ to identify a set of 2-3 resonant transitions to employ to modulate the intensities of sets of transitions due to a single component. The most intense transition in the broadband spectrum is chosen as the resonant frequency for the first single frequency pulse (SFP) that follows the broadband sweep. This frequency is pulsed 50 ns after the broadband excitation for a duration of 150 ns. After acquiring the spectrum with the broadband chirp and the first SFP, a spectrum with just the broadband chirp is recorded using the same collection conditions for each spectral acquisition. Using a custom MATLAB routine, the

magnitude of the difference spectrum is generated by plotting transitions whose intensities are modulated more than a threshold percentage of their original intensities by the SFP.

The selection criteria for subsequent resonant frequencies involves searching for additional transitions that do not have other transitions within a 10 MHz window on either side, in order to avoid non-selective excitation of satellite bands by the wings of the amplified 150 ns SFP. The SFPs are also chosen to avoid the edges of our spectral range, yet subtend much of the 10 GHz bandwidth to increase the probability that the transitions modulated by each SFP will cover a range of J-levels in the frequency range of the broadband pulse. Each additional transition selected should be relatively strong in the linear fast passage spectrum (and thereby have a large transition dipole moment), but weak in the difference spectrum (and therefore be less strongly connected to the transition resonant with the first SFP) in order to maximize the number of potential transitions in the final difference spectrum. Initially, percent intensity modulation thresholds are set high enough to minimize the possibility of false positives in the difference spectrum. After selection of subsequent SFPs, these resonant frequencies are used in a longer average, with each 150 ns SFP separated by a small gap (5 ns typically). Difference spectra are recorded until enough transitions are modulated to begin the fitting process.

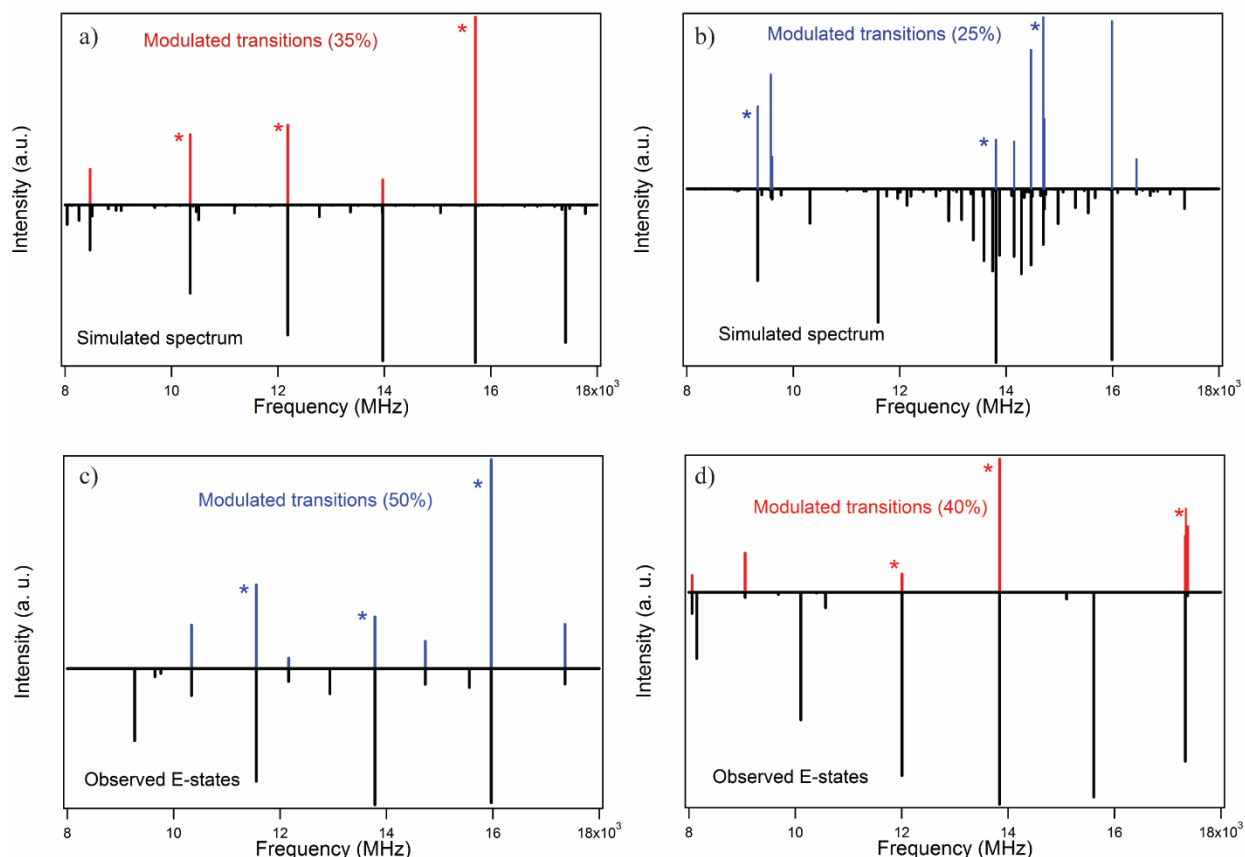


Figure 4.3 ((a) and (b)): Conformer-specific and methyl rotor specific spectra for the 0a₁ methyl rotor state of the (a) all *trans* and (b) *tgt* conformers of 2-hexanone using strong field coherence breaking. Black lines are simulated spectra. Transitions whose intensities were modulated by more than (a) 35% and (b) 25% are displayed in red and blue, respectively. ((c) and (d)):
Conformer-specific and internal methyl rotor specific spectra for the 1e methyl rotor states of (c) *tgt* and (d) all *trans* conformers of 2-hexanone using strong field coherence breaking. Black lines are observed e-state transitions in the spectrum. Transitions whose intensities were modulated by more than (c) 50% and (d) 40% are displayed in blue and red, respectively. Asterisks denote the resonant single frequencies used in the experiment.

4.3 Results

The line picking scheme was used to determine the resonant frequencies to be used in the SFCB method. Under our experimental conditions, the most intense transition in the broadband spectrum of 2-hexanone had a frequency of 10350.8125 MHz (later assigned as 2_{1,2}-1_{0,1}), which led subsequently to the choice of 12184.1875 MHz (3_{1,3}-2_{0,2}) and 15709.4375 MHz (5_{1,5}-4_{0,4}) as the second and third resonant frequencies, respectively. The final difference spectrum yielded a

total of 5 b-type rotational transitions whose intensities were modulated by more than 35%, as shown in **Figure 4.3(b)**. These intensity-modulated transitions were plotted against the predictions of the DFT B3LYP/Def 2TZP-D3BJ calculations of all four conformers. After analyzing the spacing and patterns of the experimental spectrum, these modulated transitions best match with the *ttt* conformer. Using this conformer-specific spectrum as a starting point in the fitting process, a total of 18 transitions were assigned using Pickett's SPFIT and SPCAT suite of programs³³ with a Watson S type Hamiltonian. As a result, we assign this spectrum to the *ttt* conformers in its $0a_1$ methyl torsional state.

Once all possible $0a_1$ transitions for the *ttt* conformer were assigned, SFCB was re-implemented starting with the next most intense unassigned transition at 9330.6875 MHz ($2_{1,2}-1_{0,1}$) followed by resonant frequencies at 13878.5000 MHz ($2_{2,0}-2_{1,1}$) and 14700.5000 ($5_{2,4}-5_{1,5}$). The final difference spectrum, shown in **Figure 4.3(a)**, consists of 9 conformer-specific a-, b- and c-type transitions whose intensities were modulated by more than 25%. The modulated transitions were once again plotted against the predictions for the remaining plausible structures and best matched the *tgt* conformer. After using the 9 modulated transitions to obtain a preliminary fit, a total of 39 transitions were assigned to the $0a_1$ methyl torsional state of the *tgt* conformer.

After fitting all $0a_1$ transitions from the two lowest energy conformers, numerous intense transitions remained unassigned in the spectrum. With these remaining intense transitions located near the main and most intense transitions belonging to the *ttt* and *tgt* conformers, and given the energetics and dipole moments of the two assigned conformers, we tentatively attributed these transitions to be due to the 1e methyl rotor states of the *ttt* and *tgt* conformers. However, with shifts of hundreds of MHz from the $0a_1$ states, identification of the 1e transitions was not trivial, as the 1e states of both conformers are intermingled with one another.

As noted already, SFCB can serve as a useful tool to selectively modulate rotational transitions built off the $0a_1$ and $1e$ methyl rotor states. Indeed, the fact that the method modulated the intensities of lines that could all be fit as arising from a single vibration/torsion level is already evidence that, in 2-hexanone, selective modulation of $0a_1$ and $1e$ states is possible.

To aid in assignment of the $1e$ spectra, SFCB was carried out on the remaining unassigned transitions, using resonant frequencies at 15968.3125 MHz ($5_{1,5}-4_{0,4}$), 13783.5625 MHz ($4_{1,4}-3_{0,3}$) and 11552.8125 MHz ($3_{1,3}-2_{0,2}$). **Figure 4.3(c)** shows the final difference spectrum arising from this procedure, which consists of 7 conformer/internal rotor specific transitions whose intensities were modulated by more than 50%. This difference spectrum was used as starting point for fitting the $1e$ methyl rotor spectrum using the XIAM fitting program.³⁴ A total of 12 rotational transitions were assigned to the $1e$ methyl rotor state of the *tgt* conformer of 2-hexanone.

The procedure was repeated a final time using resonant frequencies at 13839.9375 ($4_{1,4}-3_{0,3}$), 17330 MHz ($6_{1,6}-5_{0,5}$) and 12005.0625 ($3_{1,3}-2_{0,2}$), respectively. The final difference spectrum shown in **Figure 4.3(d)** contained a total of 6 transitions whose intensities were modulated by more than 40%. These transitions were assigned to the $1e$ methyl rotor state of the *ttt* conformer. The preliminary fit was subsequently refined to assign a total of 13 *ttt* $1e$ rotational transitions.

After all possible $0a_1$ and $1e$ torsional states for the *tgt* and *ttt* conformers were assigned, remaining unassigned rotational transitions were due to the $0a_1$ and $1e$ torsional states of the *ttg* conformer of 2-hexanone. Since all could be identified with a single conformer, SFCB was not helpful to the assignment process, and therefore was not carried out.

Table 4.1 Experimentally determined structural parameters of the three identified conformations of 2-hexanone.

	Theory^b	<i>tgt</i> Experimental	Theory^b	<i>ttt</i> Experimental	Theory^b	<i>ttg</i> Experimental
A (MHz)	5807.642 0	5864.8301(33)	7560.171 7	7510.3539(99)	5860.971 6	5847.4445(17)
B (MHz)	1241.713 0	1244.3694(45)	1039.357 8	1040.7343(13)	1177.037 2	1173.7582(62)
C (MHz)	1157.327 3	1153.4418(32)	940.1517	941.1316(10)	1045.518 3	1052.4360(34)
μ_a (D)	-0.601	---	0.250	---	0.941	---
μ_b (D)	-2.540	---	2.810	---	-2.522	---
μ_c (D)	-0.829	---	-0.030	---	0.642	---
Δ_J (kHz)	---	0.316(23)	---	0.031(10)	---	-0.189(77)
Δ_K (kHz)	---	34.282(2.6)	---	---	---	---
Δ_{JK} (kHz)	---	-3.534(85)	---	-0.412(32)	---	---
δ_J (kHz)	---	-0.016(12)	---	-0.00549(26)	---	0.118(59)
δ_K (kHz)	---	-0.018(06)	---	---	---	---
D_{pi2J} (MHz)	---	0.241(14)	---	0.00932(32)	---	---
D_{pi2K} (MHz)	---	-5.131(32)	---	---	---	---
D_{pi2-} (MHz)	---	0.166(03)	---	0.00255(73)	---	---
F_0 (GHz) ^c	---	158	---	158	---	158
E_{rel} (kJ/mol) ^a	0	---	0.24	---	2.69	---
N_A/N_E	---	39/12	---	18/13	---	13/4
V_3 (cm ⁻¹)	193.1	233.24(43)	139.6	187.46(02)	137.9	182.47(10)
T_{rot} (K)	---	1.00 ± 0.15	---	0.90 ± 0.11	---	0.87 ± 0.17
σ (MHz)	---	0.0242	---	0.0216	---	0.0295

^aZero-point corrected relative energy. ^bDFT B3LYP Def2TZVP-D3BJ level of theory.

^cInternal rotor constant was fixed to 158 GHz for all three structures.

4.4 Discussion

By applying SFCB to the rotational spectrum, we were able to effectively identify rotational transitions belonging to the 0a₁ and 1e methyl torsional levels of the three populated conformers of 2-hexanone, ultimately assigning and extracting structural parameters unique to each conformer as shown in **Table 4.1**. Rotational temperature plots are shown for all three identified structures in **Figures 4.4-4.6** for *ttt*, *tgt* and *ttg* conformers, respectively. The rotational transitions assigned for *tgt*, *ttg* and *ttt* conformers are provided in **Tables 4.2-4.4**, respectively. The rotational spectrum is dominated by the *tgt* and *ttt* conformers as these are the two lowest energy structures, with the *tgt*

conformer being the global minimum followed by the *ttt* conformer just 0.24 kJ/mol higher in energy. The observed conformers are always *trans* about the first dihedral. According to the calculations (**Table 4.1**), there is little cost in energy when the second dihedral angle is *gauche*; however, a *gauche* conformation in the third dihedral (a pure alkyl chain *gauche* defect) raises the relative energy of the *ttg* and *tgg* conformers to 2.69 kJ/mol and 3.09 kJ/mol, respectively. Of these two less stable conformers, only the *ttg* conformer was observed experimentally. All three observed conformers are near prolate symmetric tops ($A > B = C$). Since the polar C=O bond is responsible for much of the permanent dipole moment, the projection of this C=O vector on the inertial axes will give an approximate measure of the intensities of a-, b- and c-type transitions (μ_a , μ_b and μ_c), as the intensity of a microwave transition in CP-FTMW scales with the square of the dipole moment.³⁵ The major component of the dipole moment projects primarily along the b inertial axis for all three conformers, resulting in predominately b-type transitions in the microwave spectrum. The full list of assigned transitions is included in supplementary material.

The predicted barrier heights are relatively low (**Table 4.1**), leading to large splittings of up to several hundred MHz, making these splittings difficult to recognize in some cases. Even though some of the splittings due to internal rotation were clearer than others, SFCB identified rotational transitions built off the 1e torsional states that could not have been easily identified otherwise. As a part of the fitting procedure, the XIAM fitting program was used to determine the barriers to methyl internal rotation for all three observed conformers, using a total of 13, 12 and 4 0a₁/1e methyl rotor pairs for the *ttt*, *tgt* and *ttg* conformers, respectively. XIAM was chosen over other internal rotor fitting programs since our fit is confined to relatively low *J* and *K_a* values and has been successfully used to fit intermediate barriers in previous studies including 2-pentanone.¹⁹ The magnitude of the barrier derived from the fits are nearly the same as those reported previously for

methyl ketones with the shorter alkyl chains present in ethyl methyl ketone (183.17 cm^{-1})³⁶ and the all-trans conformer of 2-pentanone (188 cm^{-1}).¹⁹ However, in the case of 2-pentanone, the conformation of the alkyl chain influenced the barrier height, as the higher energy C_1 structure (*tg* in our notation) had a fitted barrier height of 238 cm^{-1} , more than 50 cm^{-1} higher than the all-*trans* conformer. Our best-fit barrier for the analogous *tgt* conformer of 2-hexanone (also of C_1 symmetry) is 233 cm^{-1} , very close to the barrier in 2-pentanone. That this is a common feature of the low-symmetry conformers of a range of methyl ketones is evident from the barriers determined previously for allyl acetone (225 cm^{-1})³⁷ and methyl isobutyl ketone (250 cm^{-1}).³⁸

4.5 Conclusions

Strong field coherence breaking is a powerful tool for identifying rotational transitions belonging to a single component in a gas mixture. The method has already been applied to identify transitions due to conformational isomers, ^{13}C isotopomers in natural abundance, and to identify transitions due to free radicals in the complex chemical mixture emanating from a flash pyrolysis source. Here, strong field coherence breaking was successfully implemented for the first time in selectively modulating $0a_1$ and $1e$ torsional states of the two lowest energy conformers of 2-hexanone. There are other circumstances in which SFCB is likely to prove itself a useful tool. For instance, CP-FTMW spectroscopy is being used to record microwave spectra at room temperature, where vibrational hot bands are present in significant abundance.^{39,40} Identification and assignment of the rotational transitions due to each vibrationally excited state provides insight to the nature of the low-frequency vibrations that are populated. SFCB has the potential to assist in this process, as each vibrational level supports a set of rotational levels in which SFCB can be carried out, although the congestion of these spectra will require care in choice of resonant frequencies used in the SFCB technique. In addition, there are tunneling splittings due to other

motions than methyl internal rotation. Particularly when more than one such tunneling process is present, the identification of sets of rotational transitions due to each could be a sizable help in sorting through the multi-dimensional quantum mechanics responsible for it.

4.6 References

- ¹L. Goodman, V. Pophristic, and F. Weinhold, *Accounts Chem. Res.* **32**, 983 (1999).
- ²P. R. Bunker and P. Jensen, *Molecular Symmetry and Spectroscopy*, 2nd Ed. NRC Research Press, 748 (2006).
- ³J. M. Hollas, *High Resolution Spectroscopy*, 2nd Ed. Wiley (New York), 260 (1998).
- ⁴L. H. Spangler, *Annu. Rev. Phys. Chem.* **48**, 481 (1997).
- ⁵B. J. van der Veken, R. Maas, G. A. Guirgis, H. D. Stidham, T. G. Sheehan, and J. R. Durig, *J. Phys. Chem-US* **94**, 4029 (1990).
- ⁶J. R. During and D. A. C. Compton, *J. Phys. Chem-US* **83**, 2873 (1979).
- ⁷D. Gorse, D. Cavagnat, M. Pesquer, and C. Lapouge, *J. Phys. Chem.* **97**, 4262 (1993).
- ⁸W. G. Fateley and F. A. Miller, *Spectrochim. Acta* **17**, 857 (1961).
- ⁹J. C. Dean, P. Navotnaya, A. P. Parobek, R. M. Clayton, and T. S. Zwier, *J. Chem. Phys.* **139**, 144313 (2013).
- ¹⁰G. Williams, N. L. Owen, and J. Sheridan, *Trans. Faraday Soc.* **67**, 922 (1971).
- ¹¹H. V. L. Nguyen, W. Stahl, and I. Kleiner, *Mol. Phys.* **110**, 2035 (2012).
- ¹²C. C. Lin and J. D. Swalen, *Rev. Mod. Phys.* **33**, 841 (1959).
- ¹³H. V. L. Nguyen and W. Stahl, *J. Chem. Phys.* **135**, 024310 (2011).
- ¹⁴J. T. A. Gall, J. Thomas, F. Xie, Z. Wang, W. Jäger, and Y. Xu, *Phys. Chem. Chem. Phys.* **19**, 29508 (2017).
- ¹⁵K. P. Rajappan Nair, S. Herbers, D. A. Obenchain, J. Grabow, and A. Lesarri, *J. Mol. Spectrosc.* **344**, 21 (2018).
- ¹⁶R. Kannengießer, W. Stahl, H. V. L. Nguyen, and I. Kleiner, *J. Phys. Chem. A* **120**, 3992 (2016).

- ¹⁷W. Li, A. Vigorito, C. Calabrese, L. Evangelisti, L. B. Favero, A. Maris, and S. Melandri, *J. Mol. Spectrosc.* **337**, 3 (2017).
- ¹⁸L. Ferres, H. Mouhib, W. Stahl, and H. V. L. Nguyen, *Chem. Phys. Chem.* **18**, 1855 (2017).
- ¹⁹M. Andresen, I. Kleiner, M. Schwell, W. Stahl, and H. V. L. Nguyen, *J. Phys. Chem. A* **122**, 7071 (2018).
- ²⁰M. Nakajima and Y. Endo, *J. Chem. Phys.* **140**, 011101 (2013).
- ²¹A. O. Hernandez-Castillo, C. Abeysekera, B. M. Hays, and T. S. Zwier, *J. Chem. Phys.* **145**, 114203 (2016).
- ²²A. O. Hernandez-Castillo, C. Abeysekera, B. M. Hays, I. Kleiner, H. V. L. Nguyen, and T. S. Zwier, *J. Mol. Spectrosc.* **337**, 51 (2017).
- ²³S. M. Fritz, A. O. Hernandez-Castillo, C. Abeysekera, B. M. Hays, and T. S. Zwier, *J. Mol. Spectrosc.* **349**, 10 (2018).
- ²⁴C. Abeysekera, A. O. Hernandez-Castillo, J. F. Stanton, and T. S. Zwier, *J. Phys. Chem. A* **122**, 6879 (2018).
- ²⁵J. Pieper, C. Hemken, R. Büttgen, I. Graf, N. Hansen, K. A. Heufer, and K. Kohse-Höinghaus, *P. Combust. Inst.* **37**, 1683 (2019).
- ²⁶F. Hoppe, U. Burke, M. Thewes, A. Heufer, F. Kremer, and S. Pischinger, *Fuel* **167**, 106 (2016).
- ²⁷U. Burke, J. Beeckmann, W. A. Kopp, Y. Uygun, H. Olivier, K. Leonhard, H. Pitsch, and K. A. Heufer, *Combust. Flame* **168**, 296 (2016).
- ²⁸A. Elfasakhany, *Eng. Sci. Technol. Int. J.* **19**, 1224 (2016).
- ²⁹S. M. Fritz, B. M. Hays, A. O. Hernandez-Castillo, C. Abeysekera, and T. S. Zwier, *Rev. Sci. Instrum.* **89**, 093101 (2018).
- ³⁰T. A. Halgren, *J. Comput. Chem.* **17**, 490 (1996).
- ³¹D. J. Frisch, M. J. Trucks, G. W. Schlegel, H. B. Scuseria, G. E. Robb, M. A. Cheeseman, J. R. Scalmani, G. Barone, V. Mennucci, B. Petersson, G. A. Nakatsuji, H. Caricato, M. Li, X. Hratchian, H. P. Izmaylov, A. F. Bloino, J. Zheng, and G. Sonnenb, Gaussian 09, Revis. E.01, Gaussian Inc., Wallingford CT, 2009.
- ³²S. Grimme, *J. Chem. Phys.* **124**, 034108 (2006).
- ³³H. M. Pickett, *J. Mol. Spectrosc.* **377**, 371 (1991).
- ³⁴H. Hartwig, H. Dreizler, and Z. Naturforsch, **51a**, 923 (1996).

- ³⁵G. G. Brown, B. C. Dian, K. O. Douglass, S. M. Geyer, S. T. Shipman, and B. H. Pate, Rev. Sci. Instrum. **79**, 053103 (2008).
- ³⁶H. V. L. Nguyen, V. Van, W. Stahl, and I. Kleiner, J. Chem. Phys. **140**, 214303 (2014).
- ³⁷L. Tulimat, H. Mouhib, I. Kleiner, and W. Stahl, J. Mol. Spectrosc. **312**, 46 (2015).
- ³⁸Y. Zhao, W. Stahl, and H. V. L. Nguyen, Chem. Phys. Lett. **545**, 9 (2012).
- ³⁹B. Reinhold, I. A. Finneran, and S. T. Shipman, J. Mol. Spectrosc. **270**, 89 (2011).
- ⁴⁰S. Samdal, H. Møllendal, and J. C. Guillemin, J. Phys. Chem. A **119**, 3375 (2015).

4.7 Supplementary Material

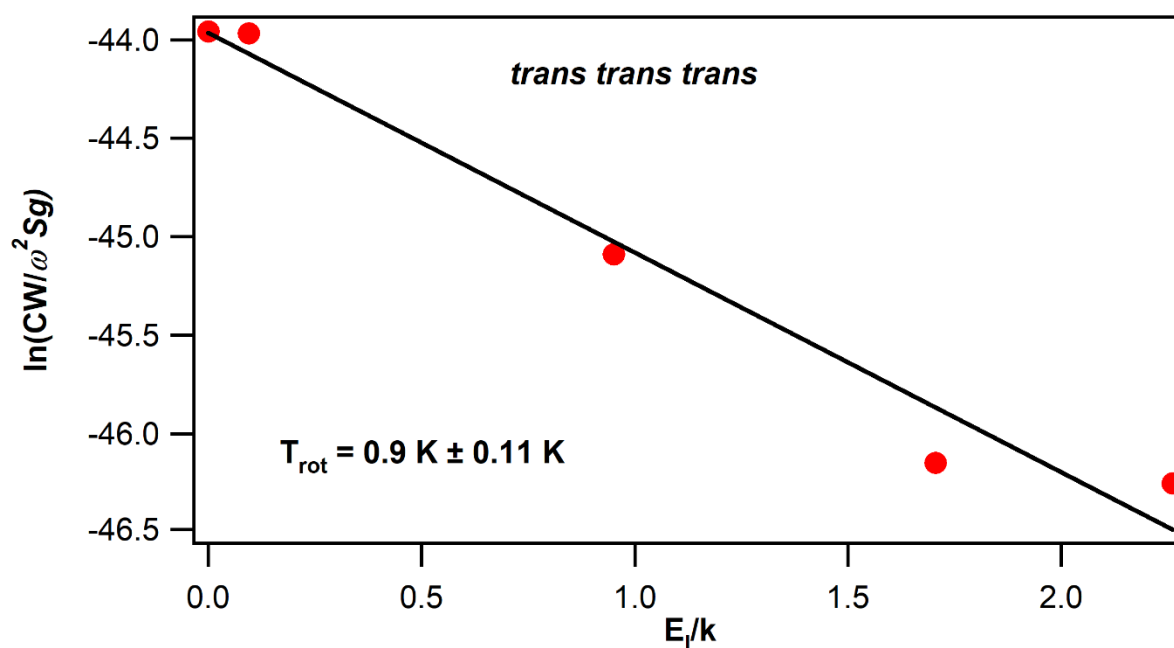


Figure 4.4 The Boltzmann plot for the *ttt* conformer of 2-hexanone. The rotational temperature was calculated to be $0.9 (\pm 0.11) \text{ K}$

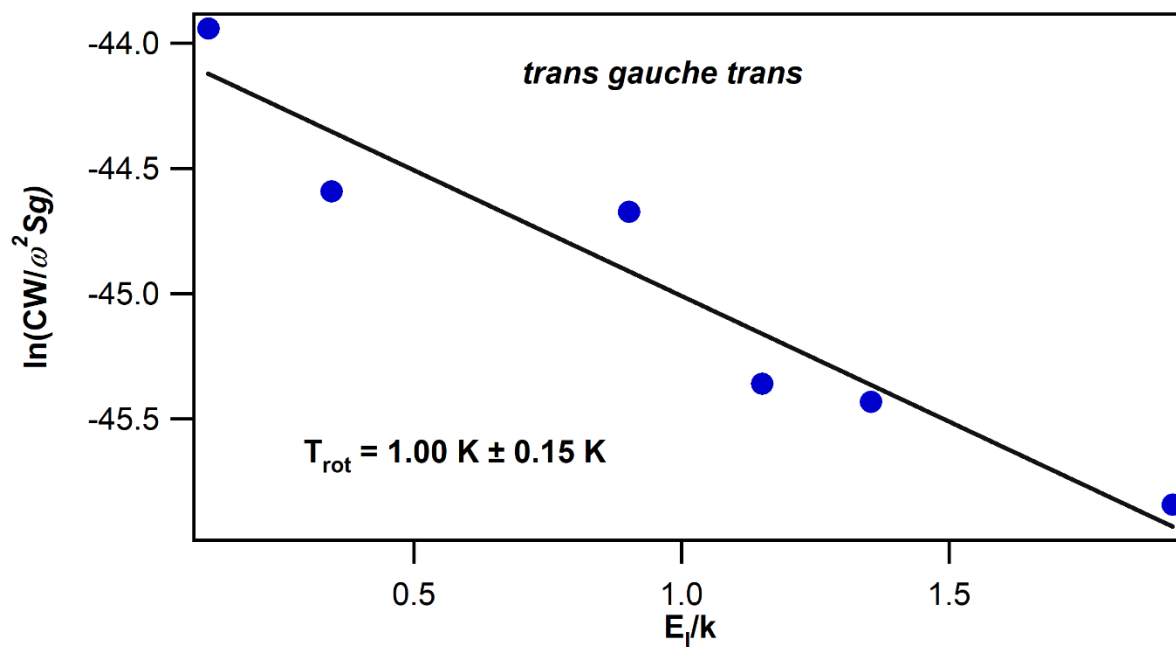


Figure 4.5 The Boltzmann plot for the *tgt* conformer of 2-hexanone. The rotational temperature was calculated to be 1.48 (± 0.10) K

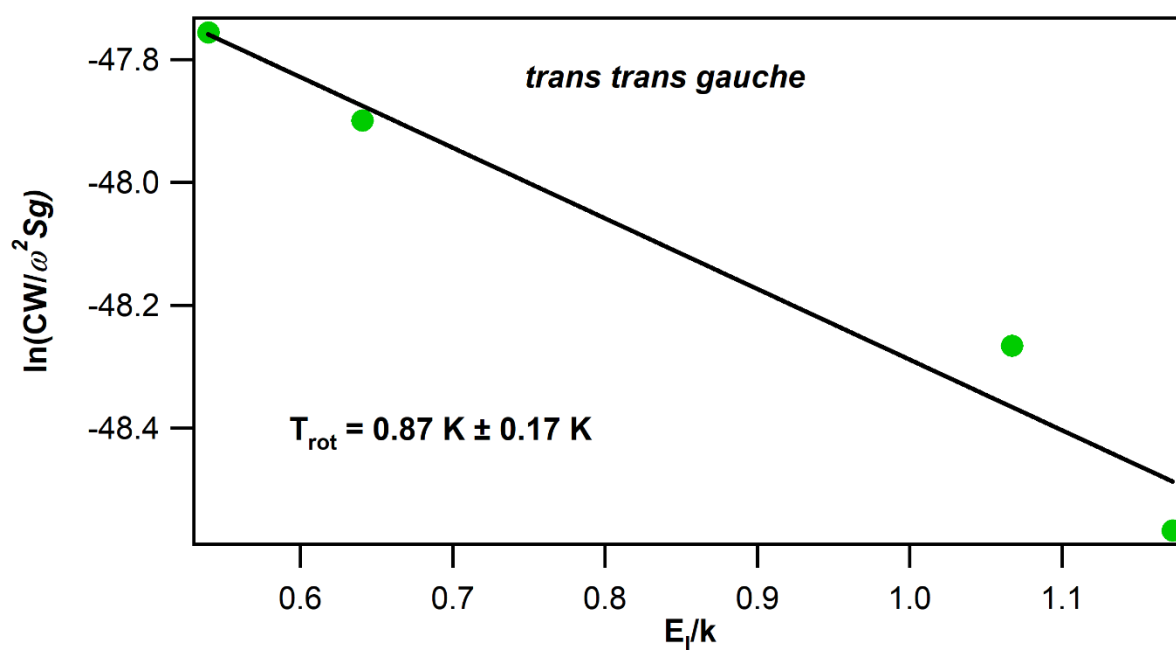


Figure 4.6 The Boltzmann plot for the *tgt* conformer of 2-hexanone. The rotational temperature was calculated to be 0.87 (± 0.17) K

Table 4.2 Observed A and E species frequencies ($\nu_{\text{Obs.}}$) of 51 rotational transitions of the *tgt* conformer of 2-hexanone. $\nu_{\text{Obs.}} - \nu_{\text{Calc.}}$ values as obtained after a fit with the program *XIAM*.

<i>J</i>	<i>K_a</i>	<i>K_c</i>	<i>J</i>	<i>K_a</i>	<i>K_c</i>	Sym.	$\nu_{\text{Obs.}}$	$\nu_{\text{Obs.}} - \nu_{\text{Calc.}}$
upper level			lower level				MHz	<i>XIAM</i> MHz
2	1	2	1	0	1	A	9330.6875	0.0179
						E	9267.0000	0.0027
3	1	3	2	0	2	A	11592.6875	0.0033
						E	11552.8125	-0.0022
4	1	4	3	0	3	A	13811.3750	-0.0457
						E	13783.5625	0.0051
5	1	5	4	0	4	A	15989.5625	-0.0095
						E	15968.3125	0.0009
2	1	1	1	0	1	A	9603.3750	0.0177
						E	9649.1875	-0.0044
3	1	2	2	0	2	A	12138.0625	0.0173
						E	12160.3125	-0.0109
4	1	3	3	0	3	A	14720.3125	0.0264
						E	14730.9375	0.0176
5	1	4	4	0	4	A	17352.6250	-0.0243
						E	17357.1875	-0.0008
4	1	3	3	1	2	A	9770.5000	0.0257
						E	9758.7500	-0.0218
6	0	6	5	1	5	A	10313.8750	0.0038
						E	10334.7500	0.0288
7	0	7	6	1	6	A	12921.1250	0.0073
						E	12937.6250	-0.0192
8	0	8	7	1	7	A	15544.3750	-0.0087
						E	15557.6875	0.0045
9	2	7	9	1	8	A	12445.4375	0.0233
8	2	6	8	1	7	A	12683.0625	-0.0146
7	2	5	7	1	6	A	12925.5625	0.0028
6	2	4	6	1	5	A	13162.3125	-0.0272
5	2	3	5	1	4	A	13383.8125	0.0000
4	2	2	4	1	3	A	13581.5000	-0.0251
3	2	1	3	1	2	A	13748.3750	0.0450
2	2	0	2	1	1	A	13878.5000	0.0272
2	2	1	2	1	2	A	14149.8125	-0.0224

Table 4.3 Observed A and E species frequencies ($\nu_{\text{Obs.}}$) of 18 rotational transitions of the *ttg* conformer of 2-hexanone. $\nu_{\text{Obs.}} - \nu_{\text{Calc.}}$ values as obtained after a fit with the program *XIAM*.

<i>J</i>	<i>K_a</i>	<i>K_c</i>	<i>J</i>	<i>K_a</i>	<i>K_c</i>	Sym.	$\nu_{\text{Obs.}}$	$\nu_{\text{Obs.}} - \nu_{\text{Calc.}}$
upper level			lower level				MHz	<i>XIAM</i> MHz
3	2	2	3	1	3	A	14287.0625	-0.0026
4	2	3	4	1	4	A	14470.5000	-0.0267
5	2	4	5	1	5	A	14700.6250	0.0277
6	2	5	6	1	6	A	14977.7500	0.0234
3	2	1	3	1	3	A	14293.6875	-0.0035
4	2	2	4	1	4	A	14490.3750	-0.0156
8	2	7	8	1	8	A	15674.9375	-0.0126
5	1	5	4	1	4	A	11756.2500	-0.0019
5	0	5	4	0	4	A	11962.6875	0.0021
4	2	3	3	2	2	A	9590.4375	0.0061
4	2	2	3	2	1	A	9603.6875	0.0180
5	2	4	4	2	3	A	11986.3125	-0.0151
4	2	3	4	1	3	A	13561.6875	0.0263
6	1	6	5	1	5	A	14103.9375	-0.0215
7	2	6	7	1	7	A	15302.3125	-0.0462
9	2	8	9	1	9	A	16095.9375	0.0269
7	1	7	6	1	6	A	16449.8750	0.0350
5	1	4	4	1	3	A	12210.4375	-0.0263

Table 4.4 Observed A and E species frequencies ($\nu_{\text{Obs.}}$) of 31 rotational transitions of the *ttt* conformer of 2-hexanone. $\nu_{\text{Obs.}} - \nu_{\text{Calc.}}$ values as obtained after a fit with the program *XIAM*.

<i>J</i>	<i>K_a</i>	<i>K_c</i>	<i>J</i>	<i>K_a</i>	<i>K_c</i>	Sym.	$\nu_{\text{Obs.}}$	$\nu_{\text{Obs.}} - \nu_{\text{Calc.}}$
upper level			lower level				MHz	<i>XIAM</i> MHz
2	1	2	1	0	1	A	10350.8125	-0.0021
						E	10103.1875	0.0412
3	1	3	2	0	2	A	12184.1250	-0.0160
						E	12005.0625	0.0108
4	1	4	3	0	3	A	13969.5625	-0.0135
						E	13839.9375	-0.0501
5	1	5	4	0	4	A	15709.4375	0.0122
						E	15611.8750	0.0123
6	1	6	5	0	5	A	17406.8750	0.0092
						E	17330.0000	0.0015

Table 4.4 cont.

1	1	1	0	0	0	A	8468.1875	0.0259
						E	8148.5000	-0.0182
7	1	6	7	0	7	A	8038.5625	-0.0106
						E	8057.2993	-0.0049
9	1	8	9	0	9	A	9053.7500	-0.0041
						E	9057.0635	0.0110
10	1	9	10	0	10	A	9684.3750	-0.0045
						E	9682.5962	0.0087
11	1	10	11	0	11	A	10404.5625	0.0146
						E	10398.5000	-0.0176
11	0	11	10	1	10	A	17339.3438	0.0195
						E	17375.0625	-0.0145
10	0	10	9	1	9	A	15056.4375	-0.0245
						E	15098.1250	0.0062
9	0	9	8	1	8	A	12777.3750	0.0091
8	0	8	7	1	7	A	10509.0625	-0.0020
						E	10568.4688	0.0153
7	0	7	6	1	6	A	8258.4375	-0.0166
5	2	3	6	1	6	A	8812.0625	-0.0159
4	2	3	5	1	4	A	8957.1875	-0.0056
4	2	2	5	1	5	A	10466.6875	0.0139

CHAPTER 5. MEASURING COMBUSTION INTERMEDIATES VIA BROADBAND CHIRPED-PULSE MICROWAVE SPECTROSCOPY

5.1 Introduction

Microwave (MW) spectroscopy, also known as rotational spectroscopy, measures the energies of transitions between quantized rotational states of rotating polar molecules in the gas phase. Originally used as an absorption technique, MW spectroscopy has been continuously developed for decades to improve sensitivity and resolution. In pioneering work, Balle and Flygare reported the combination of a rotationally cold molecular beam (MB) with the Fourier transform (FT) technique using a Fabry-Pérot cavity.¹ The energy resolution of $\nu/\Delta\nu \sim 10^7$ is unmatched by other spectroscopic techniques and thus, MW spectroscopy presents the most accurate method for the determination of molecular structures of gas-phase molecules.² Recently, a new breakthrough in MW spectroscopy has been reported: the chirped-pulse Fourier-transform microwave (CP-FTMW) technique.³⁻⁵ This technique's rate of acquisition of broadband spectral data is unparalleled and it holds great potential for identification of polar species without prior knowledge of the sample composition. This feature, which is shared with widely used mass spectrometric experiments,⁶⁻⁸ makes microwave spectroscopy appealing for combustion chemistry research. While it has become evident after decades of combustion chemistry research that not a single laser technique or even the widely used mass spectrometry technique can provide all quantities of interest to characterize a complex reaction network,^{6,9} microwave spectroscopy can potentially overcome some of the limitations the sampling mass spectrometry experiments face,¹⁰ *e.g.* dissociative ionization may preclude isomer-resolved quantification.

Motivated by the superb identification capabilities of microwave spectroscopy and the broadband capabilities of chirped-pulse microwave spectroscopy, we show here that rotational

spectroscopy can be developed into a new diagnostic tool for combustion research. In exploratory work, Hansen *et al.* had already shown that molecular samples drawn from the hot environment of laboratory-scale model flames can be sufficiently cooled to enable the sensitive detection via rotational spectroscopy.¹⁰ Typically, rotational temperatures are required in the order of 10 K or less to achieve substantial depopulation of rotationally excited states. Such low temperatures consequently lead to an increase of the relative concentrations in the population of lower rotational states, with its attendant increase in sensitivity, and at the same time resulting in a simplification of the broadband rotational spectra.

In the experiments discussed here, molecular samples are withdrawn at various temperatures from a jet-stirred reactor (JSR) operated at atmospheric pressure. The JSR is typically used to probe low-temperature oxidation chemistry that is governed by a multifaceted reaction network of oxygenated species.¹¹ For these exploratory experiments, we chose to study the oxidation of dimethyl ether (DME, CH_3OCH_3), dimethoxy methane (DMM, $\text{CH}_3\text{OCH}_2\text{OCH}_3$), and the ozone-assisted oxidation of ethylene. Both, DME and DMM are prototypical ethers and their oxidation at low temperatures continues to receive attention in the combustion community.¹²⁻
¹⁴ The ozone-assisted oxidation reactions recently attracted significant interest in fundamental combustion studies, motivated by the rise of non-equilibrium plasma-assisted combustion.¹⁵⁻¹⁷ While this paper does not intend to provide new insights into the complex oxidation chemistry, it highlights the unique capabilities microwave spectroscopy has to offer for detecting elusive intermediates in complex mixtures.

5.2 Experimental Procedures

Rotational spectra were recorded by coupling a jet-stirred reactor with a chirped-pulse Fourier transform microwave (CP-FTMW) spectrometer at Purdue University¹⁸ described in Chapter 2. This spectrometer, which covers the frequency range from 8 to 18 GHz, is well suited for the experiments because the pure rotational transitions of many combustion intermediates are located in this range. Furthermore, SFCB (strong field coherence breaking) can be used to selectively modulate the intensities of a set of transitions belonging to the same molecule¹⁹, thus potentially facilitating the assignment of the broadband spectra.

The experimental set-up is shown schematically in **Figure 5.1**. Gaseous molecules were sampled from a jet-stirred reactor, using a quartz capillary, and transferred through a heated stainless-steel tube to the pulsed molecular-beam nozzle of the microwave spectrometer. Details of the jet-stirred reactor have been described elsewhere.¹² The quartz reactor consists of a sphere of 33.5 cm³ volume. The fuel and oxidizer stream (both diluted with Ar) were guided through two concentric tubes, mixed at their outlets and entered the reactor through four injectors with exit nozzles located in the center of the JSR.

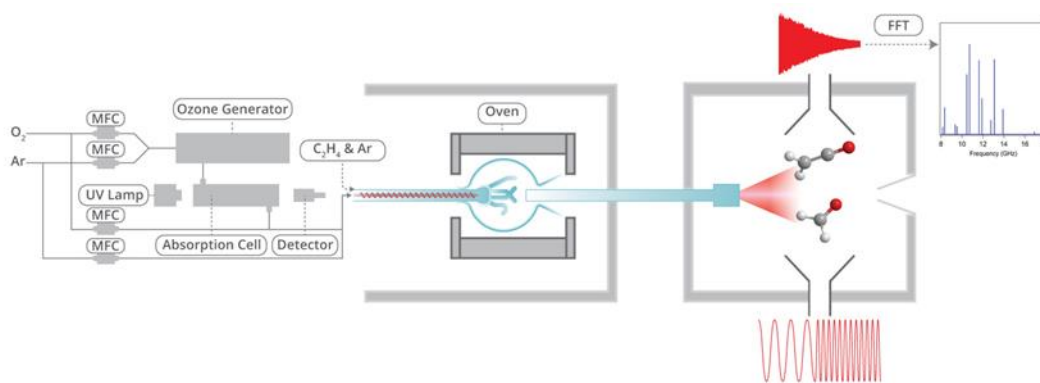


Figure 5.1 Schematic of the experimental set-up, which consists of the gas-delivery system, the jet-stirred reactor and the microwave spectrometer.

As mentioned above, low-temperature oxidation of DME and DMM and the ozone-assisted oxidation of ethylene were used as test cases. The flow conditions are given in **Table 5.1** and are consistent with previous experiments.¹²⁻¹⁶ The gas flows were regulated by calibrated mass flow controllers. For the ozonolysis experiments, a fraction of the O₂ stream was guided through an ozone generator, followed by a UV absorption cell to determine the absolute O₃ concentration.¹⁶ The reactor is completely enclosed by an electrical oven that enables adjustment of the temperature over the desired range. The oven and the reactor are surrounded by a water-cooled stainless-steel chamber. Exhaust gases were continuously removed to keep the pressure constant at 700 Torr (933 mbar). The temperature of the oven was measured with a K-type thermocouple.

Table 5.1 Flow conditions of the jet stirred reactor. Stoichiometry, residence time (in ms), pressures (in mbar), argon dilution in %, and ozone concentration in ppm of the JSR experiments.

	stoichiometry	residence time	pressure	Ar dilution	O ₃ concentration	Ref.
DME	0.35	4000	933	78		[1]
DMM	0.5	3000	1000	82		[2]
Ethylene	0.5	1300	933	86	1000	[3, 4]

To obtain the rotational spectra, broadband MW radiation frequency ramps (chirps) were generated by a 10 GS/s arbitrary waveform generator (AWG). The AWG outputs broadband sweeps up to 5 GHz and serves as the master clock for other electronics involved in the experiment. The output passes through a 5 GHz low-pass filter and is levelled with a +14.2 dB pre-amplifier before it is multiplied with a quadrupler to achieve an 8-18 GHz chirp. The chirp power is set with a step attenuator before it is amplified using a 200 W travelling wave tube amplifier (TWTA). The amplified chirp is introduced into the vacuum chamber with a 2-18 GHz broadcasting horn, which thereby interacts with the molecules of interest.

The JSR-sampled species are introduced into the vacuum chamber using a pulsed General valve with a 1 mm orifice diameter operating at 10 Hz. The resulting supersonic expansion cools the molecules down to their vibrational zero-point energy levels and quenches any reactions. The supersonic expansion is interrogated with the microwave radiation and the molecular ensemble is polarized and subsequently undergoes free induction decay (FID). This time domain signal is collected for 16 μ s with a receiving horn and passes through a PIN diode limiter and a reflective single pole single throw switch before it is amplified with a +45 dB low noise amplifier. The amplified signal is down converted using a triple balanced mixer with an 18.9 GHz phase locked dielectric resonator oscillator (PLDRO). The signal then passes through a DC block and a 12 GHz low pass filter before it is phase coherently averaged by a 13 GHz, 40 GS/s real time digitizer. The time domain signal is filtered with a Kaiser-Bessel window and is fast Fourier transformed using a custom MatLab routine to yield the frequency domain spectrum. The experimental timing allowed for the collection of 20 FIDs per gas pulse, separated by 20 μ s. A 16 μ s FID collection period results in an experimental resolution of 60 kHz.

To facilitate assignment of observed rotational transition to structural features, strong-field coherence breaking (SFCB) was applied.¹⁹ This technique simplifies line assignments of the congested rotational spectra by producing molecule-specific microwave spectra with a sufficient number of transitions that enables preliminary assignments. Following the original broadband sweep of microwave radiation to create the rotational coherence among the rotating molecules, short intense microwave pulses of specific frequencies are used to alter the population differences between sets of rotational levels. By operating in the rapid adiabatic passage regime, the intense microwave pulses lead to a breakdown of the coherence not only in the levels interrogated by the single frequency pulses (SFPs), but by others connected to them. These are observed in the

magnitude of the difference of the free-induction decays, providing a set of transitions whose intensities have been modulated by a user-defined threshold percentage of their original intensity, as shown schematically in **Figure 5.2**.

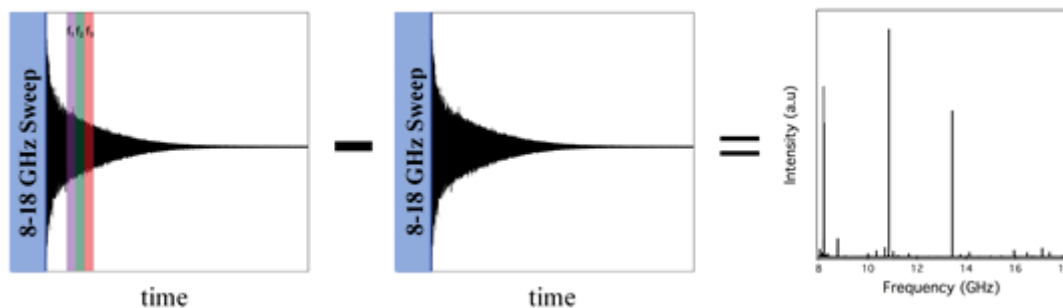


Figure 5.2 Schematic representation of the strong-field coherence breaking approach to identify rotational transitions that belong to the same molecular structure. Short pulses of intense microwave radiation of specific frequencies are used to break the coherence that was generated by the initial broadband microwave sweep. Via comparison to the unperturbed FID, difference spectra are formed that reveal a set of rotational transitions due to a single species in the mixture.

5.3 Results and Discussion

In this work, we demonstrate that chirped-pulse microwave spectroscopy can be successfully applied for species identification using its superb frequency resolution. Examples of broad-band chirped pulse microwave spectra are shown in **Figure 5.3** after sampling from reactive mixtures of (a) DME/O₂/Ar, (b) DMM/O₂/Ar, and (c) ethylene/O₂/O₃/Ar. The clearly observable differences in the rotational spectra are indicative of the respective different gas mixture composition in the jet-stirred reactor.

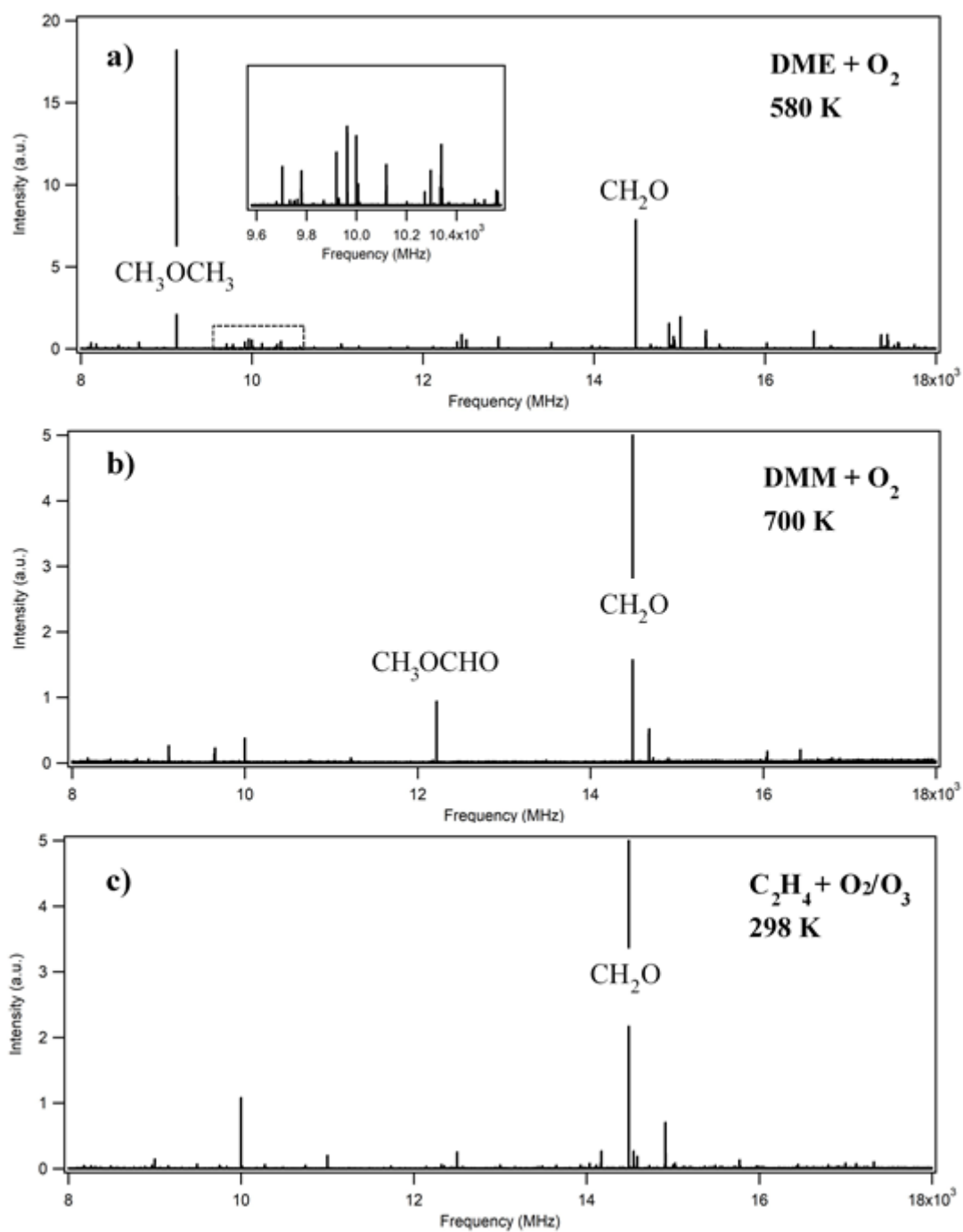


Figure 5.3 Broad-band rotational spectra from 8 to 18 GHz after sampling from a reacting mixture of (a) DME/O₂/Ar at 580 K, (b) DMM/O₂/Ar at 700 K, and (c) C₂H₄/O₂/O₃/Ar at 298 K. The observed differences are indicative of the different mixture compositions sampled from the reactive mixture. See text for details concerning their assignments to specific molecular structures.

Different from mass spectrometry, where the sampled reactants, intermediates and products are sorted by molecular mass, or laser spectroscopy, where typically only one specific molecule is probed, microwave spectra can be more challenging to interpret. The observed rotational frequencies depend on the specific molecular structure, and the rotational transitions from the different components of the reactive system appear interspersed amongst one another. While automated routines to interpret these broadband rotational spectra are currently being developed,²⁰⁻²² here, we have used tabulated rotational frequencies for assignments of transitions and species identification based on our chemical knowledge about low-temperature oxidation. The assignment of some spectral features to molecular structures is discussed next.

The microwave spectrum of dimethyl ether in the frequency range from 8 to 18 GHz is well known and transitions were observed near 9.120 and 15.310 GHz that correspond to the $2_{1,1}$ - $2_{1,2}$ and $5_{1,4}$ - $4_{2,3}$ rotational transitions of DME, respectively.²³ The DME rotational spectrum near 9.120 GHz is shown in **Figure 5.4(a)**. The triplet results from coupling between the molecular rotation with the two internal methyl rotors, leading to transitions that are referred to as AA, AE, and EE based on the symmetry. These rotational splittings are unique indicators for the molecular structure. A total of 9 DME transitions (including the splittings due to internal rotation effects) have been observed in the applied frequency range. While the assignment of DME to the observed transitions is based on the literature data, it should be mentioned that at least four transitions of an unknown species would be necessary for its positive identification.

The second species which is easy identifiable is formaldehyde (CH_2O) – a common intermediate in low-temperature oxidation and ethylene ozonolysis reactions. A first assessment of the broad-band microwave spectra shown in **Figure 5.3(a)** reveals a strong rotational transition near 14.488 GHz – the well-known $2_{1,1}$ - $2_{1,2}$ transition of CH_2O .²⁴ The transition, which consists of

a single peak, is shown in **Figure 5.4(b)**. The weak shoulder that is visible in **Figure 5.4(b)** at somewhat lower frequencies results from the DME-CO₂ complex and will be discussed further below.

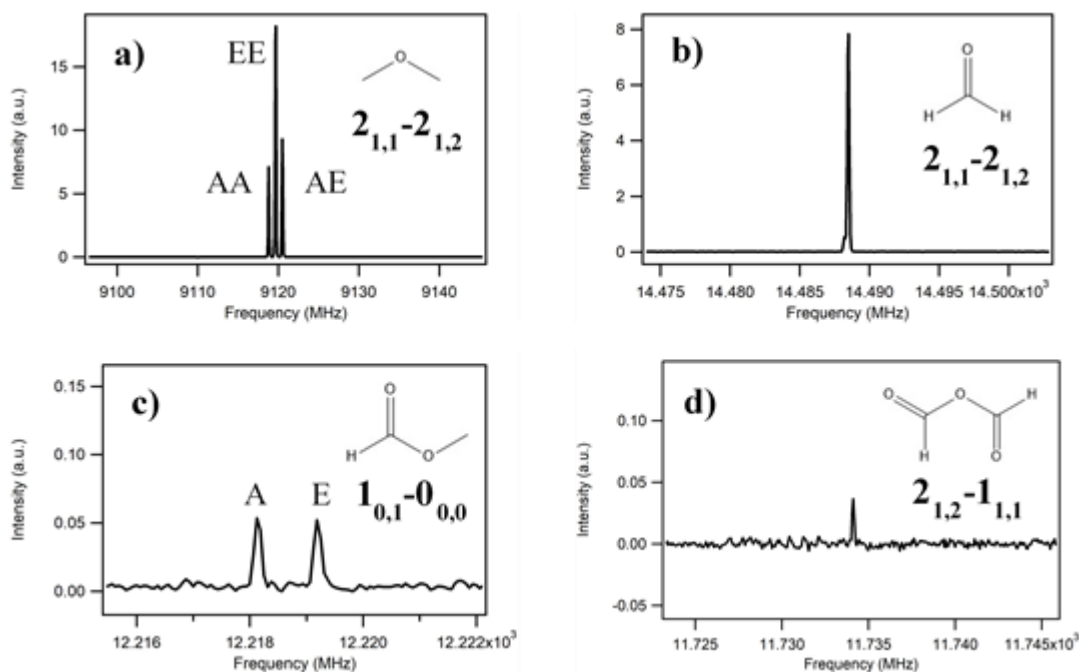


Figure 5.4 The unique identification capabilities of broad-band microwave spectroscopy is shown by identification of **(a)** the $2_{1,1}$ - $2_{1,2}$ transition of dimethyl ether, **(b)** the $2_{1,1}$ - $2_{1,2}$ transition of formaldehyde, **(c)** the $1_{0,1}$ - $0_{0,0}$ transition of methyl formate, and **(d)** the $2_{1,2}$ - $1_{1,1}$ transition of formic acid anhydride after sampling from reactive mixtures.

As a third example for the unique identification capabilities of microwave spectroscopy, we zoom into the region near 12.219 GHz of the rotational spectra after sampling from the reactive DMM/O₂/Ar mixture, see **Figure 5.4(c)**. The two observable transitions belong to the internal rotor states (labeled A and E) of the $1_{0,1}$ - $0_{0,0}$ transition of methyl formate [HC(=O)OCH₃].²⁵ **Figure 5.4(d)** shows the observed weak transition ($2_{1,2}$ - $1_{1,1}$ at 11.7341 GHz) of formic acid anhydride [FAA, HC(=O)OC(=O)H]. FAA had been detected earlier in the ethylene/ozone gas-phase reaction,²⁶ and this specific transition had been reported by Vaccani *et al.*²⁷ It belongs to the

asymmetric EA conformer in which the atoms are oriented in a way that allow for an internal hydrogen bond between the C=O function and the aldehyde-H atom from the other C-atom.

We also observed the accessible $3_{1,2}$ - $3_{1,3}$ transition of formic acid [HC(=O)OH] and the $1_{1,1}$ - $0_{0,0}$ transition of the primary ethylene ozonide at 9.8320 and 12.8286 GHz, respectively (not shown).²⁸⁻³⁰ The primary ozonide was not observed in the related mass spectrometry experiments,¹⁶ thus highlighting the additional insight potentially available from microwave spectroscopy. The microwave spectrum of hydroperoxy methyl formate (HPMF), the ketohydroperoxide in the DME oxidation system, had recently been reported,²⁹ however, improvements in the transfer line to the microwave spectrometer are needed to detect more reactive species with maximum sensitivity.

These examples clearly highlight the superb identification capabilities of microwave spectroscopy. However, it is also clear that assignment of the observed rotational transitions to a specific molecular carrier can be a difficult task, and many observed transitions in the spectra of **Figure 5.3** remained unassigned. Since searchable databases are scarce and automated routines are still being developed, experimental techniques must be employed that help with the assignments. Therefore, we have chosen the SFCB approach described above.

An example of this approach to assign rotational transitions is shown in **Figure 5.5**. Here, the upper trace shows the broadband microwave spectra during partial DME oxidation. To identify the origin of the observed peak at 14.945 GHz (marked with a '1' in **Figure 5.5**), a new spectrum was recorded in which the broadband chirped pulse was followed by an intense single frequency pulse (SFP) resonant with this transition. This SFP destroyed the coherence created by the chirp and, compared to the chirped pulse spectrum without the SFP, we identified a transition at 17.434 GHz whose intensity was modulated by the first SFP, proving that the two transitions belong to

the same species. In the next step, both the 14.945 GHz ('1') and 17.434 GHz ('2') transition frequencies were used as coherence breaking SFPs, identifying a transition near 12.289 GHz whose intensity was modulated. Following a third SFCB spectrum ('3'), a total of six transitions were modulated, identifying them as from a single species. From these transitions, we could estimate rotational constants based on a preliminary assignment and eventually we were able to identify the transitions as due to the DME dimer,³¹ formed during the cooling in the supersonic expansion.

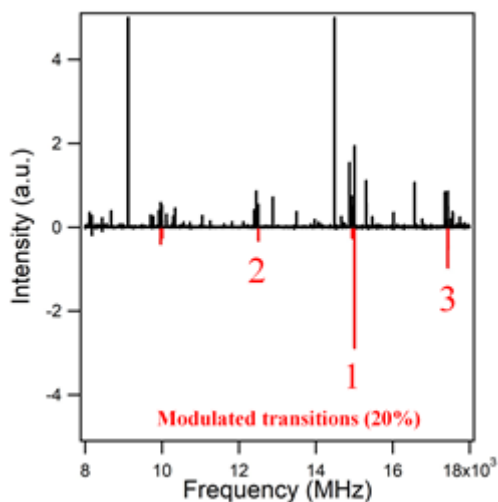


Figure 5.5 Upper trace: Broadband microwave spectra after sampling from the DME/O₂/Ar mixture. Lower trace: Difference spectra after implementation of the SFCB method. The six transitions whose intensities were modulated by more than 20% are marked. Numbers denote the single frequency pulses used in the experiment.

Based on this observation, we checked for the presence of other complexes and were able to identify rotational transitions that belong to the dimethyl ether-carbon dioxide,³² formaldehyde-water,³³ ethylene-water,³⁴ carbon dioxide-water,³⁶ and water-water dimers.³⁷ Although the transitions are not related to an intermediate that was formed in the reactor, they still provide useful information. The collisional cooling process that occurs in the supersonic free jets commonly used

in modern microwave spectroscopy has been used to form molecular complexes that are regularly studied to learn about weak intermolecular interactions.^{37,38} Here, in the context of broadband chirped-pulse microwave spectroscopy as a tool for combustion chemistry research, the observation of such complexes provides an indirect way to detect intermediates and products that are typically difficult or impossible to detect as isolated molecules via microwave spectroscopy. This could occur because the molecules possess small or zero dipole moments or lack transitions in the covered frequency range. In the present work, the detected complexes described above provide experimental evidence for the presence of ethylene and CO₂. Both these molecules are non-polar but are detected by complexation with H₂O, also present in the stirred flow reactor, taking advantage of its significant dipole moment. The fact that the effluent from the stirred flow reactor is rich in molecular species like H₂O make such detection possible without addition of an external complexing agent.

5.4 Conclusion

Given the high frequency resolution of rotational spectroscopy and the unique correlation between rotational frequencies and molecular structures, the identification capabilities of microwave spectroscopy are unmatched by any other gas-phase spectroscopy. With the chirped-pulse microwave spectroscopy method, a new broadband tool exists that allows for simultaneous recording of all rotational transitions over a given frequency range of all polar molecular in the gas mixtures. As such, it provides a unique tool to investigate complex reacting mixtures. Several efforts have been undertaken to establish chirped-pulse microwave spectroscopy as an analytical tool to quantitatively probe chemical dynamics and kinetics.³⁹⁻⁴¹ However, until recently,¹⁰ rotational spectroscopy had not been applied to study the reaction network of complex gas mixtures as found in widely used laboratory-scale flames and ideal reactors. In this earlier work it

was shown that substantial cooling can be achieved after sampling from a flame and that the observed intensities of the rotational transitions are correlated with species-specific mole fractions. In this paper we show that chirped-pulse rotational spectroscopy allows for the identification of many intermediates commonly found in oxidation environments at low temperatures. However, to reach its full capabilities, further improvements are needed to the interface between the sampled combustion environment and the microwave detection in order that highly reactive species can be detected before they react. Furthermore, for maximum sensitivity, it is essential after sampling from the reactive mixture, to achieve rotational temperatures below 10 K. In future work, this might be implemented using a cooling cell.⁴² It should also be kept in mind that rotational transitions might be split by hyperfine interactions and internal rotation effects, resulting in very complex spectra. Therefore, robust routines should be developed to unambiguously assign the broadband spectra of a wide variety of species that could be present in the sampled mixture.

5.5 References

- ¹T. J. Balle, W. H. Flygare, *Rev. Sci. Instrum.* **52**, 33 (1981).
- ²C. Puzzarini, *Phys. Chem. Chem. Phys.* **15**, 6595 (2013).
- ³G. G. Brown, B. C. Dian, K. O. Douglass, S. M. Geyer, B. H. Pate, *J. Mol. Spectrosc.* **238**, 200 (2006).
- ⁴G. G. Brown, B. C. Dian, K. O. Douglass, S. M. Geyer, S. T. Shipman, B. H. Pate, *Rev. Sci. Instrum.* **79**, (2008).
- ⁵G. B. Park, R. W. Field, *J. Chem. Phys.* **144**, (2016).
- ⁶N. Hansen, T. A. Cool, P. R. Westmoreland, K. Kohse-Höinghaus, *Prog. Energy Combust. Sci.* **35**, 168 (2009).
- ⁷F. Qi, *Proc. Combust. Inst.* **34**, 33 (2013).
- ⁸B. Adamson, S. Skeen, M. Ahmed, N. Hansen, *J. Phys. Chem. A* **122**, 9338 (2018).
- ⁹K. Kohse-Höinghaus, R. S. Barlow, M. Aldén, J. Wolfrum, *Proc. Combust. Inst.* **30**, 89 (2005).

- ¹⁰N. Hansen, J. Wullenkord, D. Obenchain, I. Graf, K. Kohse-Höinghaus, J.-U. Grabow, *RSC Adv.* **7**, 37867 (2017).
- ¹¹Z. Wang, O. Herbinet, N. Hansen, F. Battin-Leclerc, *Prog. Energy Combust. Sci.* **73**, 132 (2019).
- ¹²K. Moshhammer, A. W. Jasper, D. M. Popolan-Vaida, A. Lucassen, P. Dievarti, H. Selim, A. J. Eskola, C. A. Taatjes, S. R. Leone, S. M. Sarathy, Y. G. Ju, P. Dagaut, K. Kohse-Höinghaus, N. Hansen, *J. Phys. Chem. A* **119**, 7361 (2015).
- ¹³K. Moshhammer, A. W. Jasper, D. M. Popolan-Vaida, Z. D. Wang, V. S. B. Shankar, L. Ruwe, C. A. Taatjes, P. Dagaut, N. Hansen, *J. Phys. Chem. A* **120**, 7890 (2016).
- ¹⁴W. Sun, T. Tao, M. Lailliau, N. Hansen, B. Yang, P. Dagaut, *Combust. Flame* **193**, 491 (2018).
- ¹⁵A. Rousso, N. Hansen, A. Jasper, Y. Yu, *Phys. Chem. Chem. Phys.* **21**, 7341 (2019).
- ¹⁶A. C. Rousso, N. Hansen, A. W. Jasper, Y. Yu, *J. Phys. Chem. A* **122**, 8674 (2018).
- ¹⁷Y. Ju, W. Sun, *Prog. Energy Combust. Sci.* **48**, 21 (2015).
- ¹⁸S. M. Fritz, B. M. Hays, A. O. Hernandez-Castillo, C. Abeysekera, T. S. Zwier, *Rev. Sci. Instrum.* **89**, 093101 (2018).
- ¹⁹A. O. Hernandez-Castillo, C. Abeysekera, B. M. Hays, T. S. Zwier, *J. Chem. Phys.* **145**, 114203 (2016).
- ²⁰D. P. Zaleski, K. Prozument, *J. Chem. Phys.* **149**, 104106 (2018).
- ²¹N. A. Seifert, I. A. Finneran, C. Perez, D. P. Zaleski, J. L. Neill, A. L. Steber, R. D. Suenram, A. Lesarri, S. T. Shipman, B. H. Pate, *J. Mol. Spectrosc.* **312**, 13 (2015).
- ²²W. Leo Meerts, M. Schmitt, *Int. Rev. Phys. Chem.* **25**, 353 (2006).
- ²³F. J. Lovas, H. Lutz, H. Dreizler, *J. Phys. Chem. Ref. Data* **8**, 1051 (1979).
- ²⁴R. Bocquet, J. Demaison, L. Poteau, M. Liedtke, S. Belov, K. M. T. Yamada, G. Winnewisser, C. Gerke, J. Gripp, T. Köhler, *J. Mol. Spectrosc.* **177**, 154 (1996).
- ²⁵R. F. Curl, *J. Chem. Phys.* **30**, 1529 (1959).
- ²⁶H. Kuhne, S. Vaccani, T. K. Ha, A. Bauder, H. H. Gunthard, *Chem. Phys. Lett.* **38**, 449 (1976).
- ²⁷S. Vaccani, A. Bauder, H. H. Gunthard, *Chem. Phys. Lett.* **35**, 457 (1960).
- ²⁸C. Gillies, R. Kuczkowski, *J. Am. Chem. Soc.* **94**, 6337 (1972).
- ²⁹J. P. Porterfield, K. L. K. Lee, V. Dell’Isola, P. B. Carroll, M. C. McCarthy, *Phys. Chem. Chem. Phys.* **21** 18065 (2019).

- ³⁰E. Willemot, D. Dangoisse, N. Monnanteuil, J. Bellet, *J. Phys. Chem. Ref. Data* **9**, 59 (1980).
- ³¹Y. Tatamitani, B. Liu, J. Shimada, T. Ogata, P. Ottaviani, A. Maris, W. Caminati, J. L. Alonso, *J. Am. Chem. Soc.* **124**, 2739 (2002).
- ³²J. J. Newby, R. A. Peebles, S. A. Peebles, *J. Phys. Chem. A* **108**, 11234 (2004).
- ³³F. J. Lovas, C. Lugez, *J. Mol. Spectrosc.* **179**, 320 (1996).
- ³⁴A. M. Andrews, R. L. Kuczkowski, *J. Chem. Phys.* **98**, 791 (1993).
- ³⁵G. Columberg, A. Bauder, N. Heineking, W. Stahl, J. Makarewicz, *Mol. Phys.* **93**, 215 (1998).
- ³⁶L. Coudert, J. Hougen, *J. Mol. Spectrosc.* **139**, 259 (1990).
- ³⁷M. Juanes, R. T. Saragi, W. Caminati, A. Lesarri, *Chem-Eur. J.* **25**, 11402 (2019).
- ³⁸M. Becucci, S. Melandri, *Chem. Rev.* **116**, 5014 (2016).
- ³⁹J. M. Oldham, C. Abeysekera, B. Joalland, L. N. Zack, K. Prozument, I. R. Sims, G. B. Park, R. W. Field, A. G. Suits, *J. Chem. Phys.* **141**, (2014).
- ⁴⁰C. Abeysekera, A. O. Hernandez-Castillo, J. F. Stanton, T. S. Zwier, *J. Phys. Chem. A* **122**, 6879 (2018).
- ⁴¹N. M. Kidwell, V. Vacquero-Vara, T. K. Ormond, G. T. Buckingham, D. Zhang, D. N. Mehta-Hurt, L. McCaslin, M. R. Nimlos, J. W. Daily, B. C. Dian, *J. Phys. Chem. Lett.* **5**, 2201 (2014).
- ⁴²D. Patterson, J. M. Doyle, *Mol. Phys.* **110**, 1757 (2012).

CHAPTER 6. CONTINUING PROMISING EXPERIMENTS: PENTANAL, TRANS-2-PENTENAL AND *O*-, *M*-, AND *P*- VINYLANISOLE

6.1 Introduction

The proposal of using biofuels as a sustainable source of energy has gained momentum as fossil fuel reserves continue to deplete and serve as the main source of energy worldwide.¹ This approach has placed much emphasis on the design of biofuels that would allow for progress towards the development of more efficient, lower-emitting engines. Recent biofuel studies have found that oxygen functional groups are responsible for promising fuel properties including the capacity to reduce soot as well as a high cetane number (CN).²⁻⁴ Of these oxygenated candidates, long-branched alcohols have been identified as promising additives to gasolines since they have higher energy density than ethanol and can reduce pollutants including nitrogen oxides and carbon monoxide.^{5,6}

However, the combustion of long-chained alcohols leads to the formation of other toxic emissions such as carbonyl containing compounds including aldehydes and ketones.^{7,8} Aldehydes are garnering interest in biofuel combustion research because of their significant roles in low-temperature oxidation of hydrocarbons as well as their formation as intermediate products in the combustion of bio-alcohols.⁹⁻¹² Numerous combustion studies have been carried out on short chain aldehydes including acetaldehyde^{13,14} and formaldehyde,¹³ but combustion related studies are lacking in detail for longer-chained aldehydes. In order to better understand oxygenated biofuel combustion, further studies involving longer chain aldehydes are needed to provide reliable data for addition to current models.¹⁵⁻¹⁹



Figure 6.1 Structural representation of pentanal and *trans*-2-pentenal

Pentanal and *trans*-2-pentenal, shown in **Figure 6.1**, combine long saturated and unsaturated alkyl chains with a terminal carbonyl group capturing key features interesting for the combustion chemistry in terms of longer chained aldehydes. As a result of the long alkyl chain, numerous gas phase structures can be adopted. Studying these inherent conformational preferences and energy level structure of pentanal and *trans*-2-pentenal provides a foundation of understanding to better support future combustion and pyrolysis experiments involving longer chained aldehydes.

Another promising biofuel candidate is lignin as it is one of the most naturally abundant biopolymers and is a byproduct of bioethanol production.^{20,21} Recent advances in converting lignocellulosic biomass to biofuels have stimulated the interest in second generation biofuels such as alkylated furans, furanic ethers and lactones.²² However, due to the chemical complexity of these second-generation biofuels, much remains to be learned about their pyrolysis and combustion. Vinylanisoles are an intriguing set of aromatic biofuels,²³ shown in **Figure 6.2**, as the relative positions of methoxy and vinyl groups could significantly impact their thermal cracking. Understanding the energy level structure and conformational preferences of *o*-, *m*- and *p*-vinylanisole are important first experiments to the initiation events in pyrolysis and combustion.

This chapter reports preliminary results of the broadband chirped pulse-Fourier transform microwave (CP-FTMW) spectra of jet-cooled pentanal, *trans*-2-pentenal, and *o*-, *m*- and *p*-vinylanisole over the 8-18 GHz range. In order to identify rotational transitions due to individual conformers, the strong-field coherence breaking (SFCB) technique²⁴ was applied to pentanal and

trans-2-pentenal to selectively modulate conformer-specific rotational transitions. Rotational transitions due to the four lowest-energy conformers of pentanal and two lowest energy conformers of *trans*-2-pentenal were all identified and assigned. The two lowest structures were identified and fit for *m*- and *p*-vinylanisole, whereas only the lowest energy structure was identified for *o*-vinylanisole.

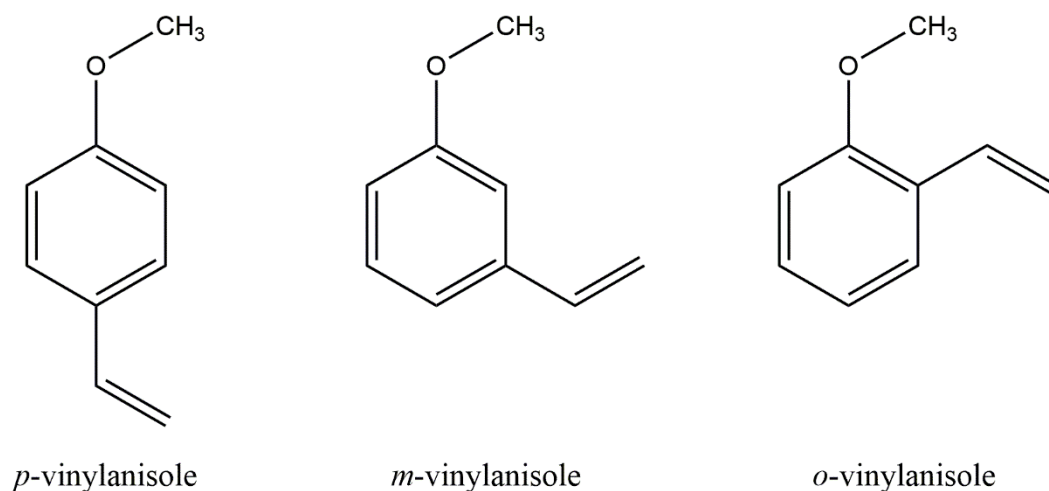


Figure 6.2 Structural representation of *p*-, *m*- and *o*-vinylanisole

6.2 Experimental

Commercial samples of pentanal, *trans*-2-pentenal and *o*-, *m*- and *p*-vinylanisole were obtained from Sigma-Aldrich and were used without further purification. The samples were heated to 40 °C, 60 °C and 125 °C for pentanal, *trans*-2-pentenal and the vinylanisole series, respectively. The samples were entrained in He buffer gas at a pressure of 2.3 bar, and expanded through the 1 mm dia. orifice of a pulsed valve (Parker General, Series 9) operating at 10 Hz. The broadband rotational spectrum of each species was recorded in the 8-18 GHz region using a CP-FTMW spectrometer, which has been described in detail in chapter 2 and elsewhere.²⁵

For pentanal and *trans*-2-pentenal, a conformational search was carried out using MacroModel with Merck molecular force field static (MMFFs).²⁶ Geometry optimizations, dihedral angle scans and internal rotation scans of the possible conformations of pentanal, *trans*-2-pentenal and the vinylanisole series were performed using the Gaussian09 program suite²⁷ at the DFT B3LYP/Def2TZVP level of theory including Grimme's dispersion (D3BJ).²⁸ Relaxed potential energy curves were carried out for methyl internal rotation and on the flexible dihedrals stepping in 10° increments at the same level of theory mentioned above. This level of theory has been shown to provide relative energies in good correspondence with experimental results for medium sized molecules. The nomenclature to describe the conformations of pentanal and *trans*-2-pentenal starts with the carbonyl group and the terms *gauche* ($\pm 60^\circ$), *trans* ($\pm 180^\circ$), *syn* ($\pm 0^\circ$) and *eclipsed* ($\pm 120^\circ$) are used to describe the dihedral angles. The atom labelling scheme is shown explicitly on the *syn trans trans* conformer in **Figure 6.3**, with the designations indicating the values of the C₁-C₂, C₂-C₃ and C₃-C₄ dihedral angles in that order. This nomenclature is used to label all conformations of pentanal and *trans*-2-pentenal. The nomenclature to describe the vinylanisole structures is *up up* if both the vinyl and methoxy groups point in the same direction and *up down* if both functional groups point in opposite directions. The structures and nomenclature of the vinylanisole series are shown in **Figure 6.4**.

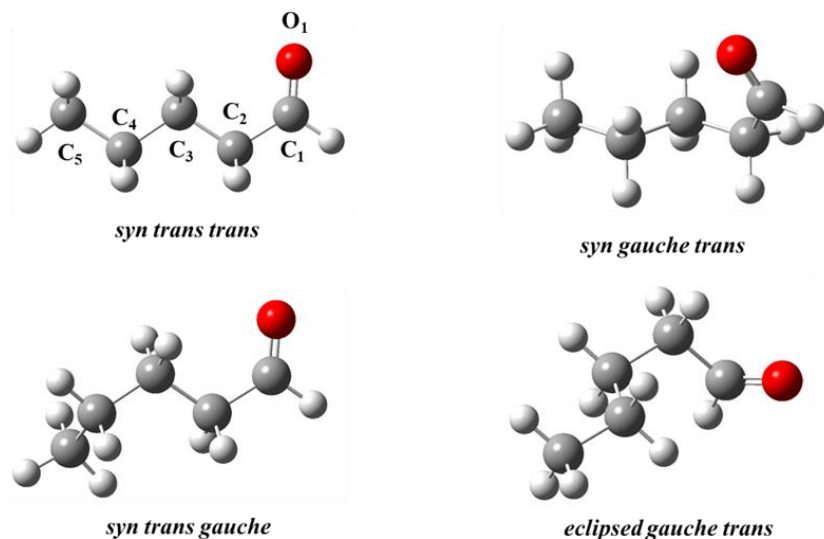


Figure 6.3 Side views of the four lowest energy conformers of pentanal predicted at the B3LYP/Def2TZVP level of theory, including Grimme's dispersion correction.

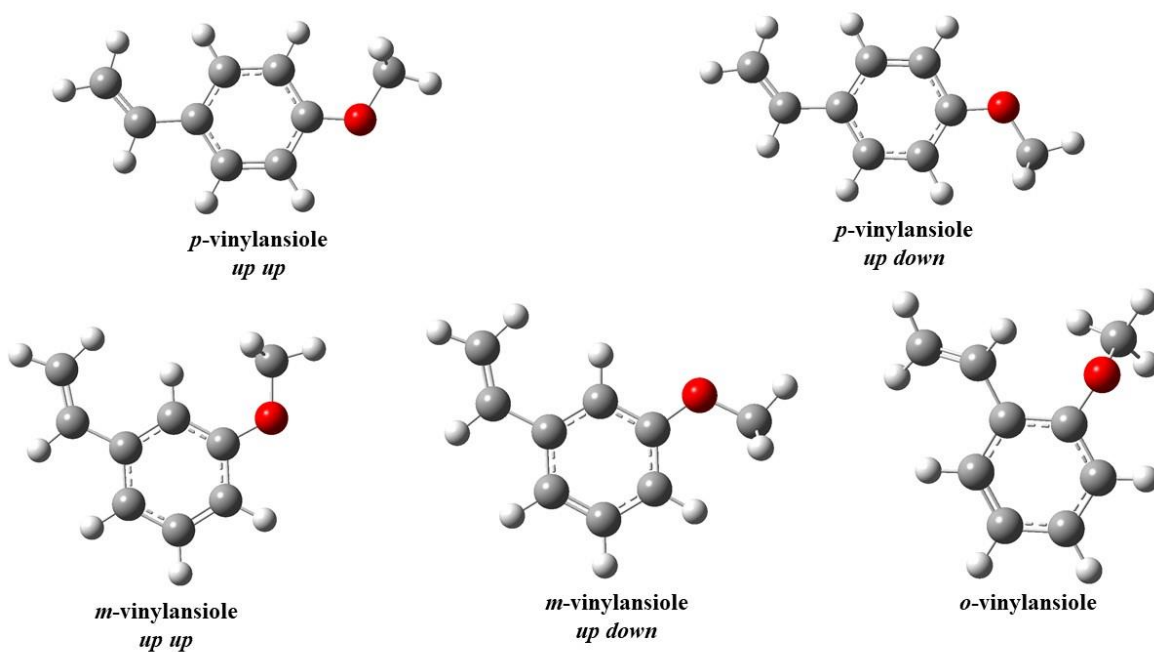


Figure 6.4 Out of plane views of the five identified structures of *p*-, *m*- and *o*-vinylanisole predicted at the B3LYP/Def2TZVP level of theory, including Grimme's dispersion correction.

6.3 Results

6.3.1 Pentanal

The DFT calculations of pentanal found six unique low energy structures within a 4 kJ/mol window as shown in **Figure 6.3**. All four structures are near-prolate asymmetric tops with non-zero dipole moment contributions along all three axes. The DFT calculations predict the *syn trans trans* conformer to be the lowest energy structure followed closely by the *syn gauche trans* (0.43 kJ/mol) conformer. Other predicted higher energy structures including the *syn trans gauche* (2.60 kJ/mol) and *eclipsed gauche trans* (2.92 kJ/mol) were anticipated to have a minor contribution to the spectrum. The broadband rotational spectrum of pentanal was recorded over the 8-18 GHz region and is shown in **Figure 6.5**. With the possibility of numerous structures contributing to the broadband spectrum, strong field coherence breaking was utilized to provide rotational transitions belonging to individual structures. The first resonance frequency chosen was 15007.1875 MHz followed by resonant frequencies at 15749.6875 MHz and 11838.3125 MHz. Utilizing these three frequencies in the SFCB technique, 7 conformer-specific transitions had their intensities modulated by more than 30% as shown in **Figure 6.6(a)**. These rotational transitions best matched those of the *syn gauche trans* conformer and the SFPs used were fit to $3_{1,3}-2_{0,2}$, $2_{2,1}-2_{1,2}$ and $2_{1,2}-1_{0,1}$, respectively. These *b*-type Q- and R-branch transitions modulated *b*- and *c*-type Q- and R-branch transitions in the difference spectrum, ultimately aiding in fitting a total of 27 transitions. Pickett's SPFIT/SPCAT²⁹ suite of programs with a Watson S-type Hamiltonian was used to fit all of the structures discussed in this text.

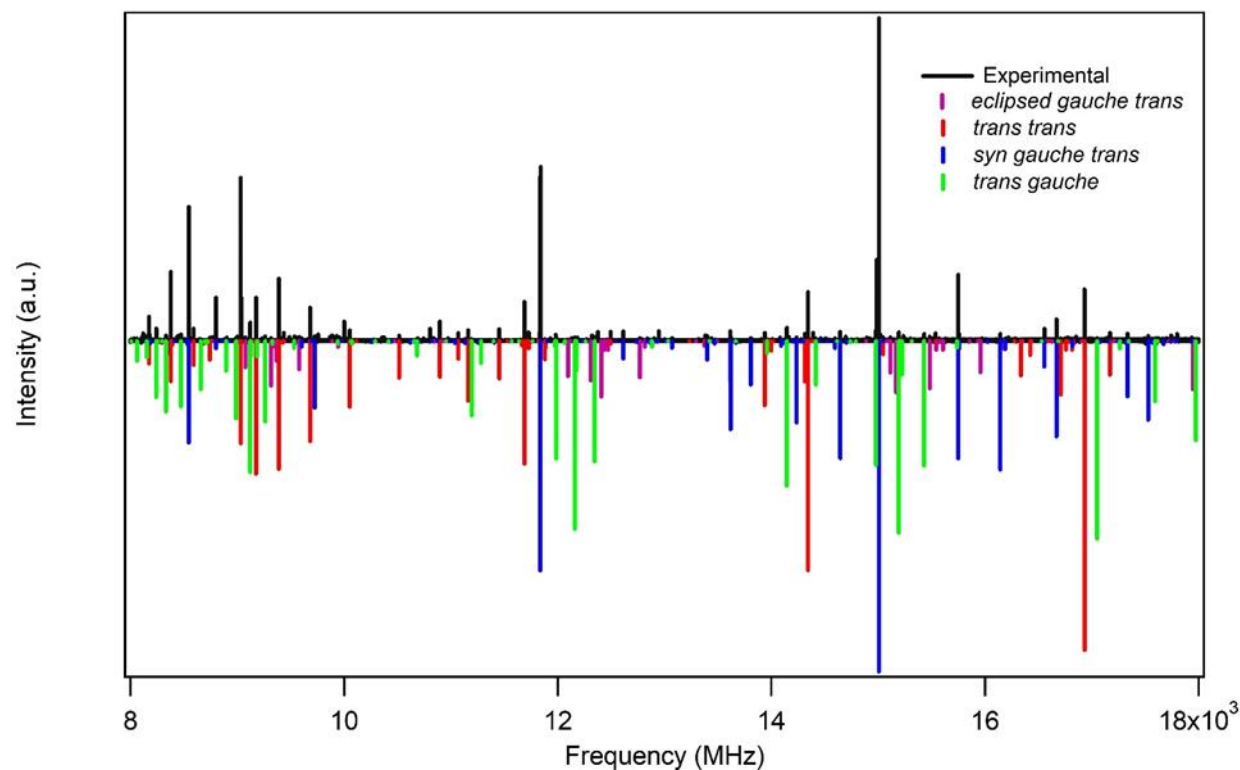


Figure 6.5 Experimental 1M average broadband spectrum of pentanal with the best fits of the four identified conformers present. The blue, red, green and purple lines are assigned to the *syn gauche trans*, *trans trans*, *trans gauche* and *eclipsed gauche trans* conformers, respectively.

After fitting all possible transitions belonging to the *syn gauche trans* conformer, intense transitions remained unassigned. SFCB was utilized starting with the most intense unassigned transition at 9033.6875 MHz followed by subsequent SFPs at 9388.8125 MHz and 16929.8750 MHz. The final difference spectrum provided 9 conformer-specific rotational transitions whose intensities were modulated by more than 40% and best matched the predicted spectrum of the *syn trans trans* conformer as shown in **Figure 6.6(b)**. The selected SFPs were assigned to $1_{1,0}-1_{0,1}$, $3_{1,2}-3_{0,3}$ and $3_{1,3}-2_{0,2}$ transitions, respectively, modulating *a*-, *b*- and *c*-type Q- and R-branch transitions in the difference spectra. The difference spectrum provided an initial assignment which facilitated the final fit of 26 rotational transitions.

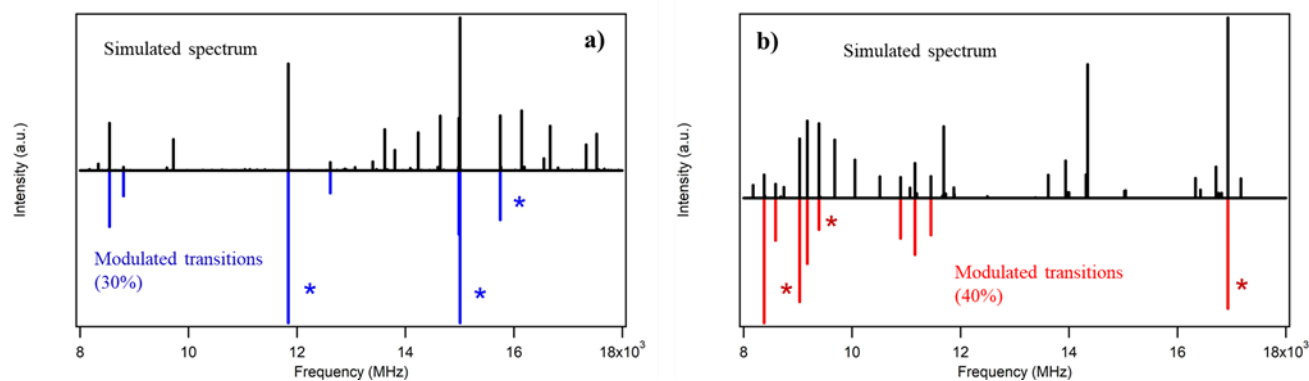


Figure 6.6 ((a) and (b)): Conformer-specific spectra of the (a) *syn gauche trans* and (b) *syn trans trans* conformers of pentanal using strong field coherence breaking. Black lines are simulated spectra. Transitions whose intensities were modulated by more than (a) 30% and (b) 40% are displayed in blue and red, respectively.

After using SFCB to dissect most of the broadband spectrum, weak unassigned transitions remained. These minor contributions in the spectrum belonged to the third and fourth energetically favorable structures which are the *syn trans gauche* and *eclipsed gauche trans* conformations. The *syn trans gauche* conformer exhibited *a*-, *b*- and *c*-type Q- and R-branch transitions throughout the spectrum totaling 20 transitions. The *eclipsed gauche trans* structure was the weakest of the four structures and only 7 total transitions could be assigned, all of which were *a*-type R-branch transitions. The structural parameters including rotational and distortion constants pertaining to all four identified conformers are reported in **Table 6.1**. The assigned transitions and frequencies for the four identified conformers are provided in **Tables 6.4-6.7**.

6.3.2 *trans*-2-pentenal

The DFT calculations predicted only two unique low energy conformers for *trans*-2-pentenal shown in **Figure 6.7**. The *trans syn* conformer is the global minimum closely followed by the *trans eclipsed* (0.41 kJ/mol). Both structures are near-prolate asymmetric tops with significant dipole moment components in the *a*-axis with the *trans syn* conformer having a non-

negligible dipole component along the *b*-axis (1.6 D) and the *trans eclipsed* having a weak dipole moment contribution along the *c*-axis (-0.9 D).

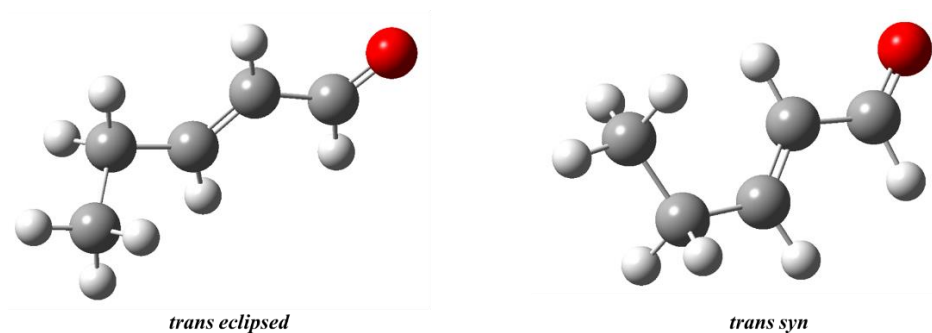


Figure 6.7 Side views of the four lowest energy conformers of pentanal predicted at the B3LYP/Def2TZVP level of theory, including Grimme's dispersion correction.

The broadband rotational spectrum was recorded over the 8-18 GHz regime and is shown in **Figure 6.8**. Strong field coherence breaking was utilized for *trans*-2-pentenal to provide sets of rotational transitions in a conformer-specific manner. The first resonant frequency chosen was 12962.1250 MHz followed by subsequent frequencies at 10407.3750 MHz and 15499.1250 MHz. Using these frequencies in the SFCB method provided a difference spectrum yielding 9 rotational transitions whose intensities were modulated by more than 50% as shown in **Figure 6.9(a)**. These 9 transitions best matched with the *trans eclipsed* structure and the resonant frequencies were later assigned to $5_{0,5}-4_{0,4}$, $4_{1,3}-3_{1,2}$ and $6_{1,6}-5_{1,5}$ transitions, respectively. These *a*-type R-branch transitions modulated both *a*- and *c*-type Q- and R-branch transitions, ultimately aiding in the fitting of 23 total transitions.

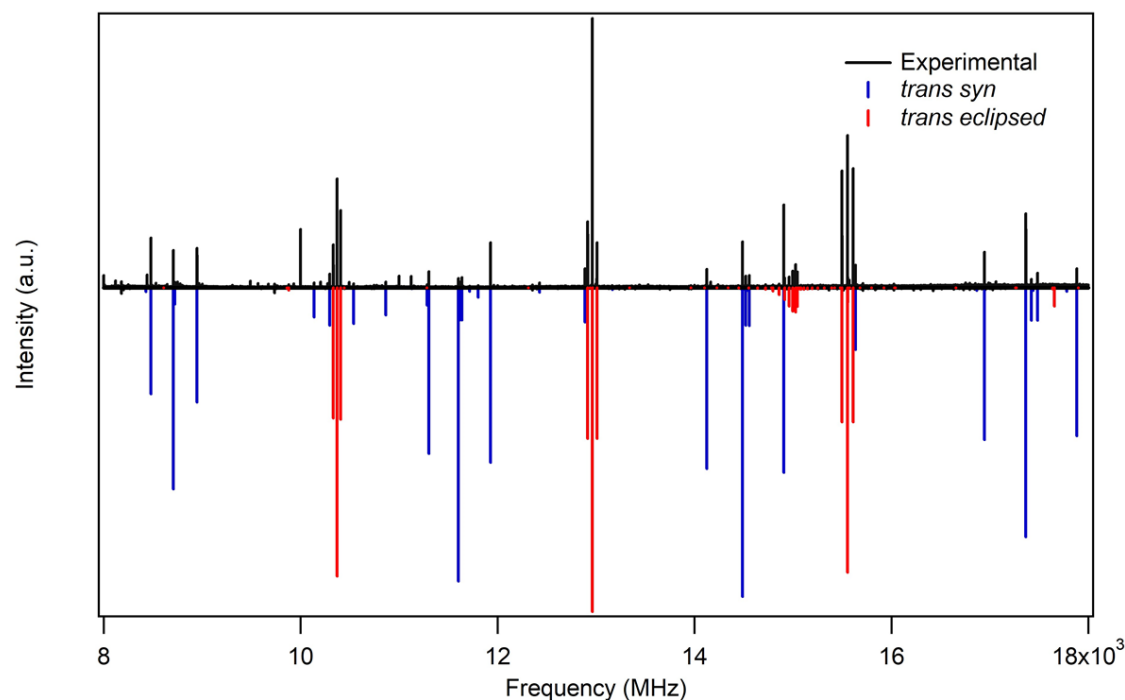


Figure 6.8 Experimental 1M average broadband spectrum of *trans*-2-pentenal with the best fits of the two identified conformers present. The blue and red lines are assigned to the *trans syn* and *trans eclipsed* conformers, respectively.

Strong field coherence breaking was carried out once again starting with the next intense unassigned transition at 17366.1250 MHz followed by resonant frequencies 8749.1250 MHz and 11929.1250 MHz. Using these frequencies in the SFCB method provided a difference spectrum yielding 8 rotational transitions whose intensities were modulated by more than 30% as shown in **Figure 6.9(b)**. These 8 transitions best matched with the *trans syn* structure and the resonant frequencies were later assigned to $6_{0,6}-5_{0,5}$, $3_{1,3}-2_{1,2}$ and $4_{1,3}-3_{1,2}$ transitions, respectively. These *a*-type R-branch transitions modulated both *a*- and *b*-type R-branch transitions, ultimately aiding in the fitting of 24 total transitions. The structural parameters including rotational and distortion constants pertaining to both identified conformers are reported in **Table 6.2**. The assigned transitions and frequencies of the two conformers are *trans*-2-pentenal are provided in **Tables 6.8** and **6.9**.

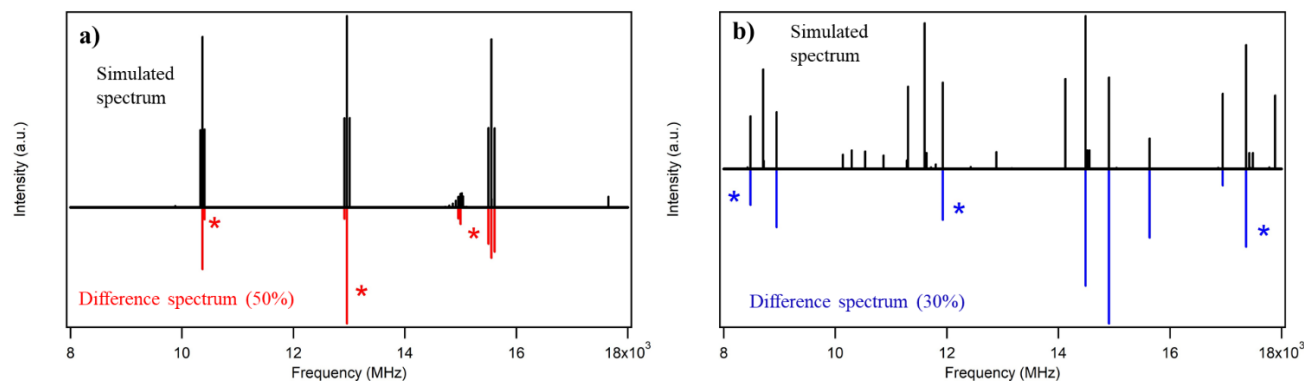


Figure 6.9 ((a) and (b)): Conformer-specific spectra of the (a) *trans eclipsed* and (b) *trans syn* conformers of *trans*-2-pentenal using strong field coherence breaking. Black lines are simulated spectra. Transitions whose intensities were modulated by more than (a) 50% and (b) 30% are displayed in red and blue, respectively.

6.3.3 *p*-Vinylanisole

The 8-18 GHz broadband rotational spectrum of *p*-vinylanisole is shown in **Figure 6.10**, with the experimental spectrum shown in black and the rotational transitions from the *up up* and *up down* structures in red and blue, respectively. Both structures are close in energy, with the *up down* structure being the global minimum and the *up up* structure 0.65 kJ/mol higher in energy. The *up down* conformer possesses relatively weak dipole moment components in the *a*-axis (1.3 D) and the *b*-axis (1.0 D) with zero dipole moment in the *c*-axis, resulting in a spectrum containing *a*- and *b*-type transitions from R- and Q-branches. The *up up* conformer also possesses relatively weak dipole moment components in the *a*-axis (1.1 D) and the *b*-axis (1.0 D) with zero dipole moment in the *c*-axis, resulting in a spectrum containing *a*- and *b*-type transitions from R- and Q-branches. No internal rotation from the methoxy group was observed. The distortion constants for both structures were calculated at the B3LYP/Def2TZVP level of theory with Grimme's dispersion and were used in the final fit of each conformer. The number of transitions fit for the *up up* conformer was 71 and 77 for the *up down* conformer with experimental accuracies of 21.6 kHz and 26.1 kHz, respectively. The structural parameters for both conformers are included in **Table**

6.3. The assigned transitions and frequencies of the two conformers of *p*-vinylanisole are provided in **Tables 6.10** and **6.11**.

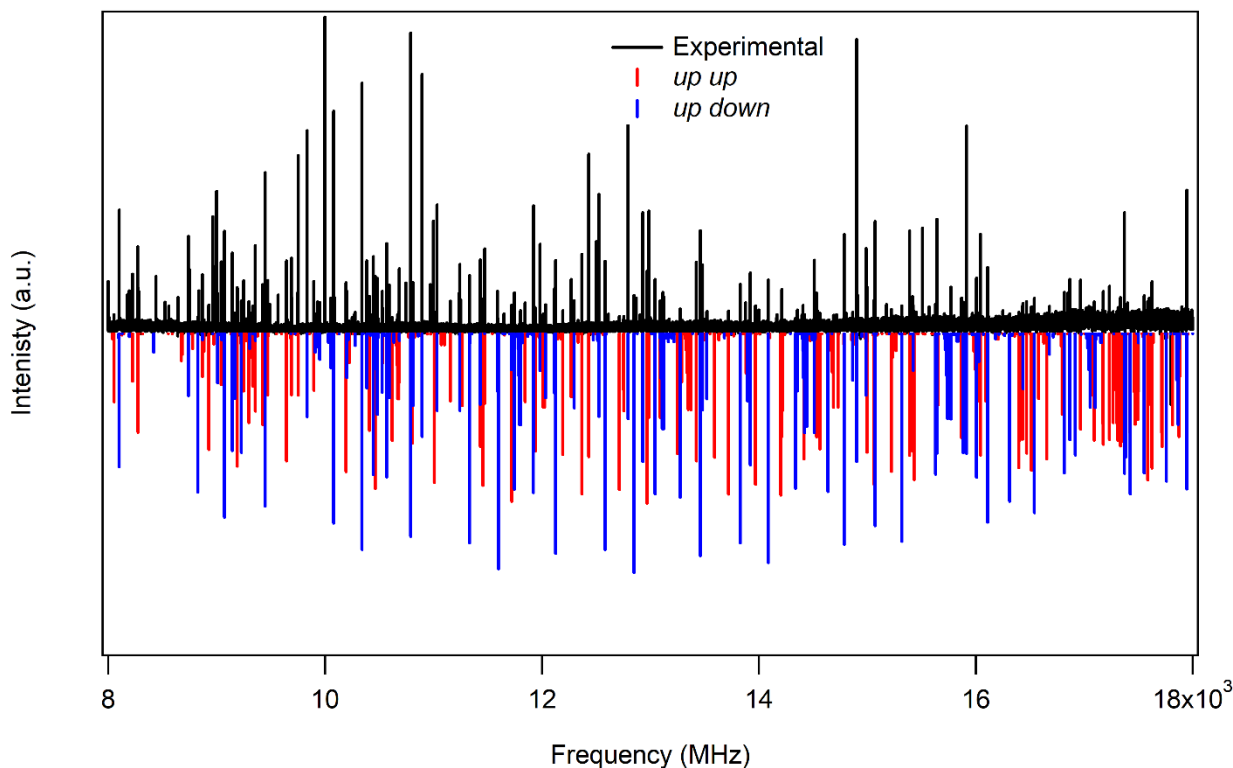


Figure 6.10 Experimental broadband spectrum of *p*-vinylanisole with the best fits of the two identified conformers present. The blue and red lines are assigned to the *up down* and *up up* conformers, respectively.

6.3.4 *m*-Vinylansiole

The 8-18 GHz broadband rotational spectrum of *m*-vinylanisole is shown in **Figure 6.11**, with the experimental spectrum shown in black and the rotational transitions from the *up up* and *up down* structures in green and purple, respectively. Unlike *p*-vinylanisole, the *up up* structure is the global minimum and the *up down* structure is 0.98 kJ/mol higher in energy. The *up up* conformer possesses a relatively weak dipole moment component in the *b*-axis (1.0 D) and zero contribution from the *a*- and *c*-axes, resulting in a spectrum containing *b*-type transitions from R-

and Q-branches. The *up down* conformer also possesses relatively weak dipole moment components in the *a*-axis (0.6 D) and the *b*-axis (1.3 D) with zero dipole moment in the *c*-axis, resulting in a spectrum containing *a*- and *b*-type transitions from R- and Q-branches. No internal rotation from the methoxy group was observed. The distortion constants for both structures were calculated at the B3LYP/Def2TZVP level of theory with Grimme's dispersion and were used in the final fit of each conformer. The number of transitions fit for the *up down* and *up up* conformers was 96 and 82 with experimental errors of 17.5 kHz and 17.9 kHz, respectively. The structural parameters for both conformers are included in **Table 6.3**. The assigned transitions and frequencies of the two conformers of *m*-vinylanisole are provided in **Tables 6.12** and **6.13**.

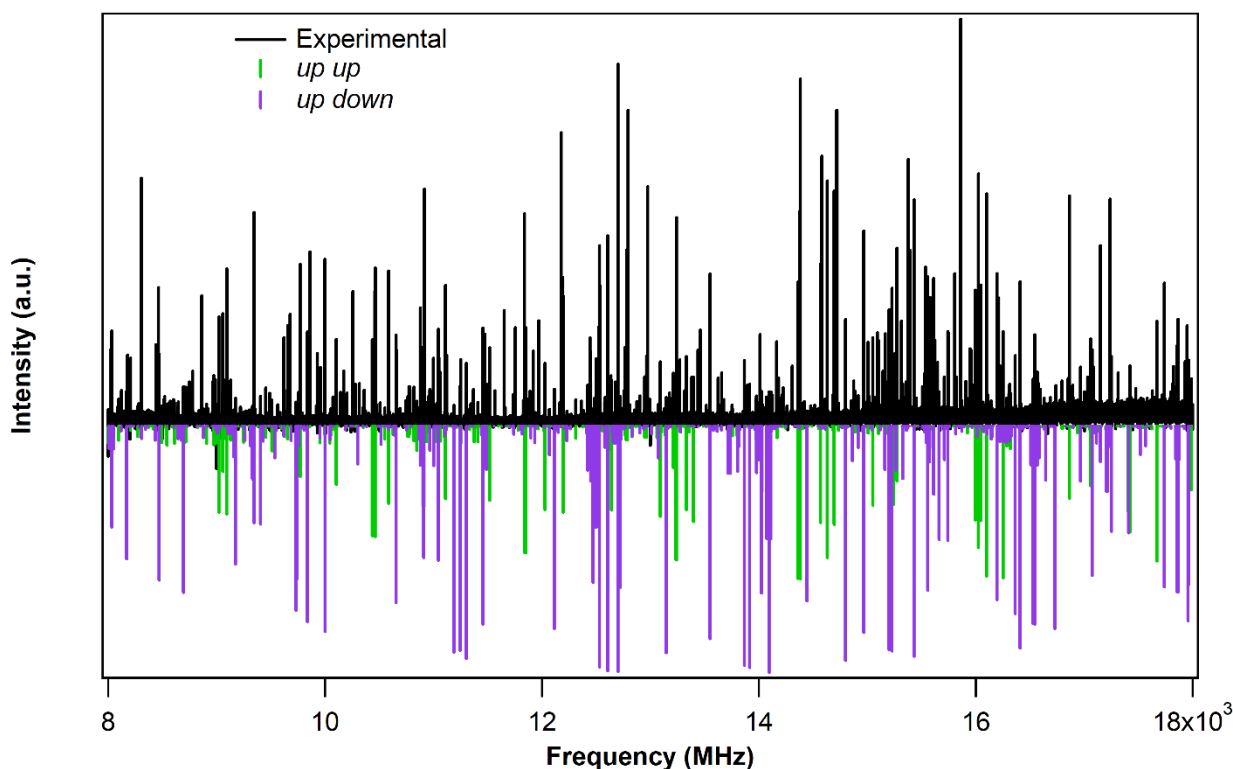


Figure 6.11 Experimental broadband spectrum of *m*-vinylanisole with the best fits of the two identified conformers present. The green and purple lines are assigned to the *up up* and *up down* conformers, respectively.

6.3.5 *o*-Vinylanisole

The 8-18 GHz broadband rotational spectrum of *m*-vinylanisole is shown in **Figure 6.12**, with the experimental spectrum shown in black and the rotational transitions from the only identified structure is in orange. No other structures were found in a 10 kJ/mol window. The global minimum structure is shown in **Figure 6.12** and possesses a relatively weak dipole moment component in the *c*-axis (1.0 D) and zero contribution from the *a*- and *b*-axes, resulting in a spectrum containing *c*-type transitions from R- and Q-branches. No internal rotation from the methoxy group was observed. The distortion constants were calculated at the B3LYP/Def2TZVP level of theory with Grimme's dispersion and were used in the final fit. The number of transitions fit for was 72 with an experimental error of 34.1 kHz. The structural parameters for both conformers are included in **Table 6.3**. The assigned transitions and frequencies of *o*-vinylanisole are provided in **Tables 6.14**.

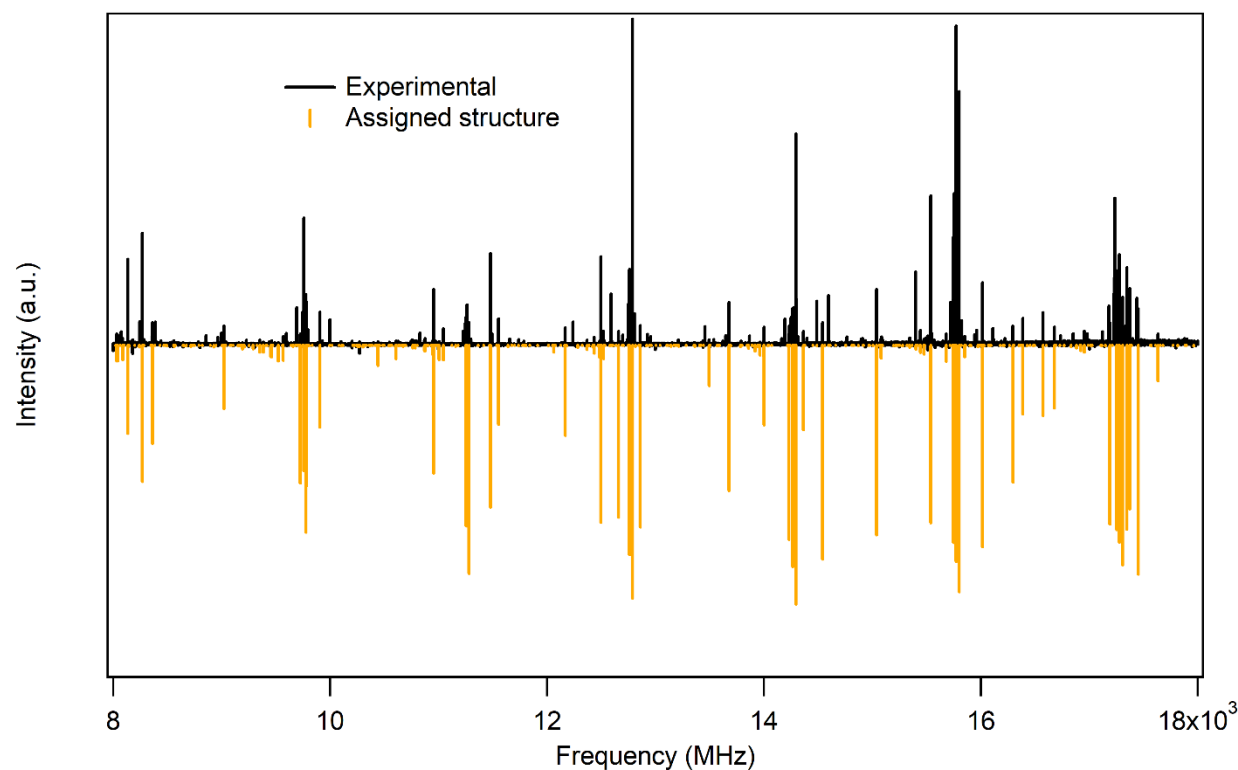


Figure 6.12 Experimental broadband spectrum of *o*-vinylanisole with the best fit of the only structure present in orange.

6.4 Discussion

We recorded the 8-18 GHz broadband microwave spectra of pentanal and *trans*-2-pentenal under jet-cooled conditions, using strong field coherence breaking to identify rotational transitions from four unique structures of pentanal and two unique structures of *trans*-2-pentenal.

In the case of pentanal, six energetically favorable structures were found in the conformational search with three pairs having similar energies. The *syn trans trans* (0 kJ/mol) and the *syn gauche trans* (0.43 kJ/mol) conformers were the two predicted lowest energy structures with the next two structures closest in energy being the *syn trans gauche* (2.60 kJ/mol) and the *eclipsed gauche trans* (2.90 kJ/mol) conformers. These two higher energy structures were followed closely by the *eclipsed trans trans* (3.40 kJ/mol) and the *syn gauche gauche* (3.55 kJ/mol) conformers. The broadband spectrum is dominated by the *syn trans trans* and *syn gauche trans* conformers as these

two structures accounted for all of the intense transitions in the spectrum. Remaining weak transitions were assigned to the *syn trans gauche* and *eclipsed gauche trans* conformers leaving no evidence of either the *eclipsed trans trans* nor the *syn gauche gauche* structures.

Table 6.1 Experimentally determined structural parameters of the four identified conformations of pentanal

	<i>stt</i>	<i>sgt</i>	<i>stg</i>	<i>egt</i>
A (MHz)	10522.7389	6960.8197	9850.3949	7976.3650
(pred^b/expt)	10361.2322(89)	6897.065(12)	9717.8363(61)	7590.7(36)
B (MHz)	1458.2264	1890.5135	1558.4185	1636.3591
(pred/expt)	1466.7628(19)	1905.1160(31)	1565.9502(25)	1639.1789(32)
C (MHz)	1322.0149	1637.6163	1467.3844	1469.3539
(pred/expt)	1327.5404(11)	1647.0819(33)	1475.6974(21)	1470.7233(32)
μ_a (D)	1.30	0.18	-1.92	2.13
μ_b (D)	-2.40	-2.50	-1.67	-1.86
μ_c (D)	0	-0.65	0.92	-0.69
D_J (kHz)	-0.194	-0.824	-0.321	-1.230
(pred/expt)	-0.278(39)	-0.863(55)	-0.318(56)	---
D_K (kHz)	-35.8	-19.7	-69.8	-107.8
(pred/expt)	-33.7(35)	-24.1(29)	---	---
D_{JK} (kHz)	2.49	3.16	3.40	17.94
(pred/expt)	1.77(56)	4.43(25)	---	---
d₁ (kHz)	-0.032	-0.200	0.017	-0.298
(pred/expt)	---	-0.221(10)	---	---
d₂ (kHz)	0.0005	-0.0102	-0.013	-0.012
(pred/expt)	---	-0.0146(91)	---	---
E_{rel} (kJ/mol)^a	0	0.43	2.60	2.92
N	26	27	20	8
σ (kHz)	15.6	22.9	17.3	12.9

^aZero-point corrected relative energy. ^bDFT B3LYP Def2TZVP-D3BJ level of theory.

With numerous plausible structures in a tight energy window, we carried out one dimensional relaxed potential energy scans of the flexible dihedrals in order to better understand the conformational preferences of pentanal. The first dihedral (D₁ = C₁-C₂-C₃-C₄) started with the optimized *syn trans trans* structure and found three minima with the first corresponding to the *syn trans trans* structure and the other two located every $\pm 60^\circ$ corresponding to a *syn gauche trans* structure. These two \pm *gauche* structures are separated by a maximum at 0° equivalent to the *syn*

syn trans structure with a calculated barrier height of 27 kJ/mol. The *syn trans trans* and *syn gauche trans* structures are separated by an 8 kJ/mol barrier. The experimental intensities match well with the predicted energies as these two are the most abundant in the spectrum, yet the more intense transitions between the two belong to the higher energy *syn gauche trans* structure which can be attributed to the double degeneracy of the gauche dihedral angle.

The second dihedral ($D_2 = C_2-C_3-C_4-C_5$) scan was aimed at understanding the preferences between the *syn trans trans* and *syn trans gauche* conformers. The potential energy scan also reveals two minima located $\pm 60^\circ$ corresponding to a *syn trans gauche* conformer. These two \pm *gauche* structures are separated by a maximum at 0° equivalent to the *syn syn trans* structure with a calculated barrier height of 20 kJ/mol. The barrier separating the *syn trans gauche* and *syn trans trans* structures is 13 kJ/mol. Even with double degeneracy, the relative intensities of the *syn trans gauche* conformer are relatively weak as it is 2.60 kJ/mol and 2.17 kJ/mol higher in energy than the *syn trans trans* and *syn gauche trans* conformers, respectively.

Lastly, the third dihedral ($D_3 = O_1-C_1-C_2-C_3$) scan was aimed at understanding the preferences and barriers between the *syn gauche trans* and *eclipsed gauche trans* structures. There are three minima in the potential energy surface with the two lowest corresponding to the *syn gauche trans* and *eclipsed gauche trans* structures at 0° and 120° and a third at 240° . The barrier separating the *syn trans gauche* and *eclipsed trans gauche* structures is 10 kJ/mol and the barrier separating the two *eclipsed* structures at 120° and 240° is 5 kJ/mol. The third *eclipsed* minima at 240° is 4.7 kJ/mol higher in energy than the *eclipsed gauche trans* and about 8 kJ/mol higher in energy than the *syn gauche trans* structures.

For *trans*-2-pentenal, one flexible dihedral scan was carried out to study the potential energy surface between *trans eclipsed* and *trans syn* structures. Starting with the optimized *trans syn*

structure, the dihedral ($D_2 = C_2-C_3-C_4-C_5$) scan found three minima 0° , 120° and 240° corresponding to *trans eclipsed*, *trans syn* and *trans eclipsed* structures, respectively, separated by 8.5 kJ/mol barriers. The relative intensities of the rotational transitions, however, indicate that the *trans eclipsed* structure is the most abundant of the two structures possibly due to the double degeneracy and higher *a*-axis dipole moment component despite being higher in energy.

We recorded the 8-18 GHz broadband microwave spectra of *p*-, *m*- and *o*-vinylanisole under jet-cooled conditions identifying the two lowest energy structures for *p*- and *m*-vinylanisole and the lowest energy structure for *o*-vinylanisole. No internal rotation was observed from the methoxy group as the barriers to internal rotation for all 5 identified structures exceeded 10 kJ/mol. With only low dipole moment structures present for *p*- and *m*-vinylanisole, SFCB was not implemented as accessing the RAP regime was not possible. SFCB was not applied for *o*-vinylanisole as only one structure was populated.

The assigned structures provide a starting point for broadband rotational spectroscopy of the vinylanisole series under thermal cracking conditions from a pyrolysis nozzle. Such a pyrolysis study has not yet been carried out. Using these assigned structures as a starting point, all rotational transitions belonging to the vinylanisoles can be accounted for. The first step in thermal cracking of the vinylanisole would be loss of a methyl radical, leaving mass 119 radical. This has been the first thermal degradation step in other lignin monomers and oxygenated biofuels including guaiacol³⁰ and 2-methoxyfuran.²² Finding the temperature at which thermal decomposition begins and where the max abundance of the radical occurs is the next step in this ongoing project, followed by structural characterization of the radicals. These free radicals would be fascinating candidates for further study, as they are vinyl-substituted phenoxy radicals, and would provide an interesting comparison with previous work in our group on phenoxy and ortho-hydroxy phenoxy radicals.^{25,31}

Table 6.2 Experimentally determined structural parameters of the two identified conformations of *trans*-2-pentenal

	<i>te</i>	<i>ts</i>
A (MHz)	16422.9343	11643.5331
(pred/expt)	16350.994(20)	11512.280(16)
B (MHz)	1309.3837	1531.3894
(pred/expt)	1305.5761(16)	1530.7180(25)
C (MHz)	1291.7907	1376.1265
(pred/expt)	1286.9532(28)	1374.2630(20)
μ_a (D)	4.13	-3.95
μ_b (D)	-0.23	-1.61
μ_c (D)	0.90	0
D_J (kHz)	-0.222	-0.167
(pred/expt)	---	---
D_K (kHz)	-569.8	-44.8
(pred/expt)	---	---
D_{JK} (kHz)	14.89	2.22
(pred/expt)	14.81(67)	2.20(53)
d_1 (kHz)	0.034	-0.030
(pred/expt)	---	---
d_2 (kHz)	-0.0026	-0.0017
(pred/expt)	---	---
E_{rel} (kJ/mol)^a	0.41	0
N	23	23
σ (kHz)	41.1	28.4

^aZero-point corrected relative energy. ^bDFT B3LYP Def2TZVP-D3BJ level of theory.

Table 6.3 Experimentally determined structural parameters of the two identified conformations of *p*- and *m*-vinylanisole and the single conformation of *o*-vinylanisole

	<i>p</i> -Vinylanisole		<i>m</i> -Vinylanisole		<i>o</i> -Vinylanisole
	<i>up up</i>	<i>up down</i>	<i>up up</i>	<i>up down</i>	
A (MHz)	4171.7219	4661.2802	1932.7134	2615.0526	1648.0014
(pred^b/expt)	4123.7490(11)	4604.0899(17)	1923.4410(12)	2590.7960(11)	1629.936(24)
B (MHz)	717.8896	699.5612	1086.650	882.524	1423.2916
(pred/expt)	717.0134(25)	698.571(24)	1084.072(80)	882.260(26)	1374.819(14)
C (MHz)	614.8801	610.6296	698.655	662.6166	805.775
(pred/expt)	613.9307(17)	609.521(21)	697.125(12)	661.718(17)	753.146(35)
μ_a (D)	1.13	1.35	-0.1	-1.37	0
μ_b (D)	-1.07	-1.06	-1.05	0.64	0.12
μ_c (D)	0	0	0	0	1.21
D_J (kHz)	-0.0119	-0.009	-0.051	-0.02	-0.453
(pred/expt)	---	---	---	---	---
D_K (kHz)	-1.318	-0.689	-0.28	-0.603	-0.27
(pred/expt)	---	---	---	---	---
D_{JK} (kHz)	0.101	0.019	0.137	0.065	0.698
(pred/expt)	---	---	---	---	---
d_1 (kHz)	0.002	-0.002	-0.02	-0.007	-0.20
(pred/expt)	---	---	---	---	---
d_2 (kHz)	-0.0001	-0.0001	-0.002	-0.701	-0.13
(pred/expt)	---	---	---	---	---
E_{rel}	-0.65	0	0	0.98	0
(kJ/mol)^a					
N	71	77	82	96	72
σ (kHz)	21.6	26.1	17.9	17.5	34.1

^aZero-point corrected relative energy. ^bDFT B3LYP Def2TZVP-D3BJ level of theory.

6.5 Conclusions

We recorded the jet-cooled broadband spectra of pentanal, *trans*-2-pentenal and *o*-, *m*- and *p*-vinylanisole in the 8-18 GHz regime. We utilized SFCB to identify sets of rotational transitions belonging to two conformers of both pentanal and *trans*-2-pentenal, ultimately facilitating assignment. The four lowest energy structures of pentanal were assigned followed by the two lowest energy structures of *trans*-2-pentenal. The two lowest energy conformers were assigned for both *p*- and *m*-vinylanisole as well as the lowest energy structure of *o*-vinylanisole. The structural parameters for all species were recorded, aiding future experiments.

6.6 References

- ¹N. Hansen, T. A. Cool, P. R. Westmoreland, K. Kohse-Höinghaus, *Prog. Energ. Combust.* **35**, 168 (2009).
- ²L. Bu, P. N. Ciesielski, D. J. Robichaud, S. Kim, R. L. McCormick, T. D. Foust, M. R. Nimlos, *J. Phys. Chem. A* **121**, 5475 (2017).
- ³T. G. Leone, J. E. Anderson, R. S. Davis, A. Iqbal, R. A. Reese, M. H. Shelby, W. M. Studzinski, *Environ. Sci. Technol.* **49**, 10778 (2015).
- ⁴C. E. Dumitrescu, C. J. Mueller, E. Kurtz, *Appl. Therm. Eng.* **101**, 639 (2016).
- ⁵S. Atsumi, T. Hanai, J. C. Liao, *Nature* **451**, 86 (2008).
- ⁶K. Yasunaga, T. Mikajiri, S. M. Sarathy, T. Koike, F. Gillespie, T. Nagy, J. M. Simmie, H. J. Curran, *Combust. Flame* **159**, 2009 (2012).
- ⁷M. Pelucchi, E. Ranzi, A. Frassoldati, T. Faravelli, *P. Combust. Inst.* **36**, 393 (2017).
- ⁸E. Sadeghinezhad, S. Kazi, F. Sadeghinejad, A. Badarudin, M. Mehrali, R. Sadri, M. R. Safaei, *Renew. Sustainable Energy Rev.* **30**, 29 (2014).
- ⁹S. W. Benson, *Prog. Energy Combust. Sci.* **7**, 125 (1981).
- ¹⁰G. Vanhove, M. Ribaucour, R. Minetti, *Proc. Combust. Inst.* **30**, 1065 (2005).
- ¹¹M. S. Kurman, R. H. Natelson, N. P. Cernansky, D. L. Miller, *Proc. Combust. Inst.* **33**, 159 (2011).
- ¹²K. A. Heufer, S. M. Sarathy, H. J. Curran, A. C. Davis, C. K. Westbrook, W. J. Pitz, *Energy Fuels* **26**, 6678 (2012).
- ¹³J. Mendes, C. W. Zhou, H. J. Curran, *J. Phys. Chem. A* **118**, 12089 (2014).
- ¹⁴P. H. Taylor, T. Yamada, P. Marshall, *Int. J. Chem. Kinet.* **38**, 489 (2006).
- ¹⁵P. S. Veloo, P. Dagaut, C. Togbe, G. Dayma, S. M. Sarathy, C. K. Westbrook, F. N. Egolfopoulos, *Proc. Comb. Inst.* **34**, 599 (2013).
- ¹⁶P. S. Veloo, P. Dagaut, C. Togbe, G. Dayma, S. M. Sarathy, C. K. Westbrook, F. N. Egolfopoulos, *Combust. Flame* **160**, 1609 (2013).
- ¹⁷M. Pelucchi, K. P. Somers, K. Yasunaga, U. Burke, A. Frassoldati, E. Ranzi, H. J. Curran, T. Faravelli, *Combust. Flame* **162**, 265 (2015).
- ¹⁸A. Rodriguez, O. Herbinet, F. Battin-Leclerc, *Proc. Comb. Inst.* **36**, 365 (2017).
- ¹⁹Z. Serinyel, C. Togbe, G. Dayma, P. Dagaut, *Energy Fuels* **31**, 3206 (2017).

- ²⁰A. Barakat, F. Monlau, J. P. Steyer, H. Carrere, *Bioresour. Technol.* **104**, 90 (2012).
- ²¹G. Jiang, D. J. Nowakowski, A. V. Bridgwater, *Thermochimica Acta* **498**, 61 (2010).
- ²²C. Abeysekera, A. O. Hernandez-Castillo, J. F. Stanton, T. S. Zwier, *J. Phys. Chem. A* **122**, 6879 (2018).
- ²³J. C. del Rio, A. G. Lino, J. L. Colodette, C. F. Lima, A. Gutierrez, A. T. Martinez, F. Lu, J. Ralph, J. Rencoret, *Biomass Bioenerg.* **81**, 322 (2015).
- ²⁴A. O. Hernandez-Castillo, C. Abeysekera, B. M. Hays, and T. S. Zwier, *J. Chem. Phys.* **145**, 114203 (2016).
- ²⁵S. M. Fritz, B. M. Hays, A. O. Hernandez-Castillo, C. Abeysekera, T. S. Zwier, *Rev. Sci. Instrum.* **89**, 093101 (2018).
- ²⁶T. A. Halgren, *J. Comput. Chem.* **17**, 490 (1996).
- ²⁷D.J. Frisch, M. J.; Trucks, G. W.; Schlegel, H. B.; Scuseria, G. E.; Robb, M. A.; Cheeseman, J. R.; Scalmani, G.; Barone, V.; Mennucci, B.; Petersson, G. A.; Nakatsuji, H.; Caricato, M.; Li, X.; Hratchian, H. P.; Izmaylov, A. F.; Bloino, J.; Zheng, G.; Sonnenb, Gaussian 09, Revis. E.01, Gaussian, Inc., Wallingford CT. (2009).
- ²⁸S. Grimme, *J. Chem. Phys.* **124**, 034108 (2006).
- ²⁹H.M. Pickett, *J. Mol. Spectrosc.* **377**, 371 (1991).
- ³⁰Scheer, A. M.; Mukarakate, C., Robichaud, D. J.; Nimlos, M. R.; Ellison, G. B., *J. Phys. Chem. A* **115**, 1381 (2011).
- ³¹A. O. Hernandez-Castillo, C. Abeysekera, J. F. Stanton, T. S. Zwier, *J. Phys. Chem. Lett.* **10**, 2919 (2019).

6.7 Supplementary Material

Table 6.4 Observed frequencies ($\nu_{\text{Obs.}}$) of 26 rotational transitions of the *syn trans trans* conformer of pentanal. $\nu_{\text{Obs.}} - \nu_{\text{Calc.}}$ values as obtained after a fit with the program *SPFIT/SPCAT*.

J	K_a	K_c	J	K_a	K_c	$\nu_{\text{Obs.}}$	$\nu_{\text{Obs.}} - \nu_{\text{Calc.}}$
upper level			lower level			MHz	<i>SPFIT/SPCAT</i> MHz
3	1	3	2	0	2	16929.8750	-0.0239
2	1	2	1	0	1	14343.8125	-0.0100
1	1	1	0	0	0	11688.7500	0.0085
3	1	3	2	1	2	8173.0625	0.0103
3	0	3	2	0	2	8376.3750	-0.0194
3	1	2	2	1	1	8590.6875	-0.0133
1	1	0	1	0	1	9033.6875	0.0259
2	1	1	2	0	2	9174.5000	-0.0117
3	1	2	3	0	3	9388.8125	-0.0056
4	1	3	4	0	4	9680.1875	-0.0051
5	1	4	5	0	5	10053.4375	0.0420
6	1	5	6	0	6	10514.2500	-0.0107
4	1	4	3	1	3	10895.5000	-0.0108
4	0	4	3	0	3	11160.9375	-0.0014
4	1	3	3	1	2	11452.3125	-0.0009
5	1	5	4	1	4	13616.3750	-0.0079
5	1	4	4	1	3	14312.2500	0.0348
6	0	6	5	1	5	8743.6250	0.00327
7	1	6	7	0	7	11069.5625	-0.0099
8	1	7	8	0	8	11726.8750	0.0017
7	0	7	6	1	6	11877.9688	0.00724
9	1	8	9	0	9	12494.1875	-0.0054
5	0	5	4	0	4	13939.0313	0.0189
3	2	2	4	1	3	15022.8438	0.0000
8	0	8	7	1	7	15045.4375	-0.0147
6	1	5	5	1	4	17169.9375	0.0036

Table 6.5 Observed frequencies ($\nu_{\text{Obs.}}$) of 20 rotational transitions of the *syn trans gauche* conformer of pentanal. $\nu_{\text{Obs.}} - \nu_{\text{Calc.}}$ values as obtained after a fit with the program *SPFIT/SPCAT*.

<i>J</i>	<i>K_a</i>	<i>K_c</i>	<i>J</i>	<i>K_a</i>	<i>K_c</i>	$\nu_{\text{Obs.}}$	$\nu_{\text{Obs.}} - \nu_{\text{Calc.}}$
upper level			lower level			MHz	<i>SPFIT/SPCAT</i> MHz
2	1	2	2	0	2	8062.3125	-0.0159
1	1	1	1	0	1	8151.8125	-0.0104
1	1	0	1	0	1	8242.0625	-0.0134
2	1	1	2	0	2	8333.1250	0.0367
3	1	2	3	0	3	8471.0000	-0.0029
4	1	3	4	0	4	8657.5000	0.0120
5	1	4	5	0	5	8894.7500	-0.0023
3	1	3	2	1	2	8989.0625	-0.0216
3	0	3	2	0	2	9121.9375	0.0097
3	1	2	2	1	1	9259.8125	-0.0300
1	1	1	0	0	0	11193.4375	-0.0320
4	1	4	3	1	3	11984.5625	0.0155
4	0	4	3	0	3	12159.0625	0.0036
4	1	3	3	1	2	12345.5625	0.0185
2	1	2	1	0	1	14144.8750	0.0065
2	1	1	1	0	1	14415.6250	-0.0033
5	1	5	4	1	4	14979.2500	-0.0011
5	0	5	4	0	4	15193.1875	0.0003
5	1	4	4	1	3	15430.4375	-0.0140
3	1	3	2	0	2	17051.4375	0.0250

Table 6.6 Observed frequencies ($\nu_{\text{Obs.}}$) of 27 rotational transitions of the *syn gauche trans* conformer of pentanal. $\nu_{\text{Obs.}} - \nu_{\text{Calc.}}$ values as obtained after a fit with the program *SPFIT/SPCAT*.

<i>J</i>	<i>K_a</i>	<i>K_c</i>	<i>J</i>	<i>K_a</i>	<i>K_c</i>	$\nu_{\text{Obs.}}$	$\nu_{\text{Obs.}} - \nu_{\text{Calc.}}$
upper level			lower level			MHz	<i>SPFIT/SPCAT</i> MHz
1	1	1	0	0	0	8544.1250	-0.0042
4	0	4	3	1	3	9722.3125	-0.0535
2	1	2	1	0	1	11838.3125	0.0187
2	1	1	1	0	1	12612.3750	-0.0049
6	2	4	6	1	5	13399.6250	0.0206
5	0	5	4	1	4	13618.3750	0.0358
5	2	3	5	1	4	13806.1875	0.0183

Table 6.6 cont.

4	2	2	4	1	3	14236.8125	0.0146
3	2	1	3	1	2	14643.4375	-0.0357
3	1	3	2	0	2	15007.1875	-0.0040
2	2	1	2	1	2	15749.6875	0.0269
2	2	0	2	1	2	15759.4375	0.0312
3	2	2	3	1	3	16142.7500	0.0006
3	1	2	2	0	2	16555.1250	0.0233
4	2	3	4	1	4	16670.1250	0.0183
5	2	4	5	1	5	17333.8125	-0.0362
6	0	6	5	1	5	17528.8125	0.0148
1	1	0	0	0	0	8802.1250	-0.0365
7	1	6	7	0	7	9602.1250	-0.0071
8	1	7	8	0	8	11132.0938	0.0119
8	2	6	8	1	7	12864.0313	0.0044
7	1	6	6	2	5	12887.2500	-0.0141
7	2	5	7	1	6	13068.6250	-0.0228
3	2	2	3	1	2	14594.8125	-0.0267
2	2	1	2	1	1	14975.5625	-0.0120
2	2	0	2	1	1	14985.3125	-0.0077
3	2	1	3	1	3	16191.3750	-0.0084

Table 6.7 Observed frequencies ($\nu_{\text{Obs.}}$) of 8 rotational transitions of the *eclipsed gauche trans* conformer of pentanal. $\nu_{\text{Obs.}} - \nu_{\text{Calc.}}$ values as obtained after a fit with the program *SPFIT/SPCAT*.

J	K_a	K_c	J	K_a	K_c	$\nu_{\text{Obs.}}$	$\nu_{\text{Obs.}} - \nu_{\text{Calc.}}$
upper level			lower level			MHz	<i>SPFIT/SPCAT</i> MHz
3	0	3	2	1	2	9075.0000	0.0264
3	0	3	2	0	2	9316.3125	0.0183
3	1	2	2	1	1	9580.2500	0.0147
4	1	4	3	1	3	12096.0625	-0.0171
4	1	3	3	1	2	12769.5312	0.0269
5	1	5	4	1	4	15113.9688	-0.0101
5	0	5	4	0	4	15482.8750	0.0050
5	1	4	4	1	3	15955.0625	-0.0383

Table 6.8 Observed frequencies ($\nu_{\text{Obs.}}$) of 23 rotational transitions of the *trans eclipsed* conformer of *trans*-2-pentenal. $\nu_{\text{Obs.}} - \nu_{\text{Calc.}}$ values as obtained after a fit with the program *SPFIT/SPCAT*.

<i>J</i>	<i>K_a</i>	<i>K_c</i>	<i>J</i>	<i>K_a</i>	<i>K_c</i>	$\nu_{\text{Obs.}}$	$\nu_{\text{Obs.}} - \nu_{\text{Calc.}}$
upper level			lower level			MHz	<i>SPFIT/SPCAT</i> MHz
2	1	2	2	0	2	15026.3750	0.0451
1	1	1	1	0	1	15044.8750	-0.0023
4	0	4	3	0	3	10369.8750	-0.0124
5	0	5	4	0	4	12962.1250	-0.0645
6	0	6	5	0	5	15554.4375	0.0590
1	1	0	2	0	2	9878.4375	-0.0288
4	1	4	3	1	3	10332.8750	-0.0147
4	1	3	3	1	2	10407.3750	-0.0236
5	1	5	4	1	4	12916.0000	-0.0336
5	1	4	4	1	3	13009.1875	0.0056
5	1	5	5	0	5	14915.3125	-0.0730
4	1	4	4	0	4	14961.5625	0.0211
3	1	3	3	0	3	14998.5000	-0.0390
6	1	6	5	1	5	15499.1250	-0.0003
6	1	5	5	1	4	15611.0000	0.0792
6	2	4	5	2	3	15556.2500	0.0300
6	2	5	5	2	4	15555.6250	0.0059
5	2	3	4	2	2	12963.3750	-0.0589
5	2	4	4	2	3	12963.0625	-0.0281
8	1	8	8	0	8	14722.6875	0.0475
7	1	7	7	0	7	14795.8125	-0.0429
6	1	6	6	0	6	14860.1875	0.0549
2	1	1	2	0	2	15082.2187	0.0176

Table 6.9 Observed frequencies ($\nu_{\text{Obs.}}$) of 23 rotational transitions of the *trans syn* conformer of *trans*-2-pentenal. $\nu_{\text{Obs.}} - \nu_{\text{Calc.}}$ values as obtained after a fit with the program *SPFIT/SPCAT*.

<i>J</i>	<i>K_a</i>	<i>K_c</i>	<i>J</i>	<i>K_a</i>	<i>K_c</i>	$\nu_{\text{Obs.}}$	$\nu_{\text{Obs.}} - \nu_{\text{Calc.}}$
upper level			lower level			MHz	<i>SPFIT/SPCAT</i> MHz
3	1	3	2	1	2	8479.1250	0.0012
3	0	3	2	0	2	8707.6250	-0.0003
3	1	2	2	1	1	8948.4375	-0.0302
4	1	4	3	1	3	11303.3750	-0.0097
4	0	4	3	0	3	11601.6250	-0.0205
4	1	3	3	1	2	11929.1250	0.0170
5	1	5	4	1	4	14125.9375	0.0636
5	0	5	4	0	4	14488.3750	-0.0228
5	1	4	4	1	3	14907.8125	-0.0251
6	1	6	5	1	5	16946.1875	-0.0096
6	0	6	5	0	5	17366.1250	-0.0207
6	1	5	5	1	4	17884.1875	0.0590
3	2	2	2	2	1	8714.9375	-0.0389
3	2	1	2	2	0	8722.2500	-0.0238
4	2	3	3	2	2	11618.5625	0.0318
4	2	2	3	2	1	11636.7500	-0.0128
5	2	4	4	2	3	14520.8125	-0.0399
5	2	3	4	2	2	14577.3125	0.0419
1	1	0	1	0	1	10138.0000	0.0195
2	1	1	2	0	2	10296.2500	-0.0178
3	1	2	3	0	3	10537.1250	0.0147
4	1	3	4	0	4	10864.5625	-0.0102
1	1	1	0	0	0	12886.5000	-0.0058
2	1	2	1	0	1	15635.0625	0.0257

Table 6.10 Observed frequencies ($\nu_{\text{Obs.}}$) of 71 rotational transitions of the *up up* conformer of *p*-vinylanisole. $\nu_{\text{Obs.}} - \nu_{\text{Calc.}}$ values as obtained after a fit with the program *SPFIT/SPCAT*.

<i>J</i>	<i>K_a</i>	<i>K_c</i>	<i>J</i>	<i>K_a</i>	<i>K_c</i>	$\nu_{\text{Obs.}}$	$\nu_{\text{Obs.}} - \nu_{\text{Calc.}}$
upper level			lower level			MHz	<i>SPFIT/SPCAT</i> MHz
7	2	6	6	2	5	9298.6875	-0.0059
7	3	5	6	3	4	9333.7500	-0.0271
7	3	4	6	3	3	9337.8125	-0.0042
7	0	7	6	0	6	9191.1875	0.0050
7	1	7	6	1	6	8927.5625	0.0175
6	1	5	5	1	4	8275.5625	0.0081
7	2	5	6	2	4	9424.0625	0.0042
7	1	6	6	1	5	9645.0625	-0.0148
8	0	8	7	0	7	10462.9375	-0.0279
8	3	6	7	3	5	10671.2500	-0.0127
8	3	5	7	3	4	10679.3125	-0.0041
8	2	6	7	2	5	10803.8750	0.0139
9	1	9	8	1	8	11455.1875	-0.0037
9	0	9	8	0	8	11721.6875	0.0302
9	2	8	8	2	7	11937.1250	0.0110
9	2	7	8	2	6	12193.6250	0.0014
8	2	7	8	1	8	12270.6875	0.0209
9	1	8	8	1	7	12368.2500	0.0299
8	1	8	7	0	7	12431.6875	-0.0247
10	0	10	9	0	9	12968.2500	0.0290
2	2	1	1	1	0	12985.1875	0.0276
2	2	0	1	1	1	13090.5625	0.0158
9	1	9	8	0	8	13423.9375	-0.0005
10	1	9	9	1	8	13719.6875	0.0338
11	1	11	10	1	10	13969.1250	-0.0149
3	2	2	2	1	1	14213.0000	-0.0225
3	2	1	2	1	2	14533.7500	-0.0333
11	2	10	10	2	9	14562.0000	-0.0030
11	3	9	10	3	8	14689.1250	0.0200
11	2	9	10	2	8	14996.6250	-0.0087
11	1	10	10	1	9	15062.6875	0.0057
12	1	12	11	1	11	15221.0625	0.0365
11	1	11	10	0	10	15417.1250	0.0368
12	0	12	11	0	11	15432.5625	0.0311
12	2	11	11	2	10	15868.5625	0.0076

Table 6.10 cont.

4	2	2	3	1	3	16041.9375	-0.0179
13	1	13	12	1	12	16469.6875	-0.0110
5	2	4	4	1	3	16513.4375	0.0636
8	3	5	8	2	6	16966.1875	-0.0320
7	3	4	7	2	5	17090.7500	-0.0140
5	3	2	5	2	3	17232.4375	0.0035
6	3	4	6	2	5	17333.9375	0.0293
6	2	5	5	1	4	17586.6875	0.0171
5	2	3	4	1	4	17624.1875	-0.0039
9	2	7	9	1	8	8869.3125	-0.0075
14	2	12	14	1	13	8972.8125	-0.0355
8	2	6	8	1	7	9043.9375	0.0210
7	2	5	7	1	6	9249.6875	-0.0120
5	1	5	4	0	4	9358.6875	0.0126
6	2	4	6	1	5	9470.6875	-0.0310
5	2	3	5	1	4	9691.5625	-0.0308
9	0	9	8	1	8	9752.9375	0.0271
4	2	2	4	1	3	9898.2500	-0.0091
3	2	1	3	1	2	10078.5625	0.0263
8	1	8	7	1	7	10193.0625	0.0151
6	1	6	5	0	5	10408.5625	0.0042
2	2	1	2	1	2	10529.4375	0.0006
3	2	2	3	1	3	10685.5000	0.0132
8	1	7	7	1	6	11009.6250	-0.0191
5	2	4	5	1	5	11156.6875	-0.0236
7	1	7	6	0	6	11429.8125	-0.0348
6	2	5	6	1	6	11473.1875	0.0432
7	2	6	7	1	7	11844.3125	0.0198
9	3	7	8	3	6	12009.8125	0.0148
9	3	6	8	3	5	12024.5000	0.0044
10	1	10	9	0	9	14416.1875	0.0182
4	2	3	3	1	2	15389.0000	-0.0080
12	1	11	11	1	10	16935.9375	-0.0179
12	1	12	11	0	11	16433.6875	-0.0080
14	0	14	13	1	13	17058.1250	-0.0307
6	3	3	6	2	4	17177.0000	-0.0056

Table 6.11 Observed frequencies ($\nu_{\text{Obs.}}$) of 77 rotational transitions of the *up down* conformer of *p*-vinylanisole. $\nu_{\text{Obs.}} - \nu_{\text{Calc.}}$ values as obtained after a fit with the program *SPFIT/SPCAT*.

<i>J</i>	<i>K_a</i>	<i>K_c</i>	<i>J</i>	<i>K_a</i>	<i>K_c</i>	$\nu_{\text{Obs.}}$	$\nu_{\text{Obs.}} - \nu_{\text{Calc.}}$
upper level			lower level			MHz	<i>SPFIT/SPCAT</i> MHz
7	1	6	6	1	5	9447.5625	0.0267
8	1	8	7	1	7	10080.3750	0.0033
8	0	8	7	0	7	10341.6875	-0.0369
8	1	7	7	1	6	10788.7500	-0.0262
6	1	5	5	1	4	8103.1875	-0.0167
7	0	7	6	0	6	9073.6875	-0.0189
7	2	6	6	2	5	9144.9375	0.0033
6	1	6	5	0	5	10894.1875	0.0105
8	2	6	7	2	5	10569.3125	0.0186
9	1	9	8	1	8	11332.1875	0.0109
4	2	2	4	1	3	11430.2500	-0.0110
3	2	2	3	1	3	12118.1875	-0.0176
9	1	8	8	1	7	12126.3125	-0.0076
5	2	4	5	1	5	12523.8125	0.0116
10	1	10	9	1	9	12581.5000	0.0208
6	2	5	6	1	6	12795.7500	-0.0331
8	1	8	7	0	7	12930.6875	-0.0160
10	2	9	9	2	8	13042.9375	0.0040
10	1	9	9	1	8	13459.5000	0.0008
11	1	11	10	1	10	13828.1875	-0.0211
9	1	9	8	0	8	13921.1875	0.0318
7	2	6	7	1	7	13114.5625	0.0320
10	3	7	9	3	6	13121.1875	0.0095
11	0	11	10	0	10	14086.9375	-0.0127
2	2	0	1	1	1	14512.3125	-0.0241
11	1	10	10	1	9	14787.5625	-0.0157
11	2	10	11	1	11	14864.9375	-0.0332
10	1	10	9	0	9	14902.6875	-0.0771
13	0	13	12	1	12	14989.8125	0.0109
12	1	12	11	1	11	15072.3750	0.0309
12	0	12	11	0	11	15317.4375	0.0796
12	2	11	12	1	12	15422.3125	0.0137
12	2	11	11	2	10	15629.6875	0.0153
3	2	2	2	1	1	15640.8750	0.0522
12	3	9	11	3	8	15770.4375	0.0009

Table 6.11 cont.

11	1	11	10	0	10	15882.8125	-0.0459
3	2	1	2	1	2	15915.5000	0.0013
12	2	10	11	2	9	16008.5000	0.0301
12	1	11	11	1	10	16109.7500	-0.0065
13	0	13	12	0	12	16540.6875	-0.0084
14	2	13	14	1	14	16679.0625	0.0379
4	2	3	3	1	2	16815.1250	0.0078
12	1	12	11	0	11	16868.2500	-0.0022
4	2	2	3	1	3	17371.9375	-0.0199
14	1	14	13	1	13	17552.9375	-0.0494
5	2	4	4	1	3	17944.8125	-0.0092
4	1	4	3	0	3	8740.8125	0.0243
9	0	9	8	1	8	9010.8750	-0.0162
7	3	5	6	3	4	9168.1875	0.0188
7	3	4	6	3	3	9170.1875	0.0189
7	2	5	6	2	4	9227.8750	0.0274
13	1	12	13	0	13	9302.7500	-0.0425
13	2	11	13	1	12	9907.6875	0.0188
12	2	10	12	1	11	9951.1875	-0.0150
11	2	9	11	1	10	10052.5000	0.0109
9	2	7	9	1	8	10384.9375	0.0311
8	2	7	7	2	6	10446.3125	-0.0290
8	3	6	7	3	5	10480.8125	-0.0207
8	3	5	7	3	4	10484.8125	-0.0133
10	0	10	9	1	9	10526.8125	-0.0169
8	2	6	8	1	7	10592.6875	0.0419
7	2	5	7	1	6	10812.1250	-0.0028
6	2	4	6	1	5	11031.8125	-0.0035
5	2	3	5	1	4	11241.0000	-0.0259
3	2	1	3	1	2	11591.4375	-0.0060
2	2	0	2	1	1	11718.0625	0.0121
9	2	8	8	2	7	11745.7500	-0.0042
9	3	6	8	3	5	11801.6875	0.0182
9	2	7	8	2	6	11918.5625	-0.0184
7	1	7	6	0	6	11924.0000	-0.0382
2	2	1	2	1	2	11983.6875	-0.0086
4	2	3	4	1	4	12298.1250	0.0261
10	0	10	9	0	9	12848.1250	0.0102
10	2	8	9	2	7	13275.5000	0.0302

Table 6.11 cont.

8	2	7	8	1	8	13480.5000	-0.0003
12	0	12	11	1	11	13521.5000	0.0502
10	2	9	10	1	10	14355.5000	-0.0321

Table 6.12 Observed frequencies ($\nu_{\text{Obs.}}$) of 82 rotational transitions of the *up up* conformer of *m*-vinylanisole. $\nu_{\text{Obs.}} - \nu_{\text{Calc.}}$ values as obtained after a fit with the program *SPFIT/SPCAT*.

<i>J</i>	<i>K_a</i>	<i>K_c</i>	<i>J</i>	<i>K_a</i>	<i>K_c</i>	$\nu_{\text{Obs.}}$	$\nu_{\text{Obs.}} - \nu_{\text{Calc.}}$
upper level			lower level			MHz	<i>SPFIT/SPCAT</i> MHz
7	1	7	6	0	6	10464.8125	-0.0201
8	0	8	7	1	7	11839.6875	-0.0006
9	1	9	8	0	8	13240.0000	-0.0058
10	0	10	9	1	9	14631.6875	-0.0305
11	1	11	10	0	10	16026.5000	0.0063
12	0	12	11	1	11	17420.3750	0.0368
7	0	7	6	1	6	10437.3125	-0.0054
8	1	8	7	0	7	11849.4375	0.0120
9	0	9	8	1	8	13236.6875	0.0212
10	1	10	9	0	9	14632.8125	-0.0238
11	0	11	10	1	10	16026.1250	-0.0011
6	2	4	5	3	3	8273.6250	0.0104
7	1	6	7	0	7	8494.9375	-0.0134
8	3	6	8	2	7	8543.1250	-0.0251
7	5	2	7	4	3	8611.8125	0.0050
7	2	6	7	1	7	8702.0625	-0.0189
6	5	1	6	4	2	8908.4375	0.0293
7	5	3	7	4	4	8973.5000	0.0299
8	5	4	8	4	5	8989.0625	0.0158
6	0	6	5	1	5	9020.8750	0.0122
5	5	0	5	4	1	9056.1250	0.0014
4	2	3	3	1	2	9056.6875	0.0091
5	5	1	5	4	2	9080.1875	-0.0125
6	1	6	5	0	5	9095.3125	0.0093
9	5	5	9	4	6	9128.8125	0.0123
10	5	6	10	4	7	9452.3125	0.0053
3	2	1	2	1	2	9508.8750	-0.0227
6	1	5	5	2	4	9770.9375	0.0086
5	2	4	4	1	3	10104.7500	0.0144

Table 6.12 cont.

3	3	1	2	2	0	10461.0000	0.0029
9	6	3	9	5	4	10549.8750	-0.0184
3	3	0	2	2	1	10586.0000	0.0096
10	6	5	10	5	6	10761.7500	-0.0146
11	6	6	11	5	7	10781.6250	0.0033
11	4	8	11	3	9	10773.7500	-0.0232
10	2	8	10	1	9	10820.5000	0.0011
9	6	4	9	5	5	10831.0000	0.0209
7	2	5	6	3	4	10847.1250	-0.0027
8	6	3	8	5	4	10933.1875	0.0210
7	6	1	7	5	2	11008.1875	-0.0020
7	6	2	7	5	3	11030.6875	-0.0207
10	3	8	10	2	9	11062.6875	-0.0031
6	2	5	5	1	4	11111.8750	-0.0269
9	2	8	9	1	9	11410.6125	-0.0097
7	1	6	6	2	5	11517.5000	-0.0335
4	3	2	3	2	1	12028.8750	0.0171
7	2	6	6	1	5	12194.2500	0.0130
11	2	9	11	1	10	12312.6250	-0.0092
11	3	9	11	2	10	12419.2500	0.0373
13	7	7	13	6	8	12475.1875	-0.0175
11	7	4	11	6	5	12481.2500	0.0032
4	2	2	3	1	3	12619.4375	0.0317
4	3	1	3	2	2	12641.9375	-0.0199
10	7	3	10	6	4	12767.7500	0.0222
10	1	9	10	0	10	12775.5000	-0.0015
10	2	9	10	1	10	12789.0000	-0.0028
9	7	2	9	6	3	12946.3125	-0.0052
9	7	3	9	6	4	12964.9375	0.0130
8	1	7	7	2	6	13092.5000	0.0162
5	3	3	4	2	2	13331.4375	-0.0031
8	2	7	7	1	6	13397.6875	-0.0238
11	1	10	11	0	11	14166.1250	0.0181
11	2	10	11	1	11	14171.1250	0.0383
4	4	1	3	3	0	14360.4375	-0.0106
6	3	4	5	2	3	14379.9375	-0.0045
4	4	0	3	3	1	14382.2500	0.0115
9	2	8	8	1	7	14695.7500	-0.0134
5	3	2	4	2	3	15051.3125	0.0174

Table 6.12 cont.

9	2	7	8	3	6	15274.3125	0.0221
12	1	11	12	0	12	15552.1250	0.0213
12	2	11	12	1	12	15553.8750	-0.0154
10	1	9	9	2	8	15996.5625	-0.0223
8	3	6	7	2	5	16025.6250	-0.0129
10	2	9	9	1	8	16046.5625	0.0118
5	4	2	4	3	1	16100.8750	-0.0163
5	4	1	4	3	2	16252.0625	-0.0142
5	2	3	4	1	4	16286.3750	-0.0205
9	3	7	8	2	6	16865.0625	-0.0298
10	2	8	9	3	7	17059.8750	-0.0002
6	4	3	5	3	2	17671.1250	-0.0223
10	3	8	9	2	7	17860.5000	-0.0188
6	3	3	5	2	4	17988.3125	0.0315

Table 6.13 Observed frequencies ($\nu_{\text{Obs.}}$) of 96 rotational transitions of the *up down* conformer of *m*-vinylanisole. $\nu_{\text{Obs.}} - \nu_{\text{Calc.}}$ values as obtained after a fit with the program *SPFIT/SPCAT*.

<i>J</i>	<i>K_a</i>	<i>K_c</i>	<i>J</i>	<i>K_a</i>	<i>K_c</i>	$\nu_{\text{Obs.}}$	$\nu_{\text{Obs.}} - \nu_{\text{Calc.}}$
upper level			lower level			MHz	<i>SPFIT/SPCAT</i> MHz
6	1	5	5	1	4	9732.9375	0.0001
7	1	6	6	1	5	11246.5625	0.0108
8	1	7	7	1	6	12701.7500	0.0169
9	1	8	8	1	7	14094.2500	-0.0197
10	1	9	9	1	8	15430.9375	-0.0134
11	1	10	10	1	9	16729.2500	-0.0079
7	0	7	6	0	6	10002.0625	0.0205
6	0	6	5	0	5	8693.8750	-0.0186
8	0	8	7	0	7	11303.0625	-0.0275
9	0	9	8	0	8	12606.3750	0.0163
10	0	10	9	0	9	13914.7500	0.0038
11	0	11	10	0	10	15228.0000	0.0097
12	0	12	11	0	11	16544.8750	-0.0099
13	0	13	12	0	12	17864.2500	0.0064
6	0	6	5	1	5	8006.1875	0.0177
5	2	3	4	2	2	8033.4375	0.0033
5	1	5	4	0	4	8049.1875	-0.0274
6	1	6	5	1	5	8471.1250	0.0009

Table 6.13 cont.

6	1	6	5	0	5	9158.8750	0.0271
6	2	5	5	2	4	9174.3750	0.0046
6	4	3	5	4	2	9331.2500	-0.0233
6	4	2	5	4	1	9333.1875	-0.0036
6	3	4	5	3	3	9344.8125	0.0219
6	3	3	5	3	2	9406.1875	-0.0023
6	2	4	5	2	3	9742.4375	0.0245
7	1	7	6	1	6	9836.0625	-0.0021
8	1	7	7	2	6	9953.3750	-0.0268
7	2	6	6	2	5	10654.4375	0.0032
7	6	2	6	6	1	10864.0625	-0.0095
7	4	4	6	4	3	10904.9375	-0.0789
7	3	5	6	3	4	10911.1250	0.0175
7	4	3	6	4	2	10911.3750	0.0324
4	2	3	3	1	2	10968.2500	0.0154
8	0	8	7	1	7	11004.1250	0.0119
7	3	4	6	3	3	11044.2500	-0.0145
8	1	8	7	1	7	11189.0000	-0.0067
7	2	5	6	2	4	11453.8750	-0.0117
8	1	8	7	0	7	11488.0000	0.0164
5	2	4	4	1	3	12070.3125	-0.0076
8	2	7	7	2	6	12113.7500	0.0088
8	7	1	7	7	0	12414.3125	0.0130
9	0	9	8	1	8	12421.4375	-0.0276
8	6	3	7	6	2	12427.5625	-0.0010
7	4	3	7	3	4	12448.3125	0.0250
8	5	4	7	5	3	12449.8750	-0.0113
8	5	3	7	5	2	12450.3750	-0.0094
8	3	6	7	3	5	12471.8750	-0.0234
8	4	5	7	4	4	12485.4375	-0.0039
8	4	4	7	4	3	12502.5625	0.0056
9	1	9	8	1	8	12532.4375	-0.0151
4	2	2	3	1	3	12580.0625	0.0101
6	4	2	6	3	3	12581.1875	-0.0219
9	1	9	8	0	8	12717.3750	0.0288
8	3	5	7	3	4	12723.0000	0.0251
6	2	5	5	1	4	13073.3750	-0.0111
8	2	6	7	2	5	13145.3125	-0.0018
9	2	8	8	2	7	13551.3125	0.0220

Table 6.13 cont.

3	3	0	2	2	1	13739.0625	0.0087
10	1	10	9	1	9	13868.8750	0.0012
9	7	2	8	7	1	13976.7500	-0.0039
10	1	10	9	0	9	13979.8750	0.0137
7	2	6	6	1	5	13994.8750	-0.0080
9	3	7	8	3	6	14022.2500	-0.0214
9	5	4	8	5	3	14028.8125	0.0013
9	4	6	8	4	5	14071.5000	-0.0194
9	3	6	8	3	5	14443.6875	0.0064
9	2	7	8	2	6	14800.5625	0.0066
10	2	9	9	2	8	14967.1875	0.0002
11	0	11	10	1	10	15162.8750	-0.0002
11	1	11	10	1	10	15200.3750	-0.0216
4	3	2	3	2	1	15219.7500	-0.0134
11	1	11	10	0	10	15265.5000	-0.0177
4	3	1	3	2	2	15326.6250	-0.0135
10	7	4	9	7	3	15543.0000	0.0064
10	3	8	9	3	7	15557.5625	0.0233
10	5	6	9	5	5	15611.5625	-0.0013
10	5	5	9	5	4	15616.0000	0.0097
10	4	7	9	4	6	15611.1250	0.0187
9	2	8	8	1	7	15711.6250	-0.0048
10	4	6	9	4	5	15744.9375	-0.0056
10	3	7	9	3	6	16196.3750	-0.0149
11	2	10	10	2	9	16362.6875	0.0079
10	2	8	9	2	7	16408.1875	0.0060
12	1	12	11	1	11	16528.6875	0.0134
12	1	12	11	0	11	16566.1875	-0.0080
11	3	9	10	3	8	17073.6875	0.0146
11	6	6	10	6	5	17148.1250	-0.0147
11	6	5	10	6	4	17148.5625	0.0319
11	5	6	10	5	5	17214.0000	-0.0101
11	4	8	10	4	7	17250.9375	0.0249
11	4	7	10	4	6	17410.3125	-0.0206
12	2	11	11	2	10	17740.0000	-0.0013
13	0	13	12	1	12	17842.9375	0.0046
13	1	13	12	1	12	17854.8750	-0.0184
11	2	9	10	2	8	17958.5625	0.0345
11	3	8	10	3	7	17959.8125	-0.0126

Table 6.14 Observed frequencies ($\nu_{\text{Obs.}}$) of 72 rotational transitions of *o*-vinylanisole. $\nu_{\text{Obs.}} - \nu_{\text{Calc.}}$ values as obtained after a fit with the program *SPFIT/SPCAT*.

J	K_a	K_c	J	K_a	K_c	$\nu_{\text{Obs.}}$	$\nu_{\text{Obs.}} - \nu_{\text{Calc.}}$
upper level			lower level			MHz	<i>SPFIT/SPCAT</i> MHz
6	2	5	5	2	4	11251.8125	-0.0157
6	1	5	5	1	4	11262.1875	0.0054
7	1	7	6	1	6	11282.5000	-0.0071
7	2	5	7	2	6	8032.0625	-0.0025
7	3	5	7	1	6	8042.8125	0.0144
6	1	5	6	1	6	8086.9375	-0.0131
4	2	3	3	2	2	8134.5000	0.0169
5	1	5	4	1	4	8269.6250	0.0111
5	0	5	4	0	4	8270.8125	-0.0196
4	1	3	3	1	2	8361.2500	0.0331
4	3	2	3	3	1	9020.5000	0.0460
10	4	6	10	4	7	9352.3750	-0.0768
10	5	6	10	3	7	9384.0000	-0.0598
9	3	6	9	3	7	9454.6250	-0.0257
9	4	6	9	2	7	9462.8750	0.0091
8	3	6	8	1	7	9523.5625	-0.0245
7	1	6	7	1	7	9566.6875	-0.0308
5	2	4	4	2	3	9726.1250	-0.0267
4	2	2	3	2	1	9759.8125	-0.0061
6	1	6	5	1	5	9776.2500	0.0028
6	0	6	5	0	5	9776.4375	0.0419
5	1	4	4	1	3	9783.6875	-0.0148
4	3	1	3	3	0	9905.8750	0.0297
5	3	3	4	3	2	10955.5000	0.0007
9	2	7	9	2	8	11004.7500	-0.0536
9	3	7	9	1	8	11005.0000	-0.0453
8	1	7	8	1	8	11044.9375	-0.0491
5	2	3	4	2	2	11479.0625	-0.0063
5	4	2	4	4	1	11553.5000	-0.0122
5	4	1	4	4	0	12169.5625	-0.0010
10	2	8	10	2	9	12485.3125	-0.0830
5	3	2	4	3	1	12499.2500	0.0440
9	1	8	9	1	9	12522.6250	-0.0838
6	3	4	5	3	3	12661.1250	-0.0058
7	2	6	6	2	5	12760.6875	-0.0248

Table 6.14 cont.

7	1	6	6	1	5	12762.2500	-0.0248
8	0	8	7	0	7	12788.6875	-0.0624
6	2	4	5	2	3	12860.4375	-0.0181
4	3	1	3	1	2	13495.6875	0.0439
6	4	3	5	4	2	13678.1875	-0.0065
6	5	2	5	5	1	14001.0000	0.0076
7	3	5	6	3	4	14229.6875	-0.0014
8	2	7	7	2	6	14266.8125	0.0081
8	1	7	7	1	6	14267.0000	-0.0164
4	4	0	3	2	1	14269.6250	-0.0437
7	2	5	6	2	4	14277.2500	-0.0391
9	0	9	8	0	8	14295.0000	-0.0009
6	5	1	5	5	0	14364.5000	-0.0005
6	3	3	5	3	2	14541.6875	-0.0043
6	4	2	5	4	1	15040.6875	-0.0195
4	2	2	3	0	3	15080.8750	0.0151
7	4	4	6	4	3	15540.0625	-0.0174
4	4	1	3	2	2	15680.6875	0.0289
8	3	6	7	3	5	15747.7500	-0.0553
8	2	6	7	2	5	15756.6250	-0.0161
9	2	8	8	2	7	15772.6875	-0.0087
10	0	10	9	0	9	15801.2500	-0.0117
4	3	2	3	1	3	15851.5000	0.0085
7	3	4	6	3	3	16015.1875	-0.0528
7	5	3	6	5	2	16296.3750	-0.0284
7	6	2	6	6	1	16386.5000	-0.0109
7	6	1	6	6	0	16572.8125	0.0120
5	4	1	4	2	2	16679.3750	-0.0386
8	4	5	7	4	4	17191.6250	-0.0380
9	3	7	8	3	6	17254.1250	-0.0563
9	2	7	8	2	6	17255.5625	-0.0356
10	1	9	9	1	8	17278.6250	-0.0714
11	0	11	10	0	10	17307.5000	-0.0269
8	3	5	7	3	4	17345.4375	-0.0582
7	5	2	6	5	1	17375.0625	0.0230
7	4	3	6	4	2	17450.3750	0.0003
5	3	2	4	1	3	17633.6875	0.0548

APPENDIX

1. Standard Operating Procedure for CP-FTMW Spectrometer

- a. Turn on digitizer, wait for green light
- b. Turn on CPU
- c. Turn on power supply for pre- and post-detection electronics (need time to warm up ~30-45 minutes)
- d. Turn on AWG
- e. Turn on BNC boxes and pulsed valve driver and synthesizer
- f. Turn on TWTA (warm up is 3 minutes)
- g. Open MatLab
- h. Go to command prompt
 - i. cd..
 - ii. cd..
 - iii. cd Guzik
 - iv. press tab key until "GSA Toolkit..."
 - v. type "gsa_avg.exe @gsa_avg4.conf 'outputfile.csv'"
- i. Check gsa_avg4.conf file to make sure number of averages, number of FIDs and other parameters are correct
- j. Turn on pulsed valve and press run on AWG CPU screen
- k. Press Enter on CPU command prompt to start recording data
- l. Take output csv file and transfer to a folder in MatLab with programs loaded into it and FFT the time domain signal

2. SOP for shutting down CPFTMW spectrometer

- a. Press run on AWG screen to stop AWG and pulsed valve
- b. Turn off pulsed valve driver and BNC boxes and pre- and post-electronics
- c. Put TWTA in standby and then flick the switch down to turn off
- d. Turn off CPU and then digitizer

3. SOP for maximizing signal in CPFTMW AND VUVTOFMS

- a. Once instrument is ready for operation, maximize flow of pulsed valve by turning the faceplate and watching the flowmeter

- b. Adjust the number of averages in the gsa_avg4.conf file to 1000 or less to take quick spectra
- c. To improve signal, adjust the position of the pulsed valve to both edges and record spectra
- d. If signal improves at the front end, back end or maximum flow, adjust timing on channel A of BNC box (ex: 0.049270→0.049270) in both directions
- e. Increase temperature
- f. For larger molecules, try reducing the backing pressure and the pulse valve opening time as well
- g. The same steps apply for pyrolysis as well, however, the time of pulsed valve opening is maximized at 0.048570 with Ar. The pulsed valve position can be adjusted, but be careful as moving the valve too much will cause the thermocouple to move and hence an improper temperature reading.
- h. For VUVTOFMS, start with a simple molecule as 2-methoxyfuran which has a massive vapor pressure. The 1:10 ratio of Xe:Ar is maximized. Make sure before testing that the dry ice is in the vessel and has had about 10 minutes to stir the gas mixture. The timing of the laser firing as well as the position of the 355nm should be the first adjustments. Watch the scope for signal and refresh each time adjustments are made, usually 500 acquisitions are recorded.

4. Fitting spectra with SPFIT/SPCAT

- a. After recording the broadband spectrum, plot the predictions using SPCAT. The files needed are **.par**, **.var** and **.int**. Take the rotational constants, dipole moments, distortion constants and nuclear hyperfine coupling constants and place the dipole moments in the **.int** file and the other constants in the **.par** and **.var** files. You only need to make the **.par** file and save the **.var** file as the same as they both need to mirror each other. Attached .par and .int files are below. The 6 in the .par file is the number of constants you are fitting and the 18 corresponds to the number of lines. Put 1000 to start with predictions, but needs to be adjusted to the actual number of lines you are fitting when the fitting process has begun. The dipole moments are a,b and c in that order and the 0.9 represents the rotational temperature.

C:\Users\Sean\Documents\2-hexanone\2-hexanone_1\rigid_rotor_final\2H_6.par - Notepad++

File Edit Search View Encoding Language Settings Tools Macro Run Plugins Window ?

2H_6.par x 2H_6.int x

```

1 2-hexanone 11: 0: 7.75 4/25/2019
2      6 18 17 0 .1500E-37 .1000E+11 .1000E+01 1.0000000000
3 s 1 1 0 80 0
4      10000. .752685250598042E+04 .39860521E+37
5      20000. .104083690028926E+04 .33622657E+37
6      30000. .941326542711261E+03 .10945818E+37
7      200. -.291117845125913E-04 .10000000E+34
8      1100. -.687027775444056E-04 .10000000E+34
9      2000. -.105345695824647E-01 .10000000E+34
10

```

C:\Users\Sean\Documents\2-hexanone\2-hexanone_1\rigid_rotor_final\2H_6.int

File Edit Search View Encoding Language Settings Tools Macro ?

2H_6.par x 2H_6.int x

```

1 2-hexanone
2 0011 710xx 240.3191, 0, 25, -8, -8, 300, 0.9
3 001 0.247
4 002 2.813
5 003 0.000
6

```

- b. Once the predicted structures are placed in the par, var and int files, run SPCAT. Open SPCAT, and type, in this case, 2H_6.par, then ENTER, 2H_6.var, then ENTER, and 2H_6.int then ENTER. The catalog file will appear and open in Notepad++. Go to edit and sort lines lexicographically ascending. The first row is the frequencies and the third row is the logarithmic intensities. Copy and paste these into excel. Take the logarithmic intensities, in column B, and use the function $(10^{(B)*100})$ to get the intensities. Plot in Igor.
- c. Once the predictions are plotted, you are now ready to start the fitting process. Start with the regions where the most intense experimental transitions are and look for intense predicted transitions usually no more than 100 MHz off. Use your catalog file to your aid. The quantum numbers and energies of the transitions can be of great use when assigning transitions. Once you find a transition you like, identify the quantum numbers, ex: $3_{03}-2_{02}$, and not how far off it is experimentally. Look further up and further down the branch using the catalog file for the $4_{04}-3_{03}$ and $2_{02}-$

1₀₁ transitions and see if they are off by the same frequency. Once you identified several transitions you are comfortable with, begin assignment.

- d. You need to build a **.lin** file. This is the linelist for your structure. First, put in the quantum numbers from the cat file, followed by the experimental frequencies and the error. Start with an error of 1.00. The lin file is attached below.

C:\Users\Sean\Documents\2-hexanone\2-hexanone_1\rigid_rotor_final\2H_6.lin - No

	2	1	2	1	0	1		
1	2	1	2	1	0	1	10350.8125	0.01
2	3	1	3	2	0	2	12184.1250	0.01
3	4	1	4	3	0	3	13969.5625	0.01
4	5	1	5	4	0	4	15709.4375	0.01
5	1	1	1	0	0	0	8468.1875	0.01
6	6	1	6	5	0	5	17406.8750	0.01
7	7	1	6	7	0	7	8038.5625	0.01
8	9	1	8	9	0	9	9053.7500	0.01

Make sure the number of lines you are fitting is the same number of lines in the par file. Once the lin file for the first attempt is done, save it and run SPFIT. Open SPFIT and type, in this case above, 2H_6.par then ENTER, 2H_6.var then ENTER, 2H_6.int then ENTER and then 2H_6.int then ENTER again once the command prompt asks if a file is missing.

- e. Open the **.fit** file in Notepad++. Look for the last iteration and note the differences in observed and theoretical frequencies. If the fit is in proper order, the differences will be 10s of MHz. If some differences are really large, check the quantum numbers again or remove this transition and fit it again. Look at the value of MICROWAVE RMS. This is the error of the fit and the value should be below 62.5 kHz. If the fit is correct, plot the predictions from this fit as described above and keep adding transitions until all possible transitions are assigned. Save progress as you go. If the fit is off, try a different branch or look for different patterns or remove just the errant lines. A **.fit** is pictured below.

	2H_6.par	2H_6.int	2H_6.lin	2H_6.fit						
61	3:	4	1	4	3	0	3	13969.56250	13969.57921	-.01671
62	4:	5	1	5	4	0	4	15709.43750	15709.42605	.01145
63	5:	1	1	1	0	0	0	8468.18750	8468.16826	.01924
64	6:	6	1	6	5	0	5	17406.87500	17406.86245	.01255
65	7:	7	1	6	7	0	7	8038.56250	8038.55595	.00655
66	8:	9	1	8	9	0	9	9053.75000	9053.74227	.00773
67	9:	10	1	9	10	0	10	9684.37500	9684.37981	-.00481
68	10:	11	1	10	11	0	11	10404.56250	10404.57001	-.00751
69	11:	9	0	9	8	1	8	12777.37500	12777.36126	.01374
70	12:	8	0	8	7	1	7	10509.06250	10509.05438	.00812
71	13:	11	0	11	10	1	10	17339.34380	17339.33537	.00843
72	14:	10	0	10	9	1	9	15056.43750	15056.46457	-.02707
73	15:	7	0	7	6	1	6	8258.43750	8258.44039	-.00289
74	16:	5	2	3	6	1	6	8812.06250	8812.06464	-.00214
75	17:	4	2	3	5	1	4	8957.18750	8957.20515	-.01765
76	18:	4	2	2	5	1	5	10466.68750	10466.66769	.01981
77	NORMALIZED DIAGONAL:									
78	1	.10000E+01	2	.99941E+00	3	.50245E+00	4	.42890E+00	5	.27914E+00
79										
80										
81	NEW PARAMETER - EST. ERROR - CHANGE THIS ITER.									
82	1	10000.		7526.8525		.0073		.0000		
83	2	20000.		1040.83690		.00072		.00000		
84	3	30000.		941.32654		.00063		.00000		
85	4	200.		-.291117845E-04	.053262944E-04	.000005927E-04				
86	5	1100.		-.000069	.000151	.000000				
87	6	2000.		-.01053	.00138	.00000				
88	MICROWAVE AVG = .24456E-04 MHz, IR AVG = .00000									
89	MICROWAVE RMS = .13707E-01 MHz, IR RMS = .00000									

The maximum difference in this fit is 27 kHz and all transitions match well with the assignments. The standard deviation is 13.7 kHz.

- f. Use the SPFIT/SPCAT user guide for full explanation of all of the terms in the .par, .var and .int files.



Contents lists available at ScienceDirect

Journal of Molecular Spectroscopy

journal homepage: www.elsevier.com/locate/jms

Conformer-specific microwave spectroscopy of 3-phenylpropionitrile by strong field coherence breaking



Sean M. Fritz, A.O. Hernandez-Castillo, Chamara Abeysekera, Brian M. Hays, Timothy S. Zwier*

Department of Chemistry, Purdue University, 560 Oval Drive, West Lafayette, IN 47907, USA

ARTICLE INFO

Article history:

Received 8 March 2018
Accepted 23 March 2018
Available online 30 March 2018

Keywords:

3-Phenylpropionitrile
Rotational spectroscopy
Strong field coherence breaking
Conformational analysis

ABSTRACT

Strong field coherence breaking (SFCB) was used with a chirped-pulse Fourier Transform microwave spectrometer to obtain conformer-specific rotational spectra of 3-phenylpropionitrile in the 8–18 GHz region. Transitions belonging to *anti* and *gauche* conformers were identified and assigned and accurate experimental rotational constants were determined to provide insight to the molecular structure. Experimental rotational transitions provided relative abundances in the supersonic expansion. A modified line picking scheme was developed in the process to modulate more transitions and improve the overall efficiency of the SFCB multiple selective excitation technique.

© 2018 Elsevier Inc. All rights reserved.

1. Introduction

Nitriles are abundant in the atmosphere of Titan, a moon of Saturn which has an atmosphere postulated to be similar to that of prebiotic Earth [1–5]. As a result, Titan has been the subject of intense study by planetary scientists, and has benefitted from the Cassini mission and Huygens probe, which have provided unprecedented sensitivity and detail regarding the atmospheric composition as a function of altitude and latitude [6,7]. The haze surrounding Titan is made up of large complex organics, but the detailed chemical composition and pathways by which they are made are still under active exploration [8]. As the sophistication of photochemical models continues to increase, laboratory studies that push into larger, more complex organics are essential for constraining the models. Results from the Cassini mission have shown the presence of smaller nitriles, but the search for larger organics will require a foundation of molecular spectroscopy for their identification [9].

Recent models recognize the importance of both neutral and ion chemistry to the formation of complex organics [10]. Solar-driven photodissociation of stable molecules produces free radicals that subsequently react to form larger products. Among the free radicals of greatest importance are resonance-stabilized radicals, in which the unpaired electron spin density is delocalized over several resonance structures that stabilize the radical. This unusual stability causes them to react only slowly with the most stable molecules, so that their concentrations can build up relative to

their non-stabilized counterparts. Since the number of possible reactions grows exponentially with size of the reactants, it is important to restrict the laboratory focus to those reactions that are most likely to play a controlling role. In this sense, radical-radical recombination reactions are important, especially when they involve two resonance-stabilized radicals (RSR), since they are present in high abundance and react via a barrierless process to form even larger hydrocarbons [11]. Aromatics and nitriles are both prominent in the composition of Titan. 3-phenylpropionitrile (3-PPN) is the radical-radical recombination product of two prototypical RSRs, benzyl ($\text{C}_6\text{H}_5\text{-}\dot{\text{C}}\text{H}_2$) and cyanomethyl ($\dot{\text{C}}\text{H}_2\text{-C}\equiv\text{N}$) as shown in Fig. 1.

Benzyl radical is the first resonance-stabilized phenyl derivative, while cyanomethyl is the nitrile equivalent of the propargyl radical ($\dot{\text{C}}\text{H}_2\text{-C}\equiv\text{CH}$) that is a major pathway to benzene formation via self-recombination [12–14]. As such, 3-PPN is postulated to be a larger phenyl derivative of some importance in Titan's atmosphere.

Resonant 2-photon ionization (R2PI) studies of 3-PPN have identified *anti* and *gauche* conformers by assigning $\text{S}_0\text{-S}_1$ origin bands based on rotational band contour measurements supported by *ab initio* calculations [15]. The present study complements this work by providing broadband microwave spectra of 3-PPN over the 8–18 GHz region. Transitions due to *anti* and *gauche* conformers are detected and assigned. In the process of carrying out this study, we have utilized the newly-developed method of Strong Field Coherence Breaking (SFCB) to selectively modulate the intensities of a set of transitions due to each of the conformers in a conformer-selective fashion, aiding the assignment [16]. Chirped-pulse FIMW is a powerful, widely used spectroscopic technique

* Corresponding author.

E-mail address: zwier@purdue.edu (T.S. Zwier).

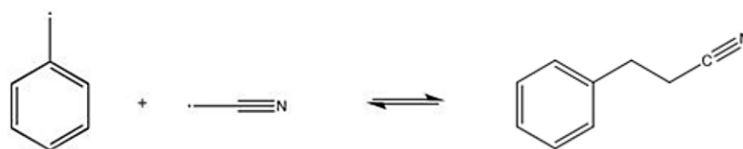


Fig. 1. Schematic diagram of the reaction of benzyl radical with cyanomethyl radical to form 3-phenylpropionitrile.

for determining molecular structure because the frequency patterns provide a direct measure of the geometry through the rotational constants and projections of the permanent dipole moments along the inertial axes [17]. In addition, the presence of a ^{14}N nucleus with its $I = 1$ nuclear spin produces nuclear hyperfine splittings that are themselves conformer-specific, providing additional evidence for the conformational assignments as well as insight to the structure. In this work, rotational constants, dipole moments, nuclear quadrupole coupling constants, centrifugal distortion constants and relative populations are determined for the two conformers of 3-phenylpropionitrile. In the process of carrying out SFCB measurements, we have refined the method from that described in the original publication [16] to increase the efficiency, streamline the process, and refine the peak selection method in ways that will make it easier to implement.

2. Experimental

2.1. Broadband spectrum

A commercial sample of 3-PPN was obtained from Sigma-Aldrich with a stated purity of 99% and used without further purification. The sample was heated to 125 °C, entrained in He buffer gas at a pressure of 2.3 bar, and expanded through the 1 mm dia. orifice of a pulsed valve (Parker General, Series 9) operating at 10 Hz. The broadband rotational spectrum of 3-phenylpropionitrile was recorded in the 8–18 GHz region using a CP-FTMW spectrometer, which has been described in detail elsewhere [16]. A 10 GS/s arbitrary waveform generator (AWG; Tektronix AWG7101) allows the generation of an array of broadband chirps and single frequency pulses that are amplified by a 200 W travelling wave tube amplifier (TWTA; Amplifier Research 200T8G18A) and introduced into the vacuum chamber via a broadcasting horn. The output of the TWTA intercepts the molecular supersonic expansion and polarizes the sample, resulting in a free induction decay (FID), which is collected by the second broadcasting horn. The molecular emission is amplified with a low noise amplifier (Miteq AMF-6F-06001800-15-10P), down-converted by mixing with a phase-locked dielectric resonator oscillator (PLDRO, Microwave Dynamics PLO-2000-18.90) at 18.9 GHz and phase coherently averaged and digitized over a 16 μs time window by a 13 GHz, 40 GS/s real-time digitizer (Guzik ADC6131). The experimental timing scheme was tuned to collect 30 molecular FIDs per gas pulse, with an experimental resolution for a 16 μs FID collection time of 62.5 kHz. The time-domain signal was filtered with a Kaiser-Bessel function and Fast Fourier Transformed using a custom MATLAB routine to obtain the final frequency domain spectrum.

Based on previous studies of 3-phenylpropionitrile [15], *anti* and *gauche* conformations were anticipated and optimized in MacroModel using an Amber[®] force field. Density Functional Theory (DFT) geometry optimizations based on these starting structures were carried out using the Gaussian 09 suite [18] at the B3LYP/def2-TZVP, B2PLYP-D3BJ/aug-cc-pVTZ, and MP2/-6-311++G(d,p) levels of theory to obtain rotational constants, dipole moments and nuclear quadrupole coupling constants. The

predictions of DFT B3LYP/def2-TZVP calculations, including Grimme's dispersion correction [19], were used for the initial rigid rotor fitting because these calculations are less expensive and were thought to provide a good preliminary estimate of the relative energies based on its use in recent studies by our group of the alkyl benzenes [20]. The barrier height due to bond rotation for both conformers was determined at the B3LYP/6-311+G (d,p) level of theory. Spectroscopic constants are reported in Table 1.

2.2. Conformer-specific spectra

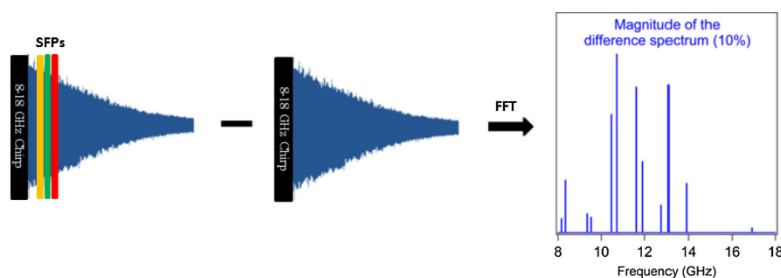
Conformer-specific microwave spectra of 3-PPN were recorded using the SFCB technique introduced recently by our group [16] and illustrated in Fig. 2. Given the complexity of the spectrum, there was a need to modify the line picking scheme described previously to select the transitions for multiple selective excitations (MSE). The new line picking scheme involves stepwise repetition of SFCB while incorporating an additional single frequency pulse in each successive spectrum. Initially, a broadband chirp with a single frequency pulse targeting the most intense line in the linear fast passage (LFP) spectrum is probed. A difference spectrum is acquired by subtracting the broadband spectrum from the broadband spectrum with the single frequency pulse present, and plotting its magnitude, while maintaining the same collection conditions for each spectral acquisition.

During the peak selection process, threshold levels were set for peak intensity modulation by the single-frequency pulse(s) (SFP) using 70% threshold percentages with each new choice of single-frequency coherence-breaking pulse. For instance, for 3-PPN, identification of transitions modulated by more than 70% by the first SFP rigorously insures no false positives in the difference spectrum. Successive difference spectra were plotted based on percent thresholds of 70% for second and third single frequency pulses. After enough single frequency pulses were selected to modulate the intensity of a sufficient number of lines, a final difference spectrum was obtained to produce a set of conformer-specific transitions modulated by more than 10%.

With increased experience, the selection criteria for the resonant frequencies has also been refined, taking the following considerations into account. First, it is important to choose a resonant transition without another transition within ~ 10 MHz so that the wings on the SFP of 150 ns duration do not overlap significantly with other transitions that would reduce selectivity. This becomes increasingly challenging as the LFP spectrum becomes more dense. Second, the frequencies of the single-frequency pulses are typically chosen to avoid the edges of our frequency range, yet spread over the spectral range, so that transitions directly connected to those chosen will be in the frequency range of the broadband pulse. Third, each additional single frequency pulse is chosen to be resonant with a transition that is weak in the SFCB spectrum but is strong under LFP conditions. Such an intensity change typically means that the transition has a large transition dipole moment and will therefore be good at modulating other lines. By not choosing the most intense transitions in the difference spectrum, transitions directly connected to the transition(s) used in

Table 1Molecular structure constants for *anti* and *gauche* conformers determined experimentally and calculate at the DFT B2PLYP-D3BJ/aug-cc-pVTZ level of theory.

	Anti-PPN		Gauche-PPN	
	Experimental	Calculated	Experimental	Calculated
A (MHz)	4432.82(79)	4458.9166	2555.0155(44)	2568.8630
B (MHz)	607.9271(13)	609.5252	911.9367(11)	914.6686
C (MHz)	561.0895(14)	563.0799	763.9775(13)	765.1122
μ_a (D)	...	-4.219467	...	-1.2955
μ_b (D)	...	-0.000091	...	-3.5074
μ_c (D)	...	-0.616711	...	0.54320
χ_{aa}	...	-4.111	1.64(10)	1.7313
$\chi_{bb\ cc}$...	0.203	-5.792(12)	-6.059
d_K (MHz)	0.00174(32)	...
D_J (MHz)	0.0003021(81)	...
D_K (MHz)	0.00339(34)	...
D_{JK} (MHz)	0.00044(18)	...	-0.000441(85)	...
E_{rel} (kJ/mol)	...	0	...	0.21
T (K)	1.48(0.10)	...	1.17(0.24)	...
Population	54(6)	...	46(6)	...
N	45	...	67	...
σ (MHz)	0.054	...	0.0258	...

**Fig. 2.** Schematic diagram for the modified strong field coherence breaking scheme.

preceding trials are avoided. When these criteria are used, additional transitions have their intensities modulated strongly by the new SFP that are largely complementary to those modulated by the first SFP. The same criterion was followed to accumulate more pulses in each attempt, as outlined in Fig. 2.

3. Results

3.1. Spectral assignment

A requirement for the SFCB method is the ability to operate in the rapid adiabatic passage (RAP) regime with strong coupling between the molecular dipole moment and the electric field. If the dipole moment of the molecule is large enough, adjusting the output of the electric field makes it possible to access both the strong and the weak coupling regimes [21]. Forward (8 GHz \rightarrow 18 GHz) and backward (18 GHz \rightarrow 8 GHz) sweeps were recorded to demonstrate the ability of 3-PPN to enter the RAP regime with our current experimental set up. Fig. 3 compares the broadband spectra of 3-PPN in the 8–18 GHz frequency range sweeping in both directions at different TWTA gains. At 10% TWT amplification, the line intensities are not influenced by the sweep direction, as anticipated if the sweep conditions are in the linear fast passage (LFP) regime. In contrast, when the electric field strength is tuned to full power (TWTA: 100%), the line intensities change significantly with changing the chirp direction, demonstrating the ability to operate in the RAP regime for both conformers.

3.1.1. Anti-3-phenylpropionitrile

The modified line picking scheme was used to determine the single frequency pulses for the SFCB/MSE method. Under our experimental conditions, the strongest transition in the LFP spectrum was at 10.71906 GHz and the next two selected frequencies were at 13.09231 GHz and 12.76675 GHz. Following fitting, these transitions were subsequently assigned to $9_{1,8}-8_{1,7}$, $11_{1,10}-10_{1,9}$, and $11_{0,11}-10_{0,10}$ transitions of *anti*-3-PPN, respectively. Each broadband sweep was 1 μ s in duration and each single frequency pulse lasted for 150 ns. The gap between the broadband chirp and the first single frequency pulse was 50 ns, whereas gaps between single frequency pulses were 5 ns to avoid beats.

Anti-3-PPN is a near prolate symmetric top that has the majority of its dipole along the a-axis ($\mu_a = -4.265$ D), a small projection along the c-axis ($\mu_c = -0.624$ D), and no component along the b-axis. Fig. 4(a) presents the final difference spectrum for *anti*-3-PPN consisting of 11 conformer specific *a*-type transitions with a modulation of more than 10%. The modulated lines are plotted against B3LYP/def 2-TZVP predictions of both conformers, and by analyzing the spacing and pattern of the LFP spectrum, the modulated transitions best match *anti*-3-PPN. The conformer-specific transitions were used to obtain a preliminary fit using Pickett's SPFIT and SPCAT programs [22]. With the same set of programs, a total of 45 transitions were assigned in the final rigid rotor fit with a standard deviation in the fit of 0.054 MHz. These fit transitions are plotted in blue against the 1.5 M average LFP experimental spectrum in Fig. 5(a). The experimental rotational constants from the fit are in closest agreement with the B2PLYP-

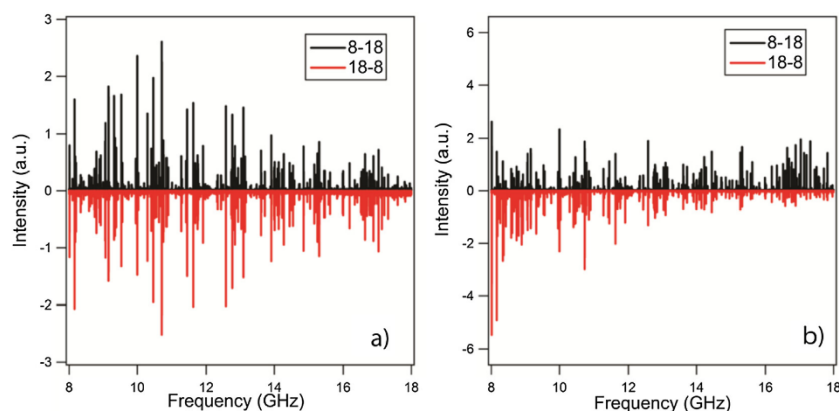


Fig. 3. ((a) and (b)): Broadband CP-FTMW spectra of 3-phenylpropionitrile over the 8–18 GHz region produced by sweeping in the forward direction (black) and in the reverse direction (red) while at (a) 10% TWTA and (b) 100% TWTA power (~200 W). (For interpretation of the references to colour in this figure legend, the reader is referred to the web version of this article.)

D3BJ/aug-cc-pVTZ predictions with a total error in the three rotational constants of 1.21%. The best-fit experimental parameters and the comparison with this level of theory are reported in Table 1. Due to the nuclear spin of the nitrogen nucleus ($I(^{14}\text{N}) = 1$), however, the hyperfine splitting were unresolvable at our resolution as demonstrated in Fig. 5(c). As a result, nuclear quadrupole coupling constants could not be determined for the *anti* conformer.

3.1.2. *Gauche*-3-phenylpropionitrile

For *gauche*-3-PPN, the method was repeated for the remaining unassigned transitions using the same microwave settings. The strongest unassigned line in the LFP spectrum was at 9.066 GHz and the next two selected frequencies were 16.9235 GHz and 12.09531 GHz. Following spectral fitting, these transitions are assigned as $5_{1,5}-4_{0,4}$, $6_{2,4}-5_{1,5}$, and $7_{2,5}-6_{2,4}$, respectively. *Gauche*-3-PPN is an asymmetric top with a large dipole component along

the b-axis ($\mu_b = -3.507$ D), a sizable component along the a-axis ($\mu_a = -1.386$ D) and a small contribution from the c-axis ($\mu_c = +0.520$ D), yielding a significant increase in the number of conformer specific transitions. Fig. 4(b) presents the magnitude of the final difference spectrum for *gauche*-3-PPN, identifying 43 conformer-specific a-, b- and c-type transitions whose intensities are modulated by more than 10% with respect to the original RAP spectrum. The modulated lines are plotted against B3LYP/def 2-TZVP predictions, with the transitions best matching the *gauche* conformer.

The nuclear hyperfine structure is well-resolved in *gauche*-3-PPN, as demonstrated in Fig. 5(b), and 32 transitions due to the hyperfine structure were assigned, resulting in a total of 67 lines accounted for in the final fit with a standard deviation of 25.8 kHz (Fig. 5(a)). Experimental nuclear quadrupole coupling constants, χ_{aa} and χ_{bb-cc} , centrifugal distortion constants and experimental rotational constants were determined and are reported in Table 1. The experimental rotational constants for this conformer

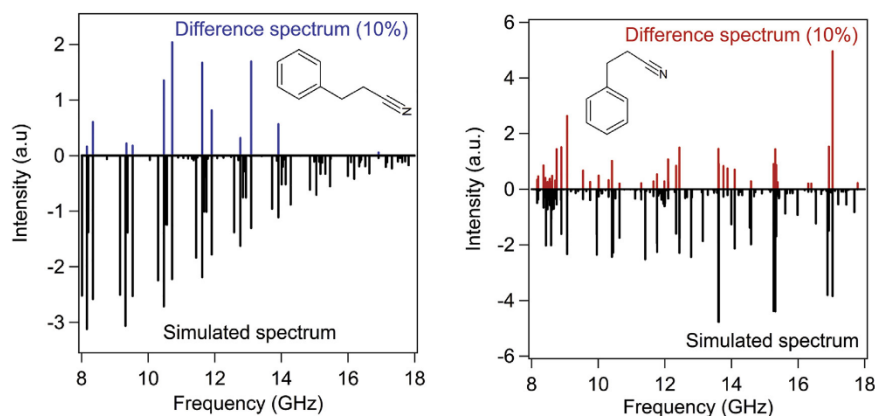


Fig. 4. ((a) and (b)): Conformer-specific spectra for (a) *anti* and (b) *gauche* conformers of 3-PPN using the modified line picking scheme. Black lines display simulated spectra. Transitions whose intensities are modulated by more than 10% are displayed in red and blue. (For interpretation of the references to colour in this figure legend, the reader is referred to the web version of this article.)

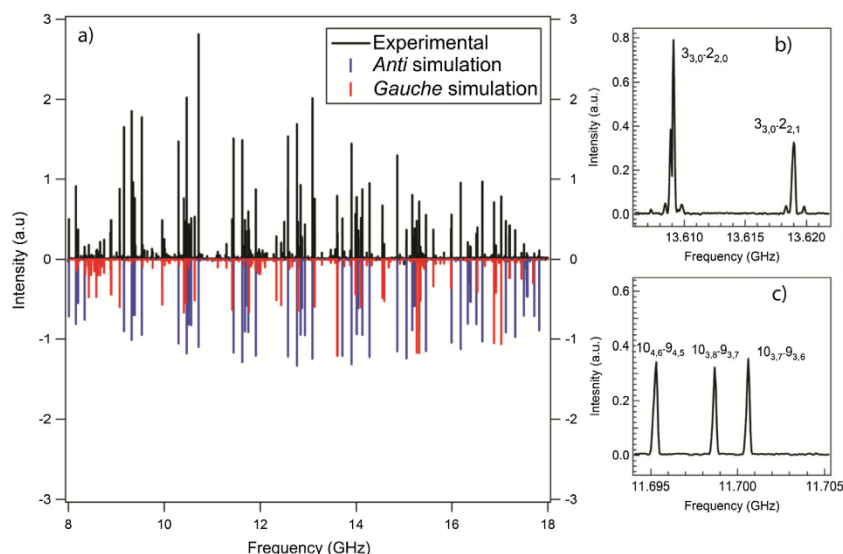


Fig. 5. (a) Comparison of the experimental broadband spectrum of 3-PPN under LFP conditions (black trace) with the final fit for both conformers. The red lines belong to the *gauche* conformer and the blue lines belong to the *anti* conformer. (b) Hyperfine structure present in the *gauche* conformer. (c) Demonstration of the absence of hyperfine structure in the *anti* conformer.

also best agree with the predictions from the B2PLYP-D3BJ/aug-cc-pVTZ level of theory with an error accounting for all rotational constants of 0.99%.

4. Discussion

We measured and assigned the rotational spectrum of *anti* and *gauche* conformers of 3-PPN in a supersonic expansion using the SFCB technique with a modified line picking scheme. The best fits from Table 1 include fitting intensities to rotational temperatures via a Boltzmann plot (Figs. S-1 and S-2). As expected, the two conformers had best-fit rotational temperatures that were approximately the same, with $T_{\text{rot}}(\text{gauche}) = 1.17 \pm 0.24$ K and $T_{\text{rot}}(\text{anti}) = 1.48 \pm 0.10$ K. Based on the experimental intensities, fractional abundances were extracted (Table 1) which showed them to be nearly equal ($54 \pm 6\%$ *anti*; $46 \pm 6\%$ *gauche*). Given that the zero-point corrected relative energies of the two conformers are very close ($\Delta E(\text{gauche-anti}) = 0.21$ kJ/mol = 17.5 cm $^{-1}$), and even exchange their energy ordering at some levels of theory, it is not particularly surprising that the two conformers have nearly equal population. However, the *gauche* conformer has twice the degeneracy of the *anti* conformer, due to the presence of *g_s* and *g_a* minima on the potential energy surface, so that a population ratio of 33% *anti*: 67% *gauche* is anticipated on that basis. A relatively low interconversion barrier would allow some conformational relaxation towards the global minimum conformer, which, if *anti*, would shift population consistent with this difference in expansion conditions. Calculations at the B3LYP/6-311+G (d,p) level were carried out to determine the interconversion barrier height by rotating the dihedral angle in ten degree steps. An isomerization barrier of 13.5 kJ/mol (1130 cm $^{-1}$) of energy is deduced. The relatively high energy barrier is consistent with significant population residing in both conformers, especially given the small energy difference between them, allowing only modest shifts in population with expansion conditions.

A set of molecular parameters (e.g., rotational constants, distortion constants, etc.) were fit from the experimental data and were compared with those obtained by quantum calculations. As mentioned in the experimental section, full geometry optimization was first carried out at the B3LYP/def2-TZVP level of theory. However, after the rotational spectrum was assigned, we noticed that at this level of theory, the calculated rotational constants differ up to 1.25% and 2.6% from the *anti* and *gauche* experimental rotational constants, respectively. In order to find a calculated structure that better matched the experimental observations, we explored other levels of theory, as shown in Table 2. From this exploration, it was clear that the rotational constants calculated at B2PLYP-D3BJ/aug-cc-pVTZ level of theory were closest to experiment, predicting rotational constants with errors of 1.20% and 0.99% for *anti* and *gauche* conformers, respectively. The rotational constants predicted at the MP2/aug-cc-pVTZ level of theory are in poorest agreement with experiment, particularly for the *gauche* conformer. As other recent studies have noted [23–25], MP2 calculations are subject to large intramolecular basis set superposition errors that are greatest when remote parts of the molecule are in dispersive contact with one another, as they are in the *gauche* conformer of 3-PPN. We have noticed this type of behavior before in the conformational study of methyl butyrate [25] where the addition of diffuse functions increases the error with respect to the experiment; therefore, the basis-set superposition error present in MP2 calculations may be the cause for the lack of accuracy in the predictions.

The technique of SFCB is valuable in identifying transitions belonging to one component in a mixture, allowing the user to extract rotational constants and other structural information for each conformer. The original scheme for SFCB [15] consisted of using single-frequency pulses (in the absence of the broadband chirp) to directly modulate a set of transitions; however, in 3-PPN, this scheme failed to modulate enough transitions to make a confident conformational assignment. Several adjustments were made to establish a new line picking scheme to speed up the line selection process and increase the number of modulated lines.

Table 2

Percent errors in rotational constants calculated at the B2PLYP-D3BJ/aug-cc-pVTZ, B3LYP/def-2TZVP and MP2/6-311++G (d,p) levels of theory.

	Anti-PPN			Gauche-PPN		
	% Error (A)	% Error (B)	% Error (C)	% Error (A)	% Error (B)	% Error (C)
B2PLYP-D3BJ/aug-cc-pVTZ	0.59	0.26	0.35	0.54	0.30	0.15
B3LYP/def-2TZVP	0.81	0.17	0.27	1.43	0.47	0.68
MP2/6-311++G (d,p)	1.75	0.17	0.25	4.25	3.88	4.43

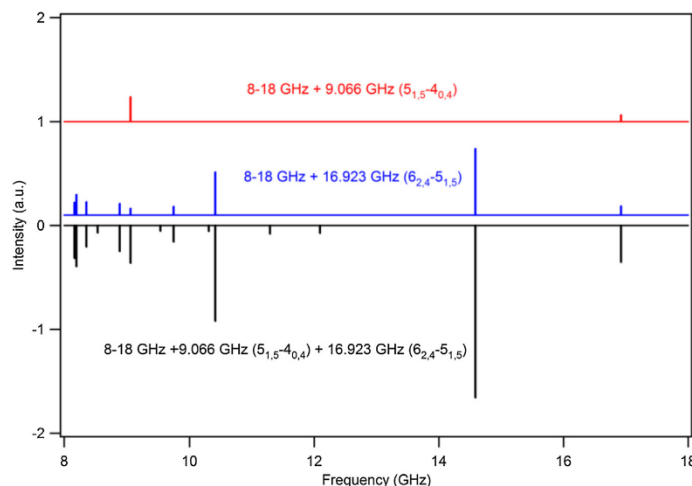


Fig. 6. Difference spectra demonstrating the new line picking scheme and its advantages for modulating the intensities of more transitions when multiple single-frequency coherence-breaking pulses (SFP) are applied. The red and blue spectra show the modulated transitions due to just one SFP applied after the broadband chirp, resonant with a microwave transition of a single conformer. The black spectrum shows the transitions modulated by applying both SFPs after the chirp. Five new lines appear in this difference spectrum. (For interpretation of the references to colour in this figure legend, the reader is referred to the web version of this article.)

The first major modification involves using the broadband chirp in conjunction with the trial single-frequency pulses. In doing so, a coherence between resonant rotational transitions is established in each attempt and subsequently broken by the single frequency pulses, thereby modulating the intensities of more transitions in the difference spectrum.

The second modification to the technique involves the sequential addition of each selected single frequency pulse after the broadband chirp to increase the number of modulated lines. The traces in Fig. 6 display the transitions whose intensities are modulated by more than 55% by the indicated single-frequency pulses. The top spectrum (red) shows just two transitions when the broadband chirp is followed by a SFP at 9.066 GHz ($5_{1,5}-4_{0,4}$), which is the strongest transition in the LFP spectrum for the *gauche* conformer. Since only one additional transition at 16.923 GHz was modulated by more than 55%, this frequency was then chosen as the frequency of the second SFP. The spectrum in blue shows the lines that were modulated when one SFP was set at 16.923 GHz ($6_{2,4}-5_{1,5}$). In this case, seven new transitions appear in the difference spectrum, with nine in total. The spectrum shown in black was recorded by using the improved line picking scheme by probing the broadband chirp followed by two SFPs at 9.066 GHz and 16.923 GHz. Compared to the two spectra above it, recorded with only one SFP, adding the second SFP sequentially after the first, five additional transitions appear in the difference spectrum. This demonstrates that the refined method provides an increase in the number of lines modulated and therefore produced more transitions to choose from when selecting the SFPs.

Lastly, we set a modulation threshold that is higher during the line-picking process (50–70%), so as to ensure fidelity in picking transitions only due to the conformer of interest. However, having done so, the final difference spectrum uses a lower modulation threshold (10%) for recording the final spectrum once three frequencies have been chosen. This increases the number of transitions in the difference spectrum still further. By restricting our choice of transitions to those whose intensities are modulated significantly, we increase the probability of transferring population to a larger number of transitions, and thus detecting more conformer-specific lines. Overall, these adjustments to the line picking scheme allowed for a set of MSE pulses that provided a confident assignment of both conformers.

The pathways to formation of larger, complex organics in Titan's atmosphere is still an area of intense investigation. Among them, we propose 3-PPN as a potential candidate due to its position as the product of a radical recombination of two resonance-stabilized radicals likely to be of importance in Titan's hydrocarbon and nitrile rich environment.

The largest molecule detected in the interstellar medium is benzonitrile in which nine *a*-type rotational transitions were identified utilizing information from databases and; laboratory data in the 7–29 GHz region [26]. As the size of the molecules detected in Titan's atmosphere or in the interstellar medium continues to increase, laboratory studies are needed to guide astronomical searches for their presence. A challenge of studying these larger molecules is spectral congestion, as multiple conformers may contribute to the spectrum. By providing a reliable set of rotational

constants from measurements in the 8–18 GHz region, the strongest rotational transitions at 70 K, the temperature of Titan's atmosphere [27], can be sought out for identification. At this temperature, the Boltzmann peaks for the *gauche* and *anti* conformers are at J levels 25 and 24, with transition frequencies near 40 GHz and 30 GHz, respectively. In the interstellar medium, where the temperatures in cold molecular clouds such as TMC-1 are 5–10 K [28,29], the Boltzmann peaks for *anti* and *gauche* conformers are at J levels 18 and 16 with frequencies near 21 GHz and 26 GHz, respectively. It is hoped that the present data can provide a set of unique transitions that can be used to identify 3-PPN in extraterrestrial environments.

5. Conclusion

Here, we demonstrate the application of strong field coherence breaking to determine the molecular structure of a molecule with potential astrochemical significance. In carrying out this study, a modified line picking scheme was developed in order to enhance and streamline the technique. Conformer-specific spectra were obtained, yielding 43 lines that belonged to the *gauche* conformer and 11 lines that belonged to the *anti* conformer. The conformer-specific transitions aid in fitting the congested broadband spectrum, which provides all of the rich information about the molecular structure including rotational constants, nuclear quadrupole coupling constants and distortion constants. A population analysis was carried out with about a 1:1 *anti* to *gauche* population ratio determined. It is hoped that the future searches for more complex organics will locate microwave transitions due to 3-PPN, guided by the data provided here.

Acknowledgments

The authors gratefully acknowledge support for this research from the NASA Planetary Atmospheres program (NASA NNX14AJ47G).

Appendix A. Supplementary material

Supplementary data associated with this article can be found, in the online version, at <https://doi.org/10.1016/j.jms.2018.03.011>.

References

- [1] A. Coustenis, *Astron. Geophys.* 48 (2007) 14–20.
- [2] N.A. Teanby, P.G.J. Irwin, R. de Kok, C.A. Nixon, A. Coustenis, B. Bezard, S.B. Calcutt, N.E. Bowles, F.M. Flasar, L. Fletcher, C. Howett, F.W. Taylor, *Icarus* 181 (2006) 243–255.
- [3] N.A. Teanby, P.G.J. Irwin, R. de Kok, S. Vinatier, B. Bezard, C.A. Nixon, F.M. Flasar, S.B. Calcutt, N.E. Bowles, L. Fletcher, C. Howett, F.W. Taylor, *Icarus* 186 (2007) 364–384.
- [4] D.W. Clarke, J.P. Ferris, *Orig. Life Evol. Biol.* 27 (1997) 225–248.
- [5] M.G. Trainer, A.A. Pavlov, H.L. DeWitt, J.L. Jimenez, C.P. McKay, O.B. Toon, M.A. Tolbert, *PNAS* 103 (2006) 18035–18042.
- [6] A. Coustenis, R.K. Achterberg, B.J. Conrath, D.E. Jennings, A. Marten, D. Gautier, C.A. Nixon, F.M. Flasar, N.A. Teanby, B. Bezard, R.E. Samuelson, R.C. Carlson, E. Lellouch, G.L. Bjoraker, P.N. Romani, F.W. Taylor, P.G.J. Irwin, T. Fouchet, A. Hubert, G.S. Orton, V.G. Kunde, S. Vinatier, J. Mondellini, M.M. Abbas, R. Courtin, *Icarus* 189 (2007) 35–62.
- [7] J. Cui, R.V. Yelle, V. Vuitton, J.H. Waite, W.T. Kasprzak, D.A. Gell, H.B. Niemann, I.C.F. Müller-Wodarg, N. Borggren, G.G. Fletcher, E.L. Patrick, E. Raaen, B.A. Magee, *Icarus* 200 (2008) 581–615.
- [8] E.H. Wilson, S.K. Atreya, *Planet. Space Sci.* 51 (2003) 1017–1033.
- [9] G. Israël, C. Szopa, F. Raulin, M. Cabane, H.B. Niemann, S.K. Atreya, S.J. Bauer, J.-F. Brun, E. Chasseffère, P. Coll, E. Condé, D. Coscia, A. Hauchecorne, P. Millian, M.-J. Nguyen, T. Owen, W. Riedler, R.E. Samuelson, J.-M. Siguier, M. Steller, R. Sternberg, C. Vidal-Madjar, *Nature* 438 (2005) 796–799.
- [10] V.A. Krasnopolsky, *Icarus* 201 (2009) 226–256.
- [11] D.S.N. Parker, F. Zhang, Y.S. Kim, R.I. Kaiser, A.M. Mebel, *J. Phys. Chem. A* 115 (2011) 593–601.
- [12] H. Richter, J.B. Howard, *Phys. Chem. Chem. Phys.* 4 (2002) 2038.
- [13] J.A. Miller, C.F. Melius, *Combust. Flame* 91 (1992) 21–39.
- [14] C. Huang, F. Zhang, R.I. Kaiser, V.V. Kislov, A.M. Mebel, R. Silva, W.K. Gichuhi, A. G. Suits, *J. Astrophys.* 714 (2010) 1249.
- [15] D.E. Marten, E.G. Robertson, R.J.S. Morrison, *Chem. Phys. Lett.* 425 (2006) 210–215.
- [16] A.O. Hernandez-Castillo, C. Abeysekera, B.M. Hays, T.S. Zwier, *J. Chem. Phys.* 145 (2016) 114203.
- [17] G.B. Park, R.W. Field, *J. Chem. Phys.* 144 (2016) 200901.
- [18] D.J. Frisch, M.J. Trucks, G.W. Schlegel, H.B. Scuseria, G.E. Robb, M.A. Cheeseman, J.R. Scalmani, G. Barone, V. Mennucci, B. Petersson, G.A. Nakatsuji, H. Caricato, M. Li, X. Hratchian, H.P. Izmaylov, A.F. Bloino, J. Zheng, G. Sonnenberg, Gaussian 09, Revis. E.01, Gaussian, Inc., Wallingford CT, 2009.
- [19] S. Grimme, *J. Chem. Phys.* 124 (2006) 034108.
- [20] D.P. Tabor, D.M. Hewett, S. Bocklitz, J.A. Korn, A.J. Tomaine, A.K. Ghosh, T.S. Zwier, E.L. Sibert, *J. Chem. Phys.* 144 (2016) 224310.
- [21] D. Schmitz, V.A. Shubert, T. Betz, M. Schnell, *J. Mol. Spec.* 280 (2012) 77–84.
- [22] H.M. Pickett, *J. Mol. Spectrosc.* 377 (1991) 371–377.
- [23] R.M. Balabin, *Mol. Phys.* 109 (2011) 943–953.
- [24] L.F. Holroyd, T. van Mourik, *Chem. Phys. Lett.* 442 (2007) 42–46.
- [25] A.O. Hernandez-Castillo, C. Abeysekera, B.M. Hays, I. Kleiner, H.V.L. Nguyen, T. S. Zwier, *J. Mol. Spec.* 337 (2017) 51–58.
- [26] B.A. McGuire, A.M. Burkhardt, S. Kalenskii, C.N. Shingledecker, A.J. Remijan, E. Herbst, M.C. McCarthy, *Science* 359 (2018) 202–205.
- [27] T.M. Selby, T.S. Zwier, *J. Phys. Chem. A* 109 (2005) 8487–8496.
- [28] R.A. Loomis et al., *Mon. Not. R. Astron. Soc.* 463 (2016) 4175–4183.
- [29] P. Gratier et al., *Astrophys. J. Suppl. Ser.* 225 (2016) 25.

Multiplexed characterization of complex gas-phase mixtures combining chirped-pulse Fourier transform microwave spectroscopy and VUV photoionization time-of-flight mass spectrometry

Sean M. Fritz, Brian M. Hays, Alicia O. Hernandez-Castillo, Chamara Abeysekera, and Timothy S. Zwier

Citation: [Review of Scientific Instruments](#) **89**, 093101 (2018); doi: 10.1063/1.5046085

View online: <https://doi.org/10.1063/1.5046085>

View Table of Contents: <http://aip.scitation.org/toc/rsi/89/9>

Published by the [American Institute of Physics](#)

PHYSICS TODAY
WHITEPAPERS

MANAGER'S GUIDE

Accelerate R&D with
Multiphysics Simulation

READ NOW

PRESENTED BY
 **COMSOL**



Multiplexed characterization of complex gas-phase mixtures combining chirped-pulse Fourier transform microwave spectroscopy and VUV photoionization time-of-flight mass spectrometry

Sean M. Fritz, Brian M. Hays,^{a)} Alicia O. Hernandez-Castillo, Chamara Abeysekera, and Timothy S. Zwier^{b)}

Department of Chemistry, Purdue University, West Lafayette, Indiana 47907-2084, USA

(Received 25 June 2018; accepted 14 August 2018; published online 6 September 2018)

We report details of the design and operation of a single apparatus that combines Chirped-Pulse Fourier Transform Microwave (CP-FTMW) spectroscopy with vacuum ultraviolet (VUV) photoionization Time-of-Flight Mass Spectrometry (TOFMS). The supersonic expansion used for cooling samples is interrogated first by passing through the region between two microwave horns capable of broadband excitation and detection in the 2-18 GHz frequency region of the microwave. After passing through this region, the expansion is skimmed to form a molecular beam, before being probed with 118 nm (10.5 eV) single-photon VUV photoionization in a linear time-of-flight mass spectrometer. The two detection schemes are powerfully complementary to one another. CP-FTMW detects all components with significant permanent dipole moments. Rotational transitions provide high-resolution structural data. VUV TOFMS provides a gentle and general method for ionizing all components of a gas phase mixture with ionization thresholds below 10.5 eV, providing their molecular formulae. The advantages, complementarity, and limitations of the combined methods are illustrated through results on two gas-phase mixtures made up of (i) three furanic compounds, two of which are structural isomers of one another, and (ii) the effluent from a flash pyrolysis source with *o*-guaiacol as the precursor. Published by AIP Publishing. <https://doi.org/10.1063/1.5046085>

I. INTRODUCTION

Chirped pulse Fourier transform microwave (CP-FTMW) spectroscopy is a powerful tool for determining the structures of gas phase molecules with high precision.¹ Fast electronics and strong electric fields are utilized to polarize all rotational transitions lying in a 10 GHz bandwidth within 1 μ s, and the resulting free induction decay (FID) is collected to obtain a spectrum at faster-than-ever rates.^{1,2} The frequency patterns from the resulting spectrum can be fit to theoretical predictions and provide a direct measure of the geometry through the rotational constants and projections of the permanent dipole moments along the inertial axes.² With rapid data acquisition, signal averaging to observe less abundant isotopes is readily achievable³ and Kraitchman equations^{4,5} can be applied to determine atomic positions and bond lengths/angles to high accuracy. CP-FTMW spectroscopy can also be utilized to determine the rotational temperatures and fractional abundances of each species contributing to the spectrum.^{6,7}

The applications of CP-FTMW spectroscopy continue to grow in ever-widening scope, as a detector in kinetic studies,⁶⁻⁸ as a probe of chemical reaction dynamics,⁹⁻¹¹ and as a probe for double resonance experiments.^{12,13} However, one of the considerable challenges of using CP-FTMW spectroscopy as a stand-alone method is that, if the carriers of the

microwave transitions arise from a multi-component gas-phase mixture, the microwave transitions due to each component are intermingled with one another, complicating the assignment process. When all components have known microwave spectra, the high resolution of the method allows look-up tables to play a role in semi-automated analysis. However, when the mixture contains unknown components, spectral assignment can become slow or impossible. Furthermore, while all molecules with permanent dipole moments are detectable, the CP-FTMW signal scales as the square of the dipole moment, making it difficult to detect mixture components that are non-polar or weakly polar ($\mu < 1$ D).

Time-of-flight mass spectrometry (TOFMS) is a widely used analytical technique to determine the molecular weights of the components of gas phase mixtures. When photoionization is used as the ionization mechanism (e.g., from a laser source), the components are ionized and accelerated into a field free region where the unique arrival time at the detector is dependent upon its mass-to-charge ratio. Using a soft ionization technique such as vacuum ultraviolet (VUV) radiation, fragmentation upon photoionization is typically small^{14,15} so that the VUV TOF mass spectrum records the molecular weights and approximate relative abundances of the components of the mixture. However, as a stand-alone method, the mass spectrum itself determines only molecular formulae and hence does not identify the presence and relative abundances of structural and/or conformational isomers. Admittedly, other methods requiring more sophisticated light sources have made headway in isomer-specific identification. For instance, with tunable VUV radiation such as is available from a synchrotron,

^{a)}Current address: 1 Institut de Physique de Rennes, UMR 6251 du CNRS—Université de Rennes 1, Campus de Beaulieu, 35042 Rennes Cedex, France.

^{b)}Author to whom correspondence should be addressed: zwier@purdue.edu

the unique ionization energies of isomers can be used in favorable cases to deduce isomer-specific composition.^{16–18} In addition, previous work using a molecular beam source with non-resonant strong field ionization in a time of flight mass spectrometer has been used to quantify isomers.¹⁹ Nevertheless, a general solution to isomer-specific detection would benefit greatly from supplementing mass spectrometry with other methods better suited to the task of isomer-specific detection.

Motivated by the complementary data provided by the two methods, we have incorporated into our CP-FTMW spectrometer a TOF mass spectrometer, resulting in a powerful multiplexed approach for determining gas phase structures. With the capability to interrogate the same molecular sample with both methods under a range of conditions, the correlation between the microwave transition intensities and the mass-resolved ion intensities in the TOF mass spectrum can be used to determine the molecular formulae of the carriers of the microwave transitions. The new instrument has great potential to extend and speed gas phase analysis of complex mixtures. This advantage extends particularly to circumstances in which the components of the gas phase mixture undergo chemical reaction, whose extent can be followed simultaneously in both the microwave and TOF spectra. Furthermore, the generality of VUV single-photon photoionization also enables detection of chemical components that do not have a dipole moment, as long as the VUV photon energy is sufficient to ionize all the mixture's components.

Herein, we describe an instrument recently modified so as to incorporate capabilities to acquire simultaneous rotational and mass spectra under identical conditions. We demonstrate the capability of the new instrument by studying gas mixtures of two complementary types. First, a mixture of three stable furanic compounds containing two structural isomers is probed: furfural ($C_5H_4O_2$), furfuryl alcohol ($C_5H_6O_2$), and 2-methoxyfuran ($C_5H_6O_2$), demonstrating the complementary strengths of the methods. While only two parent masses are identified via VUV TOF mass analysis, the CP-FTMW spectrum incorporates transitions due to all three components, including the global minimum conformational isomer of furfuryl alcohol. We extract fractional abundances

from the CP-FTMW spectrum and compare these to the VUV photoionization signals in the TOF mass spectrum. Second, a mixture resulting from flash pyrolysis of guaiacol is studied. In this case, the relative intensities of the signal in both microwave and mass spectra are followed with changes in the temperature of the pyrolysis source to identify and facilitate assignment of the molecular carriers in the pyrolysis source.

II. APPARATUS

A. Pumping system

Figure 1 shows an assembly drawing of the chamber we have designed for simultaneous CP-FTMW and photoionization TOFMS detection. This chamber is a modified version of a CP-FTMW spectrometer described previously.²⁰ A new [60 cm (length) \times 30 cm \times 30 cm] rectangular steel chamber was designed with two sets of flanges on each side to provide two platforms for simultaneous microwave and time-of-flight measurements. The chamber is evacuated by two 25-cm diam diffusion pumps (Varian VHS 10) located behind the TOF section. The diffusion pumps are backed by a roots blower (BOC Edwards EH500) and a roughing pump (Alcatel 2063). The base pressure of the chamber is 1×10^{-5} Torr with no gas flow and maintains an operating pressure of 1×10^{-4} Torr when the pulsed valve is operating at flows of about $0.85 \text{ bar cm}^3 \text{ s}^{-1}$. The interior of the microwave portion of the chamber is covered with sheets of microwave absorber (Emerson and Cuming Eccosorb HR-25/ML; LS-24) to reduce reflections due to microwave radiation resonances, thus preventing damage of the electronics.

B. Chirped-pulse Fourier transform microwave section

The CP-FTMW section of the chamber has been upgraded from its original configuration²⁰ by incorporation of a new set of horns that extend the frequency coverage from 2 to 18 GHz. As a result, we provide a brief overview of the electronics used to provide this frequency coverage. A schematic diagram for the microwave electronics is shown in Fig. 2. Chirped pulses

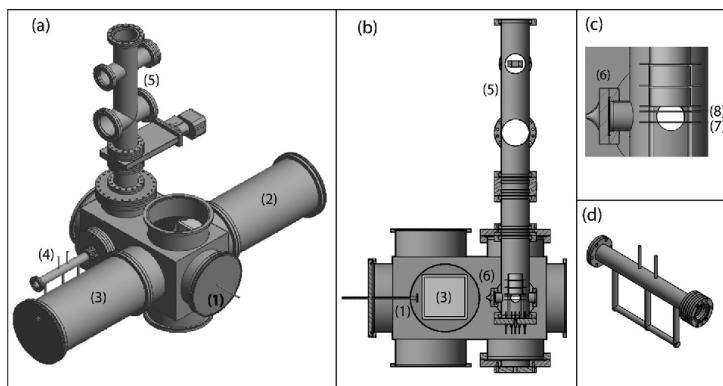


FIG. 1. (a) Assembly drawing of the combined CP-FTMW/TOFMS vacuum chamber in a 3D rendering, (b) a side-on cross-sectional view, (c) an enlarged view of the skimmer and Wiley-McLaren extraction region, and (d) a close-up of the VUV cell. Labeled components: (1) pulsed valve, (2) broad-casting horn, (3) receiving horn, (4) VUV cell, (5) TOF tube, (6) skimmer, (7) repeller plate, and (8) draw-out-grid.

of 355 nm light from a Nd:YAG laser [Continuum YG661-20(680)] are brought into the cell through a 250 mm focal length AR coated UV fused silica lens mounted 7.5 cm before the entrance window to the cell. The VUV cell is 31 cm long and has a gas manifold attached to an inlet port to allow for the introduction of argon and xenon which serve as the tripling medium. A pressure gauge (Cecomp Electronics DPG1000G-760TORRA-1) is fixed to a second port on the VUV cell to allow for accurate measurements of the pressures of each gas. The VUV cell was filled with 10 Torr of xenon and 100 Torr of argon to generate VUV radiation, a 1:10 ratio in keeping with optimal performance found in previous studies.²¹ One of the tubes of the gas manifold can be cooled with dry ice, creating temperature differentials that facilitate better mixing of the gas by convection. A MgF₂ lens (148 mm focal length, 2.5 cm diam) affixed to the end of the VUV tube is used to focus the VUV light and spatially separate it from the 355 nm light in the TOF source region where ionization occurs.

As noted above, the AWG serves as the master clock for all other components involved in the experiment, including the digital delay generator (Berkeley Nucleonics model 577) which triggers the Nd:YAG laser. The gaseous sample is photoionized in a single-photon photoionization using the 118 nm light generated in the VUV cell. Photoionization occurs between the repeller plate and the draw-out-grid of a Wiley-McLaren²³ TOF source, which are separated by 2 cm from one another. Typical voltages of +3000 V and +2750 V are placed on repeller and draw-out-grids under Wiley-McLaren conditions that give best peak resolution. A grounding plane at the entrance to the einzel lens serves as the entrance to the field-free region.

The ion packet is subsequently focused by an einzel lens operating at +1700 V and traverses the flight tube before passing through a grounded screen mounted above the detector, which ends the field-free region. The ions are accelerated onto the front surface of an 18 mm dual chevron microchannel plate (MCP) (Jordan TOF Products, Inc., C0701) with a gain of 10^7 at a typical front-surface potential of -2500 V. Typical voltages of +3000 V and +2750 V are used for repeller and draw-out-grids under Wiley-McLaren conditions that give best peak resolution. The mass resolution, $m/\Delta m$, of the TOF mass spectrometer calculated from the mass 98 peak in the mixture mass spectrum, is 360.

The current pulses from the mass-resolved photoions are amplified a second time by 25 times in a fast amplifier (Stanford Research Systems SR445) before being displayed on a 3.5 GHz, 40 GS/s digital phosphor oscilloscope (Tektronix DPO 7354C). The oscilloscope is triggered to start recording when the Q-switch of the Nd:YAG laser fires to obtain the time-of-flight signals, from which the mass-to-charge ratios of the photoions are deduced.

Each gas pulse was 500 μ s long, and 20 molecular FIDs each 16 μ s in length were collected during each gas pulse.

In studying the pyrolysis of *o*-guaiacol, a commercial sample (98%, Sigma-Aldrich) without further purification was inserted in a stainless-steel sample holder and heated to 95 °C. The samples were introduced into a 2 mm silicon carbide (SiC) micro-reactor tube. Details of the design and operation of the pyrolysis source are provided elsewhere.²⁴

III. CHARACTERIZATION OF INSTRUMENTAL CAPABILITIES

A. Furanic mixture

In order to test the new instrument, we selected a mixture of three liquid samples that were chemically similar, but contained two structural isomers. In doing so, we demonstrate the complementary strengths of the CP-FTMW and VUV TOFMS methods when they are combined with one another in a single instrument. In particular, a mixture of 2-methoxyfuran (C₅H₆O₂, 97%, Sigma-Aldrich), furfuryl alcohol (C₅H₆O₂, 98%, Sigma-Aldrich), and furfural (C₅H₄O₂, 99%, Sigma-Aldrich) was used for this test, with chemical structures shown in Fig. 3(b). Introduction of the furfural and 2-methoxyfuran vapors was accomplished by picking up the vapors by streaming helium over the liquid samples (2.4 bars backing pressure) contained in a cotton-filled stainless-steel sample holder incorporated into the gas line, located outside of the vacuum chamber. Furfuryl alcohol was added to the mixture in a similar way using a second sample holder located inside the vacuum chamber, which was heated to 60 °C.

The 8-18 GHz rotational spectrum of the mixture was obtained under linear fast passage conditions²⁵ (20% TWTA power), acquiring 200 000 averages in total. The experimental spectrum [Fig. 3(a)] is plotted against calculated predictions using the previously reported experimental rotational constants.²⁶⁻²⁸ Rotational transitions from furfuryl alcohol (green), furfural (blue), and 2-methoxyfuran (red) were identified based on the known rotational constants for these molecules. The mass spectrum acquired simultaneously is displayed in Fig. 3(b). VUV photoionization at 118 nm (10.5 eV) was used to ionize furfuryl alcohol (IE = 8.88 eV),²⁹ furfural (IE = 9.22 eV),³⁰ and 2-methoxyfuran (IE = 7.93 eV).³¹ Two peaks at m/z of 96 and 98 correspond to the molecular masses of furfural (C₅H₄O₂) and the C₅H₆O₂ structural isomers furfuryl alcohol and 2-methoxyfuran, respectively. The single C-13 peaks at mass 97 and 99 are also observable in natural abundance in the TOF mass spectrum.

The obvious deduction from Fig. 3(b) is that 118 nm VUV time-of-flight mass spectrometry as a stand-alone method is not able to distinguish and identify conformational or structural isomers present in the gas mixture. Other methods requiring more sophisticated light sources can make isomer-specific identification. For instance, with tunable VUV radiation such as is available from a synchrotron, the unique ionization energies of isomers can be used in favorable cases to deduce isomer-specific composition.¹⁶⁻¹⁸ In addition, previous work using a molecular beam source with non-resonant strong field ionization in a time of flight mass spectrometer has been used to quantify isomers.¹⁹ However, based on the 118 nm photoionization mass spectrum shown in Fig. 3(b), one might anticipate the presence of just two unique components in the gas mixture. By contrast, the rotational transitions of the structural isomers 2-methoxyfuran and furfuryl alcohol are clearly distinguishable from one another in the CP-FTMW spectrum. The rotational transitions for any conformers present are also distinct from one another and can be probed and assigned using the recently developed technique of strong field coherence breaking.^{12,13} However, in this experiment, only

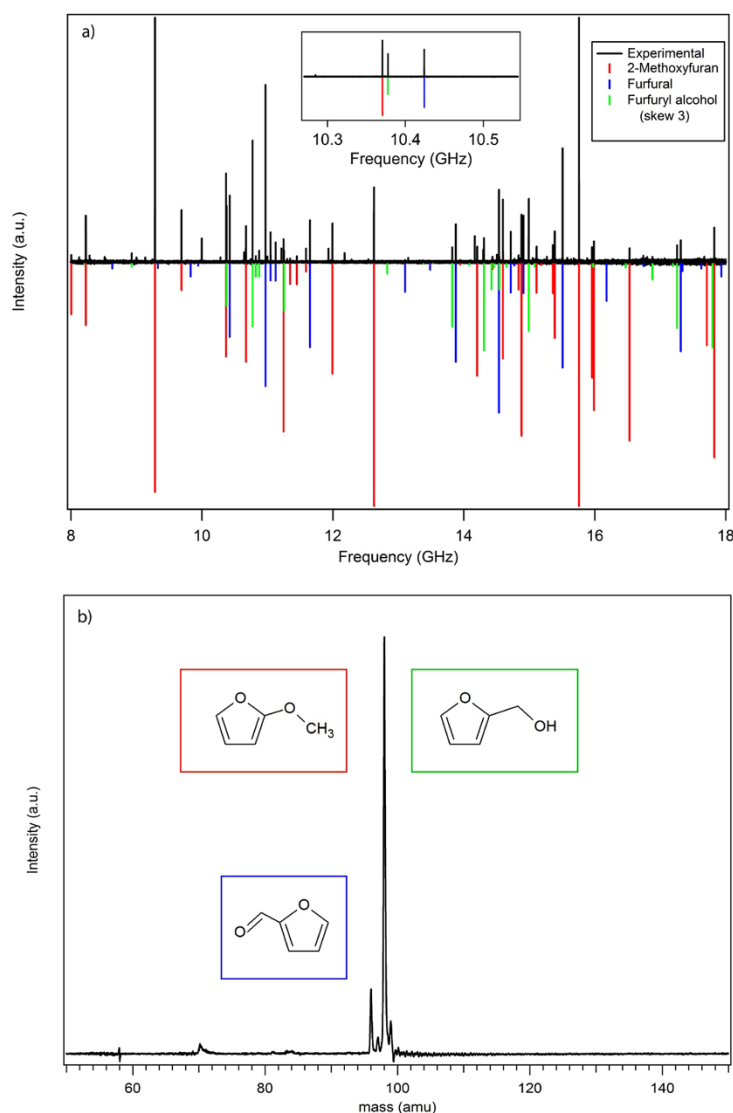


FIG. 3. (a) Broadband CP-FTMW spectrum of a gas-phase mixture of 2-methoxyfuran, furfuryl alcohol, and furfural, compared to the microwave transitions for the three molecules using known experimental rotational constants.^{21–23} The inset shows a close-up view of three transitions due to the three components of the mixture, demonstrating the isomer specificity afforded by the high resolution of the method. (b) Time-of-flight mass spectrum following 118 nm VUV photoionization of the same mixture.

the global minimum energy structures for furfuryl alcohol and 2-methoxyfuran are observed: the *skew 3* conformer of furfuryl alcohol, (*trans*-furfural) and the *syn* conformation of 2-methoxyfuran.^{26–28}

Not only is CP-FTMW spectroscopy able to identify structural isomers, the intensities of assigned rotational transitions can be used to extract their relative abundances. The intensities of the microwave transitions of each of the three components were fit to Boltzmann plots to derive the experimental rotational temperatures (furfural = 0.89 ± 0.09 K; 2-methoxyfuran = 1.30 ± 0.09 K; furfuryl alcohol = 1.12 ± 0.1 K, 1σ error bars). From the rotational temperature plots, a population analysis was carried out using the known dipole moments for the

three molecules. The mixture was found to consist of 67% furfuryl alcohol, 24% 2-methoxyfuran, and 9% furfural, with an average one-standard deviation error of $\pm 6\%$.

By contrast, the ion intensities in the 118 nm VUV photoionization TOF mass spectrum are determined by the product of the relative abundances and the 118 nm photoionization cross sections, assuming no fragmentation following photoionization,

$$I_i(m/z) = N_i \cdot \sigma_i(118 \text{ nm}).$$

From the data in Fig. 3(b), the fractional ion intensities are 13% m/z 96 and 87% m/z 98, compared to percent populations of 9% m/z 96 and 91% m/z 98 based on the microwave fitting

just described. These results are consistent with similar 118 nm photoionization cross sections for the three molecules, within the errors of the measurements.

B. Pyrolysis mixture

The combination of flash pyrolysis and CP-FTMW spectroscopy is emerging as a powerful scheme for determining the chemical structures of pyrolysis intermediates and final products at different microreactor wall temperatures.²⁴ While the temperature profile inside the SiC tube is a complicated function of conditions,³² the outer wall temperature provides a consistent measurement of heating conditions that correlates with the temperature the gas pulse experiences inside the SiC tube and therefore the pyrolysis conditions. Here we demonstrate how the combination of CP-FTMW and VUV TOFMS provides additional capabilities for diagnosing and spectroscopically characterizing the expansion-cooled effluent from

a flash pyrolysis source.^{24,33} In particular, we display here preliminary results on the flash pyrolysis of guaiacol, one of the principle components of lignin.³⁴

Figure 4(a) displays a series of VUV photoionization TOFMS for *o*-guaiacol (structure in the bottom left) recorded as a function of the wall temperatures of the SiC tube used for flash pyrolysis, over a temperature range from 320 to 1120 K. These mass spectra are similar to those recently published by Scheer *et al.* using the same 118 nm VUV TOF techniques, although the concentrations of guaiacol in the mixture were significantly lower in that previous study in order to rigorously minimize bimolecular chemistry.³⁵ The mass-to-charge ratios and known chemical structures of the key photoionizable components are labeled in the figure. Note that at 320 K, the *o*-guaiacol precursor experiences no fragmentation by 118 nm photoionization.

By recording a series of broadband microwave spectra under the same conditions, it is possible to detect and

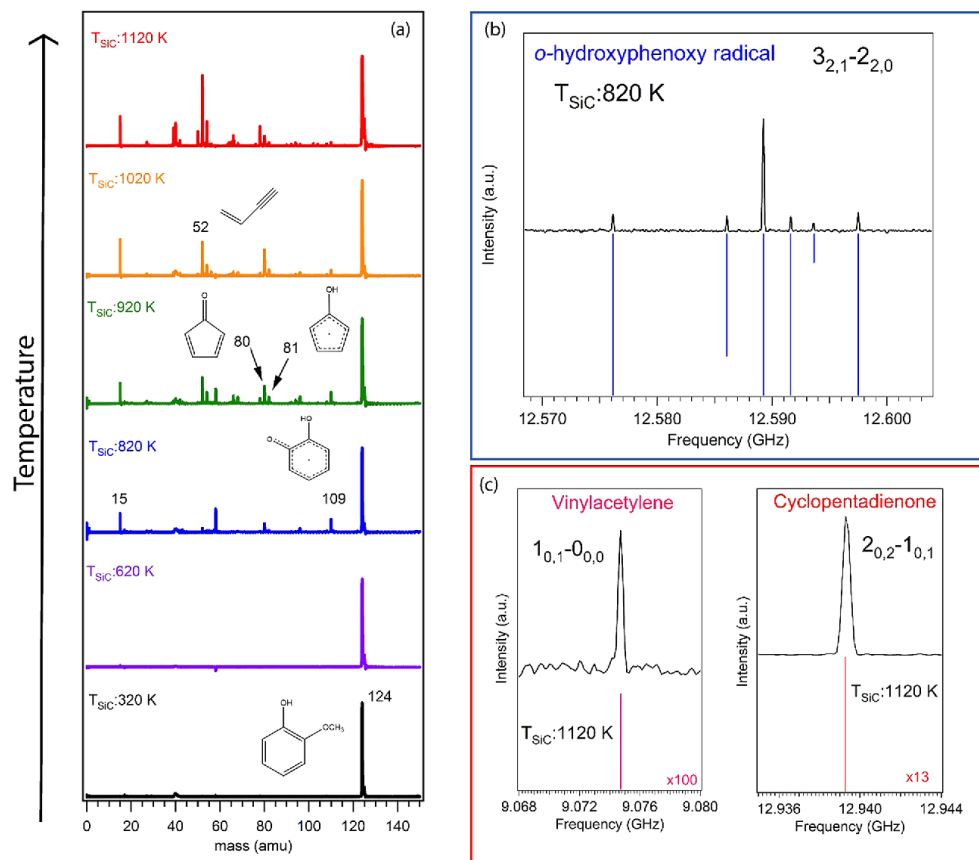


FIG. 4. (a) 118 nm photoionization TOF mass spectrum at the indicated SiC wall temperatures for flash pyrolysis of *o*-guaiacol. (b) CP-FTMW spectrum in a small frequency window around the $3_{2,1}-2_{2,0}$ transition of the *o*-hydroxyphenoxy radical. The transitions in blue are split due to coupling of the electron spin angular momentum with the molecule's rotational angular momentum. (c) CP-FTMW spectra in small frequency regions around microwave transitions due to cyclopentadienone (right) and vinylacetylene (left).

optimize conditions for characterizing the rotational spectra of transient species. The initial products of the thermal decomposition of *o*-guaiacol appear at m/z 109 and m/z 15 in the TOF mass spectrum, corresponding to the *o*-hydroxyphenoxy ($\text{HOC}_6\text{H}_4\text{O}$) and methyl (CH_3) radicals, respectively, that result from breaking the molecule's weakest bond. At 820 K, the *o*-hydroxyphenoxy radical is present at maximum concentration, with the TOF mass spectra guiding the choice of this temperature as the best one for recording a CP-FTMW spectrum with maximum signal-to-noise ratio. An expanded view of the 12.575–12.600 GHz range of the microwave spectrum is shown in Fig. 4(b), highlighting the set of $3_{2,1}-2_{2,0}$ rotational transitions of the *o*-hydroxyphenoxy radical, split by electron spin-rotation coupling. The set of transitions due to the radical in the broadband spectrum can be used to determine accurate rotational constants, centrifugal distortion constants, and spin-rotation coupling constants [Fig. 4(b)], locking in the structural assignment, but also providing new high resolution structural data on this resonance-stabilized radical. The full spectroscopic characterization of this radical will be described elsewhere.³⁶

Decarbonylation of the *o*-hydroxyphenoxy radical generates the hydroxycyclopentadienyl radical (m/z 81), which has a total dipole moment of ~ 1.5 D. The maximum concentration of this radical is achieved at ~ 920 K but its VUV photoionization signal is never very large. Despite a careful search, we do not see any evidence of it in the microwave spectrum at the present signal-to-noise ratio. The combination of modest dipole moment and small concentration both contribute to its signal being too small to detect. The hydroxycyclopentadienyl radical eliminates an H atom producing cyclopentadienone (m/z 80). Further heating generates vinylacetylene (m/z 52), which continues to build with pyrolysis temperature.

Microwave transitions due to cyclopentadienone [Fig. 4(c), right] are observed beginning at 820 K, while the vinylacetylene product only appeared in measurable concentration at 1120 K [Fig. 4(c), left]. The observed decomposition pathway of *o*-guaiacol is consistent with previous work in the literature.³⁵

This example shows how the correlation in signals in the VUV mass spectra and microwave spectra can enhance and speed the analysis of complex mixtures. VUV photoionization TOF mass spectrometry provides the molecular formulae of the mixture components, as long as they have ionization energies lower than the VUV photon energy (10.5 eV). In the case of guaiacol, this included the reactant itself, the free radicals formed in the initial pyrolysis step ($\text{CH}_3 + o$ -hydroxyphenoxy), other highly reactive intermediates (e.g., cyclopentadienone), and many of the final products. Only C_2H_2 had an ionization energy above 10.5 eV, and its presence was surmised only indirectly from the other products observed.³⁵ On the other hand, the chemical structure of the molecular components is often not uniquely prescribed by the molecular formulae. Furthermore, free radicals and reactive intermediates often have chemical structures that have not been observed or characterized previously by high resolution methods. CP-FTMW spectroscopy is a powerful tool for this characterization, relying only on the presence of a permanent dipole moment for detection. In the pyrolysis of guaiacol, this led to the first structural

characterization of the *o*-hydroxyphenoxy radical.³⁶ Finally, the combination of the two methods is put to particularly good use in identifying conditions under which particular pyrolysis intermediates are present with maximum intensity, improving the quality of the microwave spectra obtained.

IV. CONCLUSION

We have described the CP-FTMW/TOF spectrometer in detail and have demonstrated its capabilities by studying two complementary gas mixtures: one consisting of three stable furanic compounds and a second resulting from flash pyrolysis. In doing so, we have shown the power of CP-FTMW spectroscopy in its ability to determine fractional abundances and detect structural isomers that would not be distinguishable in a photoionization mass spectrum at fixed photoionization energy. We have further demonstrated the value of obtaining the complementary data from the CP-FTMW and TOFMS methods by studying the pyrolysis of *o*-guaiacol. There, the mass spectrum provides insight to the reaction pathway and enables the potential identification of intermediates that do not have a permanent dipole moment. The intensities in the mass spectrum also are useful in determining the best conditions for studying reactive intermediates and final products via CP-FTMW spectroscopy. With the data provided, we have demonstrated the promise of this instrument as a multiplexed approach in determining gas phase structures.

SUPPLEMENTARY MATERIAL

The [supplementary material](#) contains the Boltzmann plots used to determine the rotational temperatures of 2-methoxyfuran, furfural, and furfuryl alcohol.

ACKNOWLEDGMENTS

The authors gratefully acknowledge support from the Department of Energy Basic Energy Sciences Gas-Phase Chemical Physics program under Grant No. DE-FG02-96ER14656.

¹G. G. Brown, B. C. Dian, K. O. Douglass, S. M. Geyer, S. T. Shipman, and B. H. Pate, *Rev. Sci. Instrum.* **79**, 053103 (2008).

²G. B. Park and R. W. Field, *J. Chem. Phys.* **144**, 200901 (2016).

³A. L. Steber, J. L. Neill, D. P. Zaleski, B. H. Pate, A. Lesarri, R. G. Bird, V. Vaquero-Vara, and D. W. Pratt, *Faraday Discuss.* **150**, 227 (2011).

⁴J. Kraitichman, *Am. J. Phys.* **21**, 17 (1953).

⁵C. C. Costain, *J. Chem. Phys.* **29**, 864 (1958).

⁶J. M. Oldham, C. Abeysekera, B. Joalland, L. N. Zack, K. Prozumet, I. R. Sims, G. B. Park, R. W. Field, and A. G. Suits, *J. Chem. Phys.* **141**, 154202 (2014).

⁷C. Abeysekera, B. Joalland, N. Ariyasingha, L. N. Zack, I. R. Sims, R. W. Field, and A. G. Suits, *J. Phys. Chem. Lett.* **6**, 1599 (2015).

⁸C. Abeysekera, L. N. Zack, G. B. Park, B. Joalland, J. M. Oldham, K. Prozumet, N. M. Ariyasingha, I. R. Sims, R. W. Field, and A. G. Suits, *J. Chem. Phys.* **141**, 214203 (2014).

⁹K. Prozumet, Y. V. Suleimanov, B. Buesser, J. M. Oldham, W. H. Green, A. G. Suits, and R. W. Field, *J. Phys. Chem. Lett.* **5**, 3641 (2014).

¹⁰B. C. Dian, G. G. Brown, K. O. Douglass, and B. H. Pate, *Science* **320**, 924 (2008).

¹¹N. M. Kidwell, V. Vaquero-Vara, T. K. Ormond, G. T. Buckingham, D. Zhang, D. N. Mehta-Hurt, L. McCaslin, M. R. Nimlos, J. W. Daily, B. C. Dian, J. F. Stanton, G. B. Ellison, and T. S. Zwier, *J. Phys. Chem. Lett.* **5**, 2201 (2014).

- ¹²A. O. Hernandez-Castillo, C. Abeysekera, B. M. Hays, and T. S. Zwier, *J. Chem. Phys.* **145**, 114203 (2016).
- ¹³S. M. Fritz, A. O. Hernandez-Castillo, C. Abeysekera, B. M. Hays, and T. S. Zwier, *J. Mol. Spectrosc.* **349**, 10 (2018).
- ¹⁴L. Cao, F. Muhlberger, T. Adam, T. Streibel, H. Z. Wang, A. Kettrup, and R. Zimmerman, *Anal. Chem.* **75**, 5639 (2003).
- ¹⁵Y. J. Shi and R. H. Lipson, *Can. J. Chem.* **83**, 1891 (2005).
- ¹⁶S. R. Leone, M. Ahmed, and K. R. Wilson, *Phys. Chem. Chem. Phys.* **12**, 6564 (2010).
- ¹⁷F. Qi, *Proc. Combust. Inst.* **34**, 33 (2013).
- ¹⁸B. Yang, C. Huang, L. Wei, J. Wang, L. Sheng, Y. Zhang, F. Qi, W. Zheng, and W. K. Li, *Chem. Phys. Lett.* **423**, 321 (2006).
- ¹⁹F. Cudry, J. M. Oldham, S. Lingenfelter, and A. G. Suits, *J. Phys. Chem. A* **119**, 460 (2015).
- ²⁰A. J. Shirar, D. S. Wilcox, K. M. Hotopp, G. L. Storck, I. Kleiner, and B. C. Dian, *J. Phys. Chem. A* **114**, 12187 (2010).
- ²¹J. Yang, X. B. Wang, X. P. Xing, and L. S. Wang, *J. Chem. Phys.* **128**, 201102 (2008).
- ²²J. M. Beames, F. Liu, M. I. Lester, and C. Murray, *J. Chem. Phys.* **134**, 241102 (2011).
- ²³W. C. Wiley and I. H. McLaren, *Rev. Sci. Instrum.* **26**, 1150 (1955).
- ²⁴C. Abeysekera, A. O. Hernandez-Castillo, J. F. Stanton, and T. S. Zwier, *J. Phys. Chem. A* **122**, 6879 (2018).
- ²⁵D. Schmitz, V. A. Shubert, T. Betz, and M. Schnell, *J. Mol. Spectrosc.* **280**, 77 (2012).
- ²⁶J. A. Beukes, K.-M. Marstokk, and H. Møllendal, *J. Mol. Struct.* **567-568**, 19 (2001).
- ²⁷R. A. Motiyenko, E. A. Alekseev, S. F. Dyubko, and F. J. Lovas, *J. Mol. Spectrosc.* **240**, 93 (2006).
- ²⁸K.-M. Marstokk and H. Møllendal, *Acta Chem. Scand.* **48**, 25 (1994).
- ²⁹A. Giuliani, I. C. Walker, J. Delwiche, S. V. Hoffman, P. Limão-Vieira, N. J. Mason, B. Heyne, M. Hoebeke, and M.-J. Hubin-Franksin, *J. Chem. Phys.* **119**, 7282 (2003).
- ³⁰D. Klapstein, C. D. MacPherson, and R. T. O'Brien, *Can. J. Chem.* **68**, 747 (1990).
- ³¹K. N. Urness, Q. Guan, T. P. Troy, M. Ahmed, J. W. Daily, G. B. Ellison, and J. M. Simmie, *J. Phys. Chem. A* **119**, 9962 (2015).
- ³²Q. Guan, K. N. Urness, T. K. Ormond, D. E. David, G. B. Ellison, and J. W. Daily, *Int. Rev. Phys. Chem.* **33**, 447 (2014).
- ³³D. W. Kohn, H. Clauberg, and P. Chen, *Rev. Sci. Instrum.* **63**, 4003 (1992).
- ³⁴J. C. Dean, P. Navotyana, A. P. Parobek, R. M. Clayton, and T. S. Zwier, *J. Chem. Phys.* **139**, 144313 (2013).
- ³⁵A. M. Scheer, C. Mukarakate, D. J. Robichaud, M. R. Nimlos, and G. B. Ellison, *J. Phys. Chem. A* **115**, 13381 (2011).
- ³⁶A. O. Hernandez-Castillo, S. M. Fritz, J. F. Stanton, and T. S. Zwier (unpublished).


Strong-field coherence breaking as a tool for identifying methyl rotor states in microwave spectra: 2-hexanone

Cite as: J. Chem. Phys. **151**, 041104 (2019); <https://doi.org/10.1063/1.5109656>

Submitted: 10 May 2019 . Accepted: 01 July 2019 . Published Online: 24 July 2019

Sean M. Fritz, Piyush Mishra, and Timothy S. Zwier 

COLLECTIONS

 This paper was selected as Featured



View Online



Export Citation



CrossMark

ARTICLES YOU MAY BE INTERESTED IN

Near-threshold photodissociation of cool OH^+ to $\text{O} + \text{H}^+$ and $\text{O}^+ + \text{H}$

The Journal of Chemical Physics **151**, 044303 (2019); <https://doi.org/10.1063/1.5098321>

Open quantum dynamics of a three-dimensional rotor calculated using a rotationally invariant system-bath Hamiltonian: Linear and two-dimensional rotational spectra

The Journal of Chemical Physics **151**, 044105 (2019); <https://doi.org/10.1063/1.5108609>

Propagating molecular rotational coherences through single-frequency pulses in the strong field regime

The Journal of Chemical Physics **151**, 084312 (2019); <https://doi.org/10.1063/1.5099049>

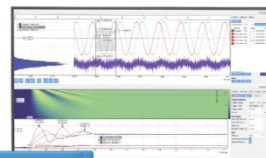


Challenge us.

What are your needs for periodic signal detection?



Zurich
Instruments



J. Chem. Phys. **151**, 041104 (2019); <https://doi.org/10.1063/1.5109656>

151, 041104

© 2019 Author(s).

Strong-field coherence breaking as a tool for identifying methyl rotor states in microwave spectra: 2-hexanone

Cite as: J. Chem. Phys. 151, 041104 (2019); doi: 10.1063/1.5109656

Submitted: 10 May 2019 • Accepted: 1 July 2019 •

Published Online: 24 July 2019



Sean M. Fritz, Piyush Mishra, and Timothy S. Zwier^{a)}

AFFILIATIONS

Department of Chemistry, Purdue University, 560 Oval Drive, West Lafayette, Indiana 47907-2084, USA

^{a)} Author to whom correspondence should be addressed: zwier@purdue.edu

ABSTRACT

The rotational spectrum of 2-hexanone was recorded over the 8–18 GHz region using a chirped pulse Fourier transform microwave spectrometer. Strong field coherence breaking (SFCB) was utilized to selectively modulate the intensities of rotational transitions belonging to the two lowest energy conformers of 2-hexanone, aiding the assignment. In addition, the SFCB method was applied for the first time to selectively identify rotational transitions built off the two lowest energy hindered methyl rotor states of each conformer, 0a₁ and 1e. Since these two states have rotational energy levels with different nuclear spin symmetries, their intensities could be selectively modulated by the resonant monochromatic pulses used in the SFCB method. The difference spectra, final fit, and structural parameters are discussed for the three assigned conformers of 2-hexanone.

Published under license by AIP Publishing. <https://doi.org/10.1063/1.5109656>

INTRODUCTION

Methyl rotors are pervasively present in organic molecules, with the CH₃ group undergoing hindered rotation about the single bond to the rest of the organic framework. Since the primary motion involves the three H-atoms of the methyl group, tunneling can occur between the equivalent minima on the potential energy surface, leading to tunneling splittings, energy levels, and wave functions that reflect the shape and height of the barrier to methyl rotation. This potential for hindered internal rotation is highly sensitive to the local electronic structural environment of the methyl group, depending on a subtle combination of dispersive, exchange, electrostatic, and steric effects between the methyl group and the rest of the molecular frame.¹

In many circumstances, methyl internal rotation can be treated as motion on a one-dimensional potential energy curve involving the dihedral angle associated with the C–X bond joining the methyl group to the molecular frame. The form of these potential energy curves are predominantly 3-fold if the frame against which the methyl rotor rotates has a distinct left-right asymmetry to it, as is often the case. Tunneling through barriers leads to splittings and

energy level structure that depends sensitively on the magnitude and shape of the barriers separating minima. If tunneling were not occurring, the 3-fold potential would support a triply degenerate methyl torsion at its zero-point level; however, in the presence of tunneling, the three levels split into a nondegenerate (a₁) and a two-fold degenerate (e) sublevel in the C_{3v} molecular symmetry group.² When the internal rotor angular momentum quantum number ($|m| = 0, 1, 2, \dots$) is included in the labeling scheme, these levels are designated as 0a₁ and 1e.³

Spectroscopic methods involving electronic,⁴ infrared,⁵ Raman,^{6,7} and far-IR⁸ have been used to study the barriers to internal rotation. In the gas phase, dispersed emission spectra from single torsional levels in the excited electronic state can be used to determine the form of the hindering rotor potential and its barrier height.^{4,9} Based on the splittings and overall rotation/internal rotation couplings, similar data on the excited state barriers can be extracted from the rotational structure of a vibronic transition. In favorable cases, infrared and Raman spectra can be used to determine the unusual frequency patterns of the methyl torsional levels; however, these torsional vibrations are usually only weakly allowed in both infrared and Raman measurements and lie in the very

far infrared region so that their detection and assignment can be difficult.¹⁰

One powerful method for studying methyl internal rotation is microwave spectroscopy.^{10–18} These gas phase measurements typically occur under expansion-cooled conditions where population is removed from higher internal rotor levels. However, due to differing nuclear spin symmetries of the $0a_1$ and $1e$ torsional levels, collisional cooling between these lowest two methyl rotor levels does not occur on the time scale of the cooling process. Microwave spectra of expansion-cooled molecules therefore exhibit rotational transitions built off both $0a_1$ and $1e$ methyl rotor levels, with resolved methyl rotor splittings for methyl rotor barriers up to $\sim 1000\text{ cm}^{-1}$.¹² As a result, the presence of these splittings is pervasive in microwave spectra and has been the subject of much previous work.^{10–18} Fitting these spectra can be a challenge, as rotational transitions due to $0a_1$, $1e$ levels are intermingled with one another and barriers to internal rotation often depend on molecular conformation^{19,20} and complex formation.¹⁴ Due to the fact that there is no interconversion between $0a_1$, $1e$ on the time scale of the experiment, “a” and “e” methyl rotor levels support separate rotational manifolds, much as if they were two conformational isomers.

Recently, we have developed the method of strong-field coherence breaking (SFCB) that enables identification of sets of rotational transitions due to a single entity in a mixture, whether separate molecular components or conformational isomers.²¹ The SFCB method involves application of a set of resonant microwave frequencies at high power to interrogate the mixture following broadband chirped-pulse (CP) excitation, thereby modulating the intensities of a set of transitions sufficient in number that they can be used as the basis for a preliminary fit of that component of the mixture. By operating the chirped-pulse at sufficient power to approach rapid adiabatic passage conditions, rotational population is moved up the rotational ladder by the broadband chirp. The single-frequency pulse(s) selectively “break” the coherence created by the chirped pulse, thereby selectively modulating the intensities of a set of transitions within the same rotational manifold as the resonantly excited levels. This combination of strong-field chirp and single-frequency pulses is required for producing a sufficient set of transitions whose intensities are modulated. While a full physical explanation for these effects is still lacking, the operational utility of the method is striking, speeding analysis and assignment of the microwave spectrum, sometimes by large factors. While SFCB has been applied previously to detect and assign conformational isomers^{21–23} and free radicals in a pyrolysis mixture,²⁴ it has not been used yet to selectively

identify microwave transitions due to methyl rotor sublevels. With this study of 2-hexanone, we present its use for this purpose for the first time.

2-hexanone is an interesting candidate to demonstrate the power of SFCB, as it has a long alkyl chain supporting several conformational isomers as well as a methyl rotor. From a combustion standpoint, ketones play an interesting role as they are important constituents in biomass-derived liquids, and small methyl ketones have high octane numbers and show low emission of soot.^{25–28} Yet, the combustion chemistry of ketones such as 2-hexanone is still in its early stages of exploration. The energy level structure and conformational preferences of 2-hexanone are relevant to the initiation events in pyrolysis and combustion. Herein, we use SFCB to selectively modulate rotational transitions built off the $0a_1$ and $1e$ torsional states of each of the conformers present in an expansion-cooled sample of 2-hexanone, thereby aiding in the assignment of its methyl rotor transitions.

The broadband rotational spectrum of 2-hexanone was recorded over the 8–18 GHz frequency regime using a chirped pulse Fourier transform microwave (CP-FTMW) spectrometer that has been described in detail elsewhere.²⁹

A conformational search of 2-hexanone was carried out using MacroModel with Merck molecular force field static (MMFFs).³⁰ Geometry optimizations of the possible conformations of 2-hexanone were performed using the Gaussian09 program suite³¹ at the density functional theory (DFT) B3LYP/Def2TZVP level of theory including Grimme’s dispersion (D3BJ).³² Based on the calculations, we anticipated the four lowest energy conformers, shown in Fig. 1, as these structures all fall into an energy window within $\sim 3\text{ kJ/mol}$ of the global minimum.

The nomenclature to describe the conformations of 2-hexanone starts with the CH_3 next to the carbonyl group, applying the terms *gauche* ($\pm 60^\circ$) and *trans* (180°) to describe the three backbone dihedral angles involved. Relaxed potential energy curves for methyl internal rotation of both terminal CH_3 groups were calculated for the low-energy conformers at the same level of theory used in the optimization. This was accomplished by scanning the dihedrals involving the two terminal CH_3 groups in 10° steps while optimizing the geometry along all other coordinates. The barriers heights for internal rotation of the CH_3 at the end of the alkyl chain were close to or in excess of 1000 cm^{-1} ; however, barriers heights for the methyl group next to the carbonyl moiety were less than 200 cm^{-1} for all four lowest energy conformers. Given the low barrier height, splittings due to methyl internal rotation from the methyl

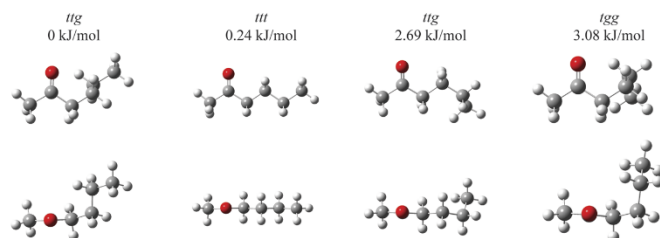


FIG. 1. Top, down, and side views of the four lowest energy conformers of 2-hexanone predicted at the B3LYP-D3BJ/Def2TZVP level of theory.

group next to the carbonyl were anticipated, while the methyl group at the end of the alkyl chain had a barrier too high to produce measurable splittings in our apparatus.

With multiple conformers and methyl internal rotation contributing to the broadband spectrum shown in Fig. 2, SFCB was used to provide sets of rotational transitions belonging to single components of the mixture. SFCB has been described in full detail previously.²¹ We used the modified algorithm described in Fritz *et al.*²³ to identify a set of 2–3 resonant transitions to employ and to modulate the intensities of sets of transitions due to a single component. The most intense transition in the broadband spectrum is chosen as the resonant frequency for the first single frequency pulse (SFP) that follows the broadband sweep. This frequency is pulsed 50 ns after the broadband excitation for a duration of 150 ns. After acquiring the spectrum with the broadband chirp and the first SFP, a spectrum with just the broadband chirp is recorded using the same collection conditions for each spectral acquisition. Using a custom MATLAB routine, the magnitude of the difference spectrum is generated by plotting transitions whose intensities are modulated more than a threshold percentage of their original intensities by the SFP.

The selection criteria for subsequent resonant frequencies involve searching for additional transitions that do not have other transitions within a 10 MHz window on either side, in order to avoid nonselective excitation of satellite bands by the wings of the amplified 150 ns SFP. The SFPs are also chosen to avoid the edges of our spectral range, yet subtend much of the 10 GHz bandwidth to increase the probability that the transitions modulated by each SFP will cover a range of *J*-levels in the frequency range of the broadband pulse. Each additional transition selected should be relatively strong in the linear fast passage spectrum (and thereby have a large transition dipole moment), but weak in the difference spectrum (and therefore be less strongly connected to the transition resonant with the first SFP) in order to maximize the number of potential transitions in the final difference spectrum. Initially, percent intensity modulation thresholds are set high enough to minimize the possibility of false positives in the difference spectrum. After selection

of subsequent SFPs, these resonant frequencies are used in a longer average, with each 150 ns SFP separated by a small gap (5 ns typically). Difference spectra are recorded until enough transitions are modulated to begin the fitting process.

The line picking scheme was used to determine the resonant frequencies to be used in the SFCB method. Under our experimental conditions, the most intense transition in the broadband spectrum of 2-hexanone had a frequency of 10 350.8125 MHz (later assigned as $2_{1,2}-1_{0,1}$), which led subsequently to the choice of 12 184.1875 MHz ($3_{1,3}-2_{0,2}$) and 15 709.4375 MHz ($5_{1,5}-4_{0,4}$) as the second and third resonant frequencies, respectively. The final difference spectrum yielded a total of 5 b-type rotational transitions whose intensities were modulated by more than 35%, as shown in Fig. 3(b). These intensity-modulated transitions were plotted against the predictions of the DFT B3LYP/Def 2TZP-D3BJ calculations of all four conformers. After analyzing the spacing and patterns of the experimental spectrum, these modulated transitions best match with the *ttt* conformer. Using this conformer-specific spectrum as a starting point in the fitting process, a total of 18 transitions were assigned using Pickett's SPFIT and SPCAT suite of programs³⁵ with a Watson S type Hamiltonian. As a result, we assign this spectrum to the *ttt* conformers in its $0a_1$ methyl torsional state.

Once all possible $0a_1$ transitions for the *ttt* conformer were assigned, SFCB was reimplemented starting with the next most intense unassigned transition at 9330.6875 MHz ($2_{1,2}-1_{0,1}$) followed by resonant frequencies at 13 878.5000 MHz ($2_{2,0}-2_{1,1}$) and 14 700.5000 MHz ($5_{2,4}-5_{1,5}$). The final difference spectrum, shown in Fig. 3(a), consists of 9 conformer-specific a-, b-, and c-type transitions whose intensities were modulated by more than 25%. The modulated transitions were once again plotted against the predictions for the remaining plausible structures and best matched the *tgt* conformer. After using the 9 modulated transitions to obtain a preliminary fit, a total of 39 transitions were assigned to the $0a_1$ methyl torsional state of the *tgt* conformer.

After fitting all $0a_1$ transitions from the two lowest energy conformers, numerous intense transitions remained unassigned in the spectrum. With these remaining intense transitions located near the main and most intense transitions belonging to the *ttt* and *tgt* conformers, and given the energetics and dipole moments of the two assigned conformers, we tentatively attributed these transitions to be due to the 1e methyl rotor states of the *ttt* and *tgt* conformers. However, with shifts of hundreds of MHz from the $0a_1$ states, identification of the 1e transitions was not trivial, as the 1e states of both conformers are intermingled with one another.

As noted already, SFCB can serve as a useful tool to selectively modulate rotational transitions built off the $0a_1$ and 1e methyl rotor states. Indeed, the fact that the method modulated the intensities of rotational transitions that could all be fit as arising from a single vibration/torsion level is already evidence that, in 2-hexanone, selective modulation of $0a_1$ and 1e states is possible.

To aid in the assignment of the 1e spectra, SFCB was carried out on the remaining unassigned transitions, using resonant frequencies at 15 968.3125 MHz ($5_{1,5}-4_{0,4}$), 13 783.5625 MHz ($4_{1,4}-3_{0,3}$), and 11 552.8125 MHz ($3_{1,3}-2_{0,2}$). Figure 3(c) shows the final difference spectrum arising from this procedure, which consists of 7 conformer/internal rotor specific transitions whose intensities were modulated by more than 50%. This difference spectrum was used

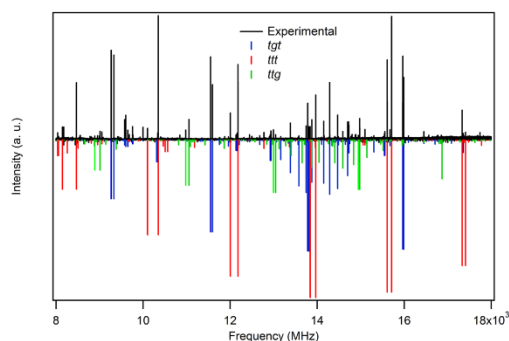


FIG. 2. Experimental 1M average broadband spectrum of 2-hexanone with the best fits of the three identified conformers present. The blue, red, and green lines are assigned to the *tgt*, *ttt*, and *ttg* conformers, respectively.

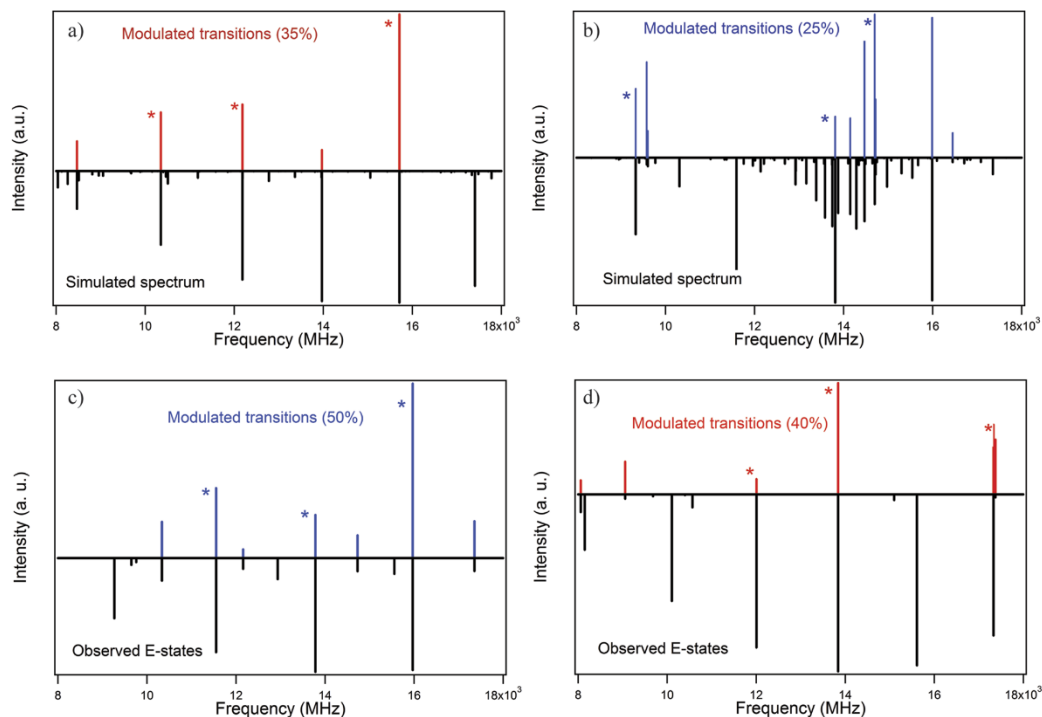


FIG. 3. Conformer-specific and methyl rotor specific spectra for the $0a_1$ methyl rotor state of the (a) all *trans* and (b) *tgt* conformers of 2-hexanone using strong field coherence breaking. Black lines are simulated spectra. Transitions whose intensities were modulated by more than (a) 35% and (b) 25% are displayed in red and blue, respectively. Conformer-specific and internal methyl rotor specific spectra for the $1e$ methyl rotor states of (c) *tgt* and (d) all *trans* conformers of 2-hexanone using strong field coherence breaking. Black lines are observed *e*-state transitions in the spectrum. Transitions whose intensities were modulated by more than (c) 50% and (d) 40% are displayed in blue and red, respectively. Asterisks denote the resonant single frequencies used in the experiment.

as a starting point for fitting the $1e$ methyl rotor spectrum using the XIAM fitting program.³¹ A total of 12 rotational transitions were assigned to the $1e$ methyl rotor state of the *tgt* conformer of 2-hexanone.

The procedure was repeated a final time using resonant frequencies at 13 839.9375 ($4_{1,4}-3_{0,3}$), 17 330 MHz ($6_{1,6}-5_{0,5}$), and 12 005.0625 ($3_{1,3}-2_{0,2}$), respectively. The final difference spectrum shown in Fig. 3(d) contained a total of 6 transitions whose intensities were modulated by more than 40%. These transitions were assigned to the $1e$ methyl rotor state of the *ttt* conformer. The preliminary fit was subsequently refined to assign a total of 13 *ttt* $1e$ rotational transitions.

After all possible $0a_1$ and $1e$ torsional states for the *tgt* and *ttt* conformers were assigned, remaining unassigned rotational transitions were due to the $0a_1$ and $1e$ torsional states of the *ttg* conformer of 2-hexanone. Since all could be identified with a single conformer, SFCB was not helpful to the assignment process and therefore was not carried out.

By applying SFCB to the rotational spectrum, we were able to effectively identify rotational transitions belonging to the $0a_1$ and $1e$ methyl torsional levels of the three populated conformers of 2-hexanone, ultimately assigning and extracting structural parameters unique to each conformer as shown in Table I. The rotational spectrum is dominated by the *tgt* and *ttt* conformers as these are the two lowest energy structures, with the *tgt* conformer being the global minimum followed by the *ttt* conformer just 0.24 kJ/mol higher in energy. The observed conformers are always *trans* about the first dihedral. According to the calculations (Table I), there is little cost in energy when the second dihedral angle is *gauche*; however, a *gauche* conformation in the third dihedral (a pure alkyl chain *gauche* defect) raises the relative energy of the *ttg* and *tgg* conformers to 2.69 kJ/mol and 3.09 kJ/mol, respectively. Of these two less stable conformers, only the *ttg* conformer was observed experimentally. All three observed conformers are near prolate symmetric tops ($A > B \approx C$). Since the polar C=O bond is responsible for much of the permanent dipole moment, the projection of this C=O vector

TABLE I. Experimentally determined structural parameters of the three identified conformations of 2-hexanone.

	<i>tgt</i>		<i>tft</i>		<i>ttg</i>	
	Theory ^a	Expt.	Theory ^a	Expt.	Theory ^a	Expt.
A (MHz)	5807.6420	5864.8301(33)	7560.1717	7510.353 9(99)	5860.9716	5847.4445(17)
B (MHz)	1241.7130	1244.3694(45)	1039.3578	1040.734 3(13)	1177.0372	1173.7582(62)
C (MHz)	1157.3273	1153.4418(32)	940.1517	941.131 6(10)	1045.5183	1052.4360(34)
μ_a (D)	−0.601	...	0.250	...	0.941	...
μ_b (D)	−2.540	...	2.810	...	−2.522	...
μ_c (D)	−0.829	...	−0.030	...	0.642	...
Δ_I (kHz)	...	0.316(23)	...	0.031(10)	...	−0.189(77)
Δ_K (kHz)	...	34.282(2.6)
Δ_{JK} (kHz)	...	−3.534(85)	...	−0.412(32)
δ_J (kHz)	...	−0.016(12)	...	−0.005 49(26)	...	0.118(59)
δ_K (kHz)	...	−0.018(06)
D_{p12I} (MHz)	...	0.241(14)	...	0.009 32(32)
D_{p12K} (MHz)	...	−5.131(32)
D_{p12-} (MHz)	...	0.166(03)	...	0.002 55(73)
F_0 (GHz) ^b	...	158	...	158	...	158
E_{rel} (kJ/mol) ^c	0	...	0.24	...	2.69	...
N_A/N_E	...	39/12	...	18/13	...	13/4
V_3 (cm ^{−1})	193.1	233.24(43)	139.6	187.46(02)	137.9	182.47(10)
T_{rot} (K)	...	1.00 ± 0.15	...	0.90 ± 0.11	...	0.87 ± 0.17
σ (MHz)	...	0.0242	...	0.0216	...	0.0295

^aDFT B3LYP DefTZVP-D3BJ level of theory.^bInternal rotor constant was fixed to 158 GHz for all three structures.^cZero-point corrected relative energy.

on the inertial axes will give an approximate measure of the intensities of a-, b-, and c-type transitions (μ_a , μ_b , and μ_c), as the intensity of a microwave transition in CP-FTMW scales with the square of the dipole moment.³⁵ The major component of the dipole moment projects primarily along the b inertial axis for all three conformers, resulting in predominately b-type transitions in the microwave spectrum. The full list of assigned transitions is included in the [supplementary material](#).

The predicted barrier heights are relatively low (Table I), leading to large splittings of up to several hundred MHz, making these splittings difficult to recognize in some cases. Even though some of the splittings due to internal rotation were clearer than others, SFCB identified rotational transitions built off the 1e torsional states that could not have been easily identified otherwise. As a part of the fitting procedure, the XIAM fitting program was used to determine the barriers to methyl internal rotation for all three observed conformers, using a total of 13, 12, and 4 0a₁/1e methyl rotor pairs for the *tft*, *tgt*, and *ttg* conformers, respectively. XIAM was chosen over other internal rotor fitting programs since our fit is confined to relatively low J and K_a values and has been successfully used to fit intermediate barriers in previous studies including 2-pentanone.¹⁹ The magnitude of the barrier derived from the fits is nearly the same as those reported previously for methyl ketones with the shorter alkyl chains present in ethyl methyl ketone (183.17 cm^{−1})³⁶ and the all-*trans* conformer of 2-pentanone (188 cm^{−1}).¹⁹ However, in the case of 2-pentanone, the conformation of the alkyl chain

influenced the barrier height, as the higher energy C₁ structure (*tg* in our notation) had a fitted barrier height of 238 cm^{−1}, more than 50 cm^{−1} higher than the all-*trans* conformer. Our best-fit barrier for the analogous *tgt* conformer of 2-hexanone (also of C₁ symmetry) is 233 cm^{−1}, very close to the barrier in 2-pentanone. That this is a common feature of the low-symmetry conformers of a range of methyl ketones is evident from the barriers determined previously for allyl acetone (225 cm^{−1})³⁷ and methyl isobutyl ketone (250 cm^{−1}).³⁸

Strong field coherence breaking is a powerful tool for identifying rotational transitions belonging to a single component in a gas mixture. The method has already been applied to identify transitions due to conformational isomers,¹³ C isotopomers in natural abundance, and to identify transitions due to free radicals in the complex chemical mixture emanating from a flash pyrolysis source. Here, strong field coherence breaking was successfully implemented for the first time in selectively modulating 0a₁ and 1e torsional states of the two lowest energy conformers of 2-hexanone. There are other circumstances in which SFCB is likely to prove itself a useful tool. For instance, CP-FTMW spectroscopy is being used to record microwave spectra at room temperature, where vibrational hot bands are present in significant abundance.^{39,40} Identification and assignment of the rotational transitions due to each vibrationally excited state provide insight to the nature of the low-frequency vibrations that are populated. SFCB has the potential to assist in this process, as each vibrational level supports a set of rotational levels

in which SFCB can be carried out, although the congestion of these spectra will require care in choice of resonant frequencies used in the SFCB technique. In addition, there are tunneling splittings due to other motions than methyl internal rotation. Particularly, when more than one such tunneling process is present, the identification of sets of rotational transitions due to each could be a sizable help in sorting through the multidimensional quantum mechanics responsible for it.

EXPERIMENTAL

2-hexanone (98%, Aldrich) was introduced to the gas phase by heating a stainless-steel sample holder to 60 °C. The sample was entrained in 3.1 bars of He before expanding into vacuum through the 1 mm diameter orifice of a solenoid driven pulsed valve (Parker General Series 9) operating at 10 Hz. The ensuing supersonic expansion is interrogated by the broadband microwave sweeps, and the free induction decay (FID) is collected and digitized for 16 μ s using a 13 GHz, 40 GS/s real time digitizer (Guzik ADC6131). The experimental timing allowed for the collection of 20 FIDs per gas pulse separated from one another by 20 μ s. The time domain signal is filtered with a Kaiser-Bessel window and is fast Fourier transformed to obtain the final frequency domain spectrum using a custom MATLAB routine. The experimental resolution for a 16 μ s collection period is 60 kHz.

SUPPLEMENTARY MATERIAL

See [supplementary material](#) for the Boltzmann plots used to determine the rotational temperatures of each assigned conformer as well as the frequency lists.

ACKNOWLEDGMENTS

The authors gratefully acknowledge support from the Department of Energy Basic Energy Sciences Gas-Phase Chemical Physics program under Grant No. DE-FG02-96ER14656.

REFERENCES

- ¹L. Goodman, V. Pophristic, and F. Weinhold, *Acc. Chem. Res.* **32**, 983 (1999).
- ²P. R. Bunker and P. Jensen, *Molecular Symmetry and Spectroscopy*, 2nd ed. (NRC Research Press, 2006), p. 748.
- ³J. M. Hollas, *High Resolution Spectroscopy*, 2nd ed. (Wiley, New York, 1998), p. 260.
- ⁴L. H. Spangler, *Annu. Rev. Phys. Chem.* **48**, 481 (1997).
- ⁵B. J. van der Veken, R. Maas, G. A. Guirgis, H. D. Stidham, T. G. Sheehan, and J. R. Durig, *J. Phys. Chem.* **94**, 4029 (1990).
- ⁶J. R. Daring and D. A. C. Compton, *J. Phys. Chem.* **83**, 2873 (1979).
- ⁷D. Gorse, D. Cavagnat, M. Pesquer, and C. Lapouge, *J. Phys. Chem.* **97**, 4262 (1993).
- ⁸W. G. Fateley and F. A. Miller, *Spectrochim. Acta* **17**, 857 (1961).
- ⁹J. C. Dean, P. Navotnaya, A. P. Parobek, R. M. Clayton, and T. S. Zwier, *J. Chem. Phys.* **139**, 144313 (2013).
- ¹⁰G. Williams, N. L. Owen, and J. Sheridan, *Trans. Faraday Soc.* **67**, 922 (1971).
- ¹¹H. V. L. Nguyen, W. Stahl, and I. Kleiner, *Mol. Phys.* **110**, 2035 (2012).
- ¹²C. C. Lin and J. D. Swalen, *Rev. Mod. Phys.* **33**, 841 (1959).
- ¹³H. V. L. Nguyen and W. Stahl, *J. Chem. Phys.* **135**, 024310 (2011).
- ¹⁴J. T. A. Gall, J. Thomas, F. Xie, Z. Wang, W. Jäger, and Y. Xu, *Phys. Chem. Chem. Phys.* **19**, 29508 (2017).
- ¹⁵K. P. Rajappan Nair, S. Herbers, D. A. Obenchain, J. Grabow, and A. Lesarri, *J. Mol. Spectrosc.* **344**, 21 (2018).
- ¹⁶R. Kannengießer, W. Stahl, H. V. L. Nguyen, and I. Kleiner, *J. Phys. Chem. A* **120**, 3992 (2016).
- ¹⁷W. Li, A. Vigorito, C. Calabrese, L. Evangelisti, L. B. Favero, A. Maris, and S. Melandri, *J. Mol. Spectrosc.* **337**, 3 (2017).
- ¹⁸L. Ferres, H. Mouhib, W. Stahl, and H. V. L. Nguyen, *Chem. Phys. Chem.* **18**, 1855 (2017).
- ¹⁹M. Andresen, I. Kleiner, M. Schwell, W. Stahl, and H. V. L. Nguyen, *J. Phys. Chem. A* **122**, 7071 (2018).
- ²⁰M. Nakajima and Y. Endo, *J. Chem. Phys.* **140**, 011101 (2013).
- ²¹A. O. Hernandez-Castillo, C. Abeysekera, B. M. Hays, and T. S. Zwier, *J. Chem. Phys.* **145**, 114203 (2016).
- ²²A. O. Hernandez-Castillo, C. Abeysekera, B. M. Hays, I. Kleiner, H. V. L. Nguyen, and T. S. Zwier, *J. Mol. Spectrosc.* **337**, 51 (2017).
- ²³S. M. Fritz, A. O. Hernandez-Castillo, C. Abeysekera, B. M. Hays, and T. S. Zwier, *J. Mol. Spectrosc.* **349**, 10 (2018).
- ²⁴C. Abeysekera, A. O. Hernandez-Castillo, J. F. Stanton, and T. S. Zwier, *J. Phys. Chem. A* **122**, 6879 (2018).
- ²⁵J. Pieper, C. Hemken, R. Büttgen, I. Graf, N. Hansen, K. A. Heufer, and K. Kohse-Höinghaus, *Proc. Combust. Inst.* **37**, 1683 (2019).
- ²⁶F. Hoppe, U. Burke, M. Thewes, A. Heufer, F. Kremer, and S. Pischinger, *Fuel* **167**, 106 (2016).
- ²⁷U. Burke, J. Beeckmann, W. A. Kopp, Y. Uygun, H. Olivier, K. Leonhard, H. Pitsch, and K. A. Heufer, *Combust. Flame* **168**, 296 (2016).
- ²⁸A. Elfasakhany, *Eng. Sci. Technol. Int. J.* **19**, 1224 (2016).
- ²⁹S. M. Fritz, B. M. Hays, A. O. Hernandez-Castillo, C. Abeysekera, and T. S. Zwier, *Rev. Sci. Instrum.* **89**, 093101 (2018).
- ³⁰T. A. Halgren, *J. Comput. Chem.* **17**, 490 (1996).
- ³¹D. J. Frisch, M. J. Trucks, G. W. Schlegel, H. B. Scuseria, G. E. Robb, M. A. Cheeseman, J. R. Scalmani, G. Barone, V. Mennucci, B. Petersson, G. A. Nakatsuji, H. Caricato, M. Li, X. Hratchian, H. P. Izmaylov, A. F. Bloino, J. Zheng, and G. Sonnenb, GAUSSIAN 09, Revision E.01, Gaussian, Inc., Wallingford, CT, 2009.
- ³²S. Grimme, *J. Chem. Phys.* **124**, 034108 (2006).
- ³³H. M. Pickett, *J. Mol. Spectrosc.* **148**, 371 (1991).
- ³⁴H. Hartwig and H. Dreizler, *Z. Naturforsch. A* **51**, 923 (1996).
- ³⁵G. G. Brown, B. C. Dian, K. O. Douglass, S. M. Geyer, S. T. Shipman, and B. H. Pate, *Rev. Sci. Instrum.* **79**, 053103 (2008).
- ³⁶H. V. L. Nguyen, V. Van, W. Stahl, and I. Kleiner, *J. Chem. Phys.* **140**, 214303 (2014).
- ³⁷L. Tulimat, H. Mouhib, I. Kleiner, and W. Stahl, *J. Mol. Spectrosc.* **312**, 46 (2015).
- ³⁸Y. Zhao, W. Stahl, and H. V. L. Nguyen, *Chem. Phys. Lett.* **545**, 9 (2012).
- ³⁹B. Reinhold, I. A. Finneran, and S. T. Shipman, *J. Mol. Spectrosc.* **270**, 89 (2011).
- ⁴⁰S. Samdal, H. Møllendal, and J. C. Guillemin, *J. Phys. Chem. A* **119**, 3375 (2015).